Normandie Université

UNIVERSITÉ DE ROUEN NORMANDIE

THÈSE

Pour obtenir le diplôme de doctorat

Spécialité **ELECTRONIQUE, MICROELECTRONIQUE, OPTIQUE ET LASERS, OPTOELECTRONIQUE MICROONDES**

Préparée au sein de l'**Université de Rouen Normandie**

En cotutelle internationale avec l'**Université de SFAX (Tunisie), TUNISIE**

Ambient Backscatter Communications for 5G-NR: Modeling, Hardware Design, and Experimental Validation

Présentée et soutenue par

LEFKI MARIEM

Thèse soutenue le 17/12/2025

devant le jury composé de :

M. KADI MONCEF	Maître de Conférences HDR - ESIGELEC ROUEN	Directeur de thèse
M. GHORBEL MOHAMED	Professeur (dans un établissement à l'étranger) - Université de SFAX (Tunisie)	Co-directeur de thèse
MME ALGANI CATHERINE	Professeur des Universités - CNAM (Paris)	Membre du jury
M. BACCAR SAHBI	Enseignant chercheur - ESIGELEC ROUEN	Membre du jury
M. MNIF HASSENE	Professeur des Universités - Université de SFAX (Tunisie)	Membre du jury
M. SHALL HANEN	Associate Professor - American University of the Middle East (AUM)	Membre du jury
M. BEN AISSA DALENDA	Maître de Conférences HDR - Université de Tunis - El Manar	Rapporteur du jury
M. VUONG TAN PHU	Professeur des Universités - Université de Grenoble Alpes	Rapporteur du jury

Thèse dirigée par **KADI MONCEF** (INSTITUT DE RECHERCHE EN SYSTEMES ELECTRONIQUES EMBARQUES) et **GHORBEL MOHAMED** (Université de SFAX (Tunisie))

ESIGELEC

MI/IΣ

irseem UR 4353

To my parents,

As a sign of love, recognition, and deep gratitude.

"I love you dearly."

To my sisters and my brother,

For your affection, support, and unfailing bond.

"You are my strength and my pride."

To all my friends,

For their presence and kindness throughout this journey.

"You are the family I choose."

Acknowledgements

My deepest gratitude goes to God, who has granted me the courage, determination, and health to accomplish this modest work.

I would like to express my sincere thanks to my thesis supervisor, Prof. Moncef Kadi, Professor at the University of Rouen Normandie / ESIGELEC / IRSEEM, for supervising me throughout this work. I also wish to convey my profound gratitude for his valuable guidance and the time he devoted to helping me carry out this research under the best possible conditions. I am deeply thankful for his exceptional qualities, both human and scientific, which made the development and completion of this research possible.

I extend my heartfelt thanks to my co-supervisor, Prof. Mohamed Ghorbel, Professor at the University of Sfax / ENET'Com / ATMS (Tunisia). His constant support, scientific rigor, and great availability were essential to the success of this work. I would also like to highlight his attentive listening, kindness, and humanity, which have deeply marked my academic journey.

My sincere gratitude also goes to Prof. Sahbi Baccar, Professor at the University of Rouen Normandie / ESIGELEC / IRSEEM, for his attentive guidance and valuable advice throughout this thesis. I especially appreciated his availability, constructive remarks, and his ability to guide discussions with clarity and precision. His attention to detail and scientific rigor greatly contributed to improving the coherence and quality of this work. I am also grateful for his continuous support and consistently kind attitude.

I would like to express my appreciation to Prof. Hanen Shall, co-supervisor and Professor at the American University of the Middle East (AUM), for her guidance and involvement throughout this work. Her constructive feedback, availability, and insightful advice were of great help in advancing my research. I am deeply thankful for her kindness, constant support, and the attention she paid to the scientific quality of this thesis.

My sincere thanks also go to Prof. Catherine Algani, Professor at Le CNAM EPN EEAM – EASY (France), for the honor she did me by agreeing to serve as a member of the thesis jury.

I would also like to thank my reviewers, Prof. Tân-Phu Vuong, Professor at Grenoble INP – Université Grenoble Alpes (France), and Prof. Dalenda Ben Aïssa, Professor at the University of Tunis El Manar (Tunisia), for the honor they did me by agreeing to review this thesis.

I wish to extend my thanks to Prof. Hassène Mnif, Professor at the University of Sfax / ENET'Com (Tunisia), for agreeing to be part of the jury.

I would like to express my special thanks to Mr. Moni Sankar, engineer at the IRSEEM Laboratory (ESIGELEC, France), for his invaluable collaboration and technical assistance

throughout this work. His availability, professionalism, and commitment were decisive in carrying out and successfully completing the experimental measurements conducted during this thesis. I am deeply grateful for his constant support, patience, and exemplary dedication, which significantly contributed to the quality of my experimental results.

I wish to thank all the members of the IRSEEM Laboratory (ESIGELEC, France) for their warm welcome, their collaboration, and the stimulating research environment they provided. A special thought goes to my colleagues from the Electronics and Systems (ES) division, with whom I shared valuable scientific and human experiences. Their support, good humor, and team spirit greatly contributed to making this research journey both enriching and enjoyable.

I also wish to thank the ATMS Laboratory (University of Sfax, Tunisia) for its hospitality and for the scientific environment it provided.

I express my deepest gratitude to my parents, for their love, sacrifices, and unwavering trust. Their moral support, prayers, and constant presence have been my greatest source of strength and motivation throughout this journey.

I would also like to thank my brother and my sisters for their affection, encouragement, and kindness, which have accompanied me through every stage of this thesis.

I would like to express my deepest respect and sincere gratitude to all my teachers at ISIMED and ISIMG.

I am certainly forgetting some people here, and I sincerely apologize for that.

Once again, my heartfelt thanks to everyone who has helped guide me to this memorable day.

Abstract

The objective of this Ph.D. thesis is to develop and evaluate propagation-based applications within the framework of Ambient Backscatter Communication (AmBC) systems. This research investigates the fundamental limitations of such technology, proposes enhancements inspired by recent advances in the field, and assesses the overall system performance through both theoretical and experimental approaches.

Particular emphasis is placed on the design and implementation of a novel backscatter tag architecture that integrates multiple components, including a sensing module and an RF communication block. Extensive measurement campaigns were conducted in controlled environments (anechoic and semi-anechoic chambers) to characterize the system's propagation behavior under realistic conditions. In parallel, an SDR-based receiver chain, developed using the USRP B210 platform and GNU Radio, was implemented for backscattered signal demodulation and communication performance analysis.

The obtained results demonstrate the feasibility and effectiveness of the proposed system architecture, highlighting its potential for low-power and scalable wireless sensing applications in future 5G and IoT networks.

Keywords: Ambient Backscatter Communication (AmBC), 5G-NR, Bistatic Propagation, Link Budget, Free Space Path Loss (FSPL), BPSK Modulation, IoT, Biomedical Applications, SDR, Experimental Validation.

Résumé

L’objectif de cette thèse de doctorat est de développer et d’évaluer des applications basées sur la propagation dans le cadre des systèmes de communication par rétrodiffusion ambiante (AmBC). Ce travail de recherche examine les limites fondamentales de cette technologie, propose des améliorations inspirées des avancées récentes dans le domaine, et évalue les performances globales du système à travers des approches à la fois théoriques et expérimentales.

Une attention particulière est portée à la conception et à la mise en œuvre d’une nouvelle architecture de tag de rétrodiffusion, intégrant plusieurs composantes, notamment un module de mesure et un bloc de communication RF. Des campagnes de mesures approfondies ont été menées dans des environnements contrôlés (chambres anéchoïque et semi-anéchoïque) afin de caractériser le comportement de propagation du système dans des conditions réalistes. En parallèle, une chaîne de réception SDR, développée à l’aide de la plateforme USRP B210 et du logiciel GNU Radio, a été mise en place pour la démodulation du signal rétrodiffusé et l’analyse des performances de communication.

Les résultats obtenus démontrent la faisabilité et l’efficacité de l’architecture proposée, soulignant son potentiel pour des applications de détection sans fil à faible consommation et à grande échelle dans les futurs réseaux 5G et IoT.

Mots-clés : Communication par rétrodiffusion ambiante (AmBC), 5G-NR, propagation bistatique, budget de liaison, pertes en espace libre (FSPL), modulation BPSK, IoT, applications biomédicales, SDR, validation expérimentale.

Glossary

3GPP	3rd Generation Partnership Project
AD8232	Single-Lead Low-Power Heart Rate Monitor Front End (Analog Devices)
ADC	Analog-to-Digital Converter
ADG902	RF Switch Model (Analog Devices)
AM	Amplitude Modulation
AmBC	Ambient Backscatter Communication
APL	Available Path Loss
ASK	Amplitude Shift Keying
AWGN	Additive White Gaussian Noise
BackCom	Backscatter Communication
BER	Bit Error Rate
BiS	Bistatic Scatter
BLE	Bluetooth Low Energy
BPM	Beats Per Minute
BPSK	Binary Phase Shift Keying
BS	Base Station
BW	Bandwidth
COTS	Commercial Off-The-Shelf
CSS	Chirp Spread Spectrum
CW	Continuous Wave
dB / dBi / dBm	Decibel / Decibel-isotropic / Decibel-milliwatt
Ded-BackCom	Dedicated Backscatter Communication
DS18B20	Digital Temperature Sensor (Maxim Integrated)
ECG	Electrocardiogram
EM	Electromagnetic
ESP8266	Wi-Fi Microcontroller (Espressif Systems)
FM	Frequency Modulation
FSK	Frequency Shift Keying
FSPL	Free-Space Path Loss
GHz / MHz / MS/s	Gigahertz / Megahertz / Mega Samples per Second
GNU	GNU Radio Software Framework
GR	Receiver Antenna Gain
IoT	Internet of Things
I/Q	In-phase and Quadrature
ISM	Industrial, Scientific and Medical Band
K	Boltzmann Constant
LM335	Analog Temperature Sensor (Texas Instruments)

LOS / NLOS	Line-of-Sight / Non-Line-of-Sight
LPF	Low-Pass Filter
LTE	Long-Term Evolution
MAX30100	Pulse Oximeter and Heart Rate Sensor (Maxim Integrated)
MCU	Microcontroller Unit
MIMO	Multiple Input Multiple Output
mmWave	Millimeter Wave
MSP430FR5969	Ultra-Low-Power Microcontroller (Texas Instruments)
NF	Noise Figure
NR	New Radio
NRZ	Non-Return-to-Zero
OOK	On-Off Keying
PAM	Pulse Amplitude Modulation
PCB	Printed Circuit Board
PL	Path Loss
PM	Phase Modulation
PM4P	Patient Monitor for Four Parameters
PSK / QPSK	Phase Shift Keying / Quadrature Phase Shift Keying
PSL	Power Sensor Loss
Pt	Transmitted Power
QAM	Quadrature Amplitude Modulation
RCS	Radar Cross Section
RF	Radio Frequency
RMa	Rural Macrocell
Rx / Tx	Receiver / Transmitter
SAS-571	Double Ridge Guide Horn Antenna (A.H. Systems)
SDR	Software-Defined Radio
SENRx	Receiver Sensitivity
SENS	Sensitivity
SMA	SubMiniature Version A (RF Connector)
SNR / SNRmin	Signal-to-Noise Ratio / Minimum Signal-to-Noise Ratio
SPST	Single-Pole Single-Throw (RF Switch Type)
SpO_2	Blood Oxygen Saturation
T	Absolute Temperature (Kelvin)
U.FL	Ultra-Miniature Coaxial RF Connector
UHD	USRP Hardware Driver
UMa	Urban Macrocell
UMi	Urban Microcell
USRP B210	Universal Software Radio Peripheral (Ettus Research)
VSWR	ding Wave Ratio
Wi-Fi	Wireless Fidelity

WPT	Wireless Power Transfer
5G / 5G-NR / 6G	Fifth / Fifth-Generation New Radio / Sixth-Generation Network

Table of Contents

Acknowledgements 2

Abstract 4

Résumé 5

General Introduction 18

References 21

Chapter 1: State of the Art 22

1. Introduction 22
2. Fundamentals of Ambient Backscatter Communication 23
   - 2.1 Backscatter communication 23
   - 2.2 Basic Principle 24
   - 2.3 Typical Architectures and Classifications of Backscatter Communication Systems 26
     - 2.3.1 Classification Based on RF Carrier Source 26
     - *2.3.2* Classification Based on System Geometry 27
3. Backscatter Modulation Techniques 29
   - 3.1 Amplitude Modulation (AM) 29
   - 3.2 Phase Modulation (PM) 30
   - 3.3 Frequency Modulation 31
4. 5G-NR as a Carrier for Ambient Backscatter communication 32
   - 4.1. Spectral and Signal Properties of 5G 32
     - 4.1.1. Frequency Spectrum and Bandwidth of 5G 32
     - 4.1.2. 5G Waveform Considerations for Ambient Backscatter 33
   - 4.2 Ambient RF Sources for Backscatter Communication 34
5. Receiver Architectures in Backscatter Communication Systems 35
   - 5.1 Classification of Receiver Types in AmBC 35
     - 5.1.1. Software-Defined Radio (SDR) Receivers 35
     - 5.1.2. Commercial Off-the-Shelf (COTS) Receivers 36
     - 5.1.3. Dedicated Ultra-Low-Power Analog Receivers 36
     - 5.1.4. Advanced and Adaptive Receiver Architectures 36
   - 5.2. Sensitivity Challenges in Backscatter Reception 37
     - 5.2.1. Sources of Sensitivity Degradation 37
     - 5.2.2. Classical Approaches 37
     - 5.2.3. Advanced Sensitivity Enhancement Techniques 38
     - 5.2.4. Practical Considerations 38
     - 5.2.5. Summary 39

6. Related Work and Existing Prototypes 39
6.1. AmBC Systems in Literature 39
6.1.1. Indoor and Controlled Environments 39
6.1.2. Outdoor and Real-World Deployments 40
6.2. Summary of Key Implementations 42
7. Challenges 44
8. Positioning of the Thesis 45
8.1. Research Gaps Identified 45
8.2. Thesis Contributions 45
8.3. Positioning within Literature 46
References 48
Chapter 2 : Propagation Modeling and Feasibility Study of 5G Ambient Backscatter Communication 54
1. Introduction 54
2. General Background on 3GPP Path-Loss Models 55
2.1. Concept of Path Loss 55
2.2. Geometrical Definitions and Parameters 57
2.3. Analytical Formulation of 3GPP Path-Loss Models 58
2.3.1. Rural Macrocell (RMa) Model 58
2.3.2. Urban Macrocell (UMa) Model 60
2.3.3. Urban Microcell / Street Canyon (UMi) Model 61
2.4. Theoretical Reference: Free-Space Path-Loss (FSPL) Model 62
2.5. Comparative Analysis of the Models 62
2.6. Discussion 64
3. Simulation Methodology 65
3.1. Geometric model parameters 65
3.2. Input Parameters 66
3.3. Link Budget Equations 67
3.4. Simulation Flow 67
4. Results and Analysis 68
4.1. Received Power Estimation 68
4.2. Comparison and Analysis of Available Path Loss (APL) for Different Receiver Sensitivities and Sensor Losses 70
4.3. BackCom Range Evaluation under Different Propagation Scenarios 72
4.4. Available Path Loss Evaluation under Different Propagation Scenarios 73
4.5. Cartography of Available Path Loss for Different Bandwidths 75
4.6. Available BackCom Range under Different Propagation and Bandwidth Scenarios 77

5. Conclusion 79
References 81
Chapter 3: Design and Experimental Validation of a Bistatic 5G Ambient Backscatter Communication System 82
1. Introduction 82
2. Backscatter Tag Architecture 82
2.1. Hardware Description and System Overview 82
2.2. Operating Principle and Theoretical Analysis of BPSK Backscatter Modulation 84
3. Bistatic AmBC System Theoretical Model 88
3.1. Particular Case 1 : Tx, Rx are collocated 90
3.2. Particular Case 2 : Tx, Sensor and Rx are aligned 91
3.3. General case: Tx, Sensor and Rx are not aligned 93
3.3.1. Received power variation as a function of geometrical parameters 93
3.3.2. Received power variation as a function of antenna gain 99
4. Measurement setup 101
4.1. Experimental scenarios 101
4.2. Measurement Environments 104
4.2.1. Collocated Measurement Setup in Full Anechoic chamber (Setup A) 106
4.2.2. Aligned Measurement Setup in Full and Semi Anechoic Chambers (Setup B) 106
4.3. Dislocated Measurement Setup in Semi and Full Anechoic Chamber With Fixed Angles of Tx and Rx (Setup C) 107
4.4. Dislocated measurement setup in semi-Anechoic Chamber With Variable Rx Angle (Setup D) 109
4.5. Dislocated Measurement Setup in Semi-Anechoic Chamber With Tx and Rx at 0° Relative to Tag (Setup E) 109
5. Results and discussion 110
5.1. Set-up A results discussion 110
5.2. Set-up B results discussion 111
5.3. Set-up C results discussion 112
5.4. Set-up D results discussion 113
5.5. Set-up E results discussion 114
5.6. Discussion on the performances of BPSK AmbC 5G-NR in Bi-Static Configuration 116
5.6.1. The received SNR 116
5.6.2. Binary Data Rate 117
5.6.3. Discussion on Sensitivity and communication range 118
6. Conclusion 119
References 121

Chapter 4 : Receiver Configuration, Signal Processing, and Experimental Validation in Real Conditions for AmBC Communications Systems-Application for Healthcare Monitoring 122
1. Introduction 122
2. Experimental configuration for receiver performance evaluation 123
2.1. Block-Level Functionality in the GNU Radio Flowgraph 124
2.1.1. USRP Source block 126
2.1.2. Complex to Magnitude conversion 127
2.1.3. Lowpass Filter 128
2.1.4. Complete Block 129
3. Modeling and Evaluation of Free Space Path Loss 130
4. Bit Error Rate (BER) Measurement and impact on Communication Reliability 130
5. Time-Synchronized Multi-Sensor Backscatter Prototypes 136
5.1. Prototype 1: Single-Sensor Backscatter Tag 137
5.2. Prototype 2: Low-Cost Biomedical Backscatter System (PM4P) 138
5.3. Effect of Sample Rate on Signal Reception at 3.5 GHz 144
6. Recovering Backscatter Information from Ambient RF Sources 149
6.1. Backscattered Signal Behavio in Wi-Fi Based Systems 149
6.2. Backscattered Signal Behavior in 5G Base Station-Oriented Communication Systems 152
7. Conclusion 154
References 156
General Conclusion 157
Appendix 160
1. Available Path Loss (APL) Comparison for RMa, UMa, and UMi (LOS/NLOS) 160
2. BackCom Range Evaluation for the RMa Scenario 162
3. 3D representation of the Available Path Loss (APL) for the UMa Scenario 163
4. Cartography of Available Path Loss for Different Bandwidths under the UMa Scenario 164
5. Cartography of Available Path Loss for Different Bandwidths under the RMa Scenario 165
6. Available BackCom Range under Different Propagation and Bandwidth Conditions for the UMi Scenario 166
7. Available BackCom Range under Different Propagation and Bandwidth Conditions for the UMi Scenario 167
List of publications 168

List of Figures

Figure 1. Conceptual Analogy Between Optical Heliograph and RF Backscatter Communication. 23
Figure 2. Illustration of an ambient backscatter communication system. 25
Figure 3. Paradigms for backscatter communications: (a) Dedicated backscatter; (b) Ambient backscatter. 27
Figure 4. Configurations of backscatter communication systems: (a) Monostatic; (b) Bistatic co-located; (c) Bistatic dis-located. 29
Figure 5. Ambient backscatter communication prototypes [67], [68], showing the fabricated RF front-end and the MSP430-based backscatter tag. 40
Figure 6. Backscatter modulator prototype, illustrating a compact PCB design equipped with an SMA connector and matching network for impedance-based modulation experiments [70]. 41
Figure 7. Backscatter communication PCB prototype, illustrating the front and back sides of the board capable of harvesting, transmitting, and receiving signals [4]. 41
Figure 8. Reflective backscatter tag prototype, illustrating a compact PCB structure equipped with an SMA connector and impedance-switching network for signal reflection and modulation [72]. 42
Figure 9. Definition of d2D and d3D for outdoor user terminals [13]. 57
Figure 10. Comparison of path loss between FSPL and 3GPP propagation models (UMa,UMi,RMa) under LOS and NLOS conditions. 63
Figure 11. Definition of geometrical parameters for the bistatic AmBC link (BS, sensor, and Rx). 66
Figure 12. Simulation methodology flowchart for bistatic AmBC feasibility analysis. 68
Figure 13. Received power at the backscatter sensor (P_S) as a function of the TX–Sensor distance for the three propagation environments (RMa, UMa, UMi) under LOS and NLOS conditions. (a) PSL = 5 dB, (b) PSL = 10 dB, (c) PSL = 15 dB, (d) PSL = 25 dB, (e) PSL = 30dB. 69
Figure 14. Comparison of Available Path Loss (APL) variations as a function of the TX–Sensor distance for the three receiver sensitivities (RX1, RX2, and RX3) and different sensor loss levels (PSL = 5, 10, 15, 25, 30 dB). 71
Figure 15. Estimated bistatic BackCom range as a function of sensor losses (PSL) and TX–Sensor distance under different 3GPP propagation environments UMa in LOS and NLOS conditions (RMa, UMi in Appendix). 73
Figure 16. 3D representation of the Available Path Loss (APL) as a function of TX–Sensor distance and sensor losses (PSL) for different propagation models UMa under LOS and NLOS conditions (UMa, UMi in Appendix). 74
Figure 17. Available Path Loss (APL) versus TX–Sensor distance and sensor losses (PSL) for (a) BW_1 = 5 MHz, (b) BW_2 = 10 MHz, and (c) BW_3 = 20 MHz under UMi LOS/NLOS conditions (RMa and UMa results in Appendix). 76
Figure 18. BackCom range maps (ρ) versus TX–Sensor distance and PSL for (a) BW_1 = 5 MHz, (b) BW_2 = 10 MHz, and (c) BW_3 = 20 MHz under UMa LOS/NLOS conditions (RMa and UMi in Appendix). 78
Figure 19. Functional Schematic of the Backscatter Tag Including Control and RF Front-End Modules. 84
Figure 20. Backscatter Tag Prototype Featuring MSP430 Microcontroller, RF Switch (ADG902), LM335 Sensor, and Dipole Antenna. 85
Figure 21. Time-Domain Simulation of BPSK Backscatter Modulation: (Top) Continuous Wave (CW) Signal at 3.5 GHz, (Middle) Baseband NRZ Data Sequence, (Bottom) Resulting BPSK-Modulated Signal. 86
Figure 22. FFT-Based Spectrum of the BPSK-Modulated Signal Illustrating Spectral Broadening Around the Carrier Frequency. 87

Figure 23. Geometric Parameters Definition for a Bi-Static AmBC System Model, (d=4.5 m in practice). 89
Figure 24. Simulated received power in the case where Tx and Rx are perfectly collocated and not perfectly collocated. 91
Figure 25. Simulated received power vs nomalized disance when Tx, Sensor and Rx are aligned..... 92
Figure 26. Definition of the limit angle and the cartography of the motonicity of the received power PR.depending on the value of θ; $x, \theta = xT, \theta T$ in (a) and $x, \theta = xR, \theta R$ in (b). 94
Figure 27. Monotonicity of the received power for different values of θ and a constant Tx-Rx distance,d=4.5m 96
Figure 28. Normalized positions of local mimima and local maxima and their power levels vs θ when PR is not monotonic ($\theta < \theta lim1$), $d = 4.5m$. 97
Figure 29. The received power in dBm as function of θ and x(m) plotted as a 3D Surface, d=4.5m ... 98
Figure 30. A planar cartography of the received power in dBm as function of θ and x 99
Figure 31. Received Backscattered Power as a Function of Rx Antenna Orientation and Tag–Rx Distance, for a Fixed Geometric Angle θ , (a): 3D plot of $PR\phi, x$, with fixed parameters values $PT = 0\text{dBm}$, $GS = 5\text{dBi}$, $GT = 12\text{dBi}$, $d = 4.5m$, and $\theta \simeq 63°$, (b): Evolution of $PR\ \phi$ under the same conditions with fixed value of $xT = 4m$, and $xR = 2m$, (c) : a 2D map of $PR\phi, x$ 101
Figure 32. Illustration of Different Tx-Tag-Rx Geometrical Configurations for Backscatter Experiments. 103
Figure 33. Collocated Measurement Setup in Full Anechoic Chamber (Setup A). 106
Figure 34. Aligned Experimental Setup in Full-Anechoic Chamber (Setup B). 107
Figure 35. Aligned Experimental Setup in Semi-Anechoic Chamber (Setup B). 107
Figure 36. Dislocated Experimental Setup in Full-Anechoic Chamber with Fixed Angles of Tx and Rx (Setup C). 108
Figure 37. Dislocated Experimental Setup in Semi-Anechoic Chamber with Fixed Angles of Tx and Rx (Setup C) 109
Figure 38. Dislocated Experimental Setup in Semi-Anechoic Chamber with Variable Rx Antenna (Setup D) 109
Figure 39. Dislocated Experimental Setup in Semi-Anechoic Chamber with Tx and Rx Antennas at 0° Relative to Tag. (Setup E) 110
Figure 40. Theoretical and Measured Received Backscatter Power for Co-Located Experimental Setup (Setup A) 110
Figure 41. Comparison of Received Backscatter Power in Full and Semi-Anechoic Chambers for Aligned Experimental Setup (Setup B) 111
Figure 42. Received Backscatter Power for Dislocated Experimental Setup with Fixed Angles of Tx and Rx in Full and Semi-Anechoic Chambers (Setup C)..... 112
Figure 43. 2D Plot of Measured Received Backscatter Power for Dislocated Experimental Setup with Variable angle Tag referred to Rx. (Setup D). 113
Figure 44. 3D Plot of Measured Received Backscatter Power for Dislocated Experimental Setup (Setup D) with as function of the geometrical angle θ and the distance Tag-Rx (variable x in the model) 114
Figure 45. Comparison of Received Backscatter Power (for Tag ON and Tag OFF States) in Dislocated Experimental Setup with Tx and Rx at 0° Relative to Tag without absorber (Setup E). 115
Figure 46. Simulation result of the SNR 117
Figure 47. Simulation result of the binary data for two different geometrical configurations of the tag. 118
Figure 48. Experimental Setup for Receiver Performance Evaluation in a Backscatter System. 123
Figure 49. Flowchart of the real-time RX signal processing in GNU Radio..... 124

Figure 50. USRP Source Block Configuration and Raw Signal Reception in GNU Radio..... 127
Figure 51. Complex to Mag Configuration and Signal Reception in GNU Radio. 127
Figure 52. Lowpass filter Configuration and Signal Reception in GNU Radio. 128
Figure 53. Complete block Configuration and Signal Reception in GNU Radio. 129
Figure 54. Receiving power of the tag antenna. 131
Figure 55. Generated Square Wave for BER Assessment. 131
Figure 56. Received Signal from USRP B210 Compared to Reference Square Wave from ESP8266. . 132
Figure 57. Received Signal from USRP B210 Compared to Reference Square-Wave from ESP8266.. 133
Figure 58. Generated Square-Wave for BER Assessment. 134
Figure 59. Measured BER vs received power. 135
Figure 60. Experimental setup in the anechoic chamber, showing the Rx and Tx antennas and the backscatter tag. 137
Figure 61. (a) Received waveform comparison between oscilloscope and USRP B210; 138
Figure 62. (a) Front view and (b) back view of the biomedical monitoring system prototype integrating the MAX30100, DS18B20, and AD8232 sensors with the ESP8266 microcontroller. The design features a 5G external antenna and a 2.4GHz PCB-embedded antenna for wirel 139
Figure 63. Time-Domain Response of Backscattered Signal Corresponding to SpO_2 Data Transmission Using MAX30100 Sensor: (a) Overall Transmission View, (b) Zoomed-In View Highlighting Binary-Encoding of SpO_2 Value. 141
Figure 64. Time-Domain Response of Backscattered Signal Encoding BPM Data Captured by USRP B210 Receiver: (a) Overall Transmission View, (b) Zoomed-In View Showing Binary-Encoding of BPM Value. 142
Figure 65. Time-Domain Response of Backscattered Signal Encoding ECG Data Captured by USRP B210 Receiver: (a) Full Transmission View, (b) Zoomed-In View Showing Binary-Encoding of ECG Value. 144
Figure 66. Time-domain response of backscattered signal encoding all biomedical sensor data captured by the USRP B210 receiver and compared with oscilloscope data. 144
Figure 67. Zoomed time-domain comparison of backscattered signal encoding biomedical data captured by the USRP B210 and oscilloscope, showing signal details and timing alignment. 145
Figure 68. (a) Transmitted signal encoding four biomedical parameters (ECG, temperature, SpO_2, and BPM). (b) Received backscattered signal captured by the USRP B210 and oscilloscope, showing signal degradation and timing variation. 146
Figure 69. Method of implementation for 4 sensors. 147
Figure 70. Final prototype for 4 sensors. 148
Figure 71. Received backscatter data of 4 sensors. 149
Figure 72. Power spectrum of ambient Wi-Fi signal in the 2.4 GHz ISM band. 150
Figure 73. Backscatter communication using ambient Wi-Fi signal for temperature data transmission. 151
Figure 74. Decoding of temperature data from backscattered signal using ambient Wi-Fi transmission. 152
Figure 75. Power spectral density of ambient 5G signals captured at different frequency bands..... 152
Figure 76. Outdoor experimental setup for backscatter communication using ambient 5G signals. 153
Figure 77. LM335 sensor data extraction using 5G ambient signal with backscatter modulation. 154
Figure 78. Comparison of Available Path Loss (APL) variations as a function of the TX–Sensor distance for the three receiver sensitivities (RX1, RX2, RX3) and different sensor loss levels (PSL = 5, 10, 15, 25, 30 dB). 161

Figure 79. Estimated bistatic BackCom range as a function of sensor losses (PSL) and TX–Sensor distance under different 3GPP propagation environments Umi and Rma in LOS and NLOS conditions. 162
Figure 80. 3D representation of the Available Path Loss (APL) as a function of TX–Sensor distance and sensor losses (PSL) for different propagation models Rma and Umi under LOS and NLOS conditions. 163
Figure 81. Available Path Loss (APL) versus TX–Sensor distance and sensor losses (PSL) for (a) BW_1 = 5 MHz, (b) BW_2 = 10 MHz, and (c) BW_3 = 20 MHz under UMa LOS/NLOS conditions. 164
Figure 82. Available Path Loss (APL) versus TX–Sensor distance and sensor losses (PSL) for (a) BW_1 = 5 MHz, (b) BW_2 = 10 MHz, and (c) BW_3 = 20 MHz under RMa LOS/NLOS conditions. 165
Figure 83. BackCom range maps (ρ) versus TX–Sensor distance and PSL for (a) BW_1 = 5 MHz, (b) BW_2 = 10 MHz, and (c) BW_3 = 20 MHz under UMi LOS/NLOS conditions. 166
Figure 84. BackCom range maps (ρ) versus TX–Sensor distance and PSL for (a) BW_1 = 5 MHz, (b) BW_2 = 10 MHz, and (c) BW_3 = 20 MHz under RMa LOS/NLOS conditions. 167

List of Tables

Table 1. Comparison of typical ambient RF sources for backscatter communication. 35

Table 2. Summary of representative AmBC system implementations in the literature. 43

Table 3. Geometric Parameters of the 3GPP Path-Loss Models and Bistatic AmBC Link. 65

Table 4. System parameters for the bistatic AmBC link budget analysis. 66

Table 5. Monotonicity of backscattered power across tag angular configurations 95

Table 6. A summary of the gain values predicted by the gaussian model 99

Table 7. Summary of the measurement setups 104

Table 8. Measurement setup parameters 105

Table 9. Biomedical Sensors and Measured Parameters 139

General Introduction

The advent of the Internet of Things (IoT) has generated unprecedented demand for massive connectivity, low-cost deployment, and energy-efficient communication technologies. Billions of sensors and smart devices are expected to be deployed in future networks (new radios) to enhance performance in several applications such as smart cities, healthcare monitoring, industrial automation, and environmental sensing, etc. [1], [2]. However, conventional wireless communication systems face major limitations when applied to large-scale IoT, particularly in terms of spectrum availability, energy consumption, and infrastructure cost. Addressing these challenges requires a paradigm shift towards new communication principles that minimize both power and spectrum usage.

Ambient Backscatter Communication (AmBC) has recently emerged as a promising solution to this problem [3], [4], [5]. Unlike traditional wireless systems where a dedicated transmitter actively generates signals, AmBC reuses existing ambient radiofrequency (RF) signals as carriers for ultra-low-power communication. A passive or semi-passive device, referred to as a tag or sensor, modulates its data by altering the reflection properties of its antenna. This eliminates the need for costly and power-hungry transmitters, Supporting quasi-battery-free functionality for IoT devices. In this way, AmBC offers an attractive approach for large-scale, sustainable IoT deployments [5].

With the rollout of 5G New Radio (5G-NR) networks, new opportunities have arisen for AmBC systems. The wide coverage, high availability, and dense deployment of 5G base stations make 5G signals an excellent candidate for ambient carriers [6], [7]. In particular, the 3.5 GHz band (n78), widely allocated for mid-band 5G services, provides a strong balance between coverage and capacity. Exploiting 5G-NR as an ambient source can therefore enable ubiquitous connectivity for low-power IoT sensors. Nevertheless, the feasibility of such systems remains a significant challenge because of path loss increase at 5G-NR higher frequencies. large power asymmetry between direct and reflected components, and the harsh propagation conditions encountered in realistic environments [8], [9].

Several scientific questions arise in this context:

- Under what conditions can bistatic 5G-NR AmBC systems operate reliably when using ambient 5G signals?
- How do standardized propagation environments (Urban Macro, Urban Micro, Rural Macro) affect the achievable link budget and communication range?

- What are the hardware requirements for AmBC tags to ensure low sensor losses and robust modulation?
- How can receiver architecture be designed to separate the weak backscattered signal from the strong direct 5G carrier?
- To what extent can experimental validation substantiate the feasibility predicted by theoretical models?

This PhD research aims to address these questions by developing a comprehensive framework for the design, modeling, and experimental validation of a bistatic 5G-NR AmBC system. To provide a clearer understanding of the research steps and the resulting findings, the present thesis is organized as follows:

- **Chapter 1** introduces the fundamentals of AmBC communication. It reviews from literature the operating principle of backscatter modulation, the typical system architectures (monostatic and bistatic), and the main modulation schemes (ASK, BPSK, FSK, QAM) [5]. The chapter also discusses the role of 5G signals as ambient carriers, existing receiver architectures, state-of-the-art implementations, and the main challenges associated with AmBC based earlier relevant investigations [3], [6].
- **Chapter 2** develops a feasibility of 5G-NR AmBC scheme in realistic environments. Relying on the standardized 3GPP TR 38.901 channel models [10], our study has aimed to assess the feasibility of a 5G-NR AmBC bistatic propagation framework for Urban Macro (UMa), Urban Micro (UMi), and Rural Macro (RMa) scenarios, both in line-of-sight (LOS) and non-line-of-sight (NLOS) conditions. A complete link budget framework is established, integrating path loss, received sensor power, receiver sensitivity, available path loss, and achievable range. The results demonstrate the critical influence of propagation, sensor insertion losses, and bandwidth on AmBC feasibility, providing clearer understanding and guidelines for real-world deployment.
- **Chapter 3** presents the design and experimental validation of a backscatter tag prototype. The architecture is based on a low-power microcontroller, an RF switch, and a 3.5 GHz antenna, enabled by embedded temperature sensor. BPSK modulation was implemented using a Single-Pole Single-Throw (SPST) reflective RF switch. The prototype is then tested in controlled conditions (anechoic and semi-anechoic chambers) to practically validate the feasibility of 5G-based AmBC communication. A theoretical bistatic propagation model was proposed and presented in this chapter to predict the received power under various spatial configurations, and its results were compared with

experimental measurements. This comparison is very important to validate the system's behavior under realistic conditions.[7].

- **Chapter 4** focuses on the receiver architecture, signal processing chain, and experimental validation in real environments. An SDR-based receiver (software-defined radio) using a USRP B210 is implemented with GNU Radio to capture and process the backscattered signals. The flowgraph includes magnitude extraction, low-pass filtering, and threshold detection. Performance is evaluated through BER (Bit Error Rate) measurements, synchronization of multi-sensor prototypes, and experiments conducted in realistic propagation environments such as corridors and outdoor regions with 5G connectivity. The results confirm the practical viability of the proposed system and highlight the design trade-offs between sensitivity, bandwidth, and complexity [9].

Taken together, these chapters present a comprehensive investigation of bistatic AmBC based on ambient 5G-NR signals, encompassing theoretical modeling, feasibility analysis, hardware prototyping, and experimental validation. This work delivers essential analytical and experimental contributions toward the development of practical 5G-based ambient backscatter IoT systems.

References

[1] I. Cheikh, S. Roy, E. Sabir, R. Aouami, “Energy, Scalability, Data and Security in Massive IoT: Current Landscape and Future Directions,” *arXiv preprint*, 2025.

[2] T. Hasnain, P. Kaur, “Scalable IoT Networking: Energy-Efficient Communication Protocols,” *Int. J. Multidiscip. Res. Trans.*, vol. 7, no. 5, 2025.

[3] N. V. Huynh, D. T. Hoang, X. Lu, D. Niyato, P. Wang, D. I. Kim, “Ambient Backscatter Communications: A Contemporary Survey,” *IEEE Commun. Surv. Tutor.*, vol. 20, no. 4, pp. 2889–2922, 2018.

[4] V. Liu, A. Parks, V. Talla, S. Gollakota, D. Wetherall, J. R. Smith, “Ambient Backscatter: Wireless Communication Out of Thin Air,” *Proc. ACM SIGCOMM*, pp. 39–50, Aug. 2013.

[5] D. T. Hoang, D. Niyato, D. I. Kim, N. V. Huynh, S. Gong, “Ambient Backscatter Communication Networks,” *Cambridge University Press*, 2020.

[6] Q. Liu, S. Sun, X. Yuan, Y. Zhang, “Ambient Backscatter Communication-Based Smart 5G IoT Network,” *EURASIP J. Wirel. Commun. Netw.*, vol. 2021, no. 34, Feb. 2021.

[7] M. Lefki, S. Baccar, M. Kadi, H. Shall, M. Ghorbel, “A First Prototype of an Ambient Backscatter Communication Tag Working in 5G-NR Frequency,” *Proc. IEEE RFID-TA*, Nov. 2024.

[8] R. Biswas, M. U. Sheikh, H. Yiğitler, J. Lempiäinen, R. Jäntti, “Direct Path Interference Suppression Requirements for Bistatic Backscatter Communication System,” *Tampere Univ. & Aalto Univ.*, 2023.

[9] R. Duan, X. Wang, H. Yiğitler, M. U. Sheikh, R. Jäntti, Z. Han, “Ambient Backscatter Communications for Future Ultra-Low-Power Machine Type Communications,” *IEEE Commun. Mag.*, vol. 58, no. 1, pp. 35–41, Jan. 2020.

[10] 3GPP, “Study on Channel Model for Frequencies from 0.5 to 100 GHz,” *3GPP TR 38.901*, V14.3.0, Jan. 2018.

Chapter 1: State of the Art

1. Introduction

The rapid expansion of the Internet of Things (IoT) has created an unprecedented demand for communication technologies that are both scalable and extremely energy-efficient. Conventional wireless systems, such as Wi-Fi, BLE, or ZigBee, rely on active radio circuits that consume significant power, making them unsuitable for large-scale deployments of battery-free or energy-harvesting devices. To address this limitation, ambient backscatter communication (AmBC) has emerged as a promising paradigm for enabling sustainable and ultra-low-power connectivity by reusing existing radio frequency (RF) signals rather than generating new ones. This concept is increasingly associated with the vision of "green IoT" and eco-friendly networking solutions, as emphasized by Javaid and al. [1] and further highlighted by comparative studies of AmBC against other low-power technologies such as Wi-Fi, BLE, FM, and LoRa [2].

The principle of communicating through reflected signals has historical roots in Stockman's seminal work on "communication by means of reflected power" [3]. Several decades later, Liu and al. [4] introduced the first modern demonstration of ambient backscatter, showing that TV and Wi-Fi signals could be repurposed to enable battery-free wireless data transmission. Since then, AmBC has rapidly evolved into a disruptive solution for next-generation IoT, with applications spanning smart cities, healthcare, logistics, and environmental monitoring.

Several surveys have comprehensively reviewed the foundations and progress of AmBC. Wu and al. [5] and Nguyen Van Huynh and al. [6] documented the main principles, architectures, signal sources, and technical challenges, highlighting the wide potential of AmBC in both short- and long-range scenarios. Complementary studies have focused on the design aspects required for efficient operation, such as circuits, antennas, and modulation techniques [7], while forward-looking perspectives have emphasized the integration of AmBC with artificial intelligence and non-terrestrial 6G networks [8]. These developments illustrate that AmBC stands at the intersection of multiple research directions propagation modeling, hardware prototyping, and intelligent signal processing positioning it as a key technology for future large-scale, sustainable wireless systems.

The remainder of this chapter is organized as follows. Section **2** introduces the fundamentals of ambient backscatter communication (AmBC), including its basic principles and typical system architectures. Section **3** presents the main modulation techniques employed in AmBC systems.

Section **4** discusses the role of 5G-NR as a promising ambient carrier and compares it with other signal sources. Section **5** reviews receiver architectures and sensitivity issues. Section **6** surveys representative implementations and existing prototypes, while Section **7** highlights the main challenges that remain open. Finally, Section **8** positions the contributions of this thesis with respect to the identified research gaps.

2. Fundamentals of Ambient Backscatter Communication

2.1 Backscatter communication

Backscatter communication is a technique that enables data transmission by reflecting existing electromagnetic (EM) signals instead of generating new ones. This concept, although extensively developed in the RF domain in recent decades, has conceptual roots in much older methods of communication, such as the heliograph. In such optical systems, an operator would modulate sunlight by pivoting a mirror, allowing another operator at a distant location to receive the reflected light and interpret the information. Similarly, in RF backscatter systems, a tag modulates and reflects an incident RF signal toward a receiver, enabling communication without generating a new carrier. Figure 1 highlights this conceptual analogy by contrasting an optical reflection setup on the left and an RF-based backscatter system on the right. This process represents an early form of passive communication relying on the reflection of an external wave.

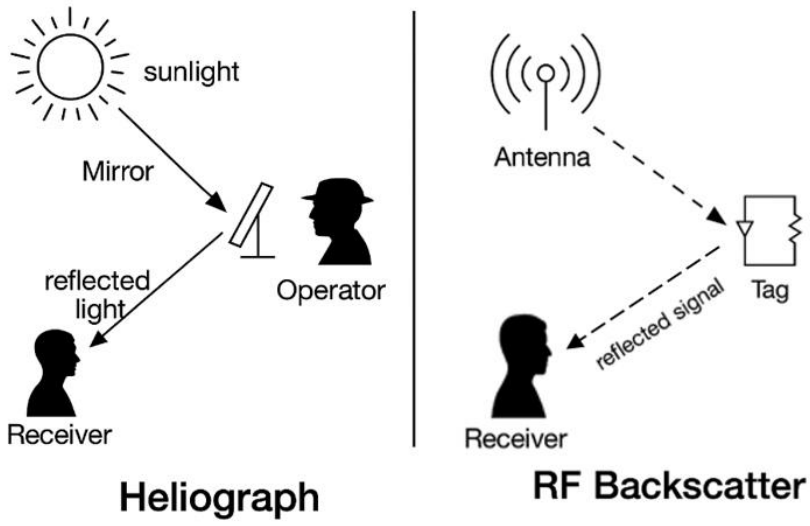

Figure 1. Conceptual Analogy Between Optical Heliograph and RF Backscatter Communication.

In modern backscatter systems, the same foundational idea is applied using RF signals rather than visible light. Instead of mirrors, small passive or semi-passive devices referred to as tags modify their reflective properties to encode information on incoming RF signals. This approach

eliminates the need for the tag to actively generate its own radio signal, leading to extremely low-power communication schemes.

From a physical perspective, backscattering occurs when an electromagnetic wave encounters an object that reflects part of the energy back toward the source or other directions. This principle is widely used in radar systems, where an incident wave is transmitted, and the portion reflected by an object (i.e., backscattered) is analyzed to detect presence and distance. The adaptation of this concept to data communication was proposed in 1948 by Stockman, who suggested using RF backscatter to transmit information by modulating the reflection characteristics of an antenna [3]. One of the most well-known applications of this technique is Radio Frequency Identification (RFID), where passive tags reflect and modulate an RF carrier emitted by a reader to transmit identification data. RFID exemplifies the advantages of backscatter communication in terms of low cost, low power consumption, and circuit simplicity. More recently, this principle has been extended to Ambient Backscatter Communication (AmBC), where existing ambient RF sources (e.g., TV, Wi-Fi, LTE, 5G) are opportunistically leveraged as carriers for modulation [9], [10].

As a preliminary step toward understanding ambient backscatter systems, the next section details the operational principles and essential building blocks of generic backscatter communication.

2.2 Basic Principle

Ambient backscatter communication enables data exchange by reflecting and modulating existing RF signals present in the environment, rather than generating a new carrier wave [11]. This paradigm supports ultra-low-power communication and is increasingly considered a sustainable solution for large-scale IoT deployments. The underlying mechanism is known as load modulation, where a passive or semi-passive device alters its antenna load impedance to encode information onto a reflected RF signal. By varying the amount and nature of reflected energy, the tag embeds data in the backscattered wave without emitting any signal of its own.

A typical ambient backscatter communication (AmBC) system comprises three fundamental components**:**

- **Ambient RF source**: This is a pre-existing RF emitter, such as a Wi-Fi access point, TV broadcast tower, 5G base station, or even a smartphone, which continuously emits a carrier signal. The backscatter system has no control over this source but instead opportunistically leverages its signal to enable communication.
- **Backscatter tag**: This device modulates and reflects an ambient RF signal in order to transmit information to a receiver. It typically consists of a 5G antenna connected to a

switch that toggles between two impedance states [12]. By dynamically altering the load impedance usually under the control of a microcontroller it modulates the reflected signal according to the data to be transmitted. This technique enables operation without generating any RF signal, resulting in extremely low power consumption. The implementation of this principle is detailed in Section 3.1.3 of Chapter 3. Tags in ambient backscatter systems are therefore considered passive or semi-passive and can even harvest energy from the surrounding environment to operate autonomously.

- **Receiver**: The receiver, often referred to as the *reader*, is the component responsible for detecting and decoding the information modulated by the backscatter tag. It typically consists of an antenna to capture the composite signal composed of the direct path from the ambient RF source and the modulated backscattered component as well as processing units to extract useful information. Depending on its complexity, the receiver may perform simple energy detection or more advanced signal processing tasks such as demodulation, synchronization, and interference mitigation. The major challenge lies in distinguishing the weak backscattered signal from the dominant direct signal, especially in environments with high ambient RF interference or multipath effects.

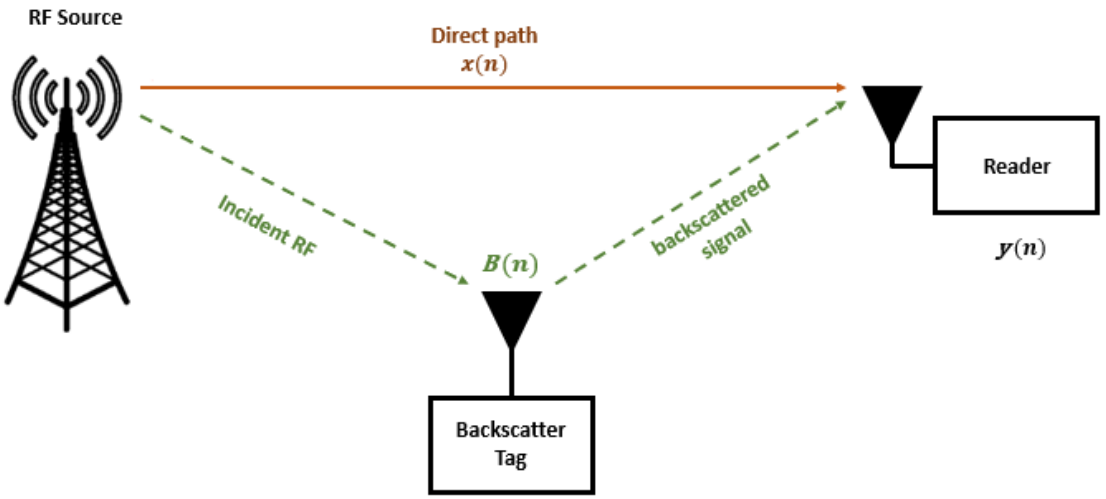

Figure 2. Illustration of an ambient backscatter communication system.

In a typical ambient backscatter system, the received signal at the reader is composed of two main components: a strong direct signal emitted by the ambient RF source and a weaker backscattered signal modulated by the tag. As illustrated in Figure 2, the tag reflects and modulates a portion of the incoming RF wave, enabling communication without generating a new carrier. The overall received signal $y(n)$ can be modeled as [4]:

$$y(n) = x(n) + \alpha B(n)x(n) + z(n) \quad (1)$$

Where represents the direct-path signal from the ambient source, $B(n)$ is the baseband modulation applied by the tag (typically a binary coefficient), α is the complex coefficient accounting for the backscatter channel response and $z(n)$ is the additive noise. In this model, the tag alternates between two distinct reflection states to implement a specific modulattion scheme. For example, in the Binary Phase Shift Keying (BPSK) modulation, the modulation symbol $B(n)$ takes values of +1 or −1, corresponding to two reflection states that induce a 0 or π phase shift in the backscattered signal. This is achieved by switching the load impedance connected to the antenna between two values that produce reflection coefficients of equal magnitude but opposite phase.

This modulation mechanism is governed by the reflection coefficient Γ, which describes the proportion of the incident wave reflected by the antenna [13]:

$$\Gamma = \frac{Z_L - Z_a^*}{Z_L + Z_a} \quad (2)$$

Where Z_L is the load impedance seen by the antenna terminals—corresponding to either Z_1 *or* Z_2 depending on the switching state and Z_a is the antenna impedance, typically 50 Ω. By alternating between Z_1 and Z_2, the tag generates two distinct reflection coefficients, Γ_1 and Γ_2, associated with the binary symbols $'0'$ and $'1'$. This passive switching modulates the phase of the reflected wave over time and allows the tag to transmit information without emitting its own RF signal, thereby enabling ultra-low-power or battery-free operation.

2.3 Typical Architectures and Classifications of Backscatter Communication Systems

Backscatter communication systems can be categorized according to two main criteria: the nature of the carrier source used to illuminate the tag, and the geometric configuration between the transmitter (source), tag, and receiver (reader). These criteria give rise to several architectural variants that differ in complexity, energy consumption, and performance. Figure 3 illustrates typical configurations of the main categories.

2.3.1 Classification Based on RF Carrier Source

This classification considers whether the carrier wave is generated by a dedicated emitter or harvested from existing signals present in the environment.

- **Dedicated BackCom (Ded-BackCom)**: In this configuration (Figure 3. a), a specific RF emitter is allocated to provide the carrier signal used for backscattering. A typical example is a Wi-Fi router transmitting continuous wave signals, while a separate reader captures the backscattered signal from the tag. This setup allows for precise control over

signal parameters and supports high throughput with minimal interference [14] [15] [16]. However, it requires additional infrastructure and energy sources, making it less attractive for large-scale or battery-free deployments.

- **Ambient BackCom (Amb-BackCom)**: In contrast, ambient backscatter systems leverage existing RF signals such as TV broadcasts, cellular signals, or Wi-Fi transmissions or a network base station (BS) as the carrier [4] [17] [18]. The tag harvests and modulates these ambient signals to encode its data. This configuration (Figure 3. b) eliminates the need for a dedicated carrier generator and enables ultra-low-power or batteryless operation. However, since ambient signals are not optimized for backscatter communication and may be weak or irregular, system performance is often limited in terms of bit rate and reliability. Tags typically modulate the impedance of their antenna using schemes such as OOK or BPSK to reflect information, and the receiver must extract the backscattered signal from a noisy background of already modulated waves.

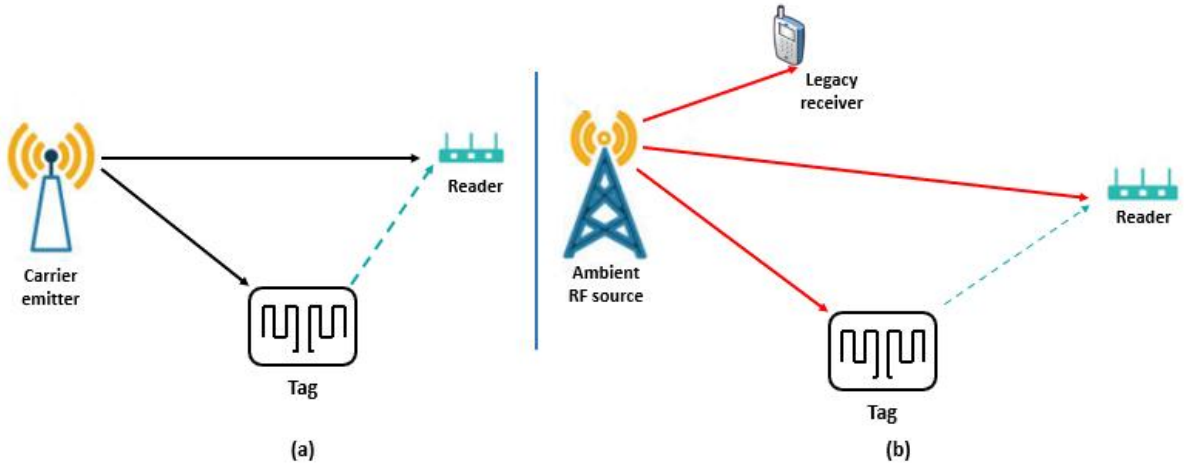

Figure 3. Paradigms for backscatter communications: (a) Dedicated backscatter; (b) Ambient backscatter.

2.3.2 Classification Based on System Geometry

This dimension considers the relative positions of the signal generator (if present), the tag, and the receiver.

Monostatic BackCom (Mon-BackCom): This configuration (Figure 4. a) uses a single device with a shared antenna is used for both transmitting the carrier signal and receiving the backscattered signal. This compact and cost-effective configuration is commonly found in legacy RFID systems and is particularly suitable for portable or handheld readers. However, simultaneous transmission and reception through the same antenna introduce significant self-interference, which limits the communication range and achievable data rate. To overcome this,

complex signal cancellation techniques are often required at the receiver to effectively extract the weak backscattered signal from the dominant direct path [19] [20]. Despite these limitations, monostatic backscatter systems remain highly effective for very short-range communication scenarios, where low complexity and minimal infrastructure are prioritized.

Bistatic BackCom (BiS): In bistatic backscatter systems, the carrier emitter and the backscatter receiver are physically separated, each equipped with its own antenna. Unlike monostatic setups where transmission and reception occur through the same device, the bistatic configuration allows greater flexibility in deployment and better adaptation to the surrounding environment. By positioning the carrier source closer to the tag, the system reduces the round-trip path loss, thereby increasing the strength of the backscattered signal and improving the overall link budget [14] [21]. As a result, bistatic systems generally outperform monostatic and ambient backscatter architectures in terms of communication range, bit error rate (BER), and robustness, especially in indoor or complex propagation environments [22].

Bistatic architectures can be further categorized based on the spatial relationship between the emitter and the receiver:

- **Co-located Bistatic BackCom:** In this configuration (Figure 4.b), the RF emitter and the receiver are placed in close proximity, often integrated within the same physical device or platform but operating independently. This proximity simplifies synchronization between the transmitted carrier and the reception of the backscattered signal, which is particularly advantageous in practical deployments. While it retains the advantages of bistatic operation such as placing the emitter near the tag it avoids the complexity of long-distance coordination between devices.
- **Dislocated Bistatic BackCom:** In dislocated setups (Figure 4.c), the RF source and the receiver are deployed at different physical locations within the environment. This spatial decoupling enables optimized geometric placement, for example, by situating the emitter very close to the tag to enhance the backscattered signal strength, while positioning the receiver at a distance to cover a broader area or to avoid interference. Although this configuration offers superior flexibility, extended communication range, and improved spatial coverage, it demands more careful synchronization, calibration, and often higher infrastructure cost.

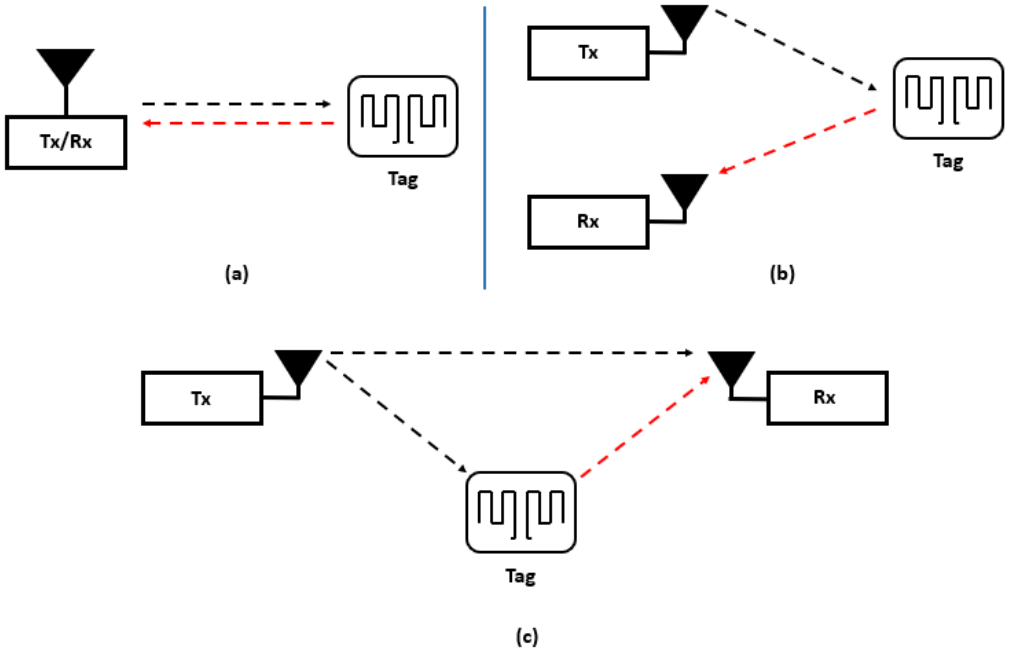

Figure 4. Configurations of backscatter communication systems: (a) Monostatic; (b) Bistatic co-located; (c) Bistatic dis-located.

3. Backscatter Modulation Techniques

In ambient backscatter communication (BackCom), digital modulation is achieved by varying the reflection coefficient of the tag's antenna through dynamic control of its load impedance. This passive modulation process enables data transmission without the need to generate a new carrier signal, making it particularly attractive for ultra-low-power communication systems. The selected modulation technique directly affects the system's performance in terms of spectral efficiency, bit error rate, power consumption, and resistance to interference.

BackCom systems generally rely on three main categories of modulation: Amplitude Modulation (AM), Frequency Modulation (FM), and Phase Modulation (PM). Each category encompasses various techniques that have been adapted from conventional wireless communication and optimized for passive reflection-based transmission. This section provides an overview of the most widely used digital modulation schemes in BackCom, namely On-Off Keying (OOK), Frequency Shift Keying (FSK), Binary and Quadrature Phase Shift Keying (BPSK/QPSK), and Quadrature Amplitude Modulation (QAM). The advantages and limitations of each approach are discussed in the context of passive RF operation.

3.1 Amplitude Modulation (AM)

Amplitude modulation in backscatter communication relies on dynamically controlling the amplitude of the reflected signal by switching the load impedance of the tag's antenna. The simplest and most widely adopted form is On-Off Keying (OOK), where the tag alternates

between two reflection states: a high-reflection state representing a binary “1” and a low-reflection or absorbing state representing a binary “0” [23], [24]. This approach, also referred to as Amplitude Shift Keying (ASK), enables ultra-low-power data transmission without generating a new carrier signal, which is why it has been extensively used in passive RFID and early ambient backscatter systems [23]. Its primary advantage lies in its simplicity and minimal energy consumption, making it particularly suitable for batteryless or energy-harvesting tags. In practice, OOK can be implemented with a single RF switch or transistor, and the receiver can detect the symbols using basic energy detection. However, amplitude modulation is inherently sensitive to noise, fading, and environmental reflections. The amplitude difference between the “on” and “off” states can be significantly attenuated in multipath or low signal-to-noise ratio (SNR) conditions, which directly impacts the achievable communication range and bit error rate (BER) [25].

To improve throughput and spectral efficiency, multi-level amplitude modulation schemes such as Pulse Amplitude Modulation (PAM) and Quadrature Amplitude Modulation (QAM) have been investigated in recent backscatter research [26], [27], [28]. These schemes encode multiple bits per symbol by either using multiple amplitude levels (PAM) or combining amplitude and phase variations (QAM). For example, 4-PAM has been successfully demonstrated in ambient FM backscatter to achieve spectrally efficient wireless sensing [28], and QAM-based tags have been proposed to support higher data rates in UHF RFID and IoT scenarios [26], [27]. Theoretical studies further analyze the BER performance of PAM and QAM, illustrating the trade-off between constellation size, detection reliability, and power consumption [29]. In summary, amplitude modulation remains a fundamental and energy-efficient technique in backscatter communication. OOK is generally preferred for ultra-low-power systems, while multi-level AM or QAM is adopted when higher data rates justify the increased complexity and synchronization requirements.

3.2 Phase Modulation (PM)

Phase modulation (PM) is one of the most widely adopted approaches for backscatter communication, owing to its robustness against multipath fading and its ability to maintain stable bit error rate (BER) performance under fluctuating channel amplitudes. In particular, binary phase-shift keying (BPSK) is frequently used in ambient and Wi-Fi backscatter systems due to its simplicity and energy efficiency, as demonstrated in BackFi, which achieves high-throughput Wi-Fi backscatter using both BPSK and QPSK modulation [30]. Ambient backscatter systems employing BPSK have also been shown to outperform simple on-off keying (OOK) in terms of BER robustness under realistic conditions [4].

Beyond BPSK, multi-level phase-shift keying (PSK) schemes such as QPSK and M-PSK enhance spectral efficiency and support higher data rates, which is particularly relevant for dense IoT and 5G ambient backscatter networks. Recent studies have demonstrated the feasibility of these modulations in ambient and bistatic backscatter systems, and surveys highlight their increasing integration into 5G and Wi-Fi bands [31] [5]. These approaches offer a practical balance between energy efficiency and throughput, making them suitable for next-generation ultra-low-power IoT devices.

From a theoretical perspective, phase modulation has been extensively analyzed in backscatter systems, with studies modeling BER performance and achievable data rates for BPSK and QPSK links under both bistatic and ambient conditions [32]. Foundational works on digital phase modulation [33] remain essential for understanding constellation design, phase tracking, and synchronization in these ultra-low-power systems. In summary, phase modulation provides an effective compromise between implementation simplicity, energy efficiency, and spectral efficiency, which explains its prevalence in modern ambient backscatter communication networks.

3.3 Frequency Modulation

Frequency modulation (FM) in backscatter communication is predominantly realized using Frequency-Shift Keying (FSK), where a backscatter tag alternates between two or more discrete reflection frequencies to encode digital information. This technique enhances link robustness compared to amplitude-only modulation, as frequency-shifted components are easier to isolate in the spectral domain, particularly in multipath and interference-rich environments. In bistatic configurations, coherent receivers can efficiently detect the shifted carriers, improving reliability under adverse propagation conditions [34].

A widely adopted scheme is binary FSK (2-FSK), which has been successfully demonstrated in ambient FM backscatter systems. For example, FM-Rider achieves outdoor communication distances exceeding 100 m with ultra-low power consumption [35]. To further optimize energy efficiency and simplify tag hardware, Selective FSK (SFSK) has been proposed, preserving bit-error rate (BER) performance while extending the effective operating range, which is advantageous for large-scale IoT deployments [36].

Recent studies have extended FSK-based backscatter to various ambient sources beyond FM radio, including LTE, Wi-Fi and Bluetooth Low Energy (BLE) carriers. For instance, Liao and al. [34] proposed ambient FSK backscatter using LTE cell-specific reference signals, while Gong and al. [37] demonstrated enhanced bistatic backscatter performance using FSK and OOK with improved dynamic range. These works highlight that frequency-modulated backscatter

provides robust and spectrally separable reflections, enabling reliable short-to-medium range communications and serving as a foundation for advanced multi-carrier techniques such as OFDM-based backscatter, which will be addressed in the next section.

4. 5G-NR as a Carrier for Ambient Backscatter communication

4.1. Spectral and Signal Properties of 5G

4.1.1. Frequency Spectrum and Bandwidth of 5G

The 5G New Radio (NR) standard introduces a highly flexible spectrum framework that spans a wide frequency range, divided into two primary regions: Frequency Range 1 (FR1) and Frequency Range 2 (FR2). FR1, often referred to as the sub-6 GHz spectrum, extends from 410 MHz to 7.125 GHz and includes widely used bands such as n77, n78, and n79. FR2, also known as the millimeter-wave (mmWave) spectrum, covers 24.25 GHz to 52.6 GHz and provides extremely wide bandwidths suitable for ultra-high data rate applications [38], [39]. Compared to previous generations, 5G's spectrum flexibility enables the deployment of channels with bandwidths up to 100 MHz in FR1 and up to 400 MHz in FR2, supporting unprecedented levels of spectral efficiency.

The bandwidth characteristics of 5G are particularly significant for ambient backscatter communication (AmBC). Standardized channel bandwidths in FR1 include 5, 10, 20, 40, 50, 80, and 100 MHz, while FR2 supports 50, 100, 200, and 400 MHz channels [39], [40]. This large bandwidth provides a natural advantage for backscatter systems: frequency-shifted or phase-modulated reflections can be more easily separated from the strong direct carrier in the spectral domain, improving detection robustness in multipath or interference-rich environments. Additionally, the availability of multiple sub-bands allows the deployment of multi-tag or multi-carrier backscatter schemes, enhancing system scalability for dense IoT networks. For AmBC applications, the 5G spectrum offers several practical benefits. First, its widespread and continuous availability ensures that ambient carriers are present in urban and suburban environments without requiring dedicated transmitters. Second, the large channel bandwidths provide better spectral isolation of backscattered signals, enabling reliable frequency-shift keying (FSK), on-off keying (OOK), or even orthogonal frequency-division multiplexing (OFDM) backscatter. Finally, although FR2 signals exhibit shorter propagation distances due to higher path loss, their directional nature and abundance of bandwidth can be leveraged for high-rate, short-range AmBC links [41], [34]. In summary, the frequency spectrum and bandwidth characteristics of 5G create a favorable environment for ambient backscatter communication. A deep understanding of the available frequency bands, bandwidth

configurations, and propagation properties is essential for designing energy-efficient and spectrally compatible AmBC systems. The following section will build upon this foundation by analyzing the deployment scenarios and interference considerations for 5G-enabled backscatter networks.

4.1.2. 5G Waveform Considerations for Ambient Backscatter

Ambient backscatter communication (AmBC) systems leveraging 5G signals rely fundamentally on the properties of orthogonal frequency-division multiplexing (OFDM), which is the baseline waveform in 5G New Radio (NR), as well as in LTE and Wi-Fi. The multicarrier structure of OFDM provides numerous subcarriers and inherent cyclostationary features, which are instrumental in detecting the weak backscattered signal in the presence of a much stronger ambient transmission.

Several studies have highlighted the advantages of OFDM for AmBC. For instance, ElMossallamy and al. [42] proposed a non-coherent FSK backscatter scheme that exploits the cyclic prefix (CP) for symbol synchronization and interference mitigation without requiring full channel estimation. Similarly, [43] demonstrated that backscatter tags can modulate data onto the null subcarriers of an ambient OFDM signal, effectively separating the tag's information from the primary transmission. Chen and al. [44] further showed that pilot-aided detection enhances the extraction of low-rate backscatter data under strong ambient interference. Moreover, a non-coherent detection framework exploiting OFDM's cyclostationarity was introduced in [45], confirming the robustness of OFDM-based AmBC even in low-SNR and frequency-selective fading conditions.

Beyond the inherent advantages of multicarrier systems, 5G-based AmBC exhibits a phenomenon known as double modulation, which distinguishes it from conventional continuous-wave (CW) backscatter. In this scenario, the tag reflects the incoming OFDM waveform while superimposing its own information via impedance modulation such as amplitude-shift keying (ASK), binary phase-shift keying (BPSK), or frequency-shift keying (FSK) resulting in a composite signal that carries both the high-rate ambient data and the low-rate tag data [46]. This spectral overlap poses a major detection challenge, as the weak backscattered component must be extracted from a dominant primary transmission. To address this, detection strategies exploit the asymmetry between the two signals: the ambient 5G waveform operates at a high data rate, allowing averaging or correlation over its symbol duration to suppress the primary component and reliably recover the tag's signal [46].

Finally, the performance of 5G-based AmBC links is heavily constrained by signal power and propagation losses. A backscatter link experiences a two-hop propagation from the ambient

source to the tag and from the tag to the receiver resulting in double free-space path loss (FSPL). This is compounded by multipath fading and the finite reflection coefficient of the tag, which is always less than unity. According to 3GPP TR 38.901 [47] and the classical wireless propagation framework of Rappaport [48], the received backscattered power is typically orders of magnitude lower than the ambient signal. As emphasized in Liu et al. [46], practical deployment requires careful link budget design, optimal tag placement, and high-sensitivity receivers. These combined constraints explain why most 5G-based AmBC systems are limited to short-range or opportunistic IoT scenarios, where ambient carriers are readily available and the weak backscattered component can still be detected reliably.

4.2 **Ambient RF Sources for Backscatter Communication**

Ambient backscatter communication (AmBC) leverages pre-existing radio frequency (RF) signals in the environment to enable battery-free data transmission. The performance of such systems heavily depends on the nature, availability, and stability of the ambient sources. Early research mainly focused on TV broadcasting**,** Wi-Fi, and FM radio signals due to their wide availability. Liu and al. [4] first demonstrated that TV signals in the 500–800 MHz band can enable passive communication over hundreds of meters. Parks and al. [49] and Qian and al. [50] extended this concept to Wi-Fi, achieving short-range communications in indoor scenarios, while Wang and al. [51] leveraged FM broadcasting in the 88–108 MHz band for ultra-low-power long-range AmBC, suitable for smart city and wearable applications. These studies provided the foundation for understanding ambient signal exploitation in various frequency bands.

In recent years, AmBC has evolved towards diversified RF sources to increase coverage and adapt to emerging IoT requirements. 5G New Radio (NR) signals have attracted growing interest due to their dense urban deployment and OFDM multicarrier structure [52]. Similarly, LTE and commercial cellular signals have been successfully used for medium-range AmBC, with LTE pilot tones supporting low-power indoor tags [53]. LoRa transmissions, operating in sub-GHz ISM bands (433 MHz and 868 MHz), provide an attractive option for long-range AmBC with low data rates [54]. In parallel, hybrid solutions such as Wi-Fi backscatter combined with SWIPT have been proposed to simultaneously deliver data and energy for autonomous indoor IoT devices [55].

Table 1 summarizes the main ambient RF sources used in AmBC research, highlighting their frequency bands, coverage potential, and application domains. Lower-frequency signals such as FM and TV broadcasting offer long-range connectivity but suffer from low data rates and large antenna requirements. Mid-frequency sources like LTE, LoRa, and Wi-Fi provide a

compromise between range and throughput, while high-frequency carriers such as 5G at 3.5 GHz and 26 GHz enable high data rates over short distances. This comparison guides the selection of suitable ambient sources depending on the target application, whether indoor IoT, urban sensing, or large-area smart city monitoring.

Amnient RF source	Frequency Band	Typical Range	Advantages	Limitations
5G NR [52]	3.5 GHz/26 GHz	5-30 m	High density OFDM structure	Short range, dynamic spectrum
Wi-Fi [55]	2.4/5 GHz	5-20 m	Widely available, indoor IoT	Limited to indoor
LoRa [54]	433/868 MHz	50-300 m	Long range, low power	Low data rate
LTE / Cellular [51] [53]	700 MHz-2.6 GHz	20-200 m	Urban coverage, reliable pilots	Interference, mobility
TV Broadcasting [49]	500-800 MHz	100-500 m	Strong signals, wide coverage	Low data rate
FM Radio [51]	88-108 MHz	200-1000 m	Very long range, ultra-low power	Large antennas, low data rate

Table 1. Comparison of typical ambient RF sources for backscatter communication.

5. Receiver Architectures in Backscatter Communication Systems

5.1 Classification of Receiver Types in AmBC

The receiver architecture plays a central role in ambient backscatter communication (AmBC) systems because it determines the capability to detect and decode the extremely weak backscattered signals in the presence of strong ambient transmissions. Depending on their implementation complexity, flexibility, and power constraints, AmBC receivers in the literature can be classified into four main categories: software-defined radio (SDR) receivers, commercial off-the-shelf (COTS) receivers, dedicated ultra-low-power analog receivers, and advanced adaptive architectures.

5.1.1. Software-Defined Radio (SDR) Receivers

SDR-based receivers, such as USRP B210, N210, and RTL-SDR dongles, provide the highest flexibility for AmBC prototyping and experimental research. They digitize the baseband or intermediate-frequency signal and perform detection and demodulation entirely in software, which allows the implementation of advanced filtering, synchronization, and interference

suppression algorithms. For instance, SDR receivers have been successfully used in Wi-Fi backscatter systems such as BackFi [30], in FM-based AmBC using RTL-SDR [51], and in full-duplex ambient backscatter experiments [56]. Their key advantage is adaptability to different ambient sources (Wi-Fi, FM, LTE, 5G) and modulation schemes without requiring hardware modifications. However, their high sampling rates and power consumption limit their use in ultra-low-power or embedded applications.

5.1.2. Commercial Off-the-Shelf (COTS) Receivers

COTS receivers include standard communication modules such as LoRa SX1276, Wi-Fi chipsets, and Bluetooth Low Energy (BLE) radios, which can be exploited to detect backscattered signals. These modules offer high sensitivity and low power consumption, which makes them attractive for practical IoT and sensor network deployments. Joshua R. Smith and al. demonstrated the LoRa Backscatter system using commodity Semtech SX1276 modules, achieving communication over several kilometers and showing that these receivers can reliably decode packets even under 95 dB higher out-of-band interference [57], [58]. Similarly, BLE and Wi-Fi modules have been used for passive sensor data collection in healthcare and industrial monitoring scenarios [59]. The main limitation of COTS receivers lies in their reduced flexibility, as they are optimized for specific protocols and may require protocol-level techniques to decode weak backscatter reflections.

5.1.3. Dedicated Ultra-Low-Power Analog Receivers

Some AmBC applications, particularly battery-free sensing, require ultra-low-power receiver architectures to minimize energy consumption. Instead of relying on full analog-to-digital conversion, these receivers use analog envelope detection and thresholding circuits to distinguish the two signal levels corresponding to binary ‘0’ and ‘1’. A typical implementation, illustrated in Fig. 5.x, consists of an envelope detector followed by an RC averaging stage and a comparator for threshold computation. Such designs are inspired by the work of Smith and al. [49], and have been widely adopted in TV and FM backscatter prototypes, where energy efficiency and hardware simplicity are crucial. Although these architectures drastically reduce power consumption, they exhibit limited sensitivity and are more susceptible to interference compared to SDRs.

5.1.4. Advanced and Adaptive Receiver Architectures

Recent research has explored advanced receiver designs to overcome the challenges of sensitivity and interference in future AmBC networks. These include architectures leveraging massive MIMO (mMIMO) arrays, reconfigurable intelligent surfaces (RIS), and hybrid digital-analog front-ends to enhance selectivity and improve the signal-to-interference ratio. In

[60] and [9], the authors discuss adaptive receivers capable of beamforming, polarization diversity, and energy-aware detection for 5G/6G ambient backscatter scenarios. Table 2 summarizes representative receiver types in the literature, along with example systems and key characteristics. This classification provides a foundation for analyzing sensitivity and selectivity challenges, which will be further addressed in Section 5.2.

5.2. Sensitivity Challenges in Backscatter Reception

In ambient backscatter communication (AmBC) systems, the receiver must detect and decode an extremely weak backscattered signal in the presence of a much stronger direct ambient transmission. This inherent power asymmetry often exceeding 60 dB between the direct path and the backscattered path makes receiver sensitivity a critical performance bottleneck. Sensitivity defines the minimum detectable signal power level, below which reliable detection of the backscatter modulation becomes impossible. This limitation directly affects the maximum communication range and the robustness of the system under varying propagation conditions.

5.2.1. Sources of Sensitivity Degradation

Several factors contribute to sensitivity degradation in AmBC receivers:

- **Low Signal-to-Noise Ratio (SNR)**: The backscattered component is typically orders of magnitude weaker than the ambient carrier, making it highly susceptible to thermal noise and quantization noise [4] [6].
- **Direct Path Interference**: The strong ambient transmission can saturate the receiver front-end, masking the weak modulated reflection. This is especially critical in bistatic configurations with short Tx–Rx separation [49] [60].
- **Lack of Channel State Information (CSI)**: In many AmBC scenarios, the channel between the tag and receiver is unknown or rapidly varying, complicating coherent demodulation [61] [31].
- **Interference from Other Ambient Sources**: In cellular and dense IoT environments, inter-cell and co-channel interference can further limit sensitivity, as shown in [62].
- **Hardware Limitations**: Ultra-low-power receivers often omit high-resolution ADCs and rely on analog envelope detection [11], which inherently reduces dynamic range and noise resilience.

5.2.2. Classical Approaches

Traditional methods for enhancing sensitivity include:

- **Energy Detection with Fixed Thresholding**: A simple yet widely used method where the average received power is compared against a predefined threshold. While

computationally efficient, this approach suffers in dynamic environments due to threshold drift.

- **Differential Encoding and Detection**: As analyzed by Qian and al. [63], effectively mitigates phase noise and frequency offset in ambient backscatter systems. However, the bit error rate (BER) performance deteriorates significantly under low signal-to-noise ratio (SNR) conditions.
- **Analog Interference Cancellation**: In ultra-low-power designs, partial suppression of the direct signal at the RF or IF stage can improve detection margins without full digital processing.

5.2.3. Advanced Sensitivity Enhancement Techniques

Recent research has proposed more sophisticated strategies to overcome these limitations:

- **Deep Learning–Based Detection**: Zargari and al. [64] developed a deep neural network (DNN) for joint channel estimation and signal detection in AmBC, improving BER performance by up to 20 % compared to conventional maximum likelihood (ML) detection, particularly in low-SNR conditions and without explicit CSI.
- **Intelligent Interference Cancellation**: Zhong and al. [64] introduced a NOMA-based algorithm for direct-path interference suppression in UAV-powered AmBC networks. Their results demonstrate a significant BER reduction under strong ambient carrier interference, directly enhancing sensitivity in aerial IoT deployments.
- **Cellular-Scale Sensitivity Optimization**: Biswas and al. [65] conducted a sensitivity analysis of ambient backscattering communications in heavily loaded cellular networks, showing that tag placement within the cell and strategic filtering can extend coverage range by mitigating inter-cell interference.
- **Machine Learning for Adaptive Detection**: Cheng and al. [66] proposed ML-based channel estimation and detection algorithms capable of adapting to non-stationary interference and noise patterns, outperforming fixed-threshold and differential schemes.

5.2.4. Practical Considerations

While advanced algorithms can significantly enhance sensitivity, they also introduce trade-offs:

- **Computational Complexity**: Deep learning and adaptive detection require higher processing power, potentially conflicting with the ultra-low-power constraint of many AmBC receivers.
- **Training Data Requirements**: ML-based solutions depend on extensive and representative datasets, which may be challenging to collect in dynamic RF environments.

- **Hardware Constraints**: Implementing complex algorithms in real time may necessitate hybrid architectures combining analog front-ends with low-power digital processors.

In this thesis, an **SDR-based receiver (USRP B210)** is used for AmBC signal acquisition and processing. This platform enables fine control over front-end gain, filtering, and sampling parameters, which is essential for preventing ADC saturation from the strong direct path while preserving the weak backscattered component. Its ability to capture raw IQ data allows offline evaluation of multiple detection algorithms, making it particularly suitable for sensitivity studies in controlled and real-world environments.

5.2.5. Summary

Sensitivity in AmBC reception is fundamentally limited by the weak nature of the backscattered signal and the dominance of the direct ambient transmission. Classical techniques provide simple, low-power solutions but struggle in challenging environments, while modern approaches leveraging deep learning, interference cancellation, and adaptive detection offer substantial gains at the expense of increased complexity.

6. Related Work and Existing Prototypes

6.1. AmBC Systems in Literature

6.1.1. Indoor and Controlled Environments

Indoor ambient backscatter communication (AmBC) experiments are typically conducted in controlled environments such as laboratories, anechoic chambers, or dedicated indoor corridors. Such conditions provide a stable and reproducible propagation channel, enabling precise evaluation of link budgets, modulation performance, and receiver sensitivity without the unpredictable variability of outdoor scenarios. These trials are particularly useful for benchmarking novel tag architectures, validating analytical models, and testing detection algorithms before deployment in real-world conditions.

Monostatic systems in indoor settings benefit from simplified synchronization and reduced hardware complexity, as the same antenna or closely spaced antennas at the reader act as both transmitter and receiver. Daskalakis and al. [67] demonstrated an indoor monostatic prototype leveraging FM broadcasting with simple on–off keying (OOK) modulation (Figure 5), achieving reliable operation over several meters with extremely low power consumption. They later extended this concept with a spectrally efficient 4-PAM modulation scheme [68], increasing throughput while preserving low energy consumption—an approach well suited for battery-free IoT devices.

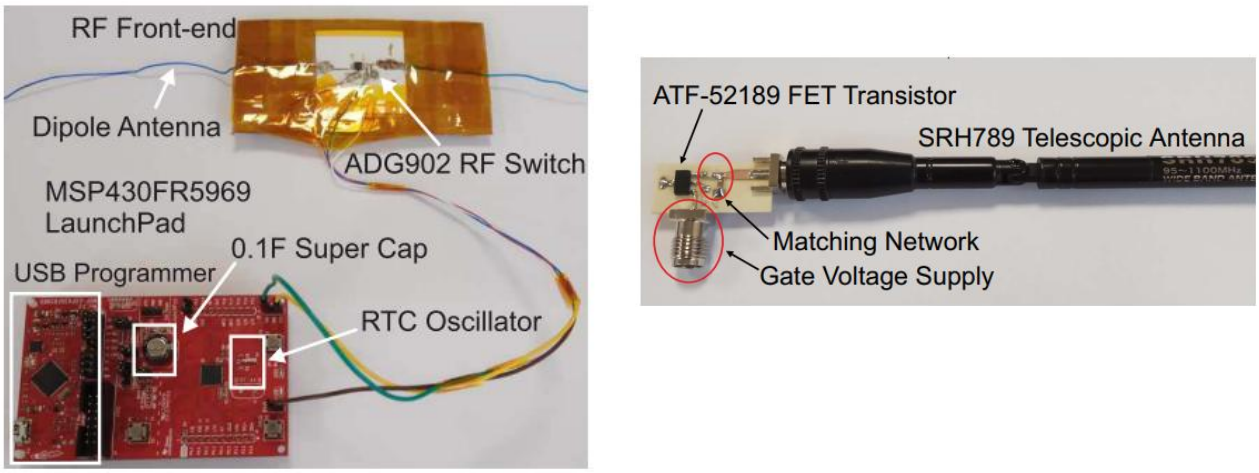

Figure 5. Ambient backscatter communication prototypes [67], [68], showing the fabricated RF front-end and the MSP430-based backscatter tag.

Bistatic systems have also been widely studied in indoor environments, as decoupling the transmitter and receiver enables flexible geometries and improved isolation from the strong direct path. Liao et al. [53] implemented a bistatic AmBC system using commercial LTE pilots in a corridor environment. Their results showed that pilot-based detection could robustly recover backscattered data even in the presence of significant direct-path interference, without requiring full channel estimation. Similarly, other indoor bistatic studies have been used to validate propagation models, investigate the impact of antenna orientation and tag placement, and optimize carrier suppression techniques for low-SNR operation.

Overall, controlled indoor environments reveal complementary strengths for both monostatic and bistatic AmBC systems. Monostatic architectures are attractive for their simplicity and compact integration, making them suitable for low-cost readers. Bistatic setups, on the other hand, offer greater deployment flexibility and improved interference suppression, which often translates into better sensitivity and robustness in multipath-rich indoor channels.

While indoor experiments provide controlled and repeatable conditions, outdoor deployments are essential to evaluate AmBC performance under the unpredictable dynamics and interference-rich nature of real-world environments.

6.1.2. Outdoor and Real-World Deployments

Outdoor ambient backscatter communication (AmBC) experiments are conducted in real-world environments where propagation conditions are less predictable and interference levels are often higher than in laboratory settings. These deployments provide a realistic assessment of system robustness, coverage range, and interference resilience, making them essential for validating the applicability of AmBC in large-scale IoT and smart city scenarios.

Monostatic outdoor systems, while less common due to increased self-interference from strong direct-path signals, have been successfully demonstrated in specialized contexts. For instance, Daskalakis et al. [69] introduced the LoRAB system, a long-range monostatic ambient backscatter platform leveraging chirp spread spectrum (CSS) modulation. With a front-end consumption as low as 130 nA, this system achieved communication over 130 m in outdoor conditions, while offering "zero-interception" capabilities for enhanced privacy.

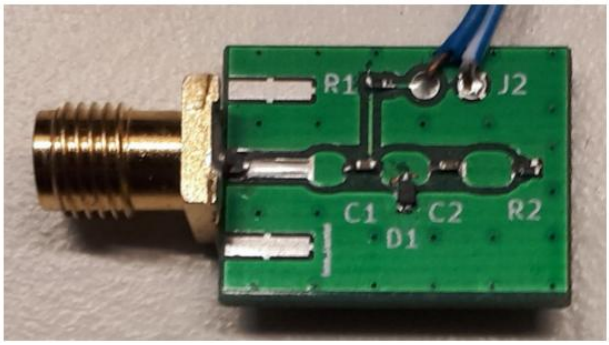

Figure 6. Backscatter modulator prototype, illustrating a compact PCB design equipped with an SMA connector and matching network for impedance-based modulation experiments [70].

Bistatic architectures dominate outdoor AmBC research due to their inherent ability to spatially separate the transmitter and receiver, thereby reducing self-interference and enabling more flexible coverage optimization. Xu et al. [35] presented FM Rider, a bistatic ambient FM backscatter system employing two-FSK modulation, achieving stable communication over distances exceeding 100 m. Similarly, Badihi et al. [70] performed a link budget validation for sub-1 GHz bistatic backscatter systems in outdoor scenarios, comparing monostatic and bistatic configurations and highlighting the superior isolation and range performance of the latter (Figure 6).

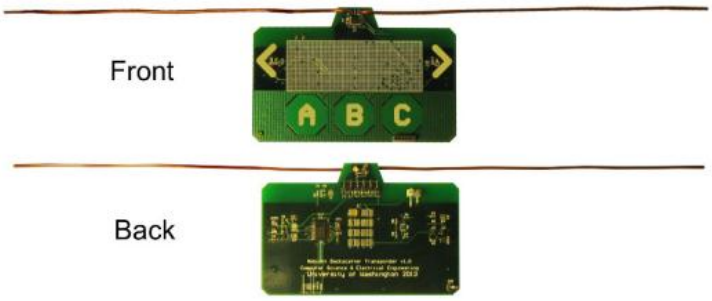

Figure 7. Backscatter communication PCB prototype, illustrating the front and back sides of the board capable of harvesting, transmitting, and receiving signals [4].

Several studies have also examined outdoor AmBC in the context of cellular networks. Biswas and Lempiäinen [52] assessed 5G-based AmBC in outdoor macrocell environments, showing that optimal tag placement within a cell and strategic filtering could extend coverage and

mitigate inter-cell interference. In an earlier study, Biswas et al. [71] analyzed the power budget for wide-area AmBC, providing theoretical and experimental insights into the achievable range and the link margin under realistic network loading conditions.

Recent outdoor experiments have also explored novel hardware implementations (Figure 8). Xie et al. [72] tested a flexible thin-film multi-antenna backscatter device in real-world environments, demonstrating its ability to adapt radiation patterns and maintain reliable connectivity despite environmental dynamics.

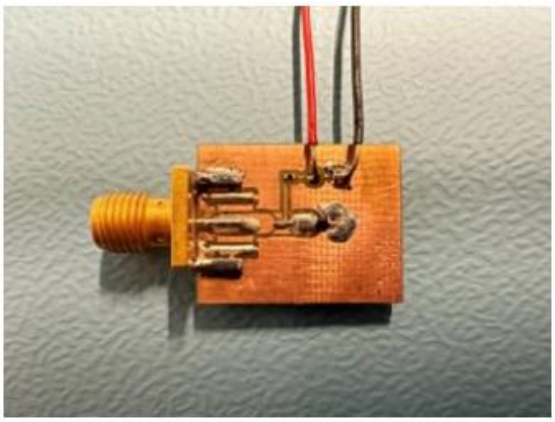

Figure 8. Reflective backscatter tag prototype, illustrating a compact PCB structure equipped with an SMA connector and impedance-switching network for signal reflection and modulation [72].

In summary, outdoor AmBC deployments confirm that bistatic configurations consistently achieve greater coverage and improved resilience against interference compared to monostatic systems, particularly in urban and suburban scenarios. However, advances in modulation schemes, antenna design, and power-efficient architectures are progressively enabling monostatic systems to reach competitive ranges in real-world environments, thereby expanding the deployment options for ambient backscatter technology.

6.2. Summary of Key Implementations

Table 2 summarizes representative implementations of ambient backscatter communication (AmBC) systems reported in the literature, encompassing both monostatic and bistatic configurations, as discussed in Section 6.1. The comparison covers key parameters, including the carrier source, operating frequency, modulation scheme, deployment environment, achievable range, and specific technical contributions. For completeness, the table also includes the author's own work on a bistatic 5G-NR AmBC system with BPSK modulation, experimentally validated in anechoic and semi-anechoic chambers, as presented in [73].

Ref	Authors & Year	configuration	Carrier source	Frequency	Modulation	Environment	Range
[67]	Daskalakis et al., 2017	Monostatic	FM broadcast	88-108 MHz	OOK	Indoor	~5 m
[68]	Daskalakis et al., 2018	Monostatic	FM broadcast	88-108 MHz	4-PAM	Indoor	~5 m
[53]	Liao et al., 2024	Bistatic	LTE pilots	2.6 GHz	ASK	Indoor corridor	~10 m
[69]	Daskalakis et al., 2022	Monostatic	LoRa CSS	868 MHz	CSS	Outdoor	130 m
[35]	Xu et al., 2024	Bistatic	FM broadcast	88-108 MHz	2-FSK	Outdoor	>100 m
[70]	Badihi et al., 2019	Bistatic	Sub-1 GHz tone	868 MHz	OOK	Outdoor	~50 m
[52]	Biswas & Lempiäinen, 2021	Bistatic	5G NR	3.5 GHz	ASK	Outdoor macrocell	~40 m
[71]	Biswas et al., 2018	Bistatic	LTE	800 MHZ	ASK	Outdoor wide area	~100 m
[72]	Xie et al., 2024	Bistatic	Sub-1 GHz tone	915 MHz	ASK	Outdoor	~30 m
[73]	Lefki et al., 2025	Bistatic	5G NR	3.5 GHz	BPSK	Anechoic & semi-anechoic	Up to 6 m

Table 2. Summary of representative AmBC system implementations in the literature.

The comparison reveals clear trends across environments and configurations. Indoor implementations often relying on FM or LTE carriers allow controlled evaluation of modulation schemes and receiver strategies, with ranges typically limited to a few meters due to multipath-rich but interference-controlled conditions. Outdoor deployments consistently show that bistatic architecture achieve greater range and interference resilience compared to monostatic counterparts, particularly in urban and suburban scenarios. However, advancements in modulation formats, antenna design, and ultra-low-power architectures (e.g., LoRa CSS) have enabled monostatic systems to close the performance gap in certain use cases. The inclusion of the present work in Table 2 highlights its originality in leveraging a 5G-NR ambient carrier in a bistatic configuration with BPSK modulation, experimentally validated under controlled RF

conditions, thereby bridging the gap between analytical models and real-world deployment feasibility.

7. Challenges

Although ambient backscatter communication (AmBC) has witnessed significant progress in recent years, several challenges remain unresolved, particularly in the context of realistic deployments.

A first limitation lies in the lack of validation in outdoor bistatic environments. Most existing studies have focused on controlled indoor scenarios, where multipath, mobility, and large-scale fading are relatively constrained. Huynh and al [6] already emphasized this gap in their survey, noting that early demonstrations were confined to proof-of-concept indoor setups. More recently, in [74] analyzed direct-path interference suppression requirements in bistatic systems, showing that leakage from the strong ambient carrier can severely limit receiver sensitivity in outdoor deployments. Kaplan and al [37] further confirmed this limitation by proposing a distributed MIMO-based beamforming strategy to enhance dynamic range, underlining that interference mitigation remains a critical bottleneck when moving beyond laboratory conditions.

Another key challenge concerns the exploitation of 5G-NR as an ambient carrier. While 5G signals offer dense OFDM structures and widespread coverage, their dynamic spectrum allocation and interference patterns introduce additional difficulties for reliable backscatter detection. In [52] assessed the feasibility of leveraging 5G signals at 3.5 GHz and 26 GHz for AmBC, showing promising opportunities but also highlighting the absence of experimental outdoor validation. This indicates that the integration of AmBC with emerging mobile networks is still in its early stage, with limited evidence of scalability beyond small-scale tests.

A further limitation is related to receiver design and evaluation. Software-defined radios (SDRs) such as USRP-based platforms have been widely used for AmBC prototyping, given their flexibility and programmability. However, only a limited number of works have assessed their performance under real ambient conditions. In [75] they demonstrated FM-based backscattering with a low-bitrate SDR receiver, but in a constrained setup with limited spectral diversity. Similarly, Kim and Lee [76] proposed *AnyScatter*, an SDR-based architecture capable of decoding heterogeneous ambient sources (Wi-Fi, Bluetooth), yet their experiments remained restricted to laboratory conditions. This underscores the need for systematic evaluations of SDR-based receivers under realistic, interference-rich environments, especially as they are often the first step toward practical system prototyping.

Finally, the development of synchronized multi-sensor AmBC systems remains an open research problem. Most existing literature still addresses single-tag scenarios, overlooking scalability and coordination. Li and al [77] introduced *MmBack*, a clock-free multi-sensor backscatter scheme enabling synchronous acquisition and multiplexing of multiple sensors. While this work is a significant step forward, it remains at a proof-of-concept stage and does not yet address large-scale deployments, energy efficiency in dense networks, or robustness in dynamic outdoor conditions.

In summary, the literature reveals important gaps that must be addressed for AmBC to evolve from proof-of-concept demonstrations to practical large-scale deployments. These include the lack of outdoor bistatic validation, limited experimental studies leveraging 5G-NR as an ambient carrier, insufficient evaluation of SDR-based receivers in realistic conditions, and the absence of mature solutions for synchronized multi-sensor systems. Addressing these challenges is essential to unlock the full potential of AmBC for smart cities, environmental monitoring, and future large-scale IoT infrastructures.

8. Positioning of the Thesis

8.1. Research Gaps Identified

Despite the significant progress made in ambient backscatter communication (AmBC) research, several limitations persist in the current state of the art. First, the majority of existing works remain focused on controlled indoor environments, whereas validation in realistic outdoor bistatic scenarios is still scarce. This gap restricts the ability to assess system performance under conditions that involve multipath fading, mobility, and large-scale path loss. Second, although 5G-NR signals have been identified as a promising ambient carrier thanks to their high density, wide coverage, and OFDM structure, very few studies have explored their use in practical AmBC deployments. Third, while software-defined radios (SDRs) have been increasingly employed for prototyping, systematic evaluations of SDR-based receivers in real ambient conditions remain limited. Finally, the development of multi-sensor backscatter systems is still in its infancy, with synchronization and multiplexing largely unexplored at scale. Addressing these gaps is essential to enable the transition of AmBC from proof-of-concept demonstrations to scalable solutions for IoT, smart cities, and environmental monitoring.

8.2. Thesis Contributions

This thesis advances the state of the art in AmBC through three main and complementary contributions, which collectively span analytical modeling, prototype design, and real-world validation:

- **Feasibility Analysis of 5G-Based AmBC:**
  A complete analytical framework was developed to evaluate the feasibility of using 5G signals as ambient carriers. The study covers macro-urban, micro-urban, and rural environments in both LOS and NLOS conditions, providing detailed propagation models, path loss characterization, and link budget analysis. This work establishes the theoretical foundation for leveraging 5G-NR as a viable ambient source for large-scale deployments.
- **Design and Experimental Validation of a Bistatic AmBC Prototype:**
  A novel backscatter tag prototype was designed and experimentally validated in anechoic and semi-anechoic chambers. The system implements BPSK modulation through impedance switching and demonstrates the feasibility of bistatic AmBC links using 5G-NR carriers. This contribution provides one of the first experimental comparisons between theoretical predictions and controlled measurements.
- **Receiver Architecture and Real-World Validation:**
  A flexible software-defined radio (SDR) receiver chain was implemented using USRP B210 and GNU Radio to detect and process weak backscattered signals. The system was evaluated in multiple environments, including anechoic, semi-anechoic, indoor, and outdoor deployments with live 5G base stations. Performance analysis included bit error rate (BER) measurements, interference resilience, and sensitivity evaluation. This contribution bridges the gap between controlled laboratory studies and realistic conditions, highlighting the potential of SDR-based architectures for practical AmBC reception.

8.3. Positioning within Literature

The proposed work distinguishes itself from prior research by its focus on bistatic configurations and its emphasis on 5G-NR as an ambient carrier. Earlier AmBC implementations such as FM-, Wi-Fi-, or LTE-based prototypes by Daskalakis and al. [67], [68], [69] and Liao and al. [53] were predominantly monostatic and confined to controlled indoor environments. By contrast, this thesis demonstrates both feasibility and practical implementation in bistatic scenarios, including outdoor experiments with real 5G infrastructure. Another originality lies in the adoption of BPSK modulation, which goes beyond the OOK or PAM schemes commonly reported in the literature, thus enhancing robustness and data recovery in low-SNR conditions. Furthermore, while prior works have frequently relied on COTS modules or simplified analog front-ends, the SDR-based receiver chain developed here

provides a flexible and adaptive platform for investigating sensitivity, interference management, and multi-sensor integration across diverse environments.

In summary, this thesis moves beyond proof-of-concept demonstrations by delivering an integrated framework that spans feasibility modeling, prototype design, and real-world validation. In doing so, it bridges the gap between analytical studies and practical deployments, thereby advancing both the theoretical foundations and the technological readiness of ambient backscatter communication for next-generation IoT and wireless networks.

References

[1] Javaid, Shumaila & Fahim, Hamza & He, Bin & Saeed, Nasir. (2024). Eco-Friendly 0G Networks: Unlocking the Power of Backscatter Communications for a Greener Future. 10.48550/arXiv.2411.13440.

[2] S. Chang and Y. Ding, "Development in Ambient Backscatter Communications," *IET Microwaves, Antennas & Propagation*, vol. 17, no. 13, pp. 963–973, Oct. 2023, doi: 10.1049/mia2.12419.

[3] H. Stockman, "Communication by means of reflected power," *Proceedings of the IRE*, vol. 36, no. 10, pp. 1196–1204, Oct. 1948, doi: 10.1109/JRPROC.1948.226245.

[4] V. Liu, A. Parks, V. Talla, S. Gollakota, D. Wetherall, and J. R. Smith, "Ambient backscatter: Wireless communication out of thin air," in *Proc. ACM SIGCOMM*, Hong Kong, China, Aug. 2013, pp. 39–50, doi: 10.1145/2486001.2486015.

[5] W. Wu, X. Wang, A. Hawbani, L. Yuan, and W. Gong, "A survey on ambient backscatter communications: Principles, systems, applications, and challenges," *Computer Networks*, vol. 216, no. 109235, pp. 1–19, Nov. 2022, doi: 10.1016/j.comnet.2022.109235.

[6] N. Van Huynh, D. T. Hoang, X. Lu, D. Niyato, P. Wang, and D. I. Kim, "Ambient backscatter communications: A contemporary survey," *IEEE Communications Surveys & Tutorials*, vol. 20, no. 4, pp. 2889–2922, 4th Quart., 2018, doi: 10.1109/COMST.2018.2841964.

[7] D. T. Hoang, N. Van Huynh, D. Niyato, and D. I. Kim, *Ambient Backscatter Communication: Circuit and Antenna Designs*. Cambridge, U.K.: Cambridge Univ. Press, 2020. doi: 10.1017/9781108883474.

[8] T. Jamshed, M. Z. Chowdhury, M. Hasan, and Y. M. Jang, "Artificial intelligence, ambient backscatter communication and non-terrestrial networks: A 6G commixture," *arXiv preprint arXiv:2501.08122*, Jan. 2025. [Online]. Available: https://arxiv.org/abs/2501.08122.

[9] D. T. Hoang, D. Niyato, D. I. Kim, N. V. Huynh, and S. Gong, Fundamentals of Ambient Backscatter Communication, in Ambient Backscatter Communication Networks, Cambridge Univ. Press, 2020, pp. 33–61.

[10] P. Zhang, J. Gummeson, and D. Ganesan, "Enabling practical backscatter communication for on-body sensors," in Proc. ACM SIGCOMM, 2016, pp. 370–383.

[11] W. Zhang et al., "A green paradigm for Internet of Things: Ambient backscatter communications," in China Communications, vol. 16, no. 7, pp. 109-119, July 2019, doi: 10.23919/JCC.2019.07.009.

[12] J. K. Schindler, R. B. Mack, and P. Blacksmith, "The control of electromagnetic scattering by impedance loading," Proc. IEEE, vol. 53, no. 8, pp. 993–1004, 1965.

[13] R. Fara, D. -T. Phan-Huy and M. D. Renzo, "Ambient backscatters-friendly 5G networks: creating hot spots for tags and good spots for readers," 2020 IEEE Wireless Communications and Networking Conference (WCNC), Seoul, Korea (South), 2020, pp. 1-7, doi: 10.1109/WCNC45663.2020.9120781.

[14] J. Kimionis, A. Bletsas and J. N. Sahalos, "Increased Range Bistatic Scatter Radio," in IEEE Transactions on Communications, vol. 62, no. 3, pp. 1091-1104, March 2014, doi: 10.1109/TCOMM.2014.020314.130559.

[15] J. Kimionis, A. Bletsas and J. N. Sahalos, "Bistatic backscatter radio for power-limited sensor networks," 2013 IEEE Global Communications Conference (GLOBECOM), Atlanta, GA, USA, 2013, pp. 353-358, doi: 10.1109/GLOCOM.2013.6831096.

[16] S. H. Choi and D. I. Kim, "Backscatter radio communication for wireless powered communication networks," 2015 21st Asia-Pacific Conference on Communications (APCC), Kyoto, Japan, 2015, pp. 370-374, doi: 10.1109/APCC.2015.7412542.

[17] Kellogg, Bryce & Talla, Vamsi & Smith, Joshua & Gollakot, Shyamnath. (2017). PASSIVE WI-FI: Bringing Low Power to Wi-Fi Transmissions. GetMobile: Mobile Computing and Communications. 20. 38-41. 10.1145/3036699.3036711.

[18] Bryce Kellogg, Aaron Parks, Shyamnath Gollakota, Joshua R. Smith, and David Wetherall. 2014. Wi-fi backscatter: internet connectivity for RF-powered devices. SIGCOMM Comput. Commun. Rev. 44, 4 (October 2014), 607–618..

[19] Abedi, Ali & Abari, Omid. (2021). Can WiFi Backscatter Achieve the Range of RFID?: Nulling to the Rescue. 171-177. 10.1145/3484266.3487372.

[20] B. Gu, D. Li, H. Ding, G. Wang and C. Tellambura, "Breaking the Interference and Fading Gridlock in Backscatter Communications: State-of-the-Art, Design Challenges, and Future Directions," in IEEE Communications Surveys & Tutorials, vol. 27, no. 2, pp. 870-911, April 2025, doi: 10.1109/COMST.2024.3436082.

[21] J. D. Griffin and G. D. Durgin, "Complete Link Budgets for Backscatter-Radio and RFID Systems," in IEEE Antennas and Propagation Magazine, vol. 51, no. 2, pp. 11-25, April 2009, doi: 10.1109/MAP.2009.5162013.

[22] N. Fasarakis-Hilliard, P. N. Alevizos and A. Bletsas, "Coherent Detection and Channel Coding for Bistatic Scatter Radio Sensor Networking," in IEEE Transactions on Communications, vol. 63, no. 5, pp. 1798-1810, May 2015, doi: 10.1109/TCOMM.2015.2412546.

[23] K. Finkenzeller, RFID Handbook: Fundamentals and Applications in Contactless Smart Cards, Radio Frequency Identification and Near-Field Communication, 3rd ed., John Wiley & Sons, Jun. 2010.

[24] J. Kimionis, A. Bletsas and J. N. Sahalos, "Bistatic backscatter radio for tag read-range extension," 2012 IEEE International Conference on RFID-Technologies and Applications (RFID-TA), Nice, France, 2012, pp. 356-361, doi: 10.1109/RFID-TA.2012.6404546.

[25] Elsayed, Ebrahim & Yousif, Bedir. (2020). Performance evaluation and enhancement of the modified OOK based IM/DD techniques for hybrid fiber/FSO communication over WDM-PON systems. Optical and Quantum Electronics. 52. 385. 10.1007/s11082-020-02497-0.

[26] Zhao, Jumin & Shi, Jiapeng & Li, Deng-ao & Li, Yajun & Cheng, Jie. (2025). Design of multi-element QAM backscatter modulated tag based on backscatter communication. Analog Integrated Circuits and Signal Processing. 124. 10.1007/s10470-025-02455-4.

[27] S. Thomas and M. S. Reynolds, "QAM backscatter for passive UHF RFID tags," 2010 IEEE International Conference on RFID (IEEE RFID 2010), Orlando, FL, USA, 2010, pp. 210-214, doi: 10.1109/RFID.2010.5467238.

[28] S. N. Daskalakis, R. Correia, G. Goussetis, M. M. Tentzeris, N. B. Carvalho and A. Georgiadis, "Spectrally Efficient 4-PAM Ambient FM Backscattering for Wireless Sensing and RFID Applications," 2018 IEEE/MTT-S International Microwave Symposium - IMS, Philadelphia, PA, USA, 2018, pp. 266-269, doi: 10.1109/MWSYM.2018.8439284.

[29] Lu, Dongxu & Zhou, Xian & Yang, Yuqiang & Huo, Jiahao & Yuan, Jin-Hui & Long, Keping & Yu, Changyuan & Lau, Alan Pak Tao & Lu, Chao. (2021). Theoretical analysis of PAM-N and M-QAM BER computation with single-sideband signal. Science China Information Sciences. 64. 10.1007/s11432-020-3025-4.
[30] Dinesh Bharadia, Kiran Raj Joshi, Manikanta Kotaru, and Sachin Katti. 2015. BackFi: High Throughput WiFi Backscatter. SIGCOMM Comput. Commun. Rev. 45, 4 (October 2015), 283–296.
[31] G. Wang, F. Gao, R. Fan and C. Tellambura, "Ambient Backscatter Communication Systems: Detection and Performance Analysis," in IEEE Transactions on Communications, vol. 64, no. 11, pp. 4836-4846, Nov. 2016, doi: 10.1109/TCOMM.2016.2602341.
[32] Weiqi Wu, Xingfu Wang, Ammar Hawbani, Longzhi Yuan, and Wei Gong. 2022. A survey on ambient backscatter communications: Principles, systems, applications, and challenges. Comput. Netw. 216, C (Oct 2022).
[33] J. B. Anderson, T. Aulin, and C.-E. Sundberg, Digital Phase Modulation. New York, NY, USA: Springer, 1986.
[34] Liao, Jingyi & Wang, Xiyu & Ruttik, Kalle & Jantti, Riku & Dinh-Thuy, Phan-Huy. (2023). Ambient FSK Backscatter Communications using LTE Cell Specific Reference Signals. 10.48550/arXiv.2301.13664.

[35] K. Xu et al., "FM Rider: Two-FSK Modulation-Based Ambient FM Backscatter Over 100 m Distance," in IEEE Transactions on Microwave Theory and Techniques, vol. 72, no. 9, pp. 5563-5575, Sept. 2024, doi: 10.1109/TMTT.2024.3367439.

[36] A. C. Y. Goay, D. Mishra, M. Matthaiou and A. Seneviratne, "Backscatter Communication with Selective FSK Modulation," 2024 IEEE 25th International Workshop on Signal Processing Advances in Wireless Communications (SPAWC), Lucca, Italy, 2024, pp. 511-515, doi: 10.1109/SPAWC60668.2024.10694350.

[37] Kaplan, Ahmet & Vieira, Joao & Larsson, Erik. (2022). Dynamic Range Improvement in Bistatic Backscatter Communication Using Distributed MIMO. 2486-2492. 10.1109/GLOBECOM48099.2022.10000927.
[38] S. Misra, "Millimeter Wave Wireless Communications (Rappaport, T., et al; 2014) [Book review]," in IEEE Wireless Communications, vol. 22, no. 5, pp. 6-7, October 2015, doi: 10.1109/MWC.2015.7306370.

[39] 3GPP TS 38.104, NR; Base Station (BS) Radio Transmission and Reception, v17.x, 2022.

[40] J. G. Andrews et al., "What Will 5G Be?," in IEEE Journal on Selected Areas in Communications, vol. 32, no. 6, pp. 1065-1082, June 2014, doi: 10.1109/JSAC.2014.2328098.

[41] M. Singh, "Ambient Backscatter Communication in 5G," 2021 Third International Conference on Inventive Research in Computing Applications (ICIRCA), Coimbatore, India, 2021, pp. 430-432, doi: 10.1109/ICIRCA51532.2021.9544698.

[42] M. ElMossallamy, Z. Han, M. Pan, R. Jantti, K. Seddik and G. Y. Li, "Noncoherent Frequency Shift Keying for Ambient Backscatter Over OFDM Signals," ICC 2019 - 2019 IEEE International Conference on Communications (ICC), Shanghai, China, 2019, pp. 1-6, doi: 10.1109/ICC.2019.8762048.

[43] M. A. ElMossallamy, Z. Han, M. Pan, R. Jäntti, K. G. Seddik and G. Y. Li, "Backscatter Communications Over Ambient OFDM Signals Using Null Subcarriers," 2018 IEEE Global Communications Conference (GLOBECOM), Abu Dhabi, United Arab Emirates, 2018, pp. 1-6, doi: 10.1109/GLOCOM.2018.8647245.
[44] H. Chen, Q. Zhang, R. Long, Y. Pei and Y. -C. Liang, "Pilot Design and Signal Detection for Symbiotic Radio Over OFDM Carriers," in IEEE Transactions on Wireless Communications, vol. 23, no. 2, pp. 1129-1142, Feb. 2024, doi: 10.1109/TWC.2023.3286395.
[45] M. A. ElMossallamy, M. Pan, R. Jäntti, K. G. Seddik, G. Y. Li and Z. Han, "Noncoherent Backscatter Communications Over Ambient OFDM Signals," in IEEE Transactions on Communications, vol. 67, no. 5, pp. 3597-3611, May 2019, doi: 10.1109/TCOMM.2019.2899301.
[46] Liu, Wanchun & Huang, Kaibin & Zhou, Xiangyun & Durrani, Salman. (2019). Next generation backscatter communication: systems, techniques, and applications. EURASIP Journal on Wireless Communications and Networking. 2019. 10.1186/s13638-019-1391-7.
[47] 3GPP, *Study on channel model for frequencies from 0.5 to 100 GHz (Release 16)*, 3GPP TR 38.901, V16.1.0, 2020.
[48] T. S. Rappaport, *Wireless Communications: Principles and Practice*, 2nd ed. Upper Saddle River, NJ, USA: Prentice Hall, 2015.
[49] Parks, Aaron & Liu, Angli & Gollakota, Shyamnath & Smith, Joshua. (2014). Turbocharging ambient backscatter communication. ACM SIGCOMM Computer Communication Review. 44. 10.1145/2619239.2626312.
[50] J. Qian, F. Gao, G. Wang, S. Jin, and H. B. Zhu, “Noncoherent Detections for Ambient Backscatter System” *IEEE Trans. Wireless Commun.*, vol. 16, no. 3, pp. 1412-1422, Apr. 2016.
[51] Wang, Anran & Iyer, Vikram & Talla, Vamsi & Smith, Joshua & Gollakota, Shyamnath. (2017). FM Backscatter: Enabling Connected Cities and Smart Fabrics. 10.48550/arXiv.1702.07044.
[52] Biswas, Ritayan & Lempiäinen, Jukka. (2021). Assessment of 5G as an ambient signal for outdoor backscattering communications. Wireless Networks. 27. 10.1007/s11276-021-02731-x.

[53] J. Liao et al., "Indoor Backscattering Communication by Using Commercial LTE Pilots," 2024 IEEE 99th Vehicular Technology Conference (VTC2024-Spring), Singapore, Singapore, 2024, pp. 1-5, doi: 10.1109/VTC2024-Spring62846.2024.10683260.

[54] Konate, Siaka & Li, Changli & Xu, Lizhong. (2023). Theoretical evaluation of the performance of ambient LoRa backscatter communication. 41. 10.1117/12.2679829.

[55] Sooriarachchi, Vishalya & Perera, Tharindu & Jayakody, Dush Nalin. (2025). Ambient Backscatter- and Simultaneous Wireless Information and Power Transfer-Enabled Switch for Indoor Internet of Things Systems. Applied Sciences. 15. 478. 10.3390/app15010478.

[56] V. Liu, V. Talla, and S. Gollakota, “Enabling instantaneous feedback with full-duplex backscatter,” in *Proc. ACM MobiCom*, Maui, HI, USA, Sept. 2014, pp. 67–78.

[57] V. Talla, B. Kellogg, J. R. Smith, and S. Gollakota, “LoRa Backscatter: Enabling The Vision of Ubiquitous Connectivity,” Proc. ACM IMWUT, vol. 1, no. 3, Article 105, Sept. 2017.

[58] M. Katanbaf, A. Saffari, and J. R. Smith, “Receiver selectivity limits on bistatic backscatter range,” in Proc. IEEE Int. Conf. RFID (RFID), Orlando, FL, USA, Sep.–Oct. 2020, pp. 1–8, doi: 10.1109/RFID49298.2020.9244826.

[59] Z. Shen, A. Athalye, and P. M. Djuric, “Phase Cancellation in Backscatter-Based Tag-to-Tag Communication Systems,” IEEE Internet of Things Journal, vol. 3, no. 6, pp. 959–970, Dec. 2016.

[60] R. Fara, Ambient Backscatter Communications in Future Mobile Networks, Ph.D. thesis, Université Paris-Saclay, 2021.

[61] S. Zargari, A. Hakimi, C. Tellambura and A. Maaref, "Enhancing AmBC Systems With Deep Learning for Joint Channel Estimation and Signal Detection," in IEEE Transactions on Communications, vol. 72, no. 3, pp. 1716-1731, March 2024, doi: 10.1109/TCOMM.2023.3333868.

[62] Elsanhoury, Ahmed & Galal, Islam & AlKady, Khaled & ElKhodary, Aml & M. Hassan, Ayman & Phan-Huy, Dinh-Thuy. (2025). First Real-Time Detection of Ambient Backscatters using Uplink Sounding Reference Signals of a Commercial 4G Smartphone. 10.48550/arXiv.2501.15576.

[63] J. Qian, F. Gao, G. Wang, and S. Jin, “Symbol detection and performance analysis of the ambient backscatter system,” in Proc. IEEE/CIC Int. Conf. Commun. China (ICCC), Chengdu, China, Jul. 2016, pp. 1–6, doi: 10.1109/ICCChina.2016.7636730.

[64] Zhong, Cheng & Zhai, Di & Lu, Yang & Li, Ke. (2024). Intelligent interference cancellation and ambient backscatter signal extraction for wireless-powered UAV IoT network. EURASIP Journal on Advances in Signal Processing. 2024. 10.1186/s13634-024-01121-7.

[65] R. Biswas and J. Lempiäinen, "Sensitivity Analysis of Ambient Backscattering Communications in Heavily Loaded Cellular Networks," 2023 18th Wireless On-Demand Network Systems and Services Conference (WONS), Madonna di Campiglio, Italy, 2023, pp. 51-55, doi: 10.23919/WONS57325.2023.10062021.

[66] D. Cheng, F. Wu, C. Zhang, J. Sun, and Y. Liu, “Machine learning for ambient backscatter channel estimation and signal detection: Opportunities and challenges,” in *Smart Grid and Innovative Frontiers in Telecommunications*, pp. 3–19, Jan. 2025. [Online]. Available: https://doi.org/10.1007/978-3-031-78806-2_1.

[67] S. N. Daskalakis, J. Kimionis, A. Collado, G. Goussetis, M. M. Tentzeris and A. Georgiadis, "Ambient Backscatterers Using FM Broadcasting for Low Cost and Low Power Wireless Applications," in IEEE Transactions on Microwave Theory and Techniques, vol. 65, no. 12, pp. 5251-5262, Dec. 2017, doi: 10.1109/TMTT.2017.2765635.

[68] S. N. Daskalakis, R. Correia, G. Goussetis, M. M. Tentzeris, N. B. Carvalho and A. Georgiadis, "Four-PAM Modulation of Ambient FM Backscattering for Spectrally Efficient Low-Power Applications," in IEEE

Transactions on Microwave Theory and Techniques, vol. 66, no. 12, pp. 5909-5921, Dec. 2018, doi: 10.1109/TMTT.2018.2879105.

[69] Daskalakis, Spyridon Nektarios & Georgiadis, Apostolos & Tentzeris, Manos & Goussetis, George & Deligeorgis, George. (2022). The New Era of Long-Range “Zero-Interception” Ambient Backscattering Systems: 130 m with 130 nA Front-End Consumption. Sensors. 22. 4151. 10.3390/s22114151.

[70] B. Badihi, A. Liljemark, M. U. Sheikh, J. Lietzén and R. Jäntti, "Link Budget Validation for Backscatter-Radio System in Sub-1GHz," 2019 IEEE Wireless Communications and Networking Conference (WCNC), Marrakesh, Morocco, 2019, pp. 1-6, doi: 10.1109/WCNC.2019.8885700.

[71] R. Biswas, J. Säe and J. Lempiäinen, "Power Budget for Wide Area Ambient Backscattering Communications," 2018 IEEE Vehicular Networking Conference (VNC), Taipei, Taiwan, 2018, pp. 1-6, doi: 10.1109/VNC.2018.8628465.

[72] B. Xie et al., "Flexible Thin Film Multi-Antenna Integrated Backscatter Device," 2024 IEEE Wireless Communications and Networking Conference (WCNC), Dubai, United Arab Emirates, 2024, pp. 1-6, doi: 10.1109/WCNC57260.2024.10571338.

[73] M. Lefki, M. S. Saha, S. Baccar, M. Kadi, H. Shall and M. Ghorbel, "Bistatic 5G-NR Ambient Backscatter Communication: Propagation Study and Experimental Validation in Anechoic Chambers," in IEEE Journal of Radio Frequency Identification, doi: 10.1109/JRFID.2025.3587632.

[74] R. Biswas, M. U. Sheikh, H. Yiğitler, J. Lempiäinen and R. Jäntti, "Direct Path Interference Suppression Requirements for Bistatic Backscatter Communication System," 2021 IEEE 93rd Vehicular Technology Conference (VTC2021-Spring), Helsinki, Finland, 2021, pp. 1-5, doi: 10.1109/VTC2021-Spring51267.2021.9448755.

[75] S. N. Daskalakis, G. Goussetis and A. Georgiadis, "Low Bitrate Ambient FM Backscattering for Low Cost and Low Power Sensing," 2018 2nd URSI Atlantic Radio Science Meeting (AT-RASC), Gran Canaria, Spain, 2018, pp. 1-2, doi: 10.23919/URSI-AT-RASC.2018.8471572.

[76] T. Kim and W. Lee, "AnyScatter: Eliminating Technology Dependency in Ambient Backscatter Systems," IEEE INFOCOM 2020 - IEEE Conference on Computer Communications, Toronto, ON, Canada, 2020, pp. 287-296, doi: 10.1109/INFOCOM41043.2020.9155276.

[77] Li, Yijie & Ling, Weichong & Lu, Taiting & Chen, Yi-Chao & Ranganathan, Vaishnavi & Qiu, Lili & Wang, Jingxian. (2025). MmBack: Clock-free Multi-Sensor Backscatter with Synchronous Acquisition and Multiplexing. 10.48550/arXiv.2507.01360.

Chapter 2 : Propagation Modeling and Feasibility Study of 5G Ambient Backscatter Communication

1. Introduction

Over the last decade, the Internet of Things (IoT) has evolved into a vast ecosystem interconnecting billions of heterogeneous smart devices capable of collecting, transmitting, and processing data in real-time. The deployment of Fifth-Generation (5G) mobile networks is considered a key enabler of this evolution, providing high throughput, low latency, and massive connectivity suitable for IoT applications that require real-time monitoring and control [1]. However, one of the greatest challenges associated with this massive IoT expansion lies in energy sustainability. Conventional battery-powered devices are unsuitable for dense or long-term deployments [2]. To overcome this limitation, energy harvesting and Wireless Power Transfer (WPT) have been investigated as potential solutions [3], [4]. In this context, Ambient Backscatter Communication (AmBC) has recently emerged as a promising paradigm for battery-free and low-power data transmission.

In AmBC systems, passive or semi-passive tags reuse existing radiofrequency (RF) waves such as those emitted by cellular, Wi-Fi, or TV broadcast transmitters to encode and transmit information without generating their own carrier signal [5], [6]. This approach allows the design of self-sustainable wireless sensors capable of communicating using energy harvested from the environment [7]. Unlike traditional active transmitters, AmBC nodes (or backscatter devices) modulate incident RF waves by switching their antenna impedance, thereby reflecting a fraction of the incoming signal toward a receiver. This reflection-based communication eliminates the need for active RF circuitry such as oscillators or power amplifiers making it ideal for ultra-low-power and cost-sensitive IoT applications [8].

Since its first demonstration in 2013 [5], numerous studies have evaluated AmBC feasibility under various ambient sources, including FM [9], Wi-Fi [10], and more recently, 5G cellular networks [11]. The integration of 5G signals as ambient RF sources is particularly attractive due to their continuous availability, dense deployment, and high-power levels in sub-6 GHz and mmWave frequency bands. This enables ambient-powered connectivity in smart cities, healthcare monitoring, and industrial automation contexts [12]. However, the feasibility of 5G-based AmBC systems strongly depends on the propagation environment, which determines the received power at the sensor, the available path loss, and consequently, the achievable

communication range. Therefore, understanding and modeling 5G propagation characteristics is a critical prerequisite for evaluating AmBC performance.

This chapter investigates the propagation behavior and link-budget feasibility of a bistatic 5G AmBC system under different deployment environments, based on the standardized 3GPP TR path-loss models [13], [14]. The study compares Rural Macrocell (RMa), Urban Macrocell (UMa), and Urban Microcell (UMi) scenarios, both in Line-of-Sight (LOS) and Non-Line-of-Sight (NLOS) conditions, in order to determine the received sensor power, available path loss (APL), and maximum achievable backscatter range. The analysis is carried out in the 3.5 GHz 5G frequency band, using a systematic simulation approach combining analytical modeling and feasibility mapping.

The results presented in this chapter provide valuable insights into the range limitations and feasibility boundaries of 5G-based AmBC links, highlighting the trade-offs between propagation conditions, sensor power losses, and receiver sensitivity. The theoretical and simulation framework established here will serve as a basis for the experimental validation presented in the subsequent chapter.

To support this analysis, the following sections present the theoretical background and mathematical formulations used to model 5G propagation losses in bistatic Ambient Backscatter systems. Section 2.1 recalls and presents the mathematical framework and general formalism within which the concept of path loss is introduced for the different propagation environments (RMa, UMa, and UMi) and visibility scenarios (LOS and NLOS)., emphasizing its impact on received power and link feasibility. Section 2.2 presents the geometric configuration of the bistatic link and defines the parameters involved in the AmBC setup. Section 2.3 details the 3GPP path-loss models (RMa, UMa, UMi) under LOS and NLOS conditions, while Section 2.4 compares these models with the Free-Space Path Loss (FSPL) reference to establish baseline propagation behavior. The final sections provide a comprehensive simulation-based feasibility study for 5G AmBC, quantifying the influence of propagation environments, sensor power losses, and receiver sensitivity on the achievable backscatter communication range.

2. General Background on 3GPP Path-Loss Models

2.1. Concept of Path Loss

In wireless communication systems, the path loss (PL) represents the attenuation of the transmitted signal power as it propagates through space and interacts with the environment. It is one of the key parameters governing the performance and reliability of radio links, as it

directly affects the received power level and, consequently, the achievable communication range and signal-to-noise ratio (SNR).

Path loss encompasses all propagation phenomena that contribute to the reduction of the transmitted signal strength, such as free-space spreading, diffraction, reflection, absorption, and scattering caused by surrounding objects. In the context of 5G New Radio (NR), accurate path-loss modeling is fundamental for predicting link budgets and designing energy-efficient wireless communication systems, particularly for ultra-low-power technologies such as Ambient Backscatter Communication (AmBC).

The general relationship between transmitted power, received power, and path loss is expressed as:

$$P_{Rx} = P_{Tx} + G_{Tx} + G_{Rx} - PL \tag{2.1}$$

where:

- P_{Tx} is the transmitted power (in dBm),
- G_{Tx} and G_{Rx} denote the transmit and receive antenna gains (in dBi), respectively,
- PL represents the path loss (in dB).

This relation highlights that the received signal power P_{Rx} depends not only on the distance between the transmitter and receiver but also on the antenna characteristics and the surrounding propagation environment.

In standardized 5G modeling, path loss is characterized by empirical and semi-deterministic formulations derived into extensive measurement campaigns. The 3GPP Technical Report TR 38.901 (Release 16) provides reference propagation models covering a wide range of scenarios and frequencies (0.5–100 GHz). These models are divided into three principal deployment environments:

- RMa (Rural Macro): representing large-cell deployments in open areas with minimal obstruction,
- UMa (Urban Macro): modeling macrocell environments in urban or suburban zones with base-station antennas above rooftop level,
- UMi (Urban Micro): characterizing dense urban environments or street-canyon configurations with lower antenna heights and rich multipath propagation.

Each environment is described under two visibility conditions:

- Line-Of-Sight (LOS**):** a direct unobstructed propagation path between transmitter and receiver,

- Non-Line-Of-Sight (NLOS): propagation dominated by reflections, scattering, and diffraction.

The 3GPP propagation models (RMa, UMa, and UMi) are adopted as the theoretical basis for estimating 5G path-loss behavior under both LOS and NLOS conditions. Their integration provides a realistic framework for evaluating the received power and assessing the feasibility of backscatter communication in various propagation environments.

2.2. Geometrical Definitions and Parameters

In wireless propagation modeling, geometric parameters play a fundamental role in defining the distances and antenna heights involved in the radio link between the transmitter (Tx), the backscatter sensor, and the receiver (Rx). In the context of this study, the three-dimensional (3D) geometry follows the specifications defined in the 3GPP Technical Report TR 38.901 for outdoor environments.

To accurately represent signal propagation, three characteristic distances are defined in accordance with the 3GPP standards. The corresponding distance definitions are indicated in illustrated in Figure 9:

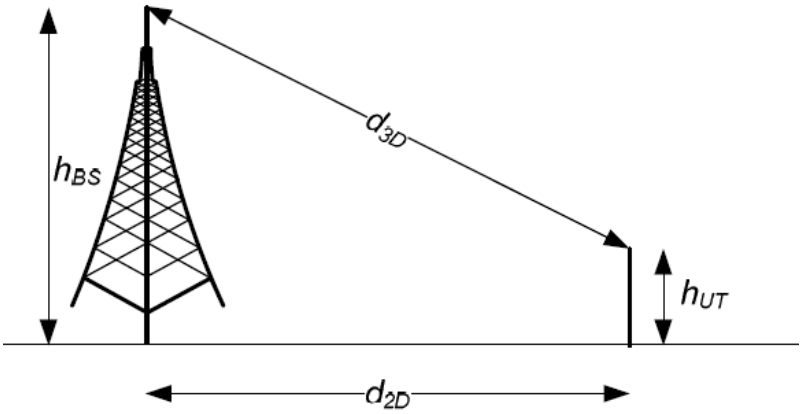

Figure 9. Definition of d2D and d3D for outdoor user terminals [13].

- d_{2D}: the horizontal distance between the base station (BS) and the user terminal (UT) or sensor.
- d_{3D}: the three-dimensional distance, which considers both the horizontal separation and the difference in antenna heights.

$$d_{3D} = \sqrt{(d_{2D})^2 + (h_{BS} - h_{UT})^2} \quad (2.2)$$

- d_{BP}: the breakpoint distance, defining the limit between two distinct propagation regions in the LOS model. Below this distance, the signal undergoes relatively low

attenuation dominated by free-space propagation, whereas beyond it, additional losses occur due to ground reflections and other multipath effects. It is expressed as:

$$d_{BP} = \frac{2\pi h_{BS} h_{UT} f_c}{c} \tag{2.3}$$

where f_c is the carrier frequency, and c is the speed of light.

Figure 9 illustrates the considered configuration, in which the 5G base station (BS) transmits a continuous wave that illuminates a backscatter device (tag) located at a distance d_{TS} from the BS. The tag modulates and reflects the incident signal toward the receiver (Rx), positioned at a distance d_{SR} from the tag. The BS, tag, and Rx antennas are installed at heights h_{BS}, h_{UT}, and h_R, respectively. These parameters are essential for computing the total propagation path between the different nodes of the bistatic backscatter link.

These geometrical definitions serve as inputs to the analytical path-loss equations presented in Section 2.3, ensuring accurate modeling of the propagation behavior under both Line-Of-Sight (LOS) and Non-Line-Of-Sight (NLOS) conditions. The proper distinction between 2D and 3D distances is critical at 5G frequencies, where elevation and antenna height differences have a significant impact on the received power.

2.3. Analytical Formulation of 3GPP Path-Loss Models

In this section, the analytical equations of the standardized 3GPP path-loss models are presented for the three main 5G deployment environments: Rural Macro (RMa), Urban Macro (UMa), and Urban Micro (UMi), each defined under Line-Of-Sight (LOS) and Non-Line-Of-Sight (NLOS) conditions.

These formulations are derived from the *3GPP Technical Report TR 38.901 (Release 16)* and have been implemented in MATLAB to estimate the large-scale propagation losses in the 3.5 GHz frequency band. The presented equations describe the deterministic mean path loss, expressed in dB, as a function of the propagation distance (d), carrier frequency (f_c), and antenna heights (h_{BS}), (h_{UT}).

These models are essential for estimating the power budget in the bistatic 5G AmBC configuration introduced in the previous section.

2.3.1. Rural Macrocell (RMa) Model

- ***LOS Condition***

The RMa Line-of-Sight (LOS) path-loss model is divided into two regions separated by the breakpoint distance d_{BP}.

$$PL_{RMa-LOS} = \begin{cases} PL_1 & 10m \le d_{2D} \le d_{BP} \\ PL_2 & d_{BP} \le d_{2D} \le 10km \end{cases} \tag{2.4}$$

where

$$PL_1 = 20\ log_{10}\left(\frac{40\pi d_{3D} f_c}{3}\right) + \min(0.03h^{1.72}, 10)\ log_{10}(d_{3D}) - \min(0.044h^{1.72}, 14.77) + 0.002\ log_{10}(h) d_{3D} \quad (2.5)$$

$$PL_2 = PL_1(d_{BP}) + 40\ log_{10}\left(\frac{d_{3D}}{d_{BP}}\right) \quad (2.6)$$

$$d_{BP} = \frac{2\pi h_{BS} h_{UT} f_c}{c} \quad (2.7)$$

Hights h'_{BS} and h'_{UT} denote the effective antenna heights above the average rooftop level or ground reference, defined as:

$$h'_{BS} = h_{BS} - h_E \quad (2.8)$$

$$h'_{UT} = h_{UT} - h_E \quad (2.9)$$

where h_E is a quantity that characterizes the environment and is referred to as the effective environment height. It depends on d_{2D} and h_{UT}. For the UMi environment, it is considered constant and has a value of exactly 1m [13].

For short distances ($10m \leq d_{2D} \leq d_{BP}$), the path loss PL_1 is mainly governed by free-space propagation, with additional empirical correction terms that depend solely on the terrain-related height parameter h. These terms, introduced through the $\min(.)$ and $log_{10}(d_{3D})$ functions, refine the model's accuracy by accounting for terrain elevation and environmental morphology typical of rural areas.

Beyond the breakpoint distance ($d_{BP} \leq d_{2D} \leq 10km$), the second expression PL_2 ensures continuity by taking $PL_1(d_{BP})$ as a reference and increasing proportionally to $40\ log_{10}(\frac{d_{3D}}{d_{BP}})$. This behavior captures the stronger attenuation caused by ground reflections and diffraction over long propagation paths.

It should be noted that the breakpoint distance d_{BP} depends on the effective antenna heights h_{BS} and h_{UT}. Although these parameters do not appear explicitly in PL_1 and PL_2, they indirectly influence the path loss through their impact on d_{BP}.

- **NLOS Condition**

The Non-Line-of-Sight (NLOS) path-loss model for the RMa environment extends the LOS formulation to scenarios where the direct path between the transmitter and receiver is obstructed. The total NLOS path loss is defined as:

$$PL_{RMa-NLOS} = \max(PL_{RMa-LOS}, PL'_{RMa-NLOS})\ for\ 10m \leq d_{2D} \leq 5km \quad (2.10)$$

Where

$$PL'_{RMa-NLOS} = 161.04 - 7.1log_{10}(W) + 7.5log_{10}(h) - \left(24.37 - 3.7\left(\frac{h}{h_{BS}}\right)^2\right) log_{10}(h_{BS}) + (43.42 - 3.1log_{10}(h_{BS}))(log_{10}(d_{3D}) - 3) + 20log_{10}(f_c) - (3.2(log_{10}(11.75(h_{UT}))^2\text{-}4.97) \quad (2.11)$$

This definition ensures that the NLOS path loss is never lower than the corresponding LOS value, maintaining physical consistency between the two propagation conditions.

The secondary expression $PL'_{RMa-NLOS}$ introduces environment-dependent parameters, namely the average building height (h) and the average street width (W), to capture the effects of diffraction and scattering in rural built-up areas. The terms involving h_{BS} and h_{UT} model how the transmitter and receiver antenna heights influence the signal diffraction above terrain or low-rise structures.

The logarithmic dependence on d_{3D} and f_c reflects the distance- and frequency-dependent attenuation, while the combined height-and geometry-related terms provide empirical corrections derived from extensive measurement campaigns.

2.3.2. Urban Macrocell (UMa) Model

- **LOS Condition**

The Urban Macrocell (UMa) Line-of-Sight (LOS) model characterizes radio propagation in dense urban environments, where base-station antennas are typically positioned above the average rooftop height. The model separates two propagation regions separated by the breakpoint distance d'_{BP}, and the path loss is expressed as:

$$PL_{RMa-LOS} = \begin{cases} PL_1 & 10m \leq d_{2D} \leq d'_{BP} \\ PL_2 & d'_{BP} \leq d_{2D} \leq 5km \end{cases} \quad (2.12)$$

with

$$PL_1 = 28.0 + 22\ log_{10}(d_{3D}) + 20\ log_{10}(f_c) \quad (2.13)$$

and

$$PL_2 = 28.0 + 40\ log_{10}(d_{3D}) + 20\ log_{10}(f_c) - 9\ log_{10}\left((d_{bp}')^2 + (h_{BS} - h_{UT})^2\right) \quad (2.14)$$

For short distances ($10m \leq d_{2D} \leq d'_{BP}$), the path loss PL_1 primarily follows the free-space propagation behavior, with a logarithmic dependence on both the three-dimensional distance d_{3D} and the carrier frequency f_c. The coefficients 28.0 and 22 are empirically fitted parameters that slightly increase the slope relative to the ideal free-space model, accounting for rooftop diffraction and partial building shadowing typical of urban macrocell environments.

Beyond the breakpoint distance ($d'_{BP} \leq d_{2D} \leq 5km$, PL_2 introduces a steeper attenuation rate through the $40\,log_{10}(d_{3D})$ term, representing the additional losses due to multi-path propagation and ground reflections over longer distances. The correction term $-9\,log_{10}\,((d_{bp}')^2 + (h_{BS} - h_{UT})^2)$ ensures continuity at the breakpoint by aligning the near- and far-distance regions.

- **NLOS Condition**

The UMa Non-Line-of-Sight (NLOS) model extends the LOS formulation to cases where buildings or other obstacles block the direct path. The overall path loss is defined as:

$$PL_{UMa-NLOS} = max(PL_{UMa-LOS}, PL'_{UMa-NLOS})\ for\ 10m \leq d_{2D} \leq 5km \quad (2.15)$$

where

$$PL'_{RMa-NLOS} = 13.54 + 39.08\log_{10}(d_{3D}) + 20\log_{10}(f_c) - 0.6((h_{UT} - 1.5) \quad (2.16)$$

The $max(\,.\,)$ operator ensures that the NLOS loss never falls below the LOS value. The first two logarithmic terms express distance- and frequency-dependent attenuation, while the height-dependent term $-0.6((h_{UT} - 1.5)$ accounts for the receiver's elevation above ground level. This empirical model captures the increased attenuation and scattering effects typical of dense urban propagation environments.

2.3.3. Urban Microcell / Street Canyon (UMi) Model

- **LOS Condition**

The Urban Microcell (UMi) Line-of-Sight (LOS) model applies to dense street-level deployments where both transmitter and receiver antennas are positioned below the rooftop level. The path loss is defined as:

$$PL_{UMi-LOS} = \begin{cases} PL_1 & 10m \leq d_{2D} \leq d'_{BP} \\ PL_2 & d'_{BP} \leq d_{2D} \leq 5km \end{cases} \quad (2.17)$$

$$PL_1 = 32.4 + 21\,log_{10}(d_{3D}) + 20\,log_{10}(f_c) \quad (2.18)$$

$$PL_2 = 32.4 + 40\,log_{10}(d_{3D}) + 20\,log_{10}(f_c) - 9.5\,log_{10}\,((d_{bp}')^2 + (h_{BS} - h_{UT})^2) \quad (2.19)$$

For short distances, PL_1 mainly follows free-space propagation, adjusted by empirical coefficients that reflect the typical urban microcell environment. Beyond the breakpoint distance, PL_1 introduces a higher slope and a correction term ensuring continuity between near- and far-field regions. This formulation captures the stronger attenuation observed at street level due to reflections and diffraction from surrounding buildings.

- **NLOS Condition**

The Urban Microcell (UMi) Non-Line-of-Sight (NLOS) model extends the LOS formulation to situations where the direct path is obstructed by surrounding buildings. The path loss is defined as:

$$PL_{UMi-NLOS}(d_{3D}) = max(PL_{UMi-LOS}(d_{3D}), PL'_{UMi-NLOS}(d_{3D})) \quad (2.20)$$

$$PL'_{UMi-NLOS}(d_{3D}) = 35.3\log_{10}(d_{3D}) + 22.4 + 21.3\log_{10}(f_c) - 0.3(h_{UT} - 1.5) \quad (2.21)$$

The $max(.)$ operator ensures that the NLOS loss remains greater than or equal to the LOS value. The logarithmic terms represent the distance and frequency dependence, while the correction term $-0.3(h_{UT} - 1.5)$ adjusts the attenuation based on the receiver height. This formulation effectively models the additional losses and diffraction mechanisms observed in confined street canyons and densely built urban areas.

2.4. Theoretical Reference: Free-Space Path-Loss (FSPL) Model

Although not part of the 3GPP standardized models, the Free-Space Path-Loss (FSPL) equation is included here as a theoretical benchmark for comparison. It represents the ideal propagation scenario, in which the transmitted signal travels through free space without any reflection, diffraction, or absorption.The FSPL provides the minimum possible attenuation and serves as a baseline reference to evaluate the additional losses introduced by the 3GPP models.

The FSPL is expressed as:

$$PL_{FSPL}(dB) = 32.45 + 20\log_{10}(d_{3D}) + 20\log_{10}(f_c) \quad (2.22)$$

In the context of AmBC (Ambient Backscatter Communication) modeling, the first propagation segment between the base station (BS) and the tag is described using an appropriate 3GPP path-loss model, selected according to the surrounding environment (RMa, UMa, or UMi). The second segment, corresponding to the tag-to-receiver link, is modeled using the free-space path-loss equation, since the backscattered signal is not transmitted by an active base station but rather results from passive reflection at the tag.

This distinction justifies the application of the FSPL model for the reflected path, ensuring a physically consistent representation of the bistatic AmBC propagation process. This reference model will be used in Section 2.2.8 for the comparative analysis of propagation behaviors across RMa, UMa, and UMi environments.

2.5. Comparative Analysis of the Models

Figure 10 illustrates the comparison between the Free-Space Path-Loss (FSPL) model and the standardized 3GPP path-loss models (RMa, UMa, and UMi) under both Line-of-Sight (LOS) and Non-Line-of-Sight (NLOS) conditions at a carrier frequency of 3.5 GHz. The plotted results

highlight the variation of large-scale attenuation as a function of the the three-dimensional propagation distance d_{3D}, from 10 m to 1 km.

The FSPL curve represents the theoretical lower bound of propagation loss, corresponding to an ideal free-space scenario without any scattering, reflection, or diffraction. In contrast, the 3GPP models account for environmental effects and antenna geometry, leading to higher path-loss values that more accurately represent realistic deployment conditions.

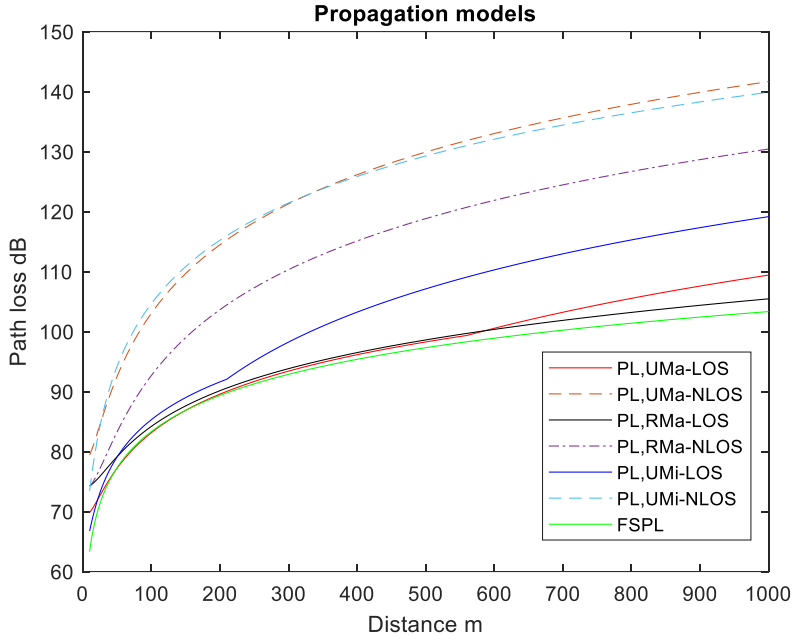

Figure 10. Comparison of path loss between FSPL and 3GPP propagation models (UMa,UMi,RMa) under LOS and NLOS conditions.

Among the considered environments, the Rural Macrocell (RMa) model exhibits the lowest attenuation, owing to the high base-station elevation and the absence of major obstacles.

The Urban Macrocell (UMa) model shows moderate losses, characteristic of suburban or urban areas with average building density.

Finally, the Urban Microcell (UMi) model yields the highest path loss, primarily due to the lower antenna height and the stronger multipath propagation typical of dense street-canyon environments.

A clear distinction is also be observed between the LOS and NLOS conditions across all models. The NLOS curves present a steeper slope and higher attenuation values, emphasizing the critical influence of diffraction and shadowing effects in obstructed propagation scenarios.

Overall, the comparative trend can be summarized as:

$$PL_{RMa} < PL_{UMa} < PL_{UMi}$$

with the FSPL serving as the theoretical reference limit.

These results confirm the expected behavior of the standardized 3GPP models and provide a solid analytical basis for evaluating the received power in the bistatic 5G Ambient Backscatter configuration analyzed in the following section.

2.6. Discussion

The comparative analysis of the standardized 3GPP path-loss models provides valuable insights into the influence of environmental topology and antenna geometry on large-scale propagation attenuation.

As illustrated in Figure 10, the Rural Macrocell (RMa), Urban Macrocell (UMa), and Urban Microcell (UMi) models exhibit distinct attenuation behaviors that correspond to their deployment conditions and base-station configurations. The RMa model presents the lowest propagation losses, mainly due to the high elevation of the base station (35 m) and the open rural environment characterized by minimal obstructions and weak multipath components.

The UMa model exhibits moderate losses, representative typical urban or suburban macro-cell deployments where buildings introduce partial shadowing and moderate diffraction effects.

Meanwhile, the UMi model results in the highest path-loss values, as expected in dense street-canyon environments with low base-station height (10 m) and strong multipath propagation.

Across all models, the difference is observed between LOS and NLOS conditions. NLOS propagation introduces additional attenuation typically ranging from 15 dB to 30 dB ─ depending on the environment and operating frequency. This distinction is particularly relevant for realistic urban deployments, where most communication links in urban scenarios are at least partially obstructed.

From the perspective of ambient backscatter communication, these findings are of primary importance. Since the backscattered signal is several orders of magnitude weaker than the incident 5G carrier, the baseline propagation model largely determines the achievable communication range and received power levels at both the tag and receiver.

Therefore, employing accurate 3GPP path-loss formulations for RMa, UMa, and UMi environments ensures that the feasibility analysis reflects realistic 5G propagation conditions across various deployment scenarios.

The next section builds upon these analytical results to perform MATLAB-based simulations using all three propagation models (RMa, UMa, UMi), under both LOS and NLOS conditions. The objective is to evaluate the received power levels at the sensor node and to assess the feasibility of bistatic 5G Ambient Backscatter communication across different environmental configurations.

3. Simulation Methodology

The theoretical models presented in Section 3 provide the analytical framework for evaluating bistatic AmBC propagation across different environments.

To translate these models into practical feasibility assessments, a simulation methodology is established. This methodology defines the input parameters, applies the link budget equations, and computes the achievable path loss and range for the selected deployment scenarios.

3.1. Geometric model parameters

The various geometrical parameters used in the simulations are listed in Table 3. These simulations correspond to six scenarios, combining three environments (RMa, UMa, and UMi) with two visibility conditions, namely Line-of-Sight (LOS) and Non-Line-of-Sight (NLOS).

It should be noted that the notations of the distances $d_{3D}$and d_{2D}, as originally defined in the 3GPP Technical Report TR 38.901, have been replaced by d_{TS1} and d_{TS2}, respectively, in order to more clearly denote the two distances defined between the transmitter (Tx) and the tag (see Figure 11).

Geometric parameter	Description	Value
h_{BS}	Base station height of RMa/UMa/RMi	35m/25m/10m
h_{UT}	sensor antenna height (tag)	1.5m
h_r	Constant	Supposed equal to h_{UT} (1.5m)
h	Building height of RMa Model	5m
w	Street width of RMa Model	20m
d_{TS1}	BS-to-sensor horizontal distance	Maximal value 1000m
d_{TS2}	BS-to-sensor 3D distance	$d_{TS2} = \sqrt{d_{TS1}^2 + (h_{BS} - h_{UT})^2}$
d_{SR}	Sensor-to-receiver distance	Maximal value 1000m
d'_{SR}	Symmetrical assumption	Supposed equal to d_{SR}

Table 3. Geometric Parameters of the 3GPP Path-Loss Models and Bistatic AmBC Link.

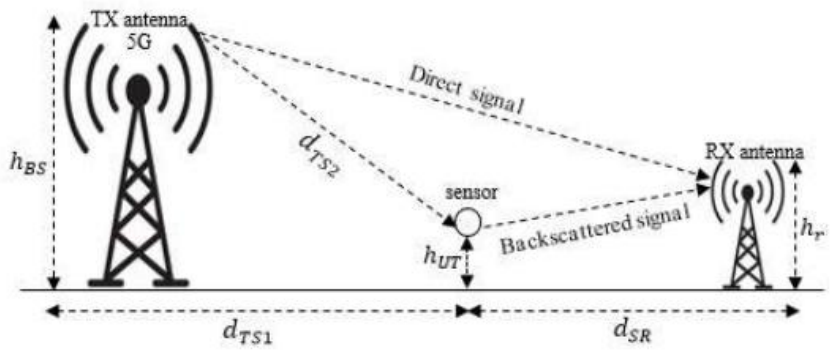

Figure 11. Definition of geometrical parameters for the bistatic AmBC link (BS, sensor, and Rx).

3.2. Input Parameters

The simulation considers both geometric and system-level parameters. The geometric parameters, such as the base station height h_{BS}, user terminal height h_{UT}, and the distances between the transmitter, the backscatter device (sensor), and the receiver, were introduced in Section 3 and are directly used to compute the path-loss terms.

In addition to the geometric parameters, the evaluation of the bistatic AmBC link requires the definition of system-level parameters related to the base station, the backscatter device, and the receiver. These parameters include the transmitted power at the base station, the sensor losses, the antenna gains, and the receiver characteristics such as noise figure, sensitivity, and bandwidth. Table 4 summarizes the values and ranges adopted in this study, distinguishing between constant parameters and variable ones that are swept during the simulations to assess the feasibility limits.

Subsystem	Parameter	Symbol	Type	Value
Base Station	Transmitted power	P_t	Constant	46dBm
Sensor	Sensor losses	PSL	Variable	From 5 to 30 dB by a step of 5dB
	Antenna Gain	G_S	Constant/variable	0dBi then until 30dBi
	Radiated power at the sensor	P_S	Variable	Calculated
Receiver	Noise Figure	NF	Constant	8dB
	Minimal Signal-to-Noise Ratio	SNR_{min}	Constant	4dB
	Bandwidth	BW	Variable	3 values, 5, 10 and 20MHz
	Sensitivity	SEN_{Rx}	Variable	Calculated
	Antenna Gain	G_R	Constat/variable	0dBi then until 30dBi

Table 4. System parameters for the bistatic AmBC link budget analysis.

3.3. Link Budget Equations

The evaluation process follows the link budget chain, in which the received power at the sensor and the receiver sensitivity are compared to determine the Available Path Loss (APL). The essential steps consist of calculating the following parameters in the order given below, as defined by the following equations:

i) Received power at the sensor:

$$P_S = P_T - (PL_{UMa/UMi/RMa} + PSL) \tag{2.23}$$

ii) Receiver sensitivity:

$$SEN_{Rx}(dBm) = 10log_{10}\left(\frac{kTBW}{0.001)}\right) + NF + SNR_{min} \tag{2.24}$$

where k is Boltzmann's constant and T is the reference temperature.

iii) Available Path Loss (APL):

$$APL = P_S - SEN_{Rx} \tag{2.25}$$

iv) Achievable range:

$$\rho(m) = 1000 \times 10^{\frac{APL(dB) - 20\log_{10}(f_{MHz}) + G_{Tx}(dBi) + G_{Rx}(dBi) - 32.45dB}{20}} \tag{2.26}$$

Additional information about these steps can be found in Subsection 3.3

3.4. Simulation Flow

The overall simulation process adopted in this study is summarized in the flowchart of Figure 12 and can be described as a sequential link-budget analysis. The procedure begins with the computation of the path loss using the appropriate 3GPP propagation model corresponding to the considered scenario (UMa, UMi, or RMa, in LOS or NLOS). This path-loss value is then combined with the transmitted power of the base station and the additional sensor losses to determine the effective power available at the backscatter device, denoted P_S.

At the receiver side, the sensitivity threshold SEN_{Rx} is calculated from the thermal noise floor associated with the selected bandwidth, to which the receiver noise figure (NF) and the minimum signal-to-noise ratio SNR_{min} are added. This sensitivity value represents the minimum power level required for reliable detection of the backscattered signal. By comparing the available sensor power P_S with the receiver sensitivity SEN_{Rx}, the Available Path Loss (APL) can be obtained, which quantifies the maximum propagation attenuation that can be tolerated by the system. Finally, the achievable range ρ is derived from the APL expression by incorporating the antenna gains of both the sensor and the receiver, as well as the carrier frequency. This sequential computation ensures that all the relevant contributions from the base

station power and sensor losses to the receiver characteristics are consistently taken into account, thereby providing a rigorous estimate of the bistatic AmBC communication range under different deployment environments.

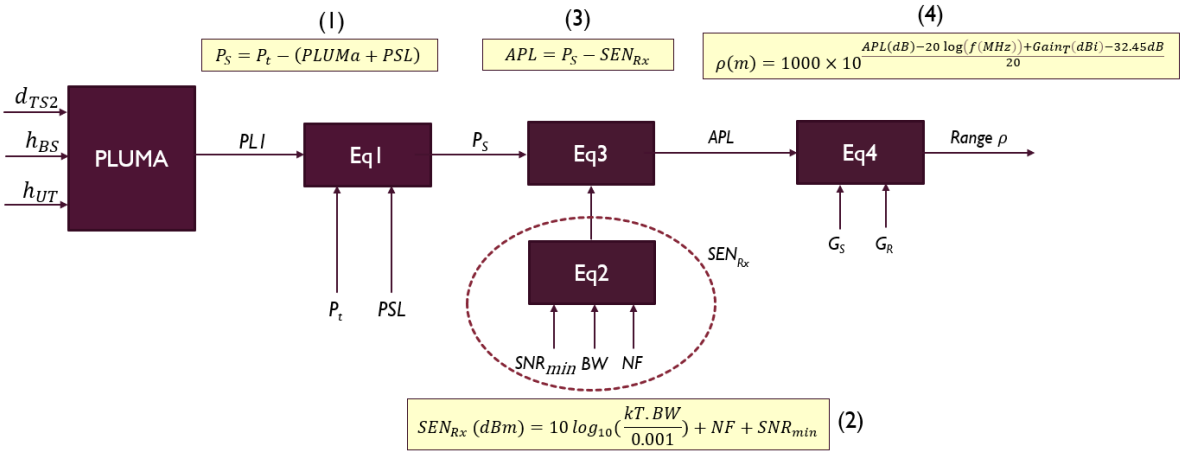

Figure 12. Simulation methodology flowchart for bistatic AmBC feasibility analysis.

4. Results and Analysis

4.1. Received Power Estimation

The results presented in Figures 13(a–e) illustrate the variation of the received power at the backscatter sensor (P_S) as a function of the distance between the transmitter and the tag sensor for all three 3GPP propagation environments (RMa, UMa, and UMi), under both LOS and NLOS conditions. The simulations were performed for five sensor-loss levels (PSL = 5, 10, 15, 25, and 30 dB) to capture the influence of tag efficiency on the available power. In all configurations, P_S decreases monotonically with increasing distance, following the typical exponential decay trend of large-scale path-loss models. The comparison among environments reveals a clear hierarchy in received power levels:

$PL_{RMa} < PL_{UMa} < PL_{UMi}$, reflecting the gradual increase in propagation attenuation from open rural areas to dense urban deployments.

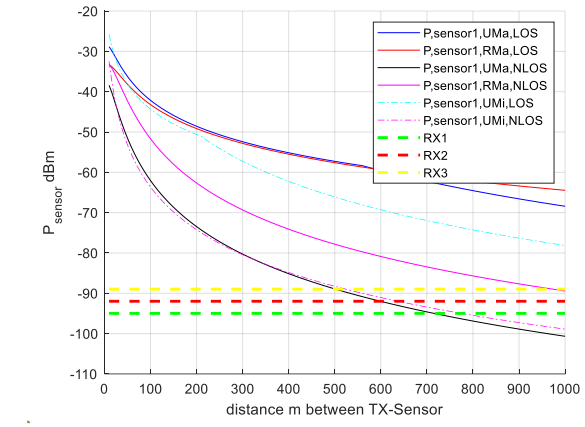

(a)

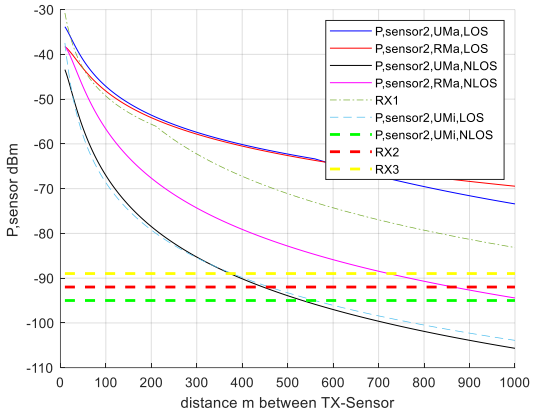

(b)

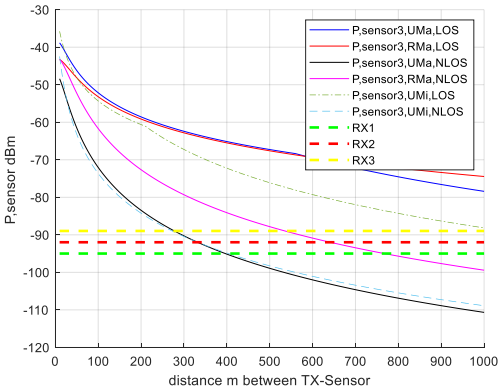

(c)

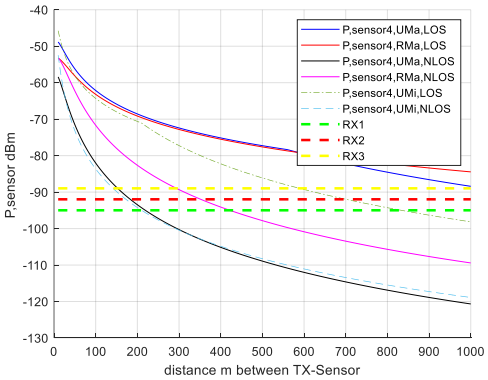

(d)

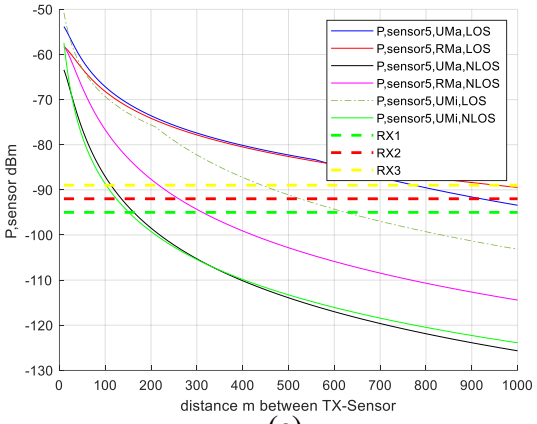

(e)

Figure 13. Received power at the backscatter sensor (P_S) as a function of the TX–Sensor distance for the three propagation environments (RMa, UMa, UMi) under LOS and NLOS conditions. (a) PSL = 5 dB, (b) PSL = 10 dB, (c) PSL = 15 dB, (d) PSL = 25 dB, (e) PSL = 30dB.

At short distances below 100 m, the received power remains relatively high (above −40 dBm in most cases), ensuring strong illumination of the backscatter tag. However, as the distance increases beyond 200–300 m, significant power degradation occurs, especially under NLOS conditions. The RMa environment maintains the highest power levels, with P_S remaining above

−80 dBm even at 600–700 m, while the UMa configuration exhibits intermediate attenuation, reaching −90 dBm around 500 m. In contrast, the UMi model experiences the steepest decline, with the received power dropping below −100 dBm beyond 300 m, mainly due to the dense urban layout and rich multipath propagation.

The effect of sensor losses (PSL) is also clearly visible: increasing PSL from 5 dB to 30 dB results in an almost parallel downward shift of all P_S curves by approximately 25 dB, demonstrating the strong dependency of the available power on tag hardware efficiency. For instance, at 500 m under RMa–LOS conditions, P_S decreases from roughly −55 dBm to −80 dBm when PSL rises from 5 to 30 dB. Consequently, higher losses directly limit the maximum operational range of the system.

The colored horizontal bands in the figures correspond to receiver sensitivity levels (RX1, RX2, RX3), associated with different bandwidths and noise figures. These sensitivity thresholds serve as practical limits for detectability: the intersection point between the received power curve and the sensitivity level indicates the maximum feasible distance for reliable backscatter communication. It can be observed that for low-loss scenarios $PSL \leq 10$ dB) and favorable propagation (RMa–LOS), P_S remains above the RX2 sensitivity (≈ −92 dBm) up to 600 m, under in UMi–NLOS conditions, the signal drops below the RX3 sensitivity (≈ −100 dBm) at less than 250 m.

Overall, these results highlight the critical influence of the propagation environment, visibility conditions, and sensor losses on the available power budget. The RMa model demonstrates the most favorable conditions for long-range bistatic AmBC links, while the UMi model imposes severe limitations in dense urban environments. The observed trends confirm that optimizing antenna gains and minimizing sensor losses are essential to extending the feasible backscatter communication range within 5G NR systems.

4.2. Comparison and Analysis of Available Path Loss (APL) for Different Receiver Sensitivities and Sensor Losses

The comparative results of the Available Path Loss (APL) for the three receiver sensitivities (RX1, RX2, and RX3) are illustrated in Figures 14(a–c). Each sensitivity level corresponds to a specific receiver configuration characterized by distinct bandwidths and noise values, which determine the minimum detectable power level. For each sensitivity, five sensor-loss cases (PSL = 5, 10, 15, 25, 30 dB) are analyzed across the three 3GPP propagation environments (RMa, UMa, and UMi) under both LOS and NLOS conditions.

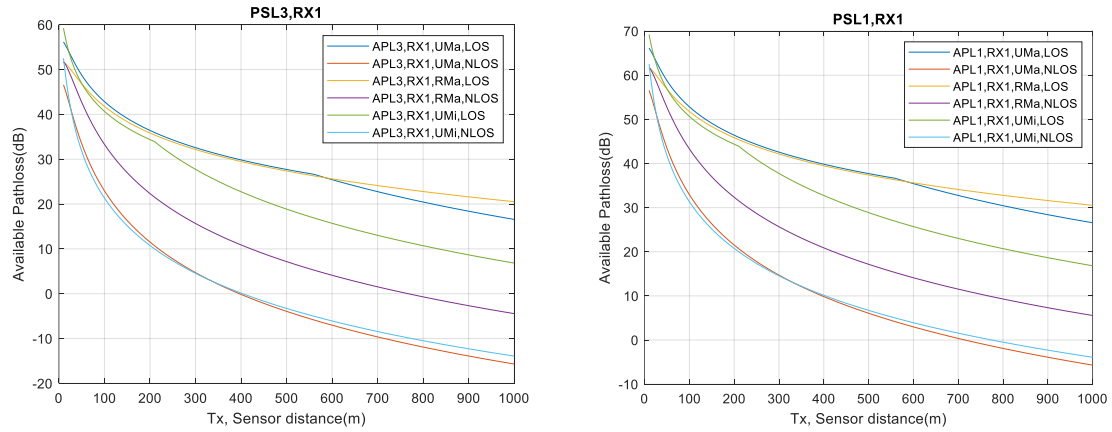

(a)

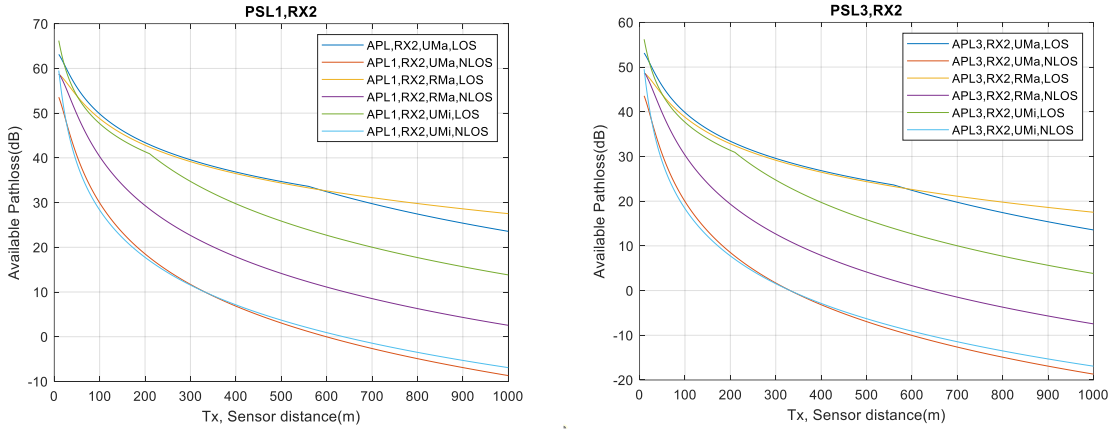

(b)

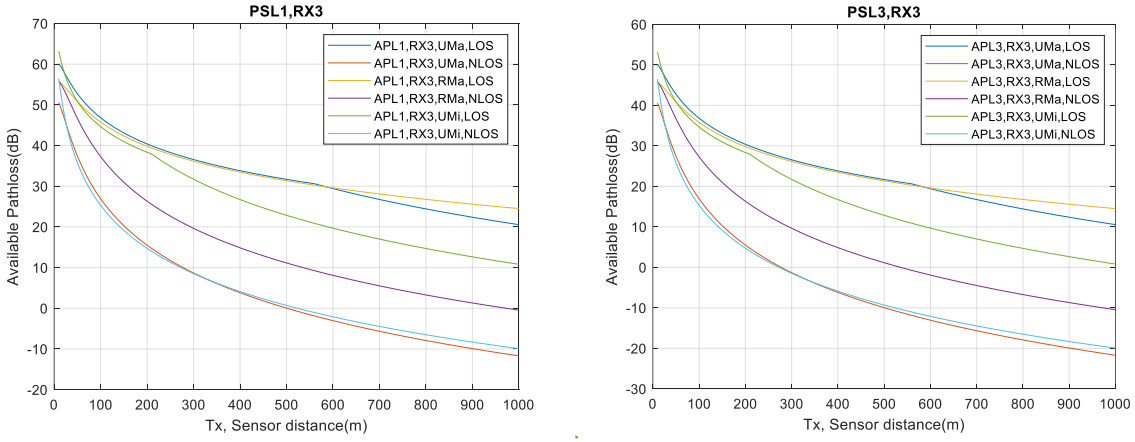

(c)

Figure 14. Comparison of Available Path Loss (APL) variations as a function of the TX–Sensor distance for the three receiver sensitivities (RX1, RX2, and RX3) and different sensor loss levels (PSL = 5, 10, 15, 25, 30 dB).

Overall, the APL curves exhibit a monotonically decreasing behavior with increasing TX–sensor distance, consistent with the reduction in received sensor power observed previously. The RMa environment consistently provides the highest APL values, meaning that it allows for

a larger tolerable propagation loss before reaching the receiver sensitivity threshold. In contrast, UMi environments particularly under NLOS conditions, yield the lowest APL values, highlighting the strong attenuation effects characteristic of dense urban scenarios.

For the RX1 configuration, which corresponds to the most sensitive receiver, the system maintains positive APL values (i.e., feasible operation) up to approximately 700–800 m in RMa–LOS conditions and around 500 m in UMa–LOS, while UMi–NLOS conditions limit the range to roughly 200–250 m. When the sensor losses increase from 5 dB to 30 dB, the APL decreases almost linearly, indicating that hardware inefficiency directly reduces the available link budget. This effect is accentuated in environments with higher path-loss exponents.

Under the RX2 and RX3 configurations, which represent less sensitive receivers, the APL values drop further, resulting in a noticeable reduction in feasible communication range. For RX2, the APL becomes negative beyond 400 m in UMa–LOS and 250 m in RMa–NLOS, meaning that the backscattered signal would fall below the detection threshold. With RX3, the degradation is even more pronounced: APL values become negative almost immediately in all NLOS conditions and in UMi environments beyond 100 m.

These results confirm the combined influence of propagation conditions, receiver sensitivity, and sensor losses on the feasibility of bistatic 5G AmBC links. High-sensitivity receivers (RX1) and low-loss sensors (PSL ≤ 10 dB) enable communication ranges of several hundred meters, whereas less optimized configurations sharply limit the operational distance. The analysis also reveals that improving receiver design or minimizing sensor losses can compensate for the harsh attenuation effects in urban or NLOS environments, thereby extending the feasible range of ambient backscatter communication systems.

4.3. BackCom Range Evaluation under Different Propagation Scenarios

Figure 15 illustrates the estimated bistatic BackCom range as a function of both the sensor losses (PSL) and the TX–sensor distance for the three 3GPP propagation environments (RMa, UMa, and UMi) under both LOS and NLOS conditions. These 3D maps are obtained from the APL computation presented in the previous subsection, using the link-budget-based range estimation method defined in Section 3.2. The color scale represents the achievable range (in meters) corresponding to each combination of distance and sensor loss-level.

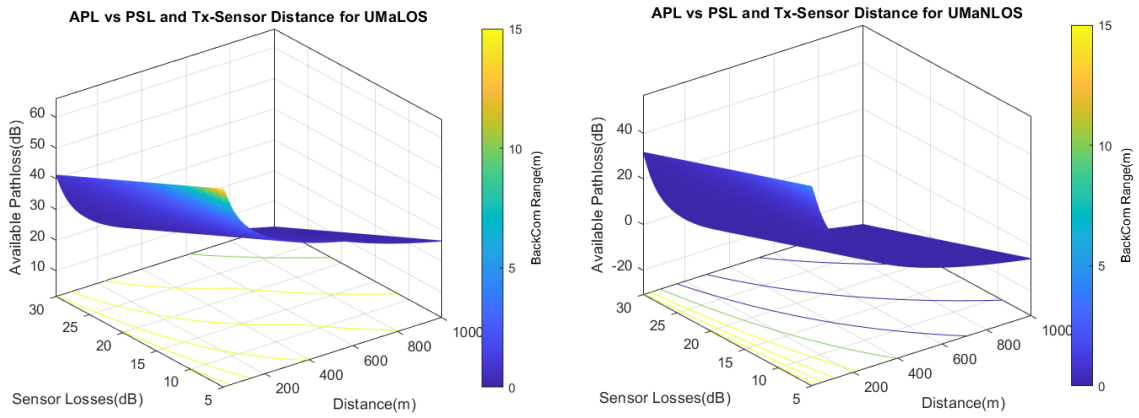

Figure 15. Estimated bistatic BackCom range as a function of sensor losses (PSL) and TX–Sensor distance under different 3GPP propagation environments UMa in LOS and NLOS conditions (RMa, UMi in Appendix).

As expected, the achievable range decreases with increasing sensor losses and with the transition from LOS to NLOS conditions. The RMa LOS environment exhibits the most favorable conditions, allowing ranges exceeding 10 m even for moderate sensor losses (≈ 15 dB). In contrast, UMi-NLOS and UMa-NLOS configurations lead to the most severe degradation, where the range drops below 5 m for the same PSL values. This behavior reflects the high path-loss exponents and additional shadowing effects present in dense urban areas. For completeness, the results and corresponding figures of the remaining scenarios, including RMa LOS/NLOS and UMi LOS/NLOS environments, are provided in the Appendix.

Furthermore, it is observed that the impact of sensor losses is more critical in NLOS conditions: small increases in PSL (from 5 dB to 15 dB) produce a steep reduction in range, while under LOS propagation the decay remains smoother. This indicates that hardware inefficiency at the sensor side (imperfect impedance switching, low antenna efficiency, etc.) can be tolerated to some extent only when favorable propagation conditions are maintained.

Overall, these results confirm that the bistatic 5G AmBC system can achieve ranges on the order of 10–15 m under realistic outdoor LOS scenarios including realistic, while in urban or NLOS environments, the range is constrained to a few meters depending on sensor design. These findings highlight the importance of jointly optimizing both the RF front-end losses and the deployment geometry (distance, angle, and environment) to ensure feasible backscatter communication performance.

4.4. Available Path Loss Evaluation under Different Propagation Scenarios

Figure 16 illustrates the variation of the available path loss (APL) as a function of the sensor losses (PSL) and the TX–sensor distance for the six 3GPP propagation conditions, namely UMa, Rma, and UMi, each considered under both LOS and NLOS situations. The APL

quantifies the maximum tolerable path attenuation between the transmitter and receiver for successful backscatter communication, as derived from the received sensor power and receiver sensitivity parameters presented in Section 3.2.

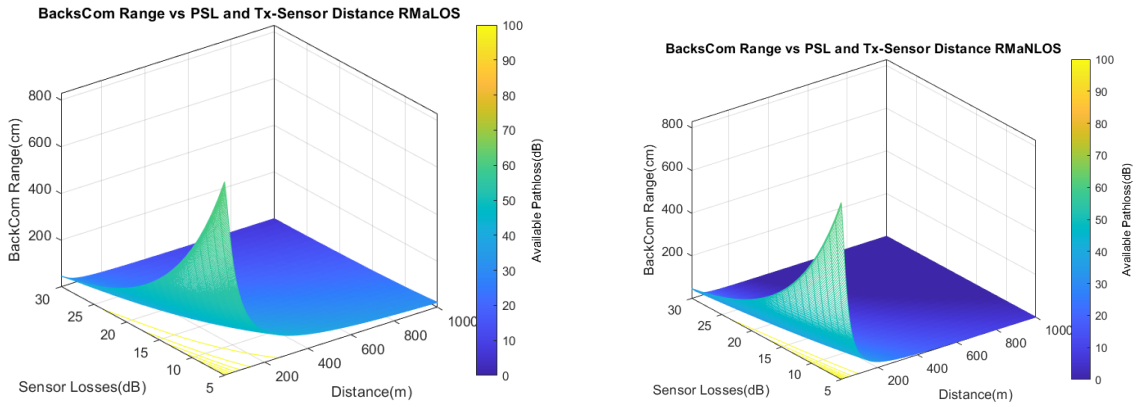

Figure 16. 3D representation of the Available Path Loss (APL) as a function of TX–Sensor distance and sensor losses (PSL) for different propagation models UMa under LOS and NLOS conditions (UMa, UMi in Appendix).

The results show that the APL increases sharply as the distance between the transmitter and the sensor decreases, as expected from the propagation-loss behavior. However, for higher sensor losses ($PSL > 20dB$), the available margin quickly diminishes, resulting in limited feasible ranges. Among the environments considered, the RMa-LOS case provides the highest available path-loss values (up to 90–100 dB), followed by UMa-LOS, while the UMi-NLOS configuration exhibits the lowest APL levels, not exceeding 60 dB beyond 300 m. Additional figures and detailed simulation results for the other propagation scenarios (UMa LOS/NLOS and UMi LOS/NLOS) are included in the Appendix.

This trend confirms that rural macro environments are more favorable for backscatter feasibility due to lower obstruction and smoother propagation. Conversely, dense urban and microcell environments introduce severe attenuation caused by diffraction, reflection, and scattering from surrounding buildings, significantly reducing the effective APL.

Additionally, it is observed that the difference between LOS and NLOS conditions becomes more pronounced in the UMi and UMa models than in the RMa case. This demonstrates that short-range dense deployments are more sensitive to shadowing and multipath effects, whereas rural deployments benefit from more stable propagation even longer distances.

Overall, these results provide a clear insight into how environmental configuration and sensor performance jointly define the feasibility region for bistatic 5G AmBC systems. The next section further extends this analysis by computing the corresponding BackCom communication range, directly derived from the obtained APL values.

4.5. Cartography of Available Path Loss for Different Bandwidths

Figures 17(a–c) illustrate the cartography of the Available Path Loss (APL) as a function of the logarithmic distance between the transmitter and the sensor and the sensor losses (PSL), for the three bandwidths considered: $BW_1 = 5MHz$, $BW_2 = 10MHz$, and $BW_3 = 20MHz$. Each subfigure corresponds to one of the 3GPP propagation environments (UMa, RMa, UMi) under both LOS and NLOS conditions. The color gradient represents the achievable APL in dB, where warmer colors indicate higher link availability (better feasibility conditions).

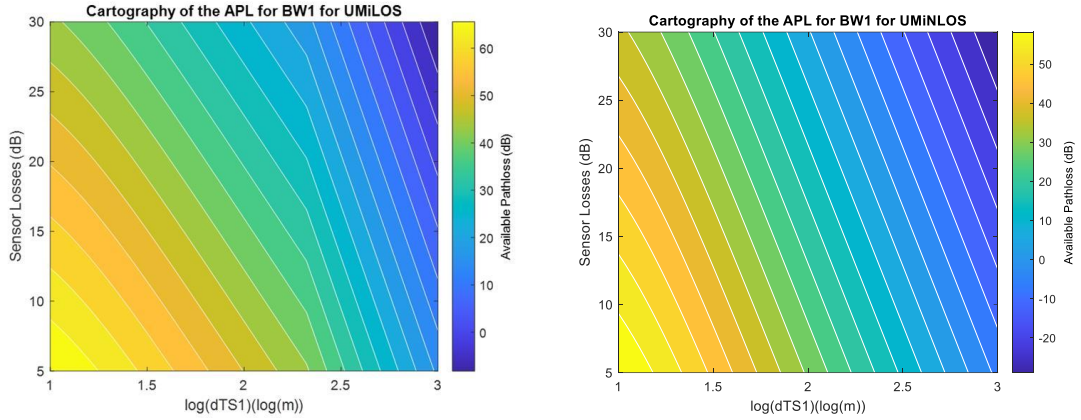

(a)

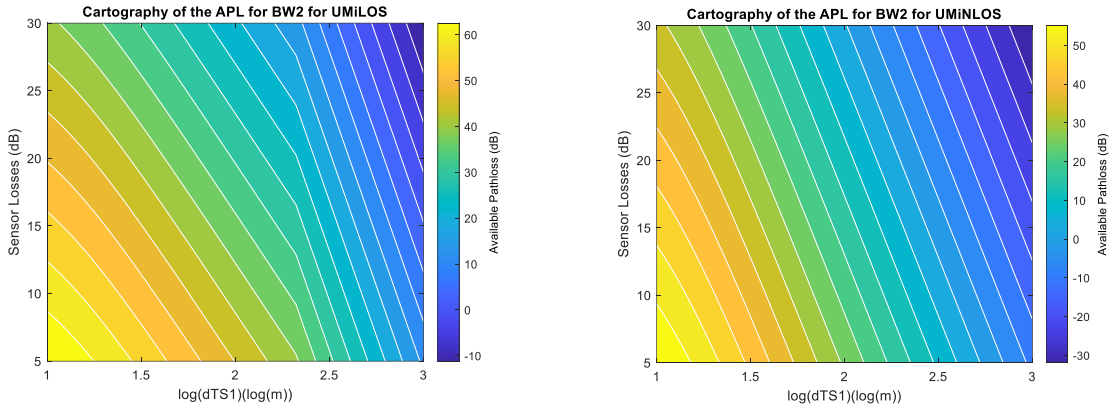

(b)

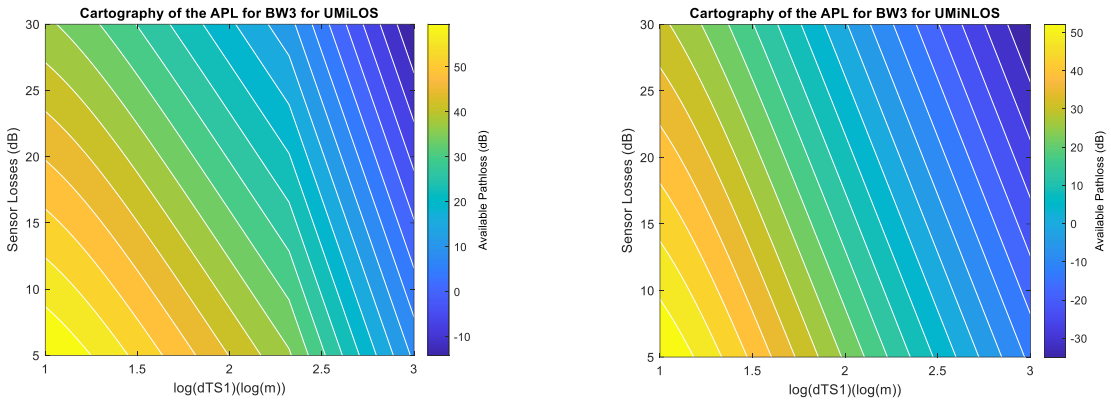

(c)

Figure 17. Available Path Loss (APL) versus TX–Sensor distance and sensor losses (PSL) for (a) BW_1 = 5 MHz, (b) BW_2 = 10 MHz, and (c) BW_3 = 20 MHz under UMi LOS/NLOS conditions (RMa and UMa results in Appendix).

As expected, increasing the bandwidth leads to a progressive degradation of the APL values across all environments. This behavior is attributed to the increase in thermal noise power with larger bandwidths, which in turn reduces the receiver sensitivity. Consequently, the feasible region (yellow–orange areas) gradually shrinks as BW increases from 5 MHz to 20 MHz, particularly under NLOS conditions and in dense urban microcells (UMi).

When comparing across propagation environments, the RMa-LOS case consistently exhibits the highest APL values, demonstrating that long-range feasibility remains achievable even at higher bandwidths. Conversely, the UMi-NLOS scenario shows a sharp decline, confirming that dense urban propagation and multipath fading significantly reduce the available margin for backscatter communication.

The cartographic representation also highlights the combined effect of distance and sensor efficiency. For small PSL values (<10 dB), the APL remains sufficiently high to enable backscatter detection over several hundred meters in LOS environments. However, when PSL exceeds 20 dB, the available margin becomes negligible beyond 200–300 m, regardless of the propagation model.

Overall, these maps provide a visual feasibility boundary for bistatic AmBC operation, illustrating how the interaction between bandwidth, sensor design, and environmental conditions determines the communication limits. This analysis serves as a precursor to the next section, which explores the achievable BackCom range derived from these APL values. A detailed presentation of the simulation results corresponding to UMa and RMa propagation models, for both LOS and NLOS cases, is provided in the Appendix.

4.6. Available BackCom Range under Different Propagation and Bandwidth Scenarios

Figures 18(a–c) present the cartography of the achievable BackCom range (ρ) as a function of the logarithmic TX–sensor distance and the sensor losses (PSL), for the three bandwidth values ($BW_1 = 5MHz$, $BW_2 = 10MHz$, and $BW_3 = 20MHz$), across the six propagation conditions (UMa, RMa, and UMi, each in LOS and NLOS). These results are derived from the previously computed Available Path Loss (APL) values using the analytical relation described in Section 2.3.5. The color gradient indicates the achievable range in meters, with warmer colors corresponding to larger feasible BackCom distances.

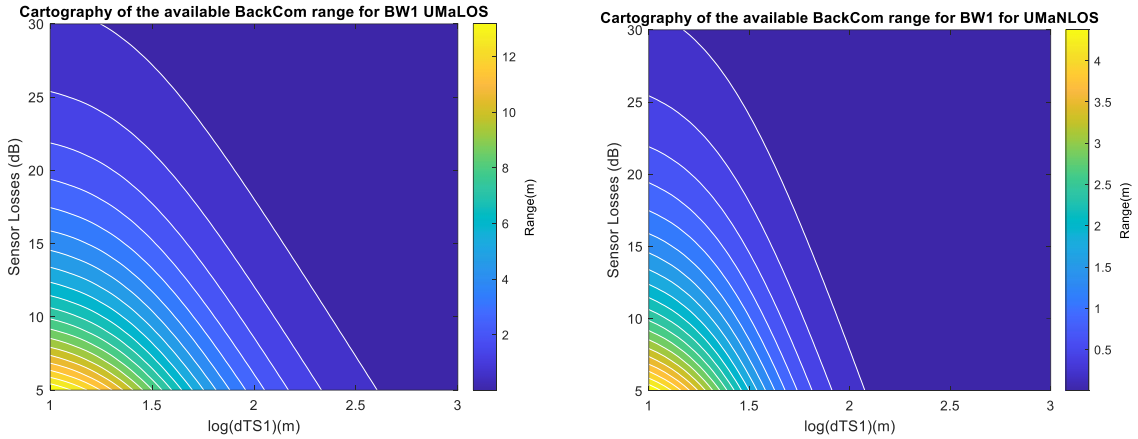

(a)

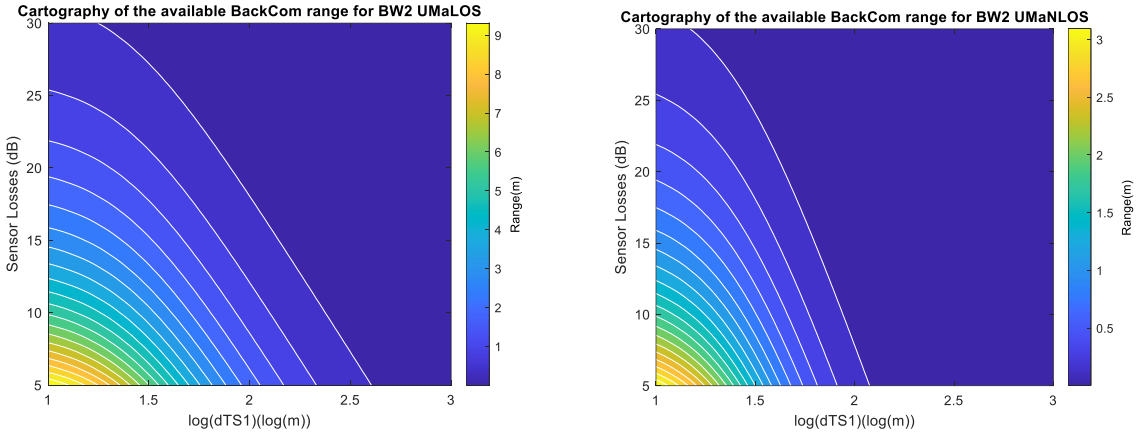

(b)

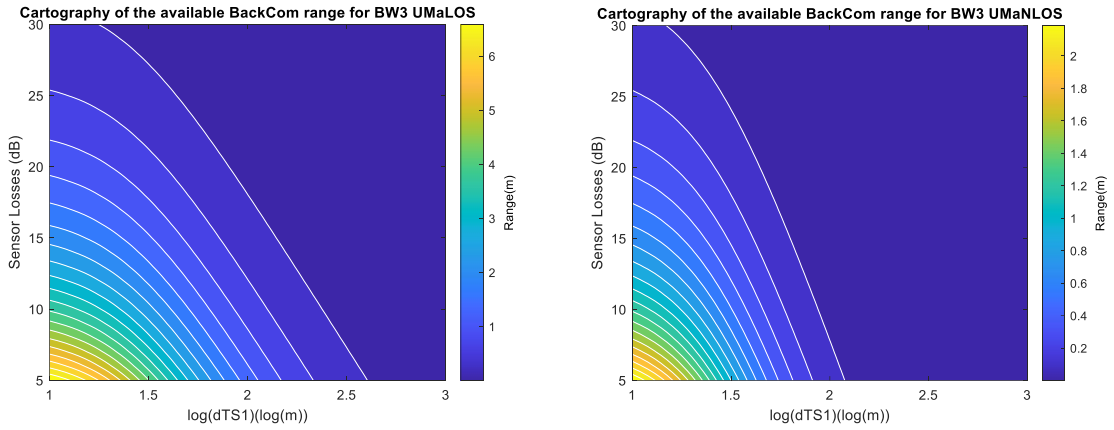

(c)

Figure 18. BackCom range maps (ρ) versus TX–Sensor distance and PSL for (a) BW_1 = 5 MHz, (b) BW_2 = 10 MHz, and (c) BW_3 = 20 MHz under UMa LOS/NLOS conditions (RMa and UMi in Appendix).

The BackCom range exhibits a strong dependency on both the propagation environment and the bandwidth. Across all scenarios, increasing the bandwidth leads to a noticeable reduction in the achievable range, mainly due to higher noise power and the corresponding decrease in receiver sensitivity. Under $BW_1 = 5MHz$**,** the system achieves its best performance, achieving ranges up to 12–15 m in the RMa-LOS configuration and around 8–10m in UMa-LOS. In contrast, UMi-NLOS conditions restrict the range to less than 3 m, illustrating the severe impact of dense multipath environments on ambient backscatter feasibility.

When comparing the environments, the RMa model consistently demonstrates the most favorable conditions, providing the feasible ranges under both LOS and NLOS scenarios. This confirms the suitability of rural and open macrocell environments for long-range AmBC operation. Conversely, the UMi scenario represents the most constrained case, consistent with its strong attenuation and scattering characteristics.

The results also highlight the role of sensor efficiency: when the sensor losses (PSL) exceed 20 dB, the feasible range rapidly collapses, even under LOS conditions. This indicates that the design of ultra-low-loss backscatter devices is essentiel for extending communication coverage, particularly at higher bandwidths or in urban contexts.

Overall, these cartographic representations provide a comprehensive view of the combined impact of environmental conditions, bandwidth, and hardware parameters on the feasibility of bistatic 5G AmBC links. They clearly demonstrate that while short-range AmBC communication (a few meters) remains achievable in dense urban NLOS settings, significantly longer ranges (up to 10–15 m) can be realized in open rural LOS configurations, thereby paving

the way for low-power IoT and sensing applications in large-scale outdoor deployments. The complete set of BackCom range maps for UMi and RMa, under both LOS and NLOS conditions, is included in the Appendix for reference.

5. Conclusion

This chapter presented a comprehensive theoretical and simulation-based study of the propagation characteristics and feasibility of bistatic 5G Ambient Backscatter Communication (AmBC) systems. It established the analytical foundation required to evaluate the received power, available path loss, and maximum achievable range of a backscatter link operating under realistic 5G NR propagation conditions.

The chapter began by introducing the concept of path loss and reviewing the 3GPP path loss models (RMa, UMa, and UMi) under both LOS and NLOS scenarios. The associated geometric parameters including base-station and terminal antenna heights, street dimensions, and breakpoint distances were defined to provide the necessary physical context for modeling the bistatic link geometry. These models were then compared to the Free-Space Path Loss (FSPL) reference to highlight the differences between ideal and practical 5G environments.

Subsequently, detailed comparative analyses of the 3GPP propagation environments revealed clear trends: RMa (Rural Macro) offers the most favorable propagation conditions with lower attenuation and smoother decay with distance, UMa (Urban Macro) presents intermediate losses and UMi (Urban Micro/Street Canyon) exhibits the strongest attenuation, especially in NLOS cases. These distinctions formed the basis for assessing the feasibility of ambient backscatter in various deployment contexts.

The second part of the chapter focused on the simulation and link-budget evaluation for bistatic AmBC operation. Using MATLAB-based simulations, the received power at the sensor was calculated for multiple sensor loss levels and receiver sensitivities, enabling an estimation of the Available Path Loss (APL) and the BackCom range for different bandwidths. The results showed that the system performance is highly sensitive to bandwidth and sensor efficiency: larger bandwidths (10–20 MHz) increase noise power and reduce receiver sensitivity, while low-loss sensors (< 10 dB) can significantly extend the feasible communication distance.

The cartographic analyses provided an intuitive visualization of the interaction between system and environmental parameters. These maps enabled the identification of the feasible regions where backscatter communication remains possible, and demonstrated how the APL and BackCom range evolve with frequency, distance, and sensor losses. The maximum feasible range was observed in RMa-LOS conditions, reaching up to 10–15 m, whereas dense UMi-

NLOS environments limited the link to only 2–3 m, emphasizing the critical influence of multipath and shadowing.

Overall, the findings of this chapter highlight the trade-offs between range, bandwidth, and propagation conditions that govern bistatic AmBC feasibility in 5G networks. The models and results established here provide not only a theoretical framework but also quantitative references for system design and experimental validation.

The insights derived from this propagation and feasibility analysis form the basis for the next chapter, which focuses on the design, implementation, and experimental validation of a bistatic 5G AmBC receiver chain. Chapter 3 builds upon these theoretical foundations to demonstrate practical signal processing strategies and validate the analytical predictions through real-world measurements.

References

[1] L. Chetti and R. Bera, “A comprehensive survey on Internet of Things (IoT) toward 5G wireless systems,” *IEEE Internet Things J.*, vol. 7, no. 1, pp. 16–32, Jan. 2020.
[2] J. Huang *et al.*, “Wireless power transfer and energy harvesting: Current status and future prospects,” *IEEE Wireless Commun.*, vol. 26, no. 4, pp. 64–71, Aug. 2019.
[3] R. Singh, R. Kaur, and D. Singh, “Energy harvesting in wireless sensor networks: A review,” *Int. J. Energy Res.*, vol. 45, no. 1, Jan. 2021.
[4] S. A. Huda, M. Y. Arafat, and S. Moh, “Wireless power transfer in wirelessly powered sensor networks: A review of recent progress,” *Sensors*, vol. 22, no. 8, p. 2952, 2022.
[5] V. Liu *et al.*, “Ambient backscatter: Wireless communication out of thin air,” in *Proc. ACM SIGCOMM*, Hong Kong, 2013, pp. 39–50.
[6] K. Van Huynh *et al.*, “Ambient backscatter communications: A contemporary survey,” *IEEE Commun. Surv. Tutor.*, vol. 20, no. 4, pp. 2889–2922, 2018.
[7] R. Fara, *Ambient backscatter communications in future mobile networks*, Ph.D. dissertation, Univ. Paris-Saclay, 2021.
[8] M. U. Sheikh *et al.*, “Ultra-low-power wide-range backscatter communication using cellular generated carrier,” *Sensors*, vol. 21, no. 8, p. 2663, 2021.
[9] R. Biswas and J. Lempiäinen, “Power budget for wide-area ambient backscattering communications,” in *Proc. IEEE VTC*, Taipei, 2018.
[10] B. Kellogg *et al.*, “Wi-Fi backscatter: Internet connectivity for RF-powered devices,” *ACM SIGCOMM Comput. Commun. Rev.*, vol. 44, pp. 607–618, 2015.
[11] R. Biswas and J. Lempiäinen, “Assessment of 5G as an ambient signal source for backscatter communications,” *Wireless Netw.*, vol. 27, pp. 4083–4094, 2021.
[12] A. H. El-Sallabi *et al.*, “Improvement in accuracy of backscatter distance model for path loss prediction,” in *PIERS – Toyama*, 2018, pp. 107–114.
[13] 3GPP TR 38.901 (V16.1.0), *“Study on channel model for frequencies from 0.5 to 100 GHz,”* Release 16, 2020.
[14] 3GPP TS 38.104 (V16.0.0), *“Base Station (BS) radio transmission and reception,”* 2020.

Chapter 3: Design and Experimental Validation of a Bistatic 5G Ambient Backscatter Communication System

1. Introduction

This chapter describes the experimental setup and validation of a bistatic Ambient Backscatter Communication (AmBC) system, following the feasibility study conducted in Chapter 2 [1]. The goal here is to analyze the empirical performance of a backscatter link implemented with a custom hardware prototype and to study the geometric configuration and environmental conditions that impact signal detectability and system performance.

The main components of the system consist of a low-power tag equipped with a microcontroller and an RF switch implementing BPSK modulation. It is tested in controlled environments both full-anechoic and semi-anechoic, using a continuous wave (CW) signal source to emulate the ambient carrier. To support the analysis, we employ a theoretical bistatic propagation model that predicts the received power under various spatial configurations. The comparison between model and measurements allows us to validate the system's behavior under realistic conditions. The experimental work provided in this chapter was first introduced in [2] and further developed in [3] which also provided a formal framework of the theoretical propagation model. It was noted that there is a remarkable alignment between the experimental outcomes and theoretical expectations. Moreover, this chapter presents additional insights into the practical difficulties and limitations of ambient backscatter implementations within the domain.

Therefore, it structured as follows: Section 2 describes the hardware architecture and operation of the backscatter tag. Section 3 presents the theoretical propagation model used to estimate the received signal power. Section 4 details the experimental setups and evaluation techniques. Section 5 discusses the measurement results, including a comparison between experimental observations and theoretical predictions. Finally, Section 6 concludes the chapter with an overview of the key concepts and contributions.

2. Backscatter Tag Architecture

2.1. Hardware Description and System Overview

To enable experimental validation of the bistatic ambient backscatter communication system, a custom hardware tag was designed and implemented. The goal was to combine ultra-low-power operation with a compact and modular design that interfaces effectively with ambient or continuous wave (CW) RF carriers. The resulting tag prototype supports real-time switching,

environmental sensing, and backscatter modulation, making it suitable for laboratory experimentation and performance evaluation.

The tag architecture is organized into two main subsystems: a control and sensing unit and an RF front-end modulation unit. The sensing unit is based on the MSP-EXP430FR5969 development board from Texas Instruments [4]. This board integrates a 16-bit microcontroller optimized for ultra-low-power applications and features a non-volatile FRAM (Ferroelectric RAM) memory, which offers fast write speeds and low energy consumption. The microcontroller operates at 3.3 V and includes a built-in 12-bit analog-to-digital converter (ADC) that is used to digitize analog signals from the integrated temperature sensor. The temperature sensing function is provided by the LM335 [5], an temperature sensor whose output voltage varies linearly with the ambient temperature. This sensor has been selected to serve as an illustrative example. The analog output of the LM335 is continuously sampled by the ADC of the MSP430 microcontroller. The resulting digital signal is then processed and used to generate a binary control signal. This control signal drives the RF front-end by modulating the impedance of the antenna according to the encoded binary data, thereby enabling backscatter communication.

The RF front-end is built around the ADG902 RF switch from Analog Devices [6], a Single-Pole Single-Throw (SPST) reflective switch known for its high isolation and low insertion loss. This switch is directly driven by a digital output from the microcontroller, enabling binary control of the antenna load impedance. The antenna used is a dipole model (ANT-5GW-FPC-LH) [7] centered at 3.5 GHz, selected for its compact form factor, mechanical flexibility, and ease of integration through a U.FL connector. Both the RF switch and the antenna are mounted on a custom-designed PCB, which interfaces with the microcontroller development board via header pins, ensuring modularity and ease of assembly.

The schematic block diagram of the complete system is shown in Figure 19, where the interconnection between the sensing block, the microcontroller, the switching logic, and the antenna interface is clearly represented. The system with the chosen components is designed to minimize power consumption while maintaining precise control over the RF behavior of the antenna via digital logic.

To validate the circuit implementation and confirm correct switching behavior, the tag was tested in a controlled laboratory environment. The assembled prototype is shown in Figure 20, where the key components of the system are clearly labeled. The setup includes the MSP430FR5969 development board, a custom RF front-end PCB integrating the ADG902 switch and the LM335 sensor, and the flexible dipole antenna. A digital oscilloscope was

connected to monitor the output control signal from the MCU and verify that the switching logic will be performed correctly in response to sensor input.

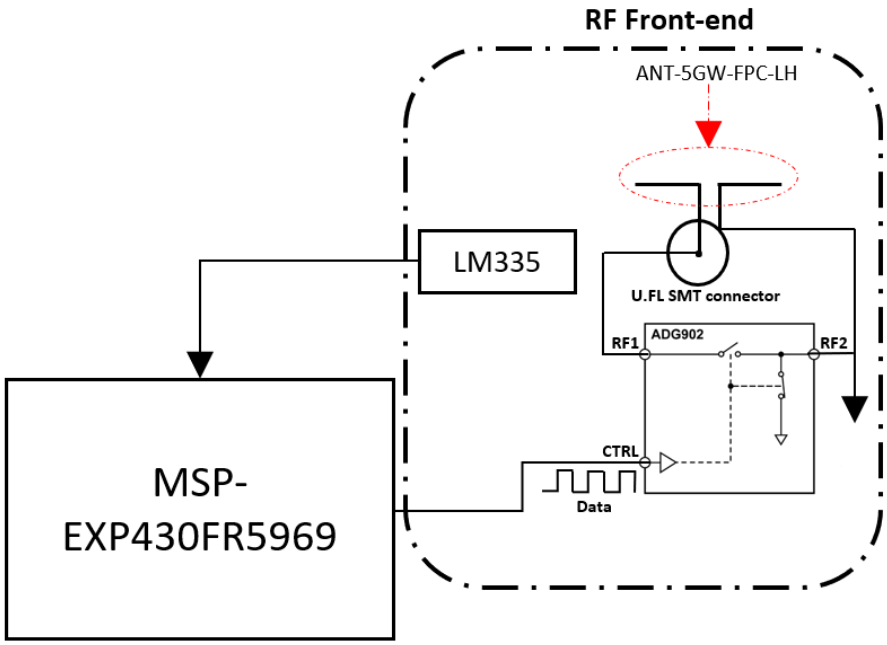

Figure 19. Functional Schematic of the Backscatter Tag Including Control and RF Front-End Modules.

Initial lab measurements confirmed that the system correctly switches between two impedance states at the antenna terminals, reflecting a continuous wave (CW) signal with a phase shift of either 0° or 180°, depending on the control bit level issued by the MCU. This simple BPSK behavior forms the basis for encoding binary information in the backscattered waveform. The reflected signal can then be detected by a remote receiver positioned according to the bistatic geometry as will be further examined in the experimental setup. Thanks to its modular and energy-efficient design, this tag serves as a foundational implementation for validating ambient backscatter communication in controlled environments and enables systematic testing across multiple configurations and measurement scenarios.

2.2. Operating Principle and Theoretical Analysis of BPSK Backscatter Modulation

The ambient backscatter tag developed in this work operates by exploiting the principle of load modulation, in which the impedance connected to the antenna is dynamically varied to encode information in the reflected signal.

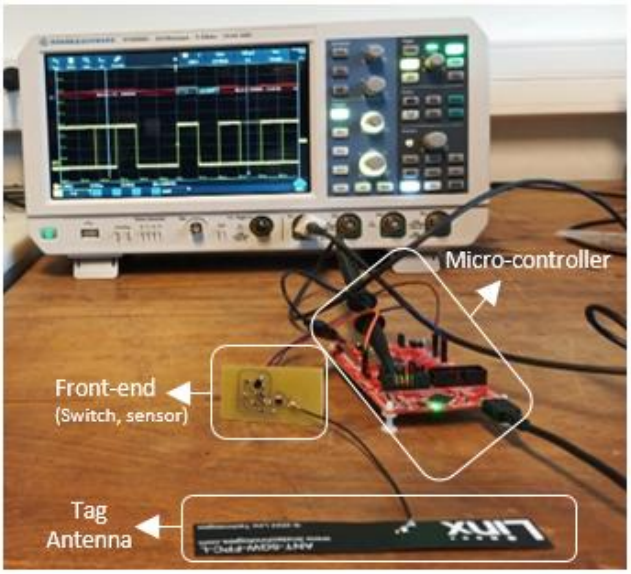

Figure 20. Backscatter Tag Prototype Featuring MSP430 Microcontroller, RF Switch (ADG902), LM335 Sensor, and Dipole Antenna.

A key feature of the designed tag lies in its capability to utilize ambient signals (5G-NR signal) to transmit the measured temperature to a remote receiver through reflection. In fact, instead of generating its own radio signal, the tag reflects an incident continuous wave (CW) carrier provided by an external source such as a 5G-NR signal generator and modulates it using binary phase modulation techniques. This method drastically reduces energy consumption, making it particularly well suited for ultra-low-power applications.

The modulation relies on a simple binary switching mechanism controlled by the microcontroller. A square-wave baseband signal carrying binary data modulates the reflection coefficient of the antenna. This is accomplished by toggling the RF switch to alternate between two load impedance states. These two impedance values, typically denoted Z_1 and Z_2, create different reflection coefficients when connected to the antenna, resulting in distinct phase shifts in the reflected signal. The two logical states (‘0’ and ‘1’) are encoded as phase shifts of 180°, corresponding to BPSK (Binary Phase Shift Keying) modulation.

It is important to note that the mathematical model of the antenna’s reflection coefficient Γ, which quantifies the backscattering behavior as a function of the impedance states, is already introduced and detailed in Chapter 1. Therefore, the current section focuses on how this switching translates into waveform behavior and modulation effects.

Mathematically, the carrier wave is described by the equation:

$$c(t) = \cos(2\pi f_c t) \tag{3.1}$$

Where, f_c is the carrier frequency. The binary data stream $m(t) \in \{-1, +1\}$ is generated by mapping a sequence of Bernoulli-distributed bits from {0,1} to NRZ (Non-Return-to-Zero) bipolar form:

$$m(t) = 2b(t) - 1 \tag{3.2}$$

The BPSK modulated reflected signal is then obtained by multiplying the CW with the binary data:

$$r(t) = m(t) \,.\, c(t) = \begin{cases} +\cos(2\pi f_c t) \; if \; m(t) = +1 \\ -\cos(2\pi f_c t) \; if \; m(t) = -1 \end{cases} \tag{3.3}$$

To further validate, understand, and illustrate this theoretical principle for application in our proposed prototype tag, a MATLAB simulation was conducted. The simulation consists of generating a CW signal at 3.5 GHz, creating a binary NRZ sequence, and performing BPSK modulation by multiplying the two. The results are depicted in Figure 21 below, where different time-domain and frequency-domain behaviors of the signal components are presented.

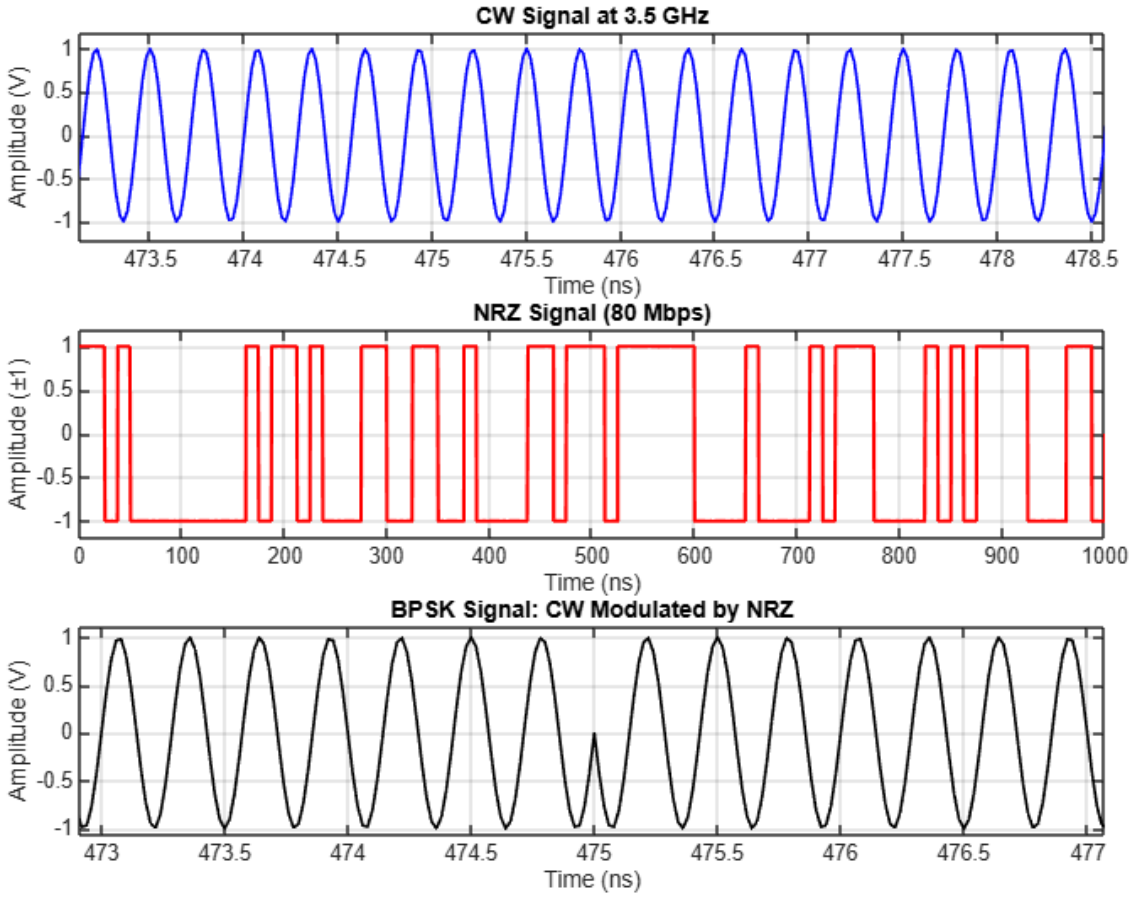

Figure 21. Time-Domain Simulation of BPSK Backscatter Modulation: (Top) Continuous Wave (CW) Signal at 3.5 GHz, (Middle) Baseband NRZ Data Sequence, (Bottom) Resulting BPSK-Modulated Signal.

Figure 21 illustrates the simulation of the BPSK modulation process used in the proposed backscatter communication system. The top plot shows the original unmodulated continuous wave (CW) signal in the time domain. Its clean sinusoidal shape reflects a stable carrier oscillation at 3.5 GHz, which serves as the reference signal to be modulated via impedance switching at the tag.

The middle plot displays the baseband NRZ binary signal used for modulation. The waveform alternates between +1 and –1 levels, corresponding to binary bits '1' and '0', respectively. This digital sequence emulates the switching control signal generated by the microcontroller in the physical system, used to toggle the reflection coefficient of the antenna between two impedance states.

The bottom plot represents the BPSK-modulated signal obtained by multiplying the CW with the NRZ data sequence. The resulting waveform retains the carrier frequency but exhibits abrupt 180° phase reversals whenever the binary bit transitions occur as shown at the bottom of Figure 21 for the transition occurring at 475 ns These phase shifts are the fundamental mechanism through which data is encoded in the backscattered signal.

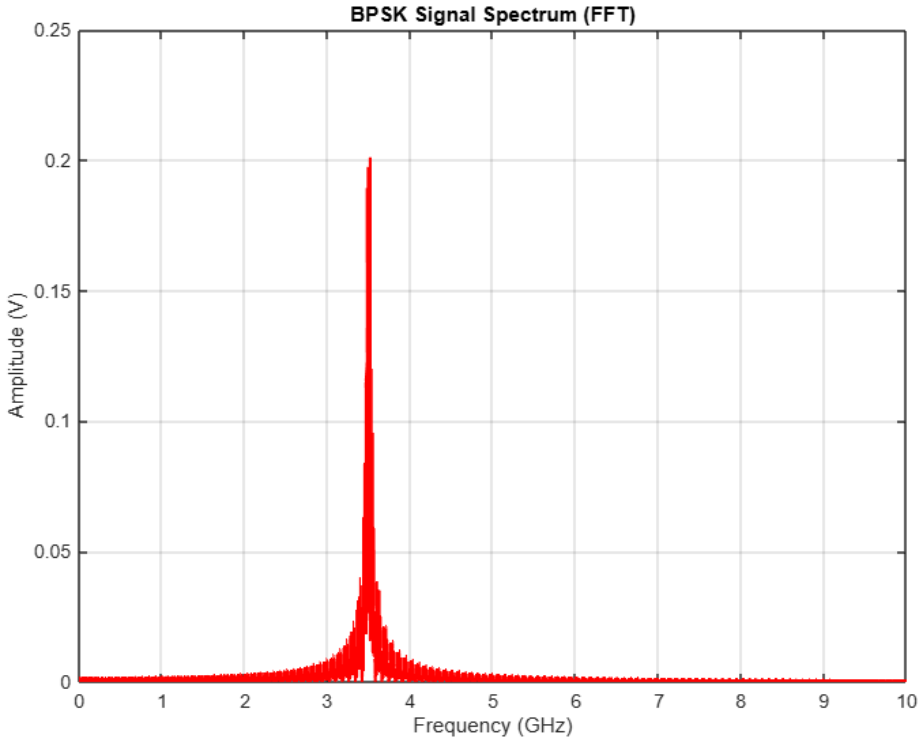

Figure 22. FFT-Based Spectrum of the BPSK-Modulated Signal Illustrating Spectral Broadening Around the Carrier Frequency.

Finally, Figure 22 illustrates the frequency spectrum of the BPSK-modulated signal. Unlike the narrow spectral line of the unmodulated CW, the BPSK spectrum is broadened, showing symmetrical sidebands around the central carrier frequency. This spectral broadening is a direct

consequence of the modulation process and validates the theoretical expectation for a BPSK signal. The sidebands' symmetry and spacing confirm that the reflected signal encodes meaningful binary information, even though it is passively generated by load modulation.

This simulation confirms that the multiplication of the binary data stream and the CW results in a phase-shifted reflection with clearly encoded binary information. These results support the theoretical framework and validate the feasibility of implementing such modulation in the designed prototype using a simple square-wave control logic. This forms the basis for the system's experimental validation in the following sections, which will analyze the performance of the tag under various bistatic geometric configurations and environmental conditions.

3. Bistatic AmBC System Theoretical Model

To evaluate the performance of the bistatic ambient backscatter communication (AmBC) system under various spatial and environmental conditions, a theoretical power budget model is developed. This model is used to predict the received power at the receiver (Rx) as a function of the geometry and propagation characteristics of the link. It provides a quantitative framework for estimating the signal strength at Rx, serving both as a reference for experimental validation and as a tool for guiding the experimental setup design.

Unlike conventional monostatic architectures, where the transmitter and receiver are co-located, the bistatic configuration introduces asymmetry in the signal path. This requires decomposing the communication link into two distinct segments: from the transmitter (Tx) to the backscatter tag (Tag), and from the Tag to the receiver (Rx). Each segment is subject to free-space path loss (FSPL), and the total received power is calculated by combining the losses on both paths, along with the antenna gains and the reflection properties of the tag. This model captures the essential dependencies between geometry, frequency, and tag behavior, enabling accurate prediction of AmBC signal performance in realistic scenarios.

To describe the spatial configuration of the bistatic backscatter communication system, we refer to the geometric arrangement illustrated in Figure 2. In this setup, the distance "d" represents the separation between the transmitter (Tx) and the receiver (Rx). The backscatter tag is positioned along a line forming angles θ_T and θ_R with respect to the transmitter and receiver, respectively. The direct distances from the tag to the transmitter and to the receiver are respectively denoted by x_T and x_R. The value $d = 4.5m$ was imposed by the geometric dimension constraints of the full anechoic chamber that will be presented in the experimental validation part.

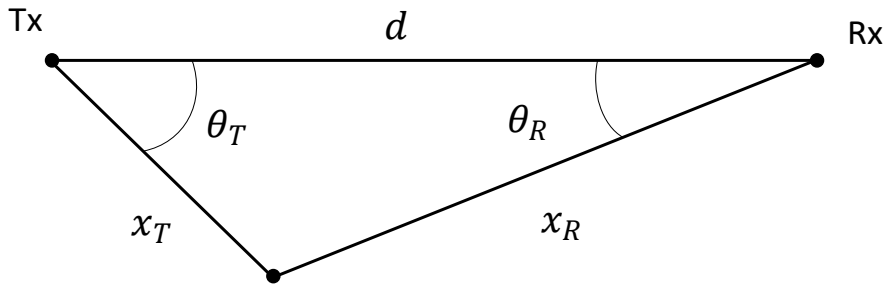

Figure 23. Geometric Parameters Definition for a Bi-Static AmBC System Model, (d=4.5 m in practice).

By applying twice propagation equations in free space from Tx to Sensor and from Sensor to Rx, we can write the received power at Rx, denoted P_R, in dBm, at Rx as follows:

$$P_R = P_T + G_T + G_R + 2G_S - 10log_{10}(x_T^2) - 10log_{10}(x_R^2) + 40log_{10}\left(\frac{c}{4\pi f}\right) + \Delta\sigma(\text{dBsm}) \quad (4)$$

where P_T is the transmitted power, P_R is the received power at Rx, G_T is the gain of Tx antenna, G_R is the gain of Rx antenna, G_s is the gain of tag antenna, $f = 3.5\ GHz$ is the frequency, and c is the propagation celerity. In equation (4), $\Delta\sigma(\text{dBsm})$ is the differential radar cross section (RCS) and $(x, \theta) = (x_T, \theta_T)$ or (x_R, θ_R). The modulation considered in this work is BPSK. The effective RCS variation due to modulation is given by the equation (9) [8, 9].

Moreover, referring to Al-Kashi's Theorem (also known as the Cosine Law), we can obtain the distances x_R and x_T according to (5) and (6):

$$x_R^2 = x_T^2 + d^2 - 2x_T \,.\, d \,.\, \cos(\theta_T) = (x_T - d)^2 + 2x_T d(1 - \cos(\theta_T)) \quad (5)$$

$$x_T^2 = x_R^2 + d^2 - 2x_R \,.\, d \,.\, \cos(\theta_R) = (x_R - d)^2 + 2x_R d(1 - \cos(\theta_R)) \quad (6)$$

By adding the expressions of x_T^2 and x_R^2, we derive the final expression of the received power P_R in terms of spatial parameters x, d and the angular offset θ:

$$P_R = P_T + G_T + G_R - 10log_{10}(x^2) - 10log_{10}\big((x - d)^2 + 2xd(1 - \cos(\theta))\big) + K \quad (7)$$

where:

$$K = 40log_{10}\left(\frac{c}{4\pi f}\right) + \Delta\sigma(dBsm) \quad (8)$$

$$\Delta\sigma(\text{dBsm}) = 10\log\left(|\Gamma_1 - \Gamma_0|^2 \sigma_{ant}\right) \quad (9)$$

Where Γ_1 and Γ_0 are denote the complex reflection coefficients corresponding to the two modulation states of the tag and σ_{ant} is the antenna's intrinsic radar cross section. For a dipole antenna, $\sigma_{ant} \simeq \frac{G^2\lambda^2}{4\pi}$, which gives almost 6dB. This implies a new expression of P_R :

$$P_R = P_T + G_T + G_R + 2G_S - 10log_{10}\left(|\Gamma_1 - \Gamma_0|^2 \frac{\lambda^2}{4\pi}\right) - 10log_{10}\big((x - d)^2 + 2xd(1 - \cos(\theta))\big) + K_1 \quad (10)$$

Where $K_1 = 40log_{10}\left(\frac{c}{4\pi f}\right) = -62.56dBm$

The angle θ should be considered as an oriented angle to cover all the possible positions in the plane formed by Tx, Rx and sensor positions: $-\pi < \theta < \pi$.

In a bistatic backscatter communication setup, aligning the Tx, Rx, and Tag such that the tag is located behind either the Tx or the Rx is not desirable, especially when the Tx and Rx antennas are placed close to the chamber wall, as is the case in our experimental setups in the fully anechoic chamber. In such configurations, it is possible for the tag to fall outside the main lobe of the transmitting or receiving antenna, leading to weak signal reception. These edge cases correspond to extreme angular positions ($\theta = \pm\pi$), which are excluded to ensure reliable measurements and to avoid boundary effects as in such cases the Tx or Rx would act as physical obstacles to effective signal backscattering.

Equation (10) represents the mathematical model of P_R that we will study in this section and that will be used as a reference model in the measurement setup section.

To ensure coherence with the experimental framework, two particular configurations were isolated and analyzed within the theoretical model. The first involves a bistatic setup where the transmitter (Tx) and receiver (Rx) are co-located but remain physically distinct. The second focuses on the aligned arrangement of Tx, the tag, and Rx in that order. These configurations correspond to Setups A and B used in the measurement campaign that will be presented in details in section 4. The third configuration corresponds to the general scenario in which the Tx, Rx and tag are positioned in a non-aligned manner. In addition, the theoretical impact of antenna rotation modifying the gain pattern of Tx and/or Rx is investigated to support the interpretation of experimental results obtained under Setup E. The remaining scenarios, Setups C and D, are encompassed by the general case treated in the theoretical analysis.

3.1. Particular Case 1 : Tx, Rx are collocated

Tx and Rx are considered co-located when, on one hand, the separation distance is nearly zero: $d \simeq 0$, and on the other hand, the distances from the tag to the transmitter (x_T) and to the receiver (x_R) are sufficiently large ($x_T = x_R = x \gg d$) such that the angles θ_T and θ_R are approximately equal to $\pi/2$. The expression of the received power P_R is then update in these conditions according to (11):

$$P_R = P_T + G_T + G_R + 2G_S + K - 40\log(x) \qquad (11)$$

Under these conditions, the power of the backscattered signal received at the Rx antenna is a strictly decreasing logarithmic function of the distance. To better analyze the received power, we considered three specific antenna gain values as follows: $G_T = G_R = 12dBi$, and $G_S =$

$5dBi$. The distance between Tx and Rx was set to $d \simeq 0$. Although the Tx and Rx antennas are directive, they operate at their maximum gain in this configuration since the angles at Tx and Rx are nearly zero due to the isosceles geometry centered at the tag (Figure 32.a). The variation of the power as a function of the distance x separating Tx and Rx is represented in Figure 24.

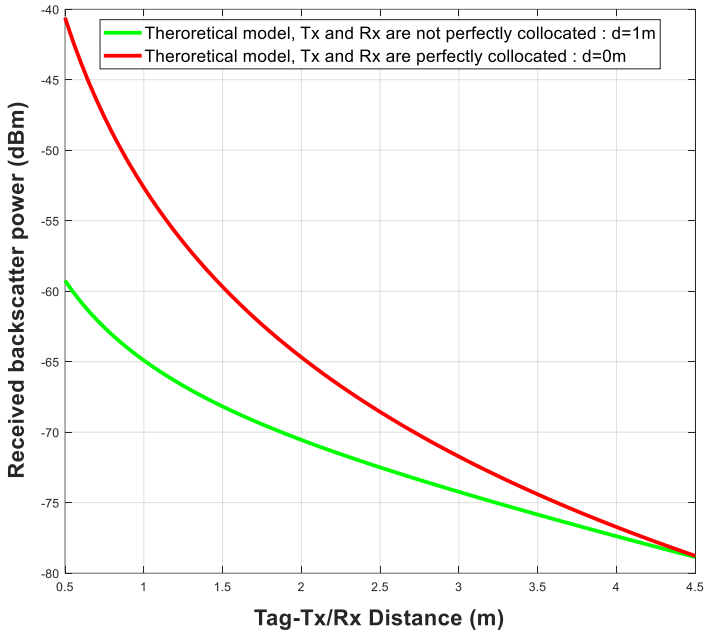

Figure 24. Simulated received power in the case where Tx and Rx are perfectly collocated and not perfectly collocated.

We compare two cases using the theoretical model: the first corresponds to a scenario where the distance between the transmitter (Tx) and the receiver (Rx) is negligible (i.e., Tx and Rx are perfectly collocated $d \simeq 0$), and the second considers a case where Tx and Rx are separated by approximately 1 meter, meaning they are not perfectly collocated ($d \simeq 1m$). We observe that the received power levels are comparable in both cases when the distance between the tag and either Tx or Rx is between 3 and 4.5 meters. However, for shorter distances, the model with perfect collocation predicts a much steeper increase in received power.

3.2. Particular Case 2 : Tx, Sensor and Rx are aligned

To verify the consistency of the theoretical model, we consider the particular case where the transmitter (Tx), the sensor, and the receiver (Rx) are aligned. In this configuration, the angular offset is $\theta = 0$. Under this condition, the expression of the received power P_{R_a} simplifies as follows:

$$P_{Ra} = P_T + G_T + G_R + 2G_S - 10log_{10}(x^2) - 10log_{10}((x-d)^2) + K \qquad (12)$$

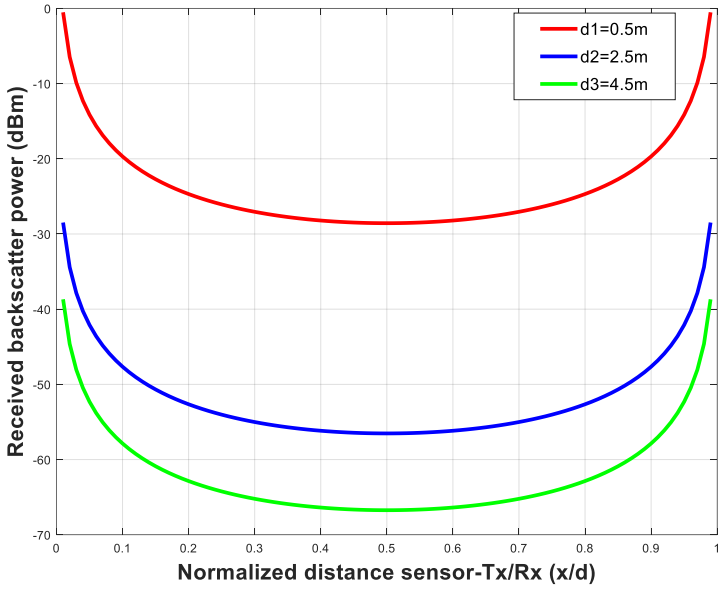

Figure 25. Simulated received power vs nomalized disance when Tx, Sensor and Rx are aligned.

The three curves are symmetrical, and the received power reaches its minimum at $x_0 = {}^{d}/_{2}$. The minimum received power is then given by:

$$P_{R_{a_{min}}} = P_T + G_T + G_R + 2G_S - 40log_{10}(d) + 40log_{10}(2) + K \qquad (13)$$

In this simulation, we considered $P_T = 0dBm$, $G_T = 12dBi$, $G_R = 12dBi$ and $G_S = 5dBi$. These values are maintained throughout the simulations presented in this section. The consistency of our results with those reported in [10] and [11] further supports the validity of our theoretical model.

It can also be observed that $P_{Ra}(x,\ \theta = 0) > P_R(x, \theta)$ for any angle θ by considering identical numerical values of d. This is also coherent since even for a same x, since the distance of the second segment of the indirect path $(i.e., x_T\ or\ x_R)$ becomes greater than $x - d$. This means that when $\theta \neq 0$, the sensor is further far from Tx or Rx compared to the aligned case $\theta = 0$. Finally, we note that although the distance d increases by 2 meters when transitioning from d_1 to d_2 and from d_2 to d_3, the received power for the same value of x does not decrease by the same amount in both transitions. This discrepancy is due to the non-linearity of the logarithmic function.

3.3. General case: Tx, Sensor and Rx are not aligned

In this sub-section, we consider the general case: Tx, Sensor and Rx are not aligned ($\theta \neq 0$). We first studied the variation of the received power as function of x when d and θ are considered as constant parameters. Then, we considered the distance x as a constant parameter and studied the variation of P_R for variable d and a variable angle.

3.3.1. Received power variation as a function of geometrical parameters

For conventional communications, where the RF signal is generated by the transmitter, the received power decreases when the distance between the transmitter and the receiver increases in a free space environment. This evolution is predicted by Friis Equation. Moreover, even for traditional monostatic configuration systems (like UHF RFID systems or radars), it is well known that the received power decreases also when the distance from the reader to the tag (for RFID systems) or the target (for radars) increases. For AmBC bistatic configuration, this result is no longer true even in the case where Tx, Sensor and Rx are aligned as explained in the previous subsection.

We check here the monotonicity of the received power depending on the values of d and θ. For that, we calculate the derivative of P_R:

$$\frac{d_{P_R}}{dx} = \frac{20(-2x^2+3dxcos(\theta)-d^2)}{x((x-d)^2+2xd(1-\cos(\theta)))\ln(10)} = \frac{N(x)}{D(x)} \qquad (14)$$

The function $D(x) = x((x-d)^2 + 2xd(1-\cos(\theta)))\ln(10)$ is positive for any value of x, d and θ.

The sign of $\frac{dP_R}{dx}$ is that of the second-degree polynomial $N(x)$, for which the number of roots and their values depend on the sign of the discriminant $\Delta_N = d^2(9cos^2(\theta) - 8)$. If $\Delta_N > 0$, which means $cos^2(\theta) > 8/9$ then N will have two different roots that should be two extrema positions x_1 and x_2 of P_R:

$$x_1 = \frac{d\left(3\cos(\theta)-\sqrt{9cos^2(\theta)-8}\right)}{4} \qquad (15)$$

$$x_2 = \frac{d\left(3\cos(\theta)+\sqrt{9cos^2(\theta)-8}\right)}{4} \qquad (16)$$

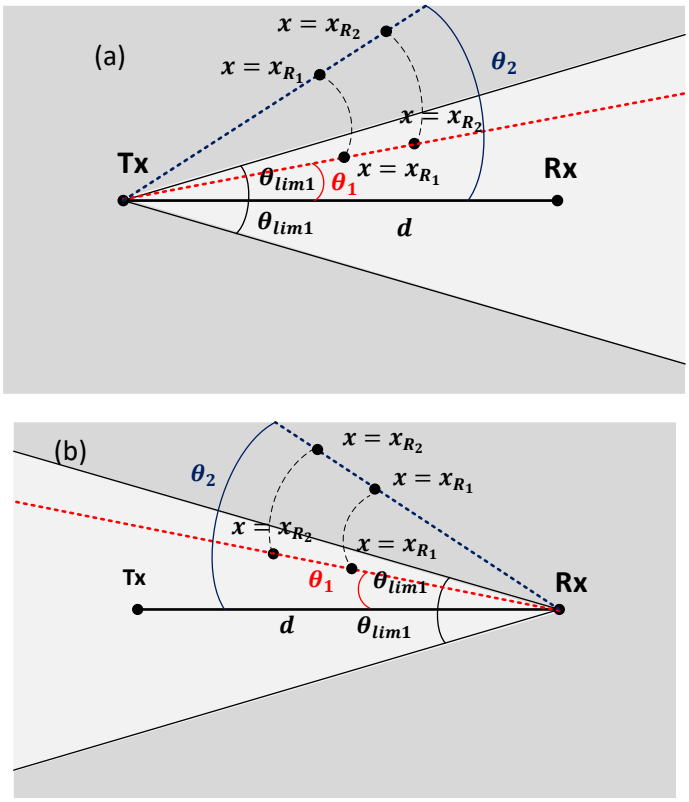

Figure 26. Definition of the limit angle and the cartography of the motonicity of the received power P_R.depending on the value of θ; $(x, \theta) = (x_T, \theta_T)$ in (a) and $(x, \theta) = (x_R, \theta_R)$ in (b).

To simplify the analysis, only positive values of θ within the interval $[0, \pi[$are considered, taking advantage of the symmetry of the problem and the properties of the cosine function. Moreover, the considered scenario is 2D, meaning that the transmitter (Tx), the receiver (Rx), and the tag lie in the same plane. The condition $cos^2(\theta) > {}^8/_9$ defines two angular limits:

$$\theta_{lim1} = \arccos\left(2\sqrt{{}^2/_3}\right) rad, \text{ and } 19.47 \text{ in degrees} \quad (17)$$

$$\theta_{lim2} = \pi - \arccos\left(2\sqrt{{}^2/_3}\right) = \pi - \theta_{lim1} rad \text{ and } 160.45 \text{ in degrees.} \quad (18)$$

It is important to emphasize that the values of these angular limits are independent of any other parameters. It is also straightforward to verify that $0 < x_1 < {}^d/_2 < x_2$, where x_1 corresponds to a local minimum and x_2 to a local maximum.

If $\theta < \theta_{lim1}$ or $\theta > \theta_{lim2}$, $\Delta_N > 0$, P_R has two extrema. Otherwise, if $\theta_{lim1} < \theta < \theta_{lim2}$ then $\Delta_N < 0$ and P_R will be strictly decreasing. Finally, if $\theta = \theta_{lim1}$ or $\theta = \theta_{lim2}$, $\Delta_N = 0$, and $x_1 = x_2 = 3dcos(\theta)/4$. Since x_1 and x_2 as distances, they should be positive, which means $x_1 = x_2 = 3dcos(\theta_{lim1})/4 = d\sqrt{2}/2$.

To simplify the analysis without loss of generality, we restrict the angular domain to $0 < \theta < \pi/2$ as illustrated in Figure 26. This restriction is sufficient to cover all possible tag positions, since for any position where $\theta_R \geq \pi/2$, the corresponding θ_T will satisfy $\theta_T \leq \pi/2$, and vice versa. In such cases, it is appropriate to swap the pair (x_T, θ_T) with (x_R, θ_R), depending on which angle exceeds $\pi/2$. As a result, all simulations in the following sections will consider $\theta \in [0, \pi/2]$ (in radians).

In the specific case where $\theta = \theta_{lim1}$, the function P_R is still decreasing but presents a horizontal inflection point at $x = d\sqrt{2}/2$. In Fig. 8, for both configurations $(x, \theta) = (x_T, \theta_T)$ or (x_R, θ_R)), the light gray area corresponds to the domain where P_R has two extrema, whereas in the dark gray area, P_R is strictly decreasing with respect to the spatial variable x, for fixed d and θ. Specifically, as illustrated in Figure 26, for any pair (x_{R_1}, θ_2) and (x_{R_2}, θ_2) such that $x_{R_1} < x_{R_2}$, we have $P_R(x_{R_1}, \theta_2) > P_R(x_{R_2}, \theta_2)$. However, it is not possible to compare $P_R(x_{R_1}, \theta_1)$ and $P_R(x_{R_2}, \theta_2)$ without first comparing both distances $x_{R_1}$and x_{R_1} relative to the extrema positions x_1 and x_2.

To clarify the different scenarios regarding the variation of the received power P_R with respect to θ and the associated limit angles, Table 5 provides a structured summary of all the cases discussed above.

Condition	θ	x	P_R
$\lvert\theta_T\rvert < \theta_{lim1} < \frac{\pi}{2}$	$\theta = \theta_T$	$x = x_T$	Non-monotonic with a minimum and a maximum
$\theta_{lim1} < \lvert\theta_T\rvert < \frac{\pi}{2}$	$\theta = \theta_T$	$x = x_T$	Decreasing function of x
$\lvert\theta_R\rvert < \theta_{lim1} < \frac{\pi}{2}$	$\theta = \theta_R$	$x = x_R$	Non-monotonic with a minimum and a maximum
$\theta_{lim1} < \lvert\theta_R\rvert < \frac{\pi}{2}$	$\theta = \theta_R$	$x = x_R$	Decreasing function of x

Table 5. Monotonicity of backscattered power across tag angular configurations

Contrarily to independence of the monotonicity to the distance d, the power levels and positions of the extrema points depend on both d and θ.

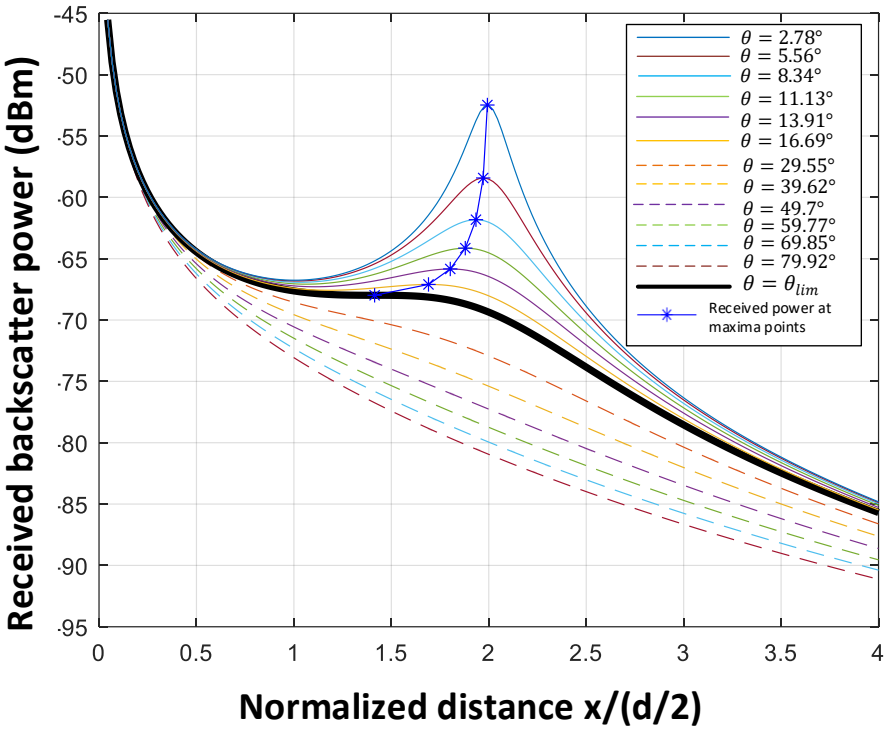

Figure 27. Monotonicity of the received power for different values of θ and a constant Tx-Rx distance,d=4.5m

Figure 27 depicts the simulation results of $P_R(x)$ for specific values of θ in two different ranges: $\theta_{lim1} \leq \theta < \pi/2$ and $0 < \theta \leq \theta_{lim1}$. All curves don't have any intersection points and for two different angles, curves for lower values are below curves for higher values, which means that if $\theta_1 < \theta_2$, then $P_R(x, \theta_2) < P_R(x, \theta_1)$. Again, note that, $P_T = 0dBm$, $G_T = 12dBi$, $G_R = 12dBi$, $G_S = 5dBi$ and this time $d = d_3 = 4.5m$. We can clearly observe the horizontal inflexion point for the specific case of $\theta = \theta_{lim1} = 19.47°$ with an almost-flat zone (the black curve). We checked also that all the curves in dashed lines are decreasing and that those in continuous lines have a local minimum and a local maximum. We matched the maxima points to observe the evolution of the received power depending of the angle: it seems to decrease in contrast to the received power at the minimum which is quite constant for all the angles. This is confirmed by Figure 28.a and Figure 28.b in which we plotted respectively the positions of the normalized extrema (x_1/d and x_2/d) and their respective received power at Rx.

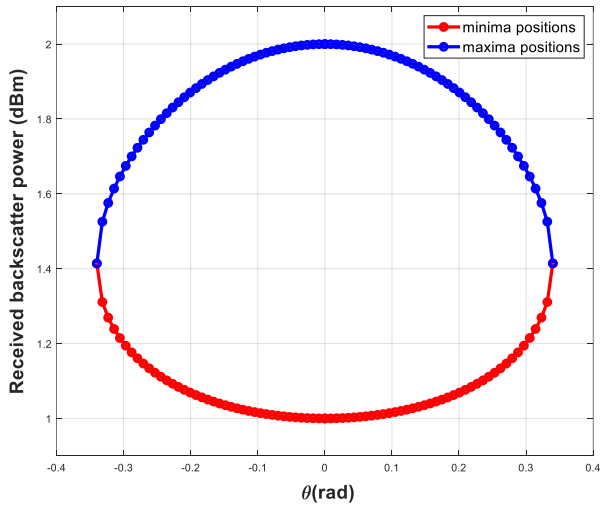

(a)

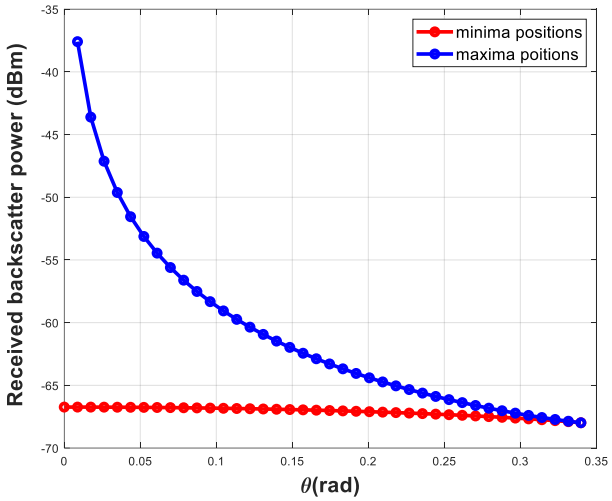

(b)

Figure 28. Normalized positions of local mimima and local maxima and their power levels vs θ when P_R is not monotonic ($\theta < \theta_{lim1}$), $d = 4.5m$.

To further analyze the behavior of the received power, a 3D plot surface of P_R as a function of the angle θ and the distance x was plotted (Figure 29), synthesizing the trends observed in the 2D curves of Figure 27. The local minima and maxima are clearly visible in Figure 29, along with a region where the received power decreases monotonically. Additionally, it is observed that for smaller values of x, the received power remains nearly constant across all angles.

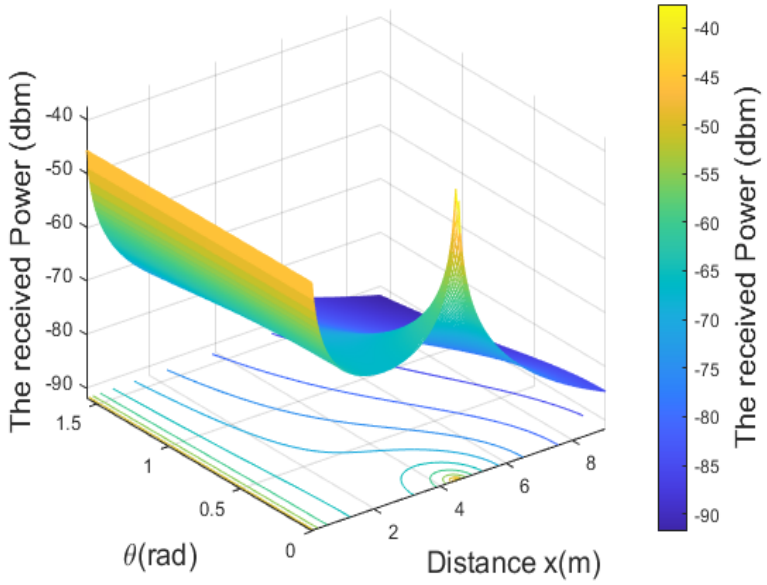

Figure 29. The received power in dBm as function of θ and x(m) plotted as a 3D Surface, d=4.5m

As indicated in the previous results, the distance d is considered constant $(d = 4.5m)$. Now, if d is treated as a variable while keeping θ and x fixed, a mathematical analysis of $P_R(d)$ shows that the function reaches an absolute maximum at $d = xcos(\theta)$, as will be demonstrated in the following derivative analysis.

$$\frac{\partial P_R}{\partial d} = -10\frac{2d-2x\cos(\theta)}{\ln(10)(x^2+d^2-2xd\cos(\theta))} \qquad (19)$$

The corresponding received power is given by:

$$P_R(d) = K_1 - 40\log(x) - 10\log(1 + sin^2(\theta)) \qquad (20)$$

Where K_1 is a constant.

This result is intuitive since if $d = x\cos(\theta)$, this configuration implies that the transmitter (Tx), receiver (Rx), and the Tag form a triangle with the right angle located at either Tx or Rx. Consequently, the sensor is positioned at the closest point to the line segment connecting Tx and Rx which explains why the maximum received power occurs at this point.

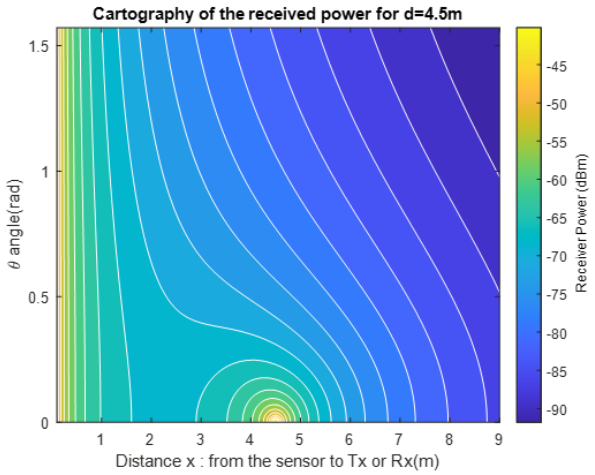

Figure 30. A planar cartography of the received power in dBm as function of θ and x

3.3.2. Received power variation as a function of antenna gain

This subsection focuses on the study of antenna gain on the received backscattered power. Our goal is to be able to compare experimental results with the proposed theoretical model involving the gain effect, mainly of Rx antenna whose orientation has been possible to change during the experimental campaigns. To this end, we considered an empirical gain model (G_R) of the directive SAS-571 antenna, which was used as Rx antenna in measurement. The 3 dB azimuth bandwidth of this antenna is 24°and its maximal gain is $G_{Rmax} = 12$ dBi. We use a Gaussian radiation pattern [12]. The gain values predicted by equation (21) for various angles ϕ are summarized in Table 6.

$$G_R(\phi) = G_{Rmax} + 10.\log\left(e^{-2.62\phi^2}\right) \quad (21)$$

where ϕ denotes the azimuth angle.

Absolute value of ϕ(°)	Gain of the SAS-571(dBi)
0	12
15	6
30	0.75
45	0.02
60	0
75	0
90	0

Table 6. A summary of the gain values predicted by the gaussian model

By integrating the gain expression in equation (7), we derive the following received backscattered power:

$$P_R(\phi) = K'(x,d,\theta) + 10\log\left(e^{-2.62\phi^2}\right) \quad (22)$$

where K' is constant for fixed values of x, d and θ. $K'(x,d,\theta) = P_T + G_T + 2G_S - 10\log(x^2) - 10\log\left((x-d)^2 + 2xd\left(1-\cos(\theta)\right)\right) + K$ (23)

However, if x is variable and d, θ keep constant, the expression of $P_R(\phi, x)$ is:

$$P_R(\phi, x) = K'(x, 4.5\ m, 63.61°) + 10\log(e^{-2.62\phi^2}) \quad (24)$$

We first considered fixed values for the parameters, including $P_T = 0\text{dBm}$, $G_S = 5\text{dBi}$, $G_T = 12\text{dBi}$, $d = 4.5m$, $x_T = 4m$, and $x_R = 2m$ (which implies $\theta_T \simeq 63.61°$ as presented in equation (24)). The corresponding simulation results are illustrated in Figure 31.

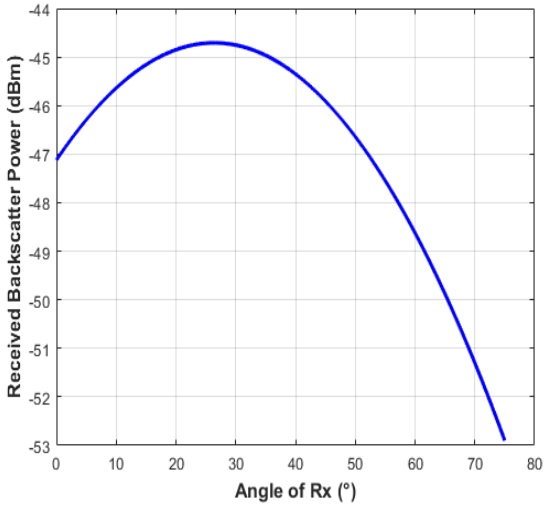

(a)

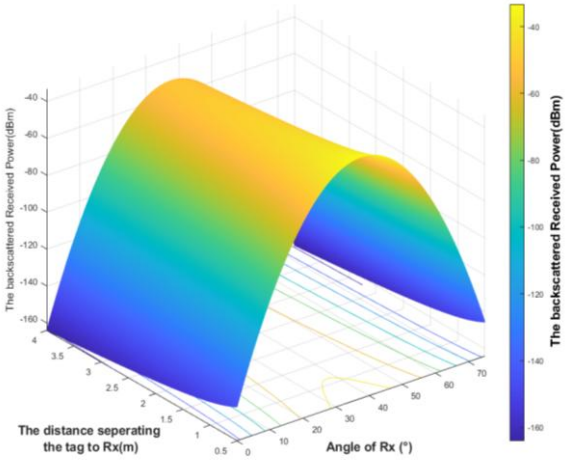

(b)

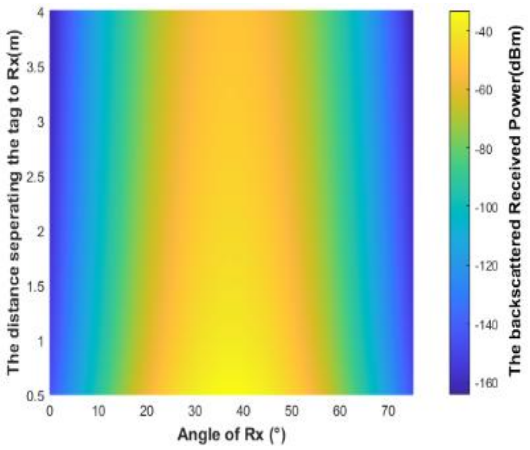

(c)

Figure 31. Received Backscattered Power as a Function of Rx Antenna Orientation and Tag–Rx Distance, for a Fixed Geometric Angle θ , (a): 3D plot of $P_R(\phi, x)$, with fixed parameters values $P_T = 0\text{dBm}$, $G_S = 5\text{dBi}$, $G_T = 12\text{dBi}$, $d = 4.5m$, and $\theta \simeq 63°$, (b): Evolution of $P_R(\phi)$ under the same conditions with fixed value of $x_T = 4m$, and $x_R = 2m$, (c) : a 2D map of $P_R(\phi, x)$

After introducing the variable gain model of the Rx antenna (SAS-571), the simulated backscattered power exhibits a profile similar to the Gaussian shape of the antenna gain. This is expected, as the power depends only on the azimuth angle and is proportional to the gain. The angle used here is the complement of θ_R , as defined in our measurements. A peak is observed near 27°, corresponding to the orientation where the Rx antenna faces the Tx, consistent with the theoretical alignment (complement of 63°). Both the 3D plot and 2D map reveal symmetry around this angle. As the distance x increases, the power decreases more sharply near this 27° alignment.

4. Measurement setup

4.1. Experimental scenarios

To analyze the received power, five distinct measurement setups were designed, as illustrated in Fig. 14 and detailed in Table 7.

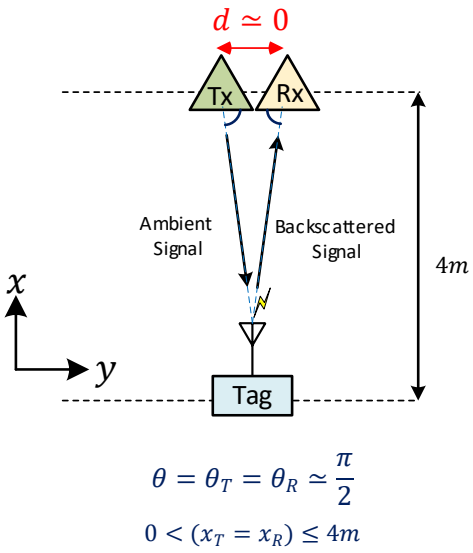

(a) Setup A

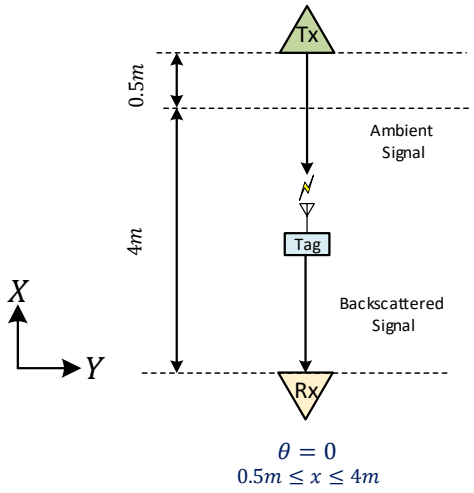

(b) Setup B

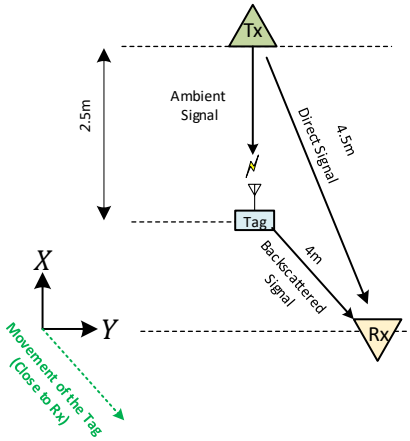

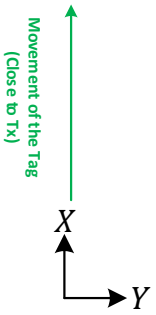

(c) Setup C

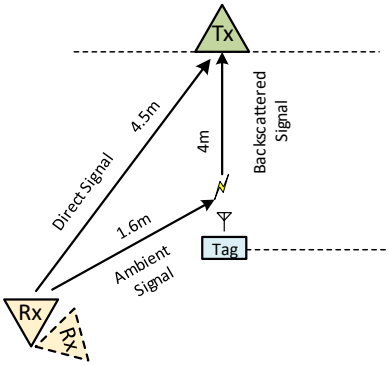

(d) Setup D

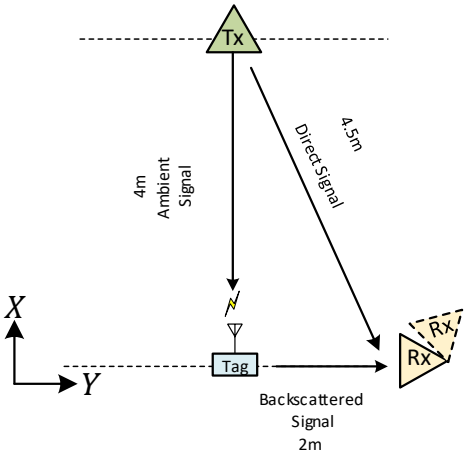

(e) Setup E

Figure 32. Illustration of Different Tx-Tag-Rx Geometrical Configurations for Backscatter Experiments.

1. **Setup A – Bistatic Collocated Configuration**

In this setup, where the transmitter (Tx) and receiver (Rx) are placed in parallel, and the tag moves along the x-axis over a 4-meter range, while maintaining a constant height relative to the ground. The distance between Rx and Tx is very small with a practical value of approximately 40 cm.

2. **Setup B – Vertical Alignment Configuration**

In this setup, the transmitter (Tx), the tag, and the receiver (Rx) are vertically aligned. The tag is constrained to remain within 0.5 meters of the Tx while moving along a 4-meter range.

3. **Setup C – Non-Aligned Configuration**

In this configuration, the transmitter (Tx), the tag, and the receiver (Rx) are arranged diagonally, with the tag positioned closer to the transmitter (at 2.5 meters). This setup introduces a significant direct path between Tx and Rx, allowing for the assessment of direct path effect on backscatter reception.

4. **Setups D and E – Bistatic Dislocated Backscatter Configurations**

Setup D employs a triangular arrangement, with a 4.5-meter separation between Tx and Rx and the tag moving vertically while positioned 1.6 meters from the Rx. Defined angular deviation of Rx antenna (75°, 30°, 75°) allow precise control of the gain effect, facilitating detailed analysis of antenna performances as well as angular and distance effects on system performance.

In Setup E, the Tx and Rx are positioned at a 90-degree angle and the tag is fixed, with the Rx antenna changing its orientation for a different angle each time. The initial configuration minimizes direct link interference, enabling isolated observation of the backscattered signal.

In summary, the five measurement setups provide a comprehensive framework for characterizing the impact of spatial deployment, movement dynamics, and interference on the reliability of AmBC communication.

Table 7 provides an overview of the spatial characteristics for each configuration. The terms x_{R0} and x_{T0} denote the initial distances between the tag and the receiver, and between the transmitter and the tag, respectively. θ_T is defined as the angle between the Tx–Rx line and the line connecting the Tx to the tag, while θ_R is the angle between the Rx–Tx line and the line connecting the Rx to the tag.

Setups	Initial setup parameters	Setup parameters subject to variation	Measurement Environment
A	• Tx and Rx are collocated. • $x_{R0} = x_{T0} = 4m$ • $\theta = \theta_R = \theta_T = \frac{\pi}{2}$ • d is very small (40 cm in practice) • Tx and Rx antennas are fixed with no change in their angular orientation.	• The tag is moving along the positive direction of the "X-axis", approaching the Tx/Rx location • x_R and x_T are variables $0 \leq x_R = x_T \leq 4m$	Full-Anechoic Chamber (Fig.33 and Fig.40)
B	• Tx, Rx and Tag are aligned. • $x_{T0} = 0.5m$ • $\theta = \theta_R = \theta_T = 0$ • $d = 4.5m$ • Face-to-face orientation of Tx and Rx antennas • Tx and Rx antennas are fixed with no change in their angular orientation.	• The tag moves along the negative direction of the "X-axis", approaching the Rx location • $0.5m \leq x_T \leq 4m$ • x_R and x_T are variables	Full-Anechoic Chamber/ Semi-Anechoic Chamber (Fig.34, Fig 35 and Fig. 41)
C	• Tx, Rx and Tag are dislocated. • $x_{T0} = 2.5m$ • $x_{R0} = 4m$ • $d = 4.5m$ • Face-to-face orientation of Tx and Rx antennas • Tx and Rx antennas are fixed with no change in their angular orientation.	• The tag moves along an oblique path relative to the "Y-axis" approaching the Rx location • $0.5m \leq x_R \leq 4m$ • x_T is variable • θ_T is variable (θ_R is constant)	Full-Anechoic Chamber Semi-Anechoic Chamber (Fig. 36, Fig. 37, and Fig. 42)
D	• Tx, Rx and Tag are dislocated. • $x_{T0} = 4m$ • $x_{R0} = 1.6m$ • $d = 4.5m$ • Tx and Rx antennas are fixed • No change in the angular orientation of Tx • Face-to-face orientation of Tx and Rx antennas	• The tag moves along the positive direction of the "X-axis", approaching the Tx location • $0.5m \leq x_T \leq 4m$ • x_R is variable • θ_R is variable (θ_T is constant) • The angular orientation of Rx is varied between 30° and 75° relative to the vertical line connecting the Tx and Rx	Semi-Anechoic Chamber (Fig.38, Fig. 43, Fig. 44)
E	• Tx, Rx and Tag are dislocated. • Positions of Tx, Rx and Tag are fixed. • $x_{T0} = 4m$ • $x_{R0} = 2m$ • $d = 4.5m$ • Tx and Rx angular orientations are facing the tag • No change in the angular orientation of Tx	• The Rx angular orientation is adjusted from 30° to 75° relative to the vertical line between the Rx and the tag.	Semi-Anechoic Chamber (with and without additional absorbers) (Fig. 39 and Fig. 45)

Table 7. Summary of the measurement setups

4.2. Measurement Environments

In this section, we present the received backscatter signal power measured under various controlled environments to assess the performance of the proposed backscatter system. Particular attention is given to the influence of key measurement parameters, including the orientation of the Rx antenna in the semi-anechoic environment, as well as the geometric configuration defined by the values of x, θ, and d.

The experimental measurements were in two distinct anechoic environments: full and semi-anechoic chambers with different dimensions. The experimental setup follows a bistatic backscatter configuration, where the transmitter (Tx) and receiver (Rx) are spatially separated, with the backscatter tag positioned between or near them depending on the test scenario More clearly, the Rx is composed of a Spectrum Analyzer and an antenna. The Tx is composed of RF generator and an antenna. The QRH400 wide-band horn antenna (400 MHz–6 GHz, RFspin, Czech) [13] having a maximal gain of 12.3 dBi gain at 3.5GHz is used as the Tx antenna. Its gain decreases with angular deviation, particularly beyond ±30°, consistent with a typical −3 dB beamwidth of 50°–60°. The antenna supports dual linear polarization and maintains a VSWR

below 2.3 across its operational band. This antenna is connected to a SMT06 signal generator (Rohde & Schwarz), which generates a CW signal centered at 3.5 GHz, corresponding to the 5G n78 band. While the CW signal does not include 5G modulation, it emulates the carrier frequency of 5G transmissions, enabling controlled evaluation of backscatter performance under realistic spectral conditions.

A directional wide-band horn antenna (SAS-571 Double Ridge Guide Horn Antenna, 700 MHz–18 GHz, A.H. Systems, Inc., CA, USA) [14] with a gain of 12 dBi is used as the Rx antenna. At 3.5 GHz, the gain is estimated between 6 dBi and 12 dBi. The typical −3 dB beamwidths are approximately 48° in the E-plane and 30° in the H-plane. The backscatter tag features a dipole antenna with a gain of 5 dBi, responsible for reflecting the incident signal by alternating its load impedance, enabling backscatter communication. This Rx antenna is connected to the spectrum analyzer Keysight FieldFox Microwave Analyzer [15].

The positioning of the signal generator and the spectrum analyzer varied depending on the measurement environment. In the full anechoic chamber, both devices were placed outside the chamber to minimize internal interference and to maintain the integrity of the controlled environment. In contrast, for the semi-anechoic chamber, the signal generator and the spectrum analyzer were positioned inside the chamber to account for potential reflections and to simplify cable management, especially during tests that involved adjusting the Rx antenna deviation angle.

All antennas, including the Tx, Rx, and Tag, were positioned at a uniform height of 1.1 meters, with a fixed distance of 4.5 meters between the Tx and Rx antennas. The entire setup maintained vertical polarization throughout the measurements to ensure consistency. A summary of all key measurement parameters, including carrier frequency, transmitted power levels, antenna gains, cable losses, antenna heights, and polarization settings, is provided in Table 8.

Parameters	**Unit**	**Value**
Carrier frequency	GHz	3.5
Transmitted power P_{Tx}	dBm	0
G_{Tx} / G_{Tag} /G_{Rx} antenna gain (maximum)	dBi	12.3/5/12
Tx/Rx/Tag antenna height	m	1.1/1.1/1.1
Tx-Rx distance (d)	m	4.5
Polarization	-	Vertical

Table 8. Measurement setup parameters

4.2.1. Collocated Measurement Setup in Full Anechoic chamber (Setup A)

The experimental validation of the bistatic collocated backscatter communication system was performed inside a full anechoic chamber, as shown in Figure 33. This chamber provides a controlled, reflection-free environment that complies with electromagnetic measurement standards, ensuring reliable measurement conditions. In this setup, the transmitter (Tx) and receiver (Rx) antennas are placed in close proximity in a fixed configuration, forming a collocated bistatic arrangement. To investigate the effect of the Tx-tag distance on the received backscatter power, the tag was moved along a straight line over a 4-meter range, as depicted in the schematic diagram (Figure 32.a). At each position, the received backscatter power at the Rx was measured.

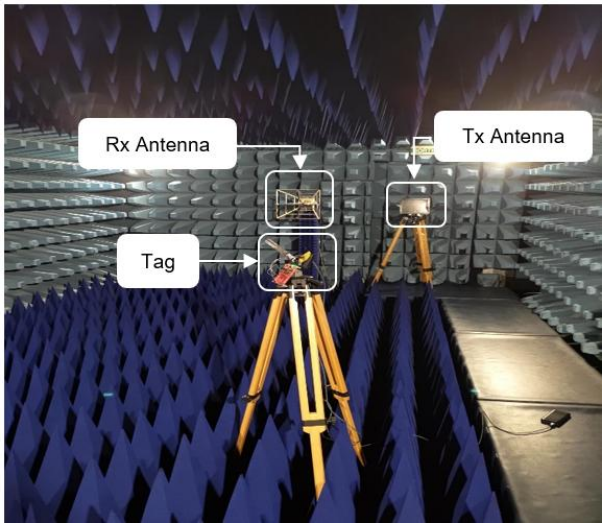

Figure 33. Collocated Measurement Setup in Full Anechoic Chamber (Setup A).

4.2.2. Aligned Measurement Setup in Full and Semi Anechoic Chambers (Setup B)

This configuration (Figure 32.b) was tested in both full and semi-anechoic chambers (Table 8). The full anechoic environment ensures reflection-free conditions, while the semi-anechoic chamber introduces controlled ground-plane reflections, simulating more realistic propagation scenarios.

In both environments, the Tx, tag, and Rx antennas were aligned along a common axis to establish a clear line-of-sight (LOS) configuration. The tag was positioned between the Tx and Rx, and a horn antenna was used to focus the transmitted signal toward the Rx.

In contrast, the semi-anechoic chamber (Figure 35) features RF absorbers on the walls and ceiling, while the floor remains reflective, typically made of conductive material such as metal to simulate ground plane conditions.

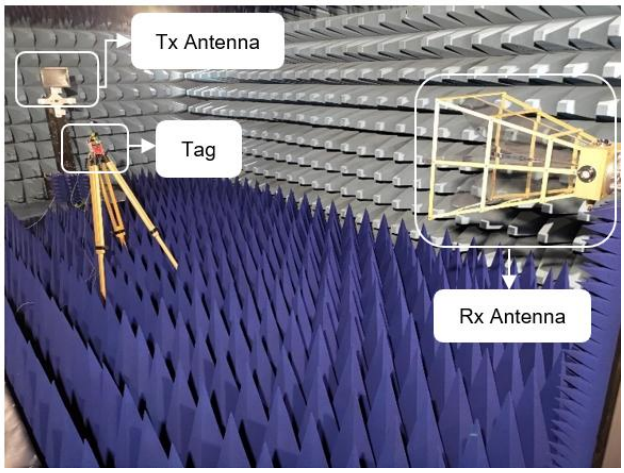

Figure 34. Aligned Experimental Setup in Full-Anechoic Chamber (Setup B).

This configuration is particularly useful for evaluating real-world scenarios where ground reflections are present. The same alignment of Tx, Rx, and tag antennas was maintained in the semi-anechoic environment to allow direct comparison with the fully anechoic results. While the LOS path remained intact, the presence of floor reflections introduced controlled multipath components, enabling the assessment of their influence on system performance. Using both chamber types provides a comprehensive understanding of antenna behavior and signal propagation under ideal free-space conditions as well as more practical environments with partial reflections.

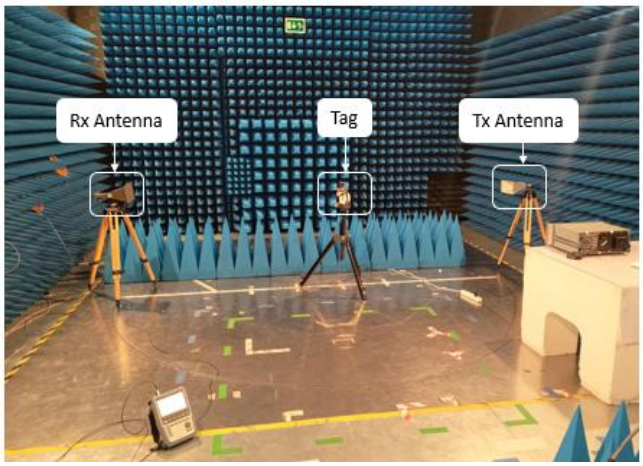

Figure 35. Aligned Experimental Setup in Semi-Anechoic Chamber (Setup B).

4.3. Dislocated Measurement Setup in Semi and Full Anechoic Chamber With Fixed Angles of Tx and Rx (Setup C)

The experimental configuration is based on a bistatic dislocated setup comprising a transmitter (Tx), a backscatter tag, and a receiver (Rx), with antenna positioning adjusted according to the chamber type (full or semi-anechoic). Figure 36 and 37 illustrate the specific

configurations used to characterize the system in both environments. The backscatter tag is located between the transmitter and receiver and can move along a predefined vertical path referred to as the Path of Tag (PT). By following PT, the angle θ_T and the distances x_T and x_R are variable while θ_R keeps constant. This path allows the tag to occupy various positions, ranging from proximity to the transmitter to proximity to the receiver. The vertical separation between the Tx and Rx is marked by evenly spaced dashed lines, with a total distance of 2.5 meters (Figure 37).

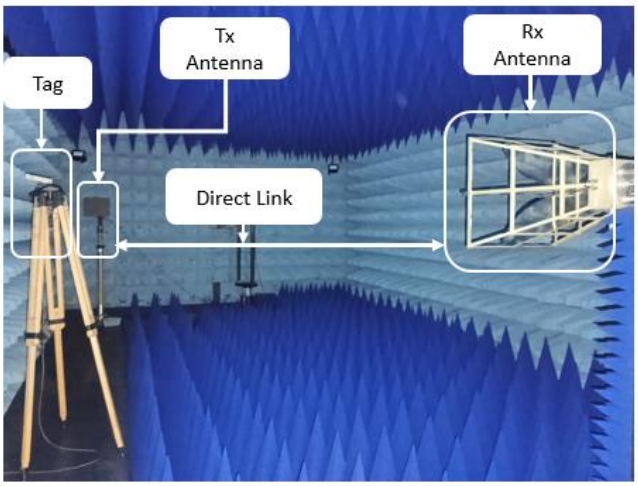

Figure 36. Dislocated Experimental Setup in Full-Anechoic Chamber with Fixed Angles of Tx and Rx (Setup C).

The experimental setup enables analysis of the influence of the tag's position on the received backscatter signal power. In particular, measurements were performed at several fixed positions as the tag was linearly moved along a trajectory from 4 m to 0.5 m away from the Rx, while maintaining a constant angle θ_R relative to the Rx (Table 7). The objective is to evaluate how proximity to either the transmitter or receiver affects the overall system performance, specifically in terms of the received signal power and potential interference from the direct link.

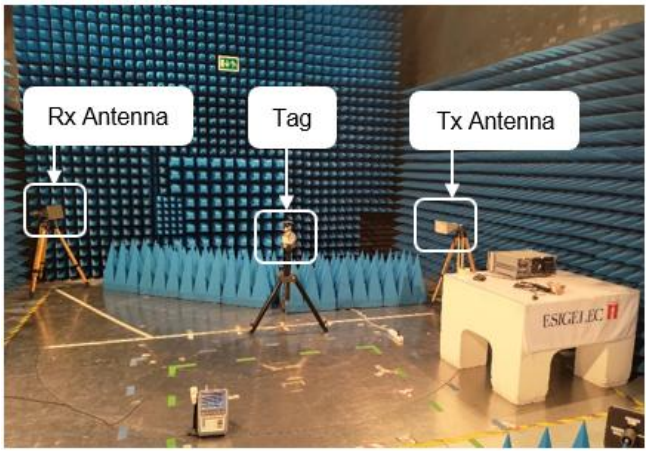

Figure 37. Dislocated Experimental Setup in Semi-Anechoic Chamber with Fixed Angles of Tx and Rx (Setup C)

The inclusion of floor-mounted RF absorbers, along with wall and ceiling treatments, ensures effective suppression of undesired reflections particularly those from the ground thus providing a controlled propagation environment.

4.4. Dislocated measurement setup in semi-Anechoic Chamber With Variable Rx Angle (Setup D)

In this setup, the impact of the Rx antenna's angular orientation on the received backscattered signal strength is investigated. As shown in Figure 38, the transmitter and receiver are separated by a fixed distance of 4.5 meters, forming a direct communication link. A backscatter tag is moved along a predefined horizontal line positioned between the Tx and Rx, with a lateral offset of 4 meters from the transmitter. The receiver is placed 1.6 meters away from this line to capture the backscattered signal. To investigate the influence of angular orientation of the Rx antenna on signal strength, the experiment is conducted under varying angular configurations, specifically at 30°, 45°, 60°, and 75°, as shown in Figure 38. When the tag moves linearly, θ_R, x_T and x_R are variable while θ_T keeps constant this time. This setup facilitates a comprehensive analysis of the system's performance under different geometric and environmental conditions.

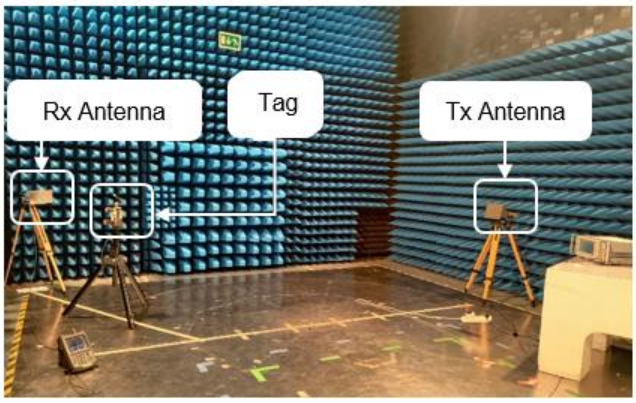

Figure 38. Dislocated Experimental Setup in Semi-Anechoic Chamber with Variable Rx Antenna (Setup D)

4.5. Dislocated Measurement Setup in Semi-Anechoic Chamber With Tx and Rx at 0° Relative to Tag (Setup E)

Figure 32.e illustrates a specific positioning of the backscatter tag, where the transmitter (Tx) and receiver (Rx) are placed 4 meters apart in a 90° configuration of the tag.

By orienting their main lobes orthogonally, this geometry should minimize the direct link between Tx and Rx. To mitigate residual reflections and enhance the measurement accuracy,

additional RF absorbers were later introduced near the Rx antenna. This configuration is depicted in Figure .39

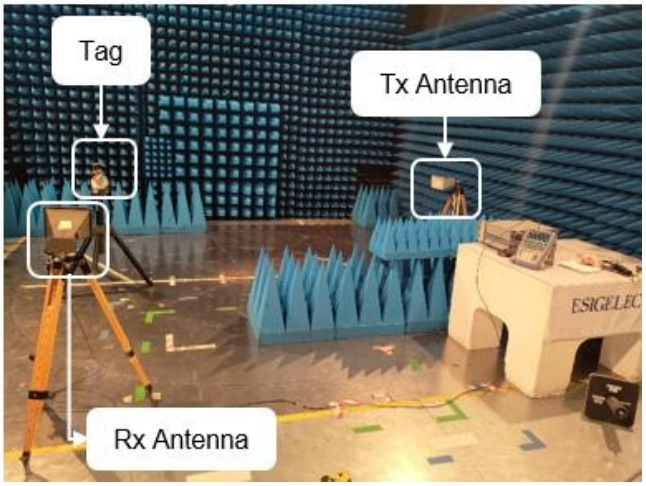

Figure 39. Dislocated Experimental Setup in Semi-Anechoic Chamber with Tx and Rx Antennas at 0° Relative to Tag. (Setup E)

5. Results and discussion

5.1. Set-up A results discussion

Figure 40 presents the measured results and the theoretical prediction of the received backscatter power as a function of the Tag-Rx distance in the bistatic collocated setup described in Section 4.

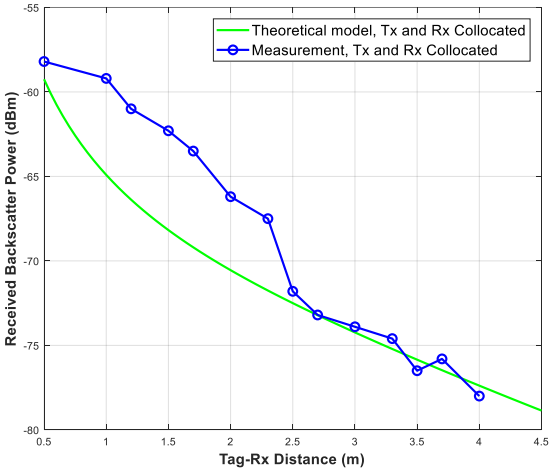

Figure 40. Theoretical and Measured Received Backscatter Power for Co-Located Experimental Setup (Setup A)

The green curve illustrates the theoretical prediction, while the blue curve corresponds to the experimentally measured data. Both curves exhibit a clear downward trend, indicating that the received backscatter power decreases as the Tag-Rx distance increases due to increased path loss. While the theoretical model provides an idealized prediction of the system's behavior, the

measured results closely follow the same trend, with minor deviations. These discrepancies are attributed to practical non-idealities such as hardware imperfections, slight misalignments, and environmental noise within the measurement setup. Coupling effects between Tx, Rx antenna on the one hand and Tag antenna on the other hand especially for small distances should be also responsible of these discrepancies. The consistency between theoretical prediction and measurement validates the reliability of the proposed system model and confirms the expected attenuation behavior in the bistatic collocated configuration.

5.2. Set-up B results discussion

Figure 41 presents the measured received backscatter power as a function of the Tag-Rx distance, obtained under two distinct measurement environments: full anechoic and semi-anechoic chambers. The results show a general downward trend as distance increases. In the full anechoic chamber, the received power exhibits a gradually decreasing pattern, closely following free-space path loss behavior. Conversely, the semi-anechoic chamber introduces partial ground-plane reflections, resulting in observable fluctuations in the received power. These irregularities can be attributed to multipath propagation and interference effects, which are more pronounced in the semi-anechoic environment.

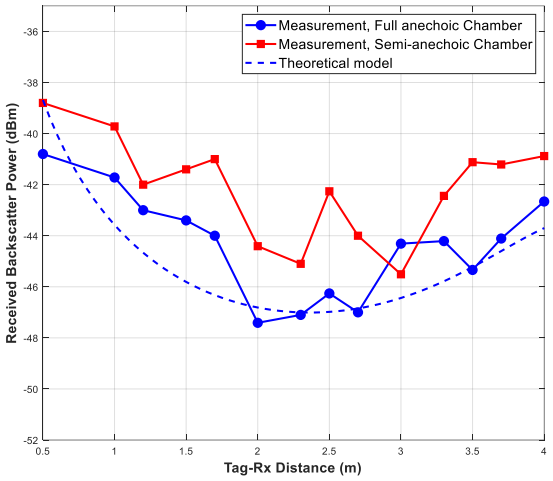

Figure 41. Comparison of Received Backscatter Power in Full and Semi-Anechoic Chambers for Aligned Experimental Setup (Setup B)

The subsequent increase in power suggests a shift toward constructive interference or improved reception conditions. The Tx, Rx and the tag are aligned with a face-to-face arrangement of their antennas. This configuration ensures that the maximum antenna gains are utilized in the theoretical model (12.3 dBi for the transmitter, 12 dBi for the receiver). The measured received power values as a function of the Tag–Rx distance closely follow the model, with data points distributed around the theoretical curve. This alignment supports the consistency and validity of the measured results in relation to the theoretical predictions.

The initial analysis focuses on the direct link, the signal path between the Tx and Rx antennas without the backscatter tag present, which represents the strongest received signal and serves as a baseline for evaluating the backscattered signal strength. In the full anechoic chamber, the received power was measured at -45.8 dBm, while in the semi-anechoic chamber, it was slightly higher at -43.66 dBm. The Free Space Path Loss (FSPL), calculated as 56.39 dB using Equation (25), provides a reference for ideal signal attenuation.

$$FSPL(dB) = 20log_{10}\big(f(MHz)\big) + 20log_{10}\big(d(m)\big) - 27.55 \quad (25)$$

5.3. Set-up C results discussion

Figure 42 presents a comparison of the received backscatter power measured in three distinct environments: Full Anechoic, Semi-Anechoic without ground absorber (Mes1), and Semi-Anechoic with ground absorber (Mes2). The Full Anechoic setup, characterized by the presence of absorbers on all surfaces (walls, ceiling, and floor), exhibits the most stable and consistent backscatter power levels, averaging around -52 dBm across all distances. In contrast, the Semi-Anechoic Mes1 configuration, which lacks a ground absorber, demonstrates significantly higher received power levels (ranging from approximately -44 dBm to -48 dBm). This increase is attributed to the reflective nature of the untreated ground surface, which introduces additional multipath components. These reflections contribute to constructive interference at certain distances, resulting in observable fluctuations in the received power. The Semi-Anechoic Mes2 environment, where a ground absorber is employed, exhibits reduced power levels compared to Mes1, with values close to those observed in the full anechoic case. The presence of the ground absorber effectively mitigates floor reflections, minimizing multipath effects and leading to more stable measurements.

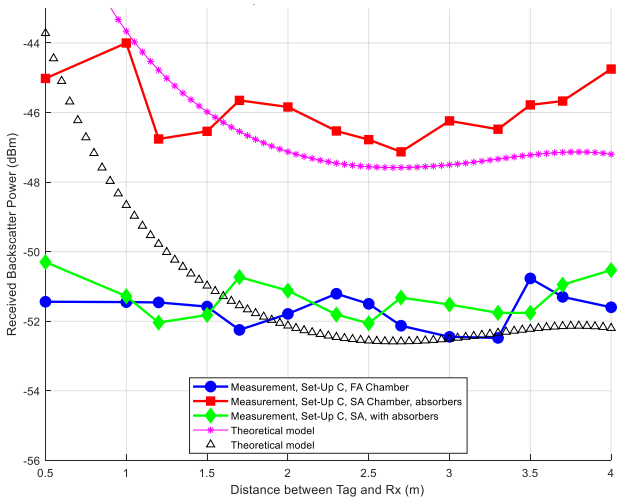

Figure 42. Received Backscatter Power for Dislocated Experimental Setup with Fixed Angles of Tx and Rx in Full and Semi-Anechoic Chambers (Setup C).

When the Rx antenna is positioned at 30°, it is more aligned with the direct and reflected signals, resulting in higher received power, often overshadowing the tag's role in modulation. As the Rx angle increases to 60° and 75°, the alignment shifts, causing the Rx antenna to be more misaligned with the Tx and tag, reducing the effective received power. This effect is particularly noticeable at 75°, where the Rx antenna's face is slightly turned away from the Tx and tag, leading to higher path loss and weaker backscatter signals.

5.4. Set-up D results discussion

Figure 43 illustrates the measured backscatter power as a function of the Tag-Tx distance, with different Rx antenna angles (30°, 45°, 60°, and 75°). The dots represent experimental data, while the solid lines indicate parabolic curve, capturing the general trend of the received signal strength. The results highlight that the Rx antenna angle significantly affects the received backscatter power, with Rx = 30° yielding the highest power levels, followed by Rx = 45°, while Rx = 60° and 75° exhibit noticeable power degradation. This indicates that lower Rx angles provide better alignment with the reflected signal, whereas larger angles introduce misalignment and higher path loss, reducing reception efficiency. Additionally, the variations in received power across different distances suggest the influence of multipath effects, where constructive and destructive interference patterns cause fluctuations in signal strength. The parabolic curve demonstrates a nonlinear trend, confirming that the backscattered signal is influenced by both direct and reflected paths. Figure 44 compares the theoretical model with the measured values of the power as a function of the distance Tag-Rx and the geometrical angle θ when the tag movens linearly from the initial position ine the direction of Tx (Setup D). We can see that the trend of the different curves is the same even if there is a shift in the values of the power.

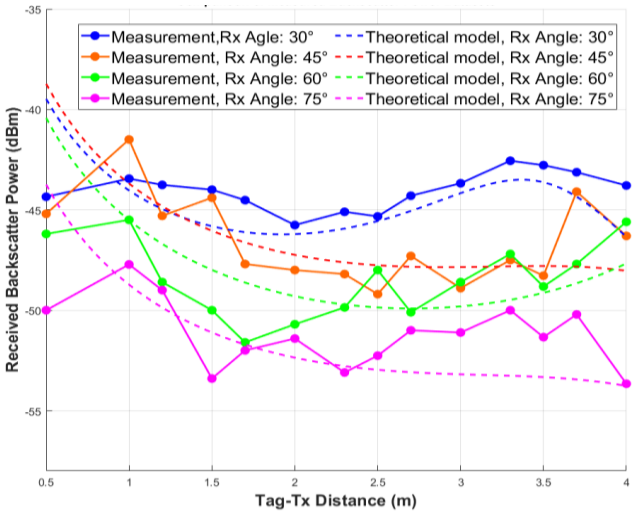

Figure 43. 2D Plot of Measured Received Backscatter Power for Dislocated Experimental Setup with Variable angle Tag referred to Rx. (Setup D).

Notably, at Rx = 30°, the received power is significantly high, suggesting that the tag's role in modulation becomes less dominant, as the received signal is likely dominated by the direct and reflected paths from the surrounding environment. Conversely, when the Rx antenna is positioned at 60° and the Tx-tag distance reaches 4 meters, the face of the Rx antenna is slightly oriented away from the Tx and tag, further reducing the received power due to poor alignment with the incoming backscatter signal. However, a shift was observed and compensated. Indeed, in the measurement part, we take into account RCS parameter as well as the potential effect of ground, reflections, and the potential effect of the direct path and its constructive interference with the backscattered signal to calibrate the constant K defined in the theoretical model (equation (7)). We observed that, for each set-up, the overall trend for spatial variation is the same in theory and measurement. A shift of 15 to 25dB is observed each time. Uncertainties about angles, antenna gains, etc. could also explain this shift. Finally, in short distances, we observed that the model increases fast however, the measurements show that the values of the power do not increase, which could be explained by coupling effect which is stronger in short distances.

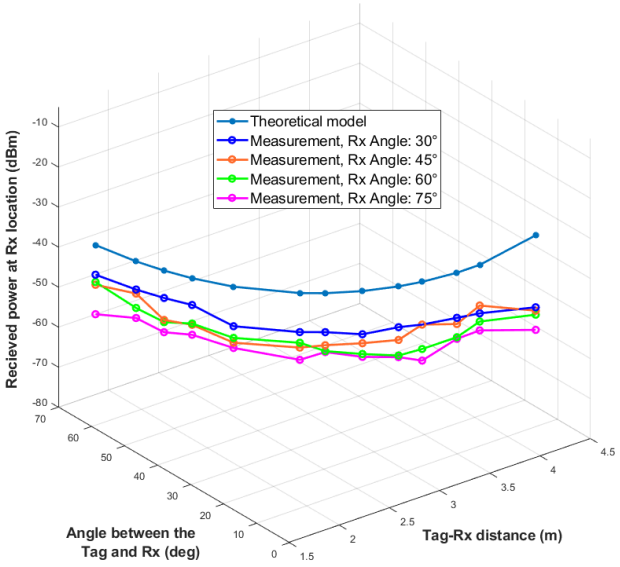

Figure 44. 3D Plot of Measured Received Backscatter Power for Dislocated Experimental Setup (Setup D) with as function of the geometrical angle θ and the distance Tag-Rx (variable x in the model)

5.5. Set-up E results discussion

Figure 45 presents the variation of the received backscatter power as a function of the Rx antenna angle in Setup E, comparing the Tag ON and Tag OFF conditions. The results show a gradual increase in received power from 0° to around 30°–40°, followed by a decrease beyond 60°, consistent with the alignment between the Rx antenna and the tag. At 0°, the Rx antenna

orientation is poorly aligned with Tx, resulting in lower power. The peak around 30°–40° corresponds to improved alignment with the backscattered signal. The power difference between the Tag ON and Tag OFF states at 0° is 2 dB, calculated as (52 – 50) dBm, indicating the tag's contribution to the received signal. This differential measurement provides experimental validation of the tag's modulation capability. While a standalone characterization of the tag is not included, the ON/OFF power comparison under various angular conditions confirms that the tag effectively modulates and reflects the incident signal, with measurable influence on the received power.

.

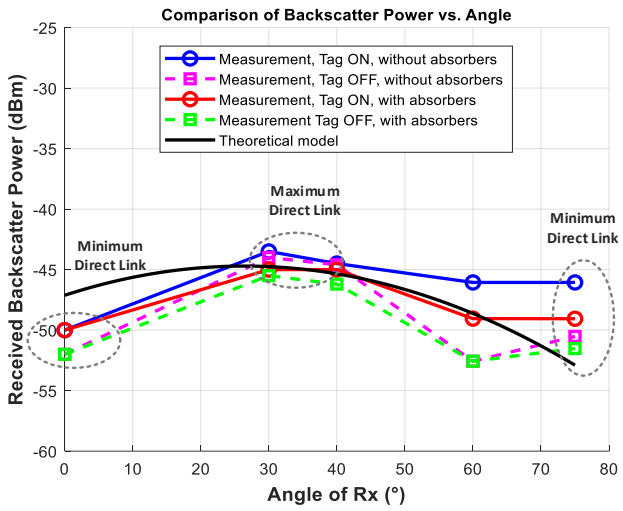

Figure 45. Comparison of Received Backscatter Power (for Tag ON and Tag OFF States) in Dislocated Experimental Setup with Tx and Rx at 0° Relative to Tag without absorber (Setup E).

While the results presented in Figure 45 follow a consistent trend up to 50◦, unexpected fluctuations in the received power in this range is observed and can be attributed to the presence of the signal generator and other measurement equipment positioned near the Rx antenna. These objects introduce unintended reflections, obstructions, and potential interferences, affecting the accuracy of the backscatter signal measurements.

To improve the test setup and mitigate these disturbances, additional RF absorbers were introduced near the Rx antenna. In fact, Figure 45 illustrates the improvement in received backscatter power measurements after the addition of RF absorbers in the experimental setup. Compared to the previous results, where significant fluctuations were observed beyond 50◦ due to interference from surrounding equipment, the new measurements show a more stable and expected trend across different Rx angles when compared to the theoretical model, (taking into account the angular Rx antenna gain variation). With the absorbers in place, unwanted

reflections and multipath interference have been minimized, ensuring that the received signal primarily originates from the intended backscatter path rather than external reflections. This improvement is particularly evident beyond 50◦, where the received power now follows more predictable decline, rather than the sharp drop seen in the previous measurements. Additionally, the difference between the Tag ON and Tag OFF conditions remains consistent, reinforcing the tag's role in enhancing backscatter signal strength. The improvement validates the effectiveness of absorber placement in reducing measurement anomalies, providing a more accurate and reliable assessment of backscatter communication performance at different Rx angles.

5.6. Discussion on the performances of BPSK AmbC 5G-NR in Bi-Static Configuration

This section builds on the previous analysis of backscattered signal power to evaluate the performance of a 5G-NR backscatter communication system at 3.5 GHz. Using the developed propagation model, we estimate the received SNR, achievable data rate with BPSK modulation, and expected communication range under a fixed BER constraint of 10^{-5}. The SNR is derived from the predicted received power, taking into account the system bandwidth and the receiver's noise figure (NF). The impact of bandwidth on both SNR and range is also examined, based on theoretical and experimental propagation results across various deployment scenarios.

5.6.1. The received SNR

The received *SNR (*in dB) is computed using the following equation (26):

$$SNR_{dB} = P_R(dBm) - 174 + 10\log(B) - NF \qquad (26)$$

For the 5G-NR, B take specific values ranging from 5MHz to 100 MHz. We will consider: $B_1 = 5\text{MHz}$ and $B_2 = 20\text{MHz}$. Similarly, particular values of *NF* are $NF_1 = 8dB$ and $NF_2 = 5dB$. These are typical values that are used in literature for 5G-AmBC systems or in deployed 5G systems and receivers [16] Under these conditions, for fixed values of B and NF the variable received power $P_R$will be decisive for the value of SNR_{dB}.

By introducing the expression of P_R, SNR will be a function of the spatial parameters (angle and distance either to Tx or Rx) and physical and system parameters:

$$SNR_{dB}(x,\theta) = P_T + G_T + G_R + 2G_S - 10\log(x^2) - 10\log\Big((x-d)^2 + 2xd\big(1 - cos(\theta)\big)\Big) + 40\log\left(\frac{c}{4\pi f}\right) - 174 + 10\log(B) - NF \qquad (27)$$

where only x and θ are variable and the other fixed parameters are $P_T = 0dBm$, $G_T = 12dBi$, $G_R = 12dBi$, $G_S = 5dBi$ and $d = 4.5m$.

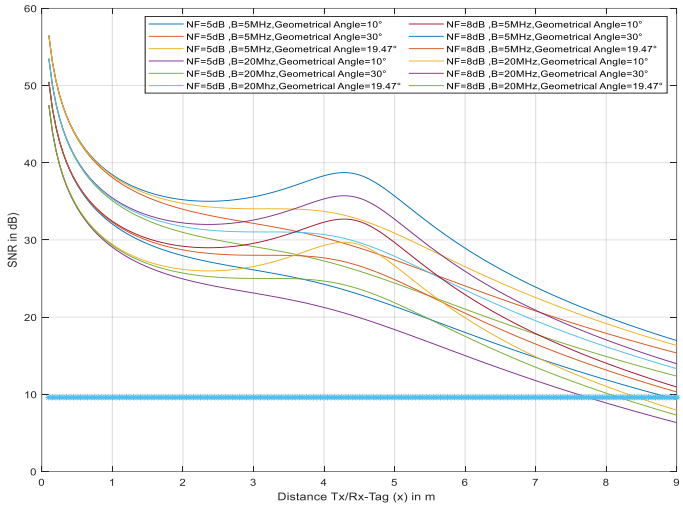

Figure 46. Simulation result of the SNR

For BPSK modulation, the signal-to-noise ratio in linear scale is $SNR_{lin} = \frac{E_b}{N_0}$, where E_b is energy per bit and N_0 is the noise power spectral density. At a

At a fixed BER target (i. e., 10−5), the minimum required ratio $\left(\frac{E_b}{N_0}\right)_{dB}^{min}$ remains constant (equation (28)).

$$\left(\frac{E_b}{N_0}\right)_{dB}^{min} = 10\log\left(\frac{1}{2}[Q^{-1}(10^{-5})]^2\right) = 9.6dB \qquad (28)$$

Where $Q(10^{-5}) = \frac{1}{\sqrt{2\pi}}\int_{10^{-5}}^{\infty} e^{\frac{-t^2}{2}} dt$ represents the error probability over an additive white Gaussian noise at the given BER threshold.

Figure 46 illustrates the monotonic behavior of SNR_{dB} as a function of the NF, B and the geometric angle θ. It is evident that NF and B do not directly affect the monotonicity of the SNR_{dB} curve, although increasing their values leads to an overall reduction in SNR_{dB}. In contrast, the angle θ plays a significant role in shaping the monotonic trend, with a noticeable change occurring at a critical angle $\theta_{lim1} = 19.47^{\circ}$. Moreover, as the distance between the receiver/transmitter and the tag increases, the SNR_{dB} drops below the critical threshold of 9.6 dB. These specific distances, along with the corresponding NF, B and θ values, define the boundary conditions for ensuring reliable communication, as constrained by the maximum tolerable BER.

5.6.2. Binary Data Rate

The achievable data rate R_b with BPSK modulation is given by equation (29):

$$R_b = 10^{(P_R(dBm) - SNR_{dB} - 174)/10} \qquad (29)$$

Simulation results in Figure 47 show that typical values of some hundreds of Mbps were observed for short distances implying strong values of $P_R(dBm)$. Similarly, data rate monotonicity depends on the geometrical angle θ as previously observed in results presented in Figure 27 and Figure 46. Greater data rates are detected for angles values smaller than θ_{lim1}.

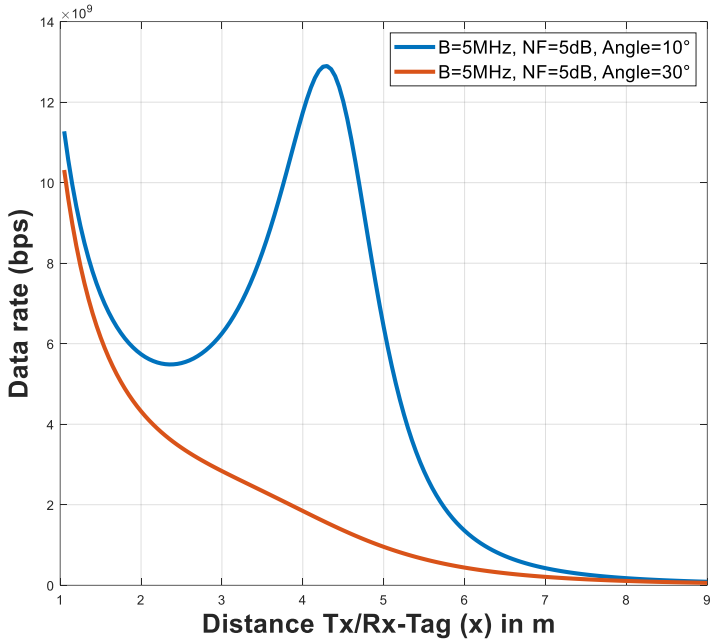

Figure 47. Simulation result of the binary data for two different geometrical configurations of the tag.

5.6.3. Discussion on Sensitivity and communication range

The receiver sensitivity SENS (dBm) is expressed in terms of the minimum required $SNR_{dB}^{min} = 9.6dB$ to maintain a target$BER = 10^{-5}$ as presented in (30):

$$\text{SENS}(dBm) = -174 + 10\log(B) + NF(dB) + SNR_{dB}^{min} \quad (30)$$

The chosen value of BER implies $SENS(dBm) = -99.4dBm$ for$NF = 5dB$ and $B = 1$MHz. The condition sensitivity consists on considering the equation (31).

$$P_R^{lin}(x,\theta) = SENS^{lin} \quad (31)$$

Where $P_R^{lin}(x,\theta)$ and $SENS^{lin}$ are respectively the received power and the sensitivity in linear scale.

If we keep only the variable terms with x and θ and define C as a general constant including all the other constants in the expression of $P_R^{lin}(x,\theta)$ referring to equation (7), then we will obtain the equation (32):

$$x^2\left(x^2 + d^2 - 2xd\cos(\theta)\right) = \frac{C}{SENS^{lin}} \quad (32)$$

It is not easy to solve analytically this equation since it deals a 4th degree polynomial. It could be achieved numerically. All the pairs (x, θ) could be found numerically by simulation.

In conventional communication systems, the communication range is defined as the maximum distance at which the received power remains above the sensitivity threshold. This implies a monotonic decrease of P_R^{lin} with distance. However, in bistatic backscatter communication, the received power depends jointly on distance and angle, and exhibits non-monotonic behavior due to the product of two distance-dependent terms $x_T.x_R$. As a result, the communication region may include non-contiguous zones where communication is possible, separated by "dead zones" where $P_R < SENS$. This behavior challenges the classical notion of range and calls for a redefinition based on the angular and geometric coverage domain rather than a single radial threshold.

Even if it is analytically difficult to solve the equation leading to the sensitivity condition, it is possible to find the region of communication geometrically. Indeed, the equation (32) is equivalent to $x_T.x_R = \sqrt{C/SENS^{lin}}$. This means, the limit of the coverage region in bistatic backscatter systems can be geometrically interpreted as a Cassini oval whose ovals are Tx and Rx. This provides a compact geometrical characterization of the coverage boundary in bistatic configurations and reveals the possible presence of disconnected or non-convex coverage zones depending on the system parameters.

This implies that, paradoxically, a tag located close to the receiver may not be detected if it lies at a certain angle, whereas another tag positioned much farther away but at a more favorable angle can still be successfully detected.

6. Conclusion

This chapter has presented the complete design, theoretical modeling, and experimental validation of a 5G-NR-based ambient backscatter communication (AmBC) system operating in a bistatic configuration. The system was evaluated through a series of controlled measurements conducted in both full anechoic and semi-anechoic environments, with particular attention to key parameters such as the spatial deployment of the nodes, Rx antenna orientation, and the influence of environmental reflections on backscatter signal strength.

The results confirmed the predictive accuracy of the proposed analytical model, especially in scenarios involving different angular alignments and tag positions. While the full anechoic chamber offered a stable propagation environment with minimal interference, the semi-anechoic chamber introduced realistic multipath effects, which in some cases enhanced the backscattered signal power due to constructive interference. Moreover, it was demonstrated that

the orientation of the receiver antenna plays a critical role in capturing the modulated signal efficiently, with certain angles yielding significantly to higher reception quality.

To mitigate reflections from surrounding equipment and improve the reliability of the measurements particularly at higher Rx angles RF absorbers were strategically introduced, leading to more consistent and predictable signal behavior. These observations underscore the importance of environmental control and hardware alignment in optimizing AmBC performance.

The comprehensive evaluation conducted in this chapter confirms the feasibility of using bistatic AmBC systems powered by 5G ambient signals for low-power wireless communication applications. The modular design and energy-efficient operation of the proposed tag architecture further reinforce its potential for real-world deployment in sensing and IoT contexts.

Building on these findings, Chapter 4 will present the implementation of a real-time signal acquisition and decoding chain using a USRP B210 software-defined radio (SDR) platform. This next stage of experimentation aims to enhance the system's capability for practical data collection, live demodulation, and adaptive analysis under dynamic propagation conditions, including outdoor environments. The objective is to assess the viability of ambient backscatter communication in more realistic scenarios, with a focus on healthcare monitoring and smart sensing applications.

References

[1] M. Lefki, S. Baccar, H. Shall, M. Ghorbel, and M. Kadi, "5G Ambient Backscatter Communications: Achievable Range and Power Levels in an Urban Environment," in 2022 IEEE 12th International Conference on RFID Technology and Applications (RFID-TA), 12-14 Sept. 2022 2022, pp. 74-77, doi: 10.1109/RFID-TA54958.2022.9924037.

[2] M. Lefki, S. Baccar, H. Shall, M. Ghorbel, and M. Kadi, "A First Prototype of an Ambient Backscatter Communication Tag Working in 5G-NR Frequency: Experimental Test and Power Levels Measurements," in *2024 IEEE 14th International Conference on RFID Technology and Applications (RFID-TA)*, Dec. 2024, doi: 10.1109/RFID-TA64374.2024.10965177.

[3] M. Lefki, M. S. Saha, S. Baccar, M. Kadi, H. Shall and M. Ghorbel, "Bistatic 5G-NR Ambient Backscatter Communication: Propagation Study and Experimental Validation in Anechoic Chambers," in IEEE Journal of Radio Frequency Identification, doi: 10.1109/JRFID.2025.3587632.

[4] Texas Instruments. (2015). MSP430FR5969 LaunchPad Development Kit, Product Manual. [Online]. Available: http://www.ti.com/lit/ug/ slau535b/slau535b.pdf

[5] LM335 High Precision Analog Temperature Sensor, product manual, Texas Instruments, 2015.

[6] Analog Devices. (2005). ADG902 RF Switch, Product Manual. [Online]. Available: http://www.analog.com/media/en/technical-documentation/ data-sheets/ADG901_902.pdfJ

[7] TE Connectivity, ANT-5GW-FPC-LH Series Flexible Embedded Cellular Sub-6 5G Antennas, Datasheet. [Online]. Available: https://docs.rs-online.com/bb5d/A700000009613541.pdf

[8] M. Alhassoun, "Spectrally Efficient Backscatter Systems: A Hardware-Oriented Survey," IEEE Access, vol. 11, pp. 8332-8344, 2023, doi: 10.1109/ACCESS.2023.3237941.

[9] C. C. Yen, A. E. Gutierrez, D. Veeramani, and D. v. d. Weide, "Radar Cross-Section Analysis of Backscattering RFID Tags," IEEE Antennas and Wireless Propagation Letters, vol. 6, pp. 279-281, 2007, doi: 10.1109/LAWP.2007.898552.

[10] B. Badihi, A. Liljemark, M. U. Sheikh, J. Lietzén, and R. Jäntti, "Link Budget Validation for Backscatter-Radio System in Sub-1GHz," in 2019 IEEE Wireless Communications and Networking Conference (WCNC), 15-18 April 2019 2019, pp. 1-6, doi: 10.1109/WCNC.2019.8885700.

[11] B. Xie et al., "Flexible Thin Film Multi-Antenna Integrated Backscatter Device," in 2024 IEEE Wireless Communications and Networking Conference (WCNC), 21-24 April 2024 2024, pp. 1-6, doi: 10.1109/WCNC57260.2024.10571338.

[12] C. A. Balanis, "Antenna Theory: Analysis and Design," Wiley, 2016,, vol. 4th ed., pp. 1195–1196, Hoboken, NJ, USA.

[13] A. K. Thyagarajan, P. Balasubramanian, D. Vydeki, and M. Karthik, "SNR-CQI Mapping for 5G Downlink Network," in Proceedings - 2021 IEEE Asia Pacific Conference on Wireless and Mobile, APWiMob 2021, 2021, pp. 173-177, doi: 10.1109/APWiMob51111.2021.9435258.

[14] Z. Cai, L. Liu, F. de Paulis, and Y. Qi, "Passive Intermodulation Measurement: Challenges and Solutions," Engineering, Review vol. 14, pp. 181-191, 2022, doi: 10.1016/j.eng.2022.02.012.

[15] L. M. YANG Yibing, XU Rongtao, WANG Gongpu, GONG Wei, "Link Budget and Enhanced Communication Distance for Ambient Internet of Things " ZTE Communications, vol. 22, no. 1, pp. 16-23, 2024. [Online]. Available: https://zte.magtechjournal.com.

[16] R. Biswas and J. Lempiäinen, "Assessment of 5G as an ambient signal for outdoor backscattering communications," Wireless Networks, vol. 27, no. 6, pp. 4083-4094, 2021/08/01 2021, doi: 10.1007/s11276-021-02731-x.

Chapter 4 : Receiver Configuration, Signal Processing, and Experimental Validation in Real Conditions for AmBC Communications Systems-Application for Healthcare Monitoring

1. Introduction

In this final chapter, we move from theoretical modeling to practical validation by conducting a comprehensive series of experimental investigations. The objective is to rigorously evaluate the performance and robustness of the proposed ambient backscatter communication system under both realistic and controlled environments. Building upon the system models and tag architectures introduced in previous chapters, this chapter focuses on the evaluation of key performance metrics, including received power levels, bit error rates (BER), sensor data recovery, and system behavior under various operational conditions.

To this end, a complete receiver setup was developed, centered on a USRP B210 software-defined radio and integrated within a GNU Radio signal processing framework. The system was tested in an anechoic chamber to ensure a low-noise environment, and experiments were conducted across multiple scenarios involving different tag prototypes, transmission parameters, and wireless channels.

Furthermore, two custom-designed, time-synchronized backscatter prototypes were implemented to enable real-time transmission of biomedical sensor data. These prototypes integrate medical sensors dedicated to physiological monitoring, such as temperature, heart rate, and oxygen saturation, to demonstrate the feasibility of healthcare-oriented backscatter applications. Their functionality and reliability were evaluated through dedicated experiments, including a detailed comparison between transmitted and received signals. Finally, the system's capability to extract backscattered information from ambient RF sources such as Wi-Fi and 5G transmissions was analyzed, demonstrating its applicability to opportunistic ambient sensing.

The chapter is structured as follows. Section II introduces the experimental receiver configuration and the signal processing chain implemented using GNU Radio. Section III provides detailed modeling and evaluation of the free-space pathloss in the bistatic configuration. Section IV presents the BER measurements obtained under various conditions and analyzes their impact on the reliability of the communication link. Section V then presents the implementation and testing of two time-synchronized sensor prototypes, with a particular focus on backscattered signal analysis and the effects of sample rate constraints. Section VI investigates the behavior of the backscattered signal when leveraging ambient RF sources,

including Wi-Fi and 5G base station emissions. Finally, Section VII concludes the chapter by summarizing the key experimental findings and discussing their implications for future ambient backscatter communication systems.

2. Experimental configuration for receiver performance evaluation

This section presents the experimental setup designed to assess the performance of the receiver subsystem within the bistatic ambient backscatter communication system developed in this work. The overall architecture consists of three main components: a transmitter (CW generator or ambient source), a backscatter tag, and a receiver. The transmitter module, located on one side of the setup, generates a continuous-wave (CW) signal at 3.5 GHz or emits ambient signals such as Wi-Fi or 5G, depending on the scenario. This signal is radiated via a dedicated Tx antenna into the environment. At the center of the setup, the backscatter tag reflects this incident signal toward the receiver by modulating its impedance states based on the sensor information to be transmitted. The tag's antenna captures the incoming wave and alters the reflection coefficient in real time through load modulation, thereby embedding data into the backscattered signal. On the receiving side, a USRP B210 platform is employed as the software-defined radio (SDR) front end [1], connected to a Rx antenna. The USRP captures both the direct CW or ambient signal and the modulated backscatter signal, and digitizes the received waveform for further analysis. This bistatic configuration allows the evaluation of signal strength and reliability under various RF excitation conditions and propagation environments, while maintaining consistent transmitter–tag–receiver geometry throughout all experiments. Figure 48 illustrates a simplified diagram of the receiver test setup, outlining the key components involved in the transmission, modulation, and reception processes.

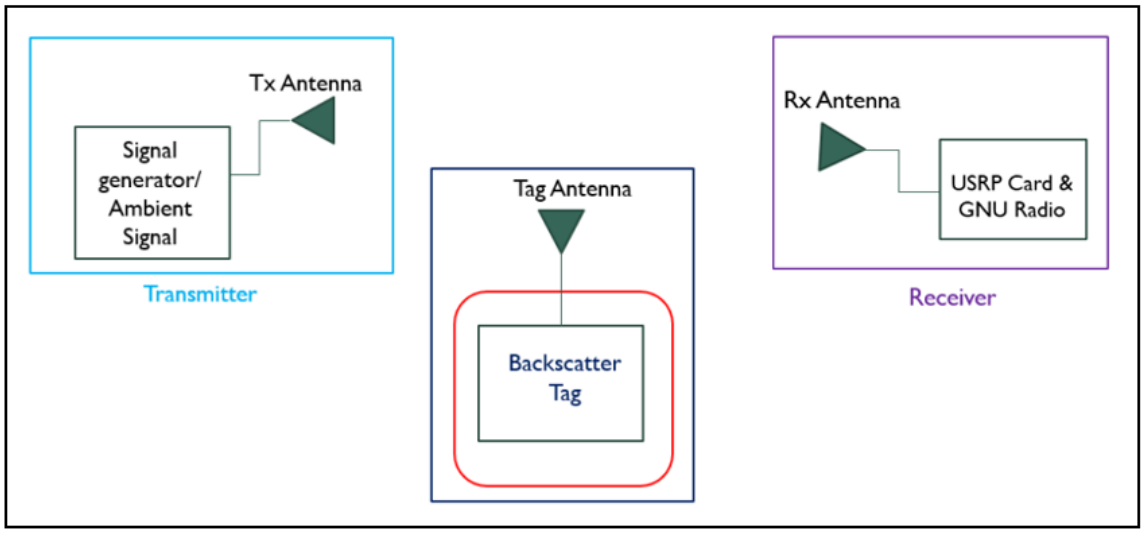

Figure 48. Experimental Setup for Receiver Performance Evaluation in a Backscatter System.

2.1. Block-Level Functionality in the GNU Radio Flowgraph

The signal reception and decoding processes are implemented using a custom flowgraph in GNU Radio. Within this framework, the USRP B210 serves as the receiving front end, capturing radio signals in real time. Thanks to its wide operating bandwidth, this SDR platform supports continuous reception over a frequency range from 70 MHz to 6 GHz. In the context of this study, the USRP is configured to operate at a center frequency of 3.5 GHz aligned with typical sub-6 GHz 5G signals with a sampling rate of 1 mega sample per second (1 MS/s). The input impedance of the receiving (Rx) channels is set to 50 Ω to match standard RF system requirements.

The overall structure of the implemented signal-processing chain is illustrated in Figure 49, which shows the main functional blocks of the real-time reception algorithm.

The backscattered signal from the tag is captured on one of the Rx channels. Before baseband conversion, a frequency transposition is performed by multiplying the received RF signal with sine and cosine carriers in the in-phase (I) and quadrature (Q) paths. This operation enables the separation of the two orthogonal components of the received waveform. Then, a direct-conversion in-phase and quadrature (I/Q) demodulator embedded in the USRP device converts the modulated carrier signal into baseband for further processing. A direct-conversion in-phase and quadrature (I/Q) demodulator embedded in the USRP device converts the modulated carrier signal into baseband for further processing.

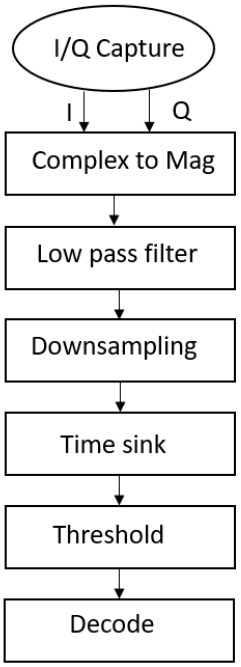

Figure 49. Flowchart of the real-time RX signal processing in GNU Radio

In backscatter communication systems, the tag does not generate its own RF signal but modulates an incident carrier by dynamically varying its reflection coefficient. Consider a continuous-wave (CW) carrier transmitted from the reader:

$$s_{Tx}(t) = A_c \cos(2\pi f_c t) \quad (1)$$

where A_c is the carrier amplitude and f_c is the carrier frequency. The tag encodes binary data $b(t) \epsilon \{0,1\}$ by switching its reflection coefficient $\Gamma(t)$ between two states:

$$\Gamma(t) = \begin{cases} +1, b(t) = 1 \\ -1, \ b(t) = 0 \end{cases} \quad (2)$$

The backscattered signal received at the reader can then be expressed as:

$$s_{Rx}(t) = \alpha \Gamma(t) A_c \cos(2\pi f_c t + \phi) \quad (3)$$

where α accounts for the propagation loss and scattering efficiency of the tag, and ϕ represents the phase shift introduced by the propagation channel. For BPSK modulation, the reflection coefficient introduces a 180° phase shift for binary '0', while binary '1' retains the original phase, i.e.,

$$s_{Rx}(t) = \alpha A_c \cos(2\pi f_c t + \pi b(t)) \quad (4)$$

In baseband representation, the received signal is:

$$r(t) = \alpha A_c b_{bpsk}(t) + n(t) \quad (5)$$

Where,

$$b_{bpsk}(t) = \begin{cases} +1, \ b(t) = 1 \\ -1, \quad b(t) = 0 \end{cases} \quad (6)$$

and n(t) denotes additive noise. This approach effectively allows the tag to implement BPSK modulation using simple switching circuits, such as the ADG902, toggling between an antenna-connected state (+1) and a grounded state (−1).

To recover the transmitted data, the received RF signal is down converted to baseband by multiplying it with $\cos(2\pi f_c t)$ and $\sin(2\pi f_c t)$ for the I (in-phase) and Q (quadrature) components:

$$I(t) = A_{Rx}(t).\cos(2\pi f_c t) \quad (7)$$

$$Q(t) = S_{Rx}(t).\sin(2\pi f_c t) \quad (8)$$

After this multiplication, the resulting I and Q signals contain two frequency components:

1. A high-frequency term at $2f_c$ (from cos^2 or sin^2multiplication)
2. A low-frequency baseband term that carries the actual BPSK data

The low-pass filter (LPF) is applied here to remove the high-frequency $2f_c$ term, leaving only the baseband signal corresponding to the transmitted data.
Thus, the filtered baseband signals are:

$$I_{bb}(t) \approx \alpha A_c b_{bpsk}(t), Q_{bb}(t) \approx 0 \qquad (9)$$

The baseband BPSK signal can then be demodulated using threshold detection. For ideal BPSK, the binary decision rule is:

$$b_T(t) = \begin{cases} 1, & I_{bb}(t) \geq 0 \\ 0, & I_{bb}(t) < 0 \end{cases} \qquad (10)$$

where $b_T(t)$ is the detected bit. The threshold is set at zero, since the BPSK modulation uses ±1 levels in baseband. This simple decision rule effectively recovers the transmitted binary data from the backscattered signal, even in the presence of additive noise.

2.1.1. USRP Source block

The first stage of the receiver signal chain is the USRP Source block, which interfaces the SDR hardware (USRP B210) with the GNU Radio software framework. In this setup, the USRP B210 is configured to operate with a center frequency of 3.5 GHz, a sampling rate of 1 1 MS/s, and a gain value of 50 to amplify the received signal. The device captures incoming radio frequency (RF) signals and outputs them in a complex I/Q format, containing both amplitude and phase information. The I/Q signal is directly retrieved from the RX2 antenna port of the USRP. This complex baseband representation serves as the input to the subsequent digital signal processing blocks designed for amplitude extraction, filtering, and threshold-based demodulation. At first, we are going to present only with the real SpO2 data in order to show how the blocks in GNU radio perform separately.
The general configuration of the USRP Source block and the corresponding output are illustrated in Figure 50. The figure on the right shows the temporal evolution of the received-signal amplitude, plotted as voltage (V) versus time (s). The captured waveform clearly shows discrete voltage transitions corresponding to Binary Phase Shift Keying (BPSK) modulation. The black peaks observed in the plot represent abrupt phase inversions inherent to BPSK, indicating bit transitions between logical '0' and '1'.
This observation confirms that the USRP B210 successfully acquired and down-converted the modulated backscatter signal, making the raw signal data available for subsequent envelope detection, filtering, and symbol recovery in the following processing stages.

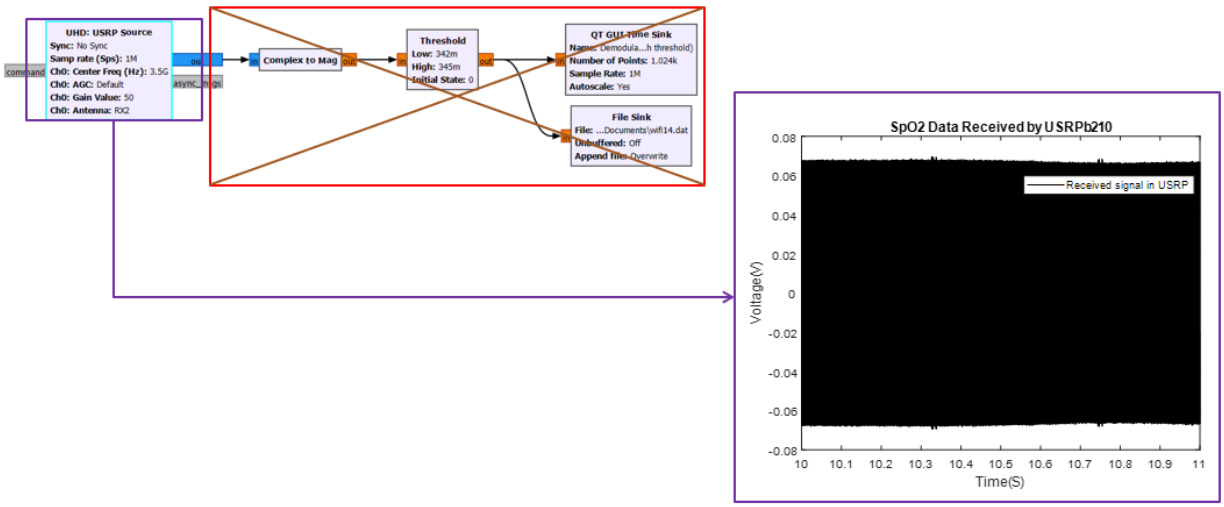

Figure 50. USRP Source Block Configuration and Raw Signal Reception in GNU Radio.

2.1.2. Complex to Magnitude conversion

After the initial reception stage, the captured signal remains in a complex I/Q format, encapsulating both amplitude and phase information. To facilitate further signal processing and simplify detection, the signal is next processed through a "Complex to Mag" block within the GNU Radio flowgraph. This block extracts the signal magnitude by computing the square root of the sum of the squared I and Q components. The output is a real-valued signal representing the envelope of the received waveform, thereby reducing the complexity associated with phase variations. This magnitude information is crucial for the subsequent filtering and thresholding operations.

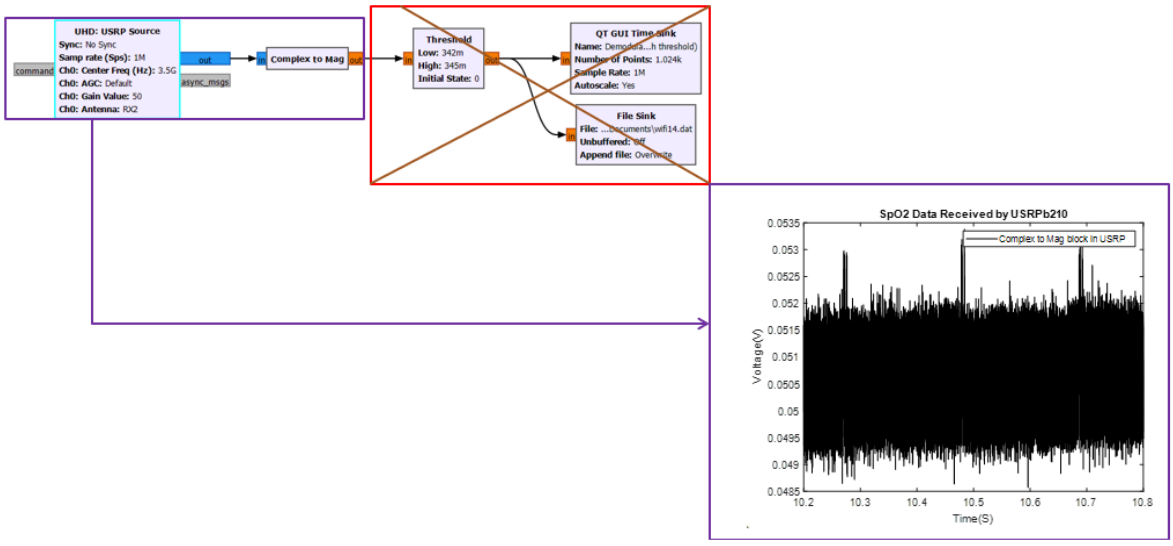

Figure 51. Complex to Mag Configuration and Signal Reception in GNU Radio.

The figure associated with this stage (Figure 51) illustrates the effect of this transformation. The plotted signal shows the amplitude variations over time, revealing the underlying

modulation pattern as well as the influence of environmental factors such as multipath reflections and channel fading. Compared to the raw I/Q data, this representation emphasizes only the signal strength, making it more suitable for detection in low SNR conditions. Therefore, the “Complex to Mag” block plays a key role in preparing the received data for efficient demodulation and binary information extraction in the subsequent processing stages.

2.1.3. Lowpass Filter

After converting the complex, I/Q signal to its magnitude, the resulting waveform still contains high-frequency noise components that can degrade the reliability of subsequent detection stages. To address this issue, the signal is processed through a low-pass filter block implemented in the GNU Radio flowgraph. In this setup, the filter is configured with a cutoff frequency of 500 kHz, allowing frequency components below this threshold to pass while attenuating higher-frequency noise. A Hamming-window- based design is employed to smooth the transition band of the filter, minimizing signal distortion while ensuring effective suppression of out-of-band noise.

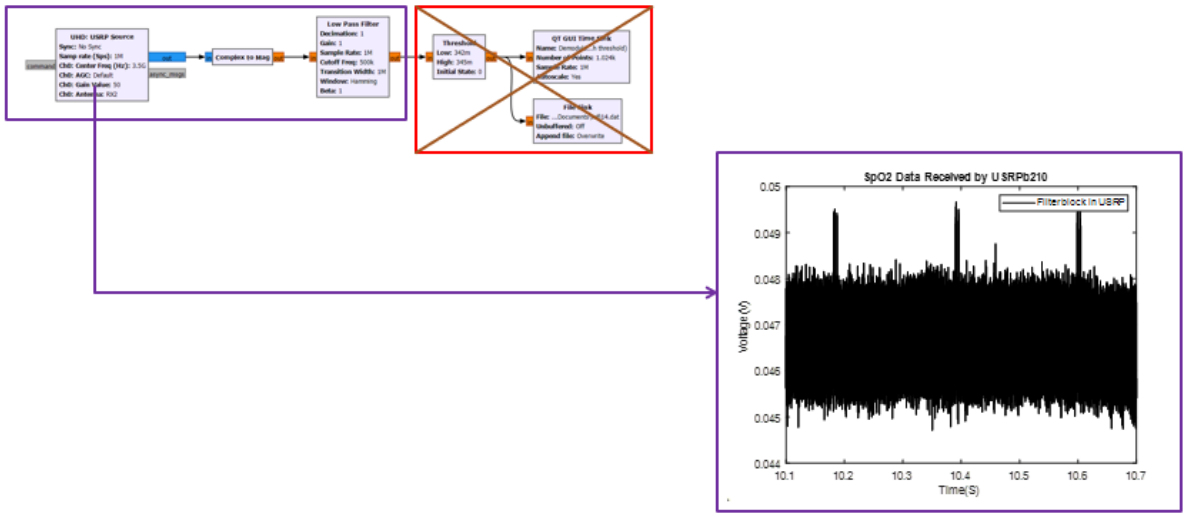

Figure 52. Lowpass filter Configuration and Signal Reception in GNU Radio.

The resulting filtered signal is shown in Figure 51, where the amplitude of the signal amplitude is plotted against time. Compared to the previous stage, the filtered output exhibits a clearer signal profile which helps to reduce the height of the random fluctuations of noise and more clearly defined amplitude levels which is shown from the base level. That means the noise level is lower than before which will help to decode the signal with minimum loosing of the data. This confirms that the low-pass filtering step successfully preserves the key characteristics of the BPSK-modulated backscatter signal while eliminating unwanted high-frequency noise. As

a result, the filtered signal becomes more suitable for threshold-based detection and subsequent processing stages.

2.1.4. Complete Block

The complete signal reception and demodulation process is illustrated by the "Complete Block" configuration implemented in the GNU Radio flowgraph. In this setup, the incoming RF signal is initially captured by the 'UHD (USRP Hardware Driver): USRP Source" block, which receives the backscattered signal at a center frequency of 3.5 GHz, with a sampling rate of 1 MS/s and a receiver gain of 50dB.After reception, the signal undergoes a series of processing steps. First, the complex I/Q data are converted to their magnitude representation through the "Complex to Mag" block. Next, the resulting magnitude signal is filtered by a low-pass filter configured to suppress high-frequency noise while preserving the essential low-frequency components associated with the backscatter modulation. Finally, the cleaned signal is passed through a "Threshold Block", which distinguishes the received binary symbols based on predefined amplitude limits (e.g., low = 68.4 mV, high = 68.5 mV). This thresholding step enables the reliable extraction of binary information encoded in the reflected signal.

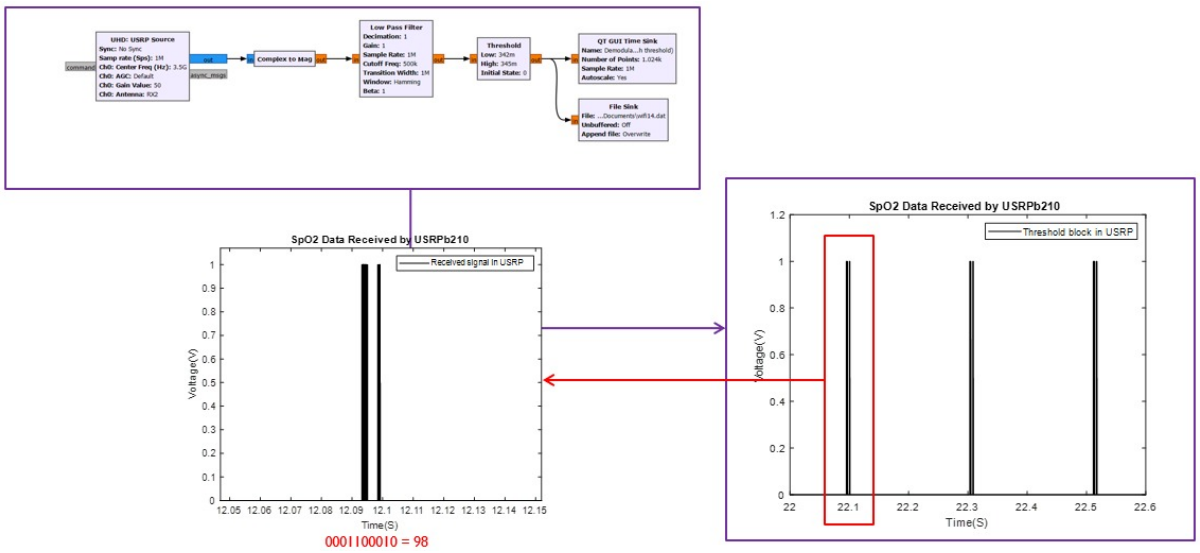

Figure 53. Complete block Configuration and Signal Reception in GNU Radio.

Figure 53 illustrates the flowgraph architecture and presents two key outputs: the raw magnitude signal after low-pass filtering and the extracted binary peaks after threshold-based detecting. The demodulated signal shows discrete transitions between binary states (0 and 1), reflecting the underlying BPSK modulation applied to the tag. As highlighted in the figure, the received sequence 0001100010 corresponds to a decimal value of 98, confirming the successful recovery of transmitted data through the designed receiver chain.

3. Modeling and Evaluation of Free Space Path Loss

FSPL quantifies the reduction in signal power that occurs as a radio wave propagates through free space, without encountering obstacles, reflections, or interference. It arises because the transmitted energy spreads over an increasingly larger area, causing a decrease in signal strength at the receiver. FSPL primarily depends on two parameters: the distance between the transmitter and the receiver, and the carrier frequency; both a larger distance and a higher frequency result in greater attenuation. In this work, the FSPL model previously introduced in Chapter 2 is used to characterize the signal attenuation between the transmitter and the receiver. The received power at the tag is similarly estimated using the link budget expression. In the experimental setup, a transmitter-receiver separation of 4 m and an operating frequency of 3.5 GHz are considered. The transmitted power is set to −40 dBm, leading to an estimated received power at the tag of approximately −78.37 dBm before accounting additional losses like T-connector, cable between tag and USRP card.

An SMA T-connector is used in experimental configuration to split the signal between the USRP receiver and the backscatter tag. This introduces an insertion loss due to signal division, which can be modeled as:

$$L_{split} = 10log_{10}\left(\frac{1}{2}\right) = -3dB \qquad (11)$$

This ideal 3 dB loss assumes perfect power splitting without additional degradation. In practice, extra losses due to impedance mismatches, dielectric losses, and connector imperfections typically range between 0.1 dB and 0.5 dB, depending on the frequency and the quality of the connectors. For instance, if an additional loss of 0.4 dB is present, the total insertion loss becomes approximately −3.4 dB. Consequently, the final effective received power at the tag is approximately −81.77 dBm. In Figure 54, the graph was obtained from the GNU Radio software. On the right side of the graph, the minimum and maximum values of the tag power are shown in green and pink, respectively, while the blue color represents the average power level of the tag.

4. Bit Error Rate (BER) Measurement and impact on Communication Reliability

The BER is a key performance metric in digital communication systems that quantifies the rate at which errors occur in the received data. It is defined as the ratio of the number of bit errors to the total number of bits transmitted over a communication channel.

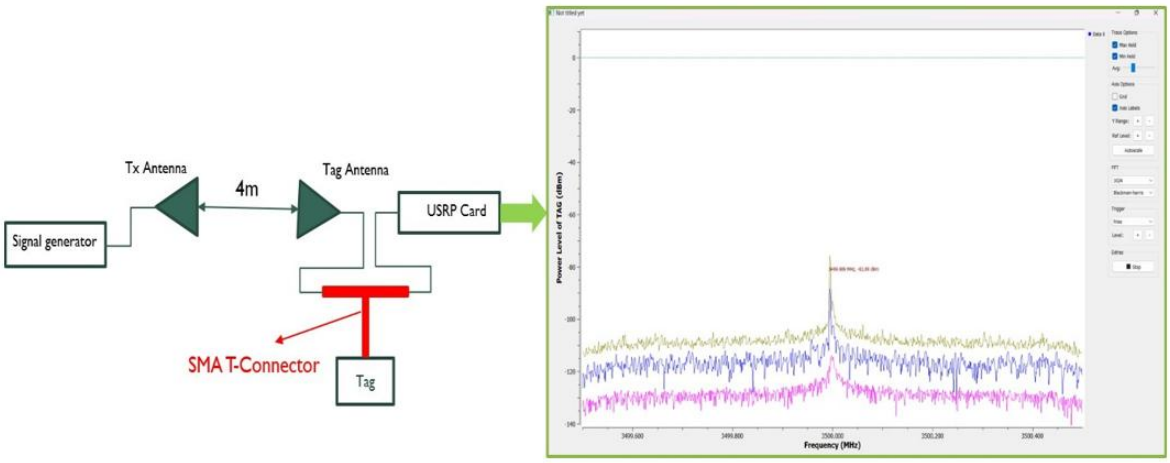

Figure 54. Receiving power of the tag antenna.

BER is influenced by factors such as noise, signal strength, modulation scheme, and channel conditions, making it essential to evaluate and optimize system performance.

The plot on the right in Figure 55 shows the waveform of the transmitted square-wave signal. The signal consists of eight bits, each bit having a duration of 102 microseconds (µs), as highlighted in the zoomed-in section of the plot. After the transmission of these eight bits, there is a delay of 20.8 milliseconds (ms) before the next sequence of bits is transmitted, creating a clear gap between transmissions. The time interval between two consecutive transmissions is marked as 727.6 µs, ensuring clear separation for demodulation at the receiver end.

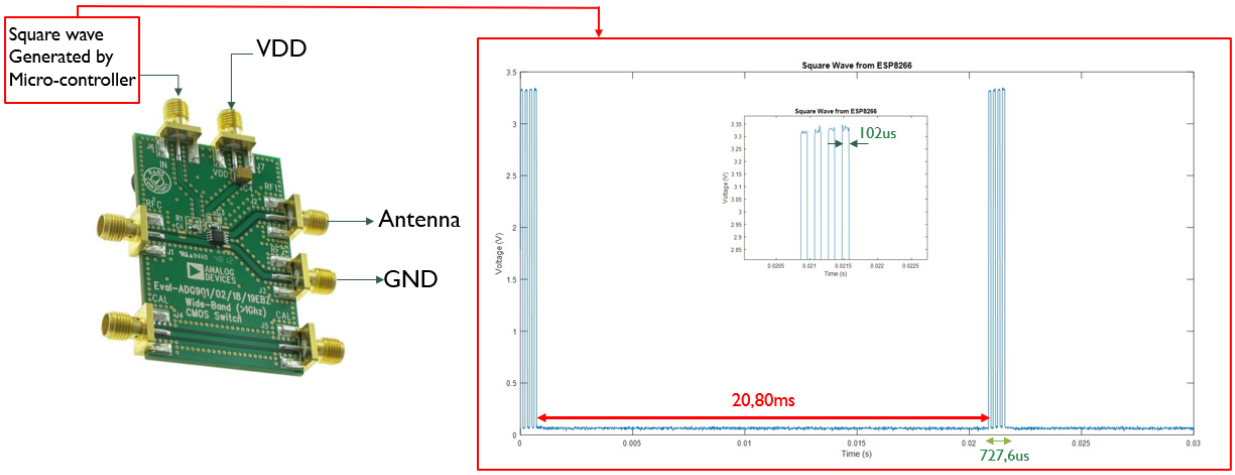

Figure 55. Generated Square Wave for BER Assessment.

Figure 56 shows a comparison between the square-wave signal generated by the ESP8266 microcontroller [2] and the signal received by the USRP B210. The red waveform represents the original square-wave signal generated by the ESP8266, while the green waveform corresponds to the signal captured by the USRP B210 receiver at 0 dBm transmitted power. In

the main plot, both signals are time aligned to facilitate comparison. The ESP8266 generates periodic bursts of square waves with clear voltage transitions, while the USRP B210 successfully receives and demodulates these signals, reproducing the same square wave-pattern.

The inset on the right zooms in on a specific portion of the signal to provide a detailed view, showing that the USRP accurately captures the square-wave pulses, preserving their shape and timing. The slight differences in amplitude and the presence of minor noise in the received signal can be attributed to factors such as transmission losses, channel noise, and the receiver's amplification and filtering settings. However, overall, the received waveform closely resembles the transmitted one, confirming that the USRP B210 reliably receives the square-wave signal transmitted by the ESP8266 microcontroller. This confirms the correct synchronization and demodulation of the transmitted signal prior to BER estimation.

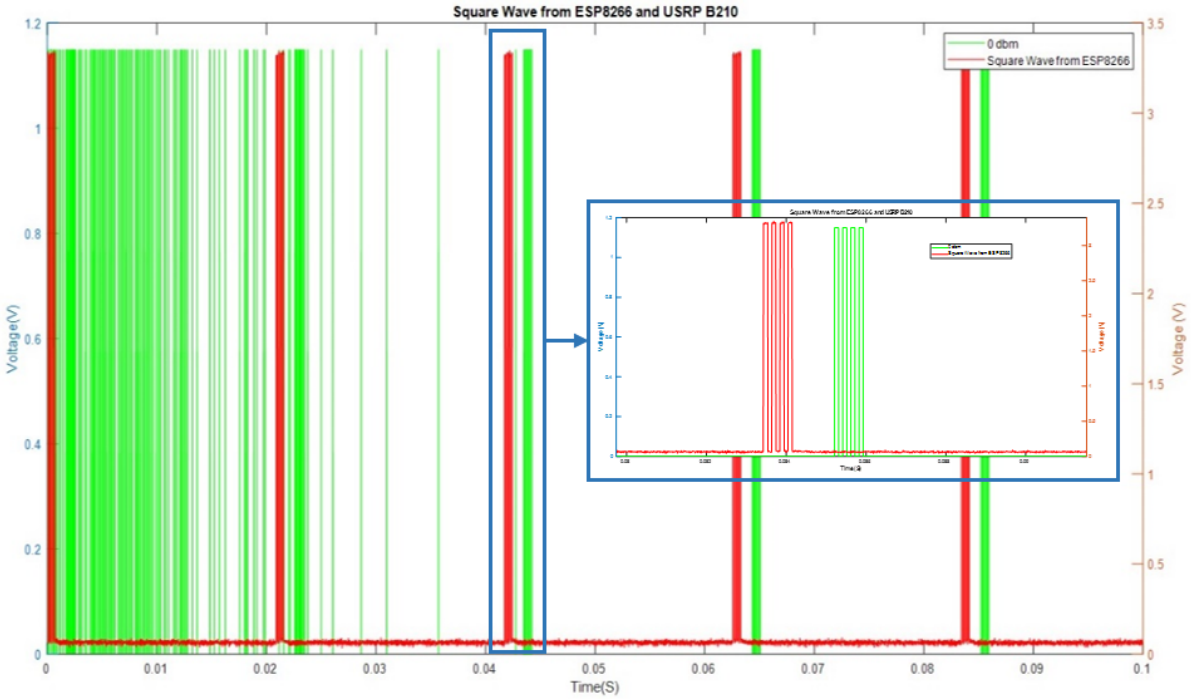

Figure 56. Received Signal from USRP B210 Compared to Reference Square Wave from ESP8266.

Figure 57 illustrates the square-wave signals transmitted by the ESP8266 and received by the USRP B210 at different transmitted power levels, specifically 0 dBm, -5 dBm, -10 dBm, -15 dBm, -20 dBm, and -25 dBm. Each received signal is shown in a distinct color, while the original square-wave generated by the ESP8266 is plotted in red.

By observing the figure, it can be noted that the first 0.04 seconds of the signal are unstable and noisy across all power levels. This is due to the fact that the USRP communication link is still

initializing, and full synchronization has not yet been established during this period. As a result, the received signals appear distorted and inconsistent.

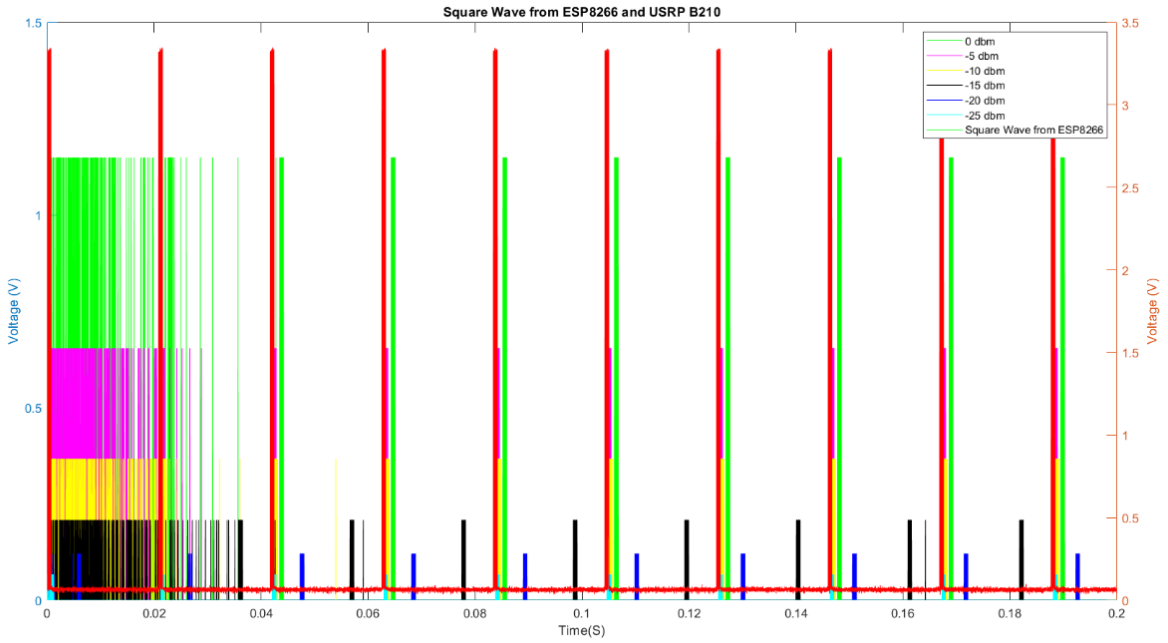

Figure 57. Received Signal from USRP B210 Compared to Reference Square-Wave from ESP8266.

After approximately 0.04 seconds, the communication link stabilizes, and the USRP B210 successfully captures the transmitted square-wave signals. The amplitude of the received signal progressively decreases as the transmission power is reduced, which is consistent with theoretical expectations. At higher power levels (0 dBm, and -5 dBm), the received signals closely follow the original waveform, while at lower power levels (-20 dBm, and -25 dBm), the received signal quality significantly degrades and the amplitude drops noticeably, making the square-wave less distinguishable due to increased noise and attenuation. Figure 57 clearly demonstrates the impact of transmitted power on the strength and the fidelity of the received signal, emphasizing the importance of sufficient transmission power to ensure reliable communication, particularly when using the USRP B210 receiver.

Figure 58 presents the BER analysis at 10 bps for square-wave signals transmitted by the ESP8266 module and received by the USRP B210 at various transmit power levels. Each colored waveform corresponds to a specific transmit power setting: 0 dBm, -5 dBm, -10 dBm, -15 dBm, -20 dBm, and -25 dBm — with the original square-wave signal from the ESP8266 shown in red. Overall, this figure clearly demonstrates the impact of transmit power on signal quality and BER performance at a low data rate of 10 bps, highlighting the importance of

maintaining adequate power levels to ensure accurate reception and minimize errors in wireless communication systems.

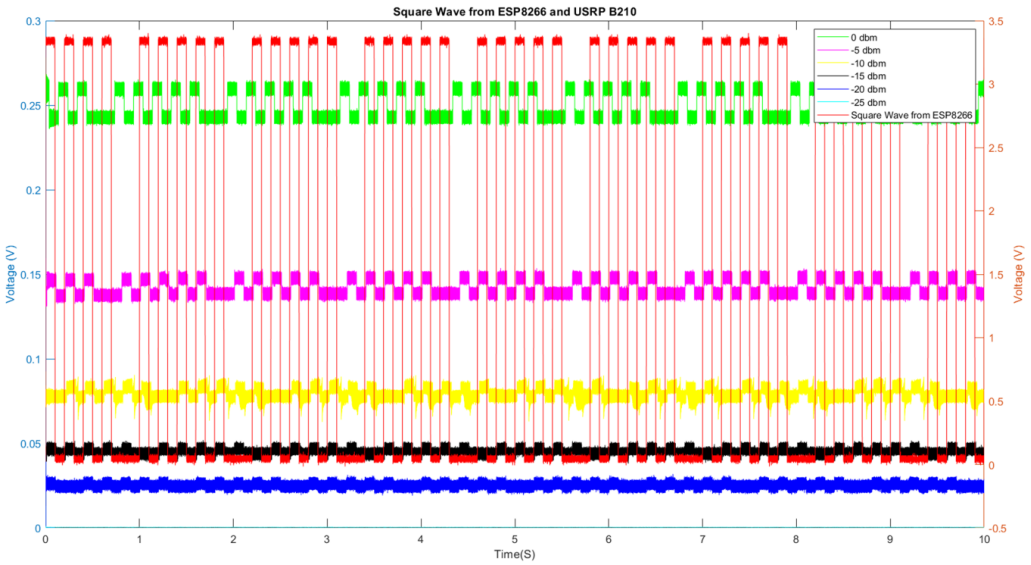

(a)

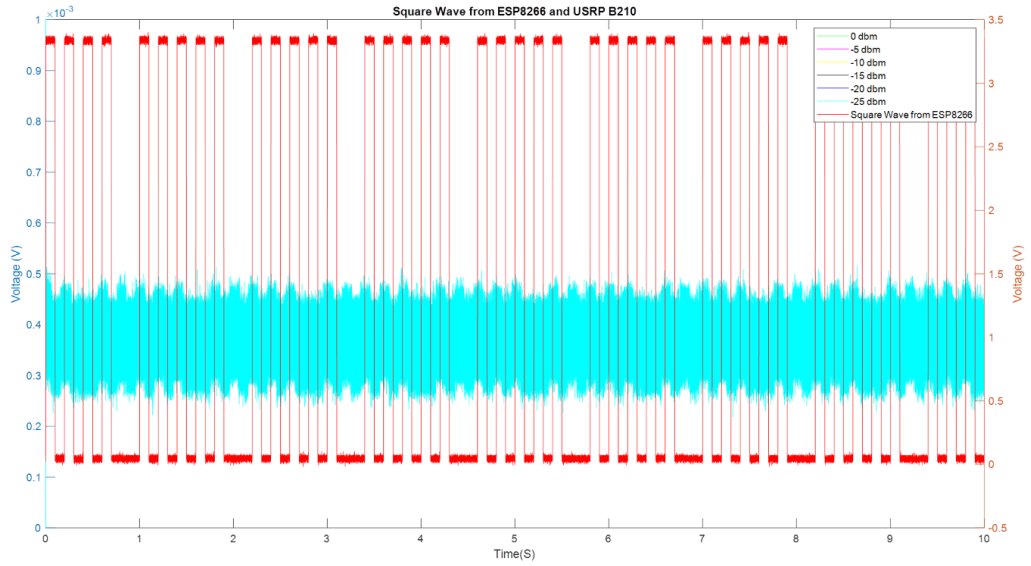

(b)

Figure 58. Generated Square-Wave for BER Assessment.

We recall that the BER for BPSK modulation in the presence of additive white Gaussian noise (AWGN) is expressed as:

$$BER = Q\left(\sqrt{\frac{2P_{Rx}}{N_0}}\right) \qquad (12)$$

where P_{Rx} denotes the received power signal, N_0 is noise power spectral density, and $Q(.)$ represents the Gaussian Q-function.

$$Q(x) = \frac{1}{\sqrt{2\pi}} \int_x^{\infty} e^{-\frac{t^2}{2}} dt \qquad (13)$$

In this section, this expression is used to compute the experimental BER values from the measured received power levels, thereby relating the observed system performance to the theoretical power-dependent behavior of BPSK modulation.

Figure 58 illustrates the relationship between received power at the tag and the BER for three different data rates: 2500 bps, 1000 bps, and 500 bps. The BER is plotted on a logarithmic scale to capture a wide range of error rates, while the x-axis represents the received signal power in dBm, varying from −25 dBm to 0 dBm. As expected, the BER decreases as the received power increases for all data rates. At lower power levels, such as −25 dBm, the BER is relatively high, particularly for the 2500 bps case, which exhibits a BER exceeding 10^{-1}, indicating significant transmission errors. In contrast, lower bit rates such as 1000 bps and 500 bps demonstrate greater robustness under weak-signal conditions, maintaining lower BER values across the same range. Notably, the 500bps configuration achieves a BER below 10^{-3} at 0 dBm, indicating highly reliable communication under favorable power conditions. These results highlight that lower data rate is more tolerant to weak signal conditions, making them suitable for power-constrained or long-range backscatter applications. Conversely, higher data rates such as 2500 bps require stronger received signal strength to maintain reliable performance.

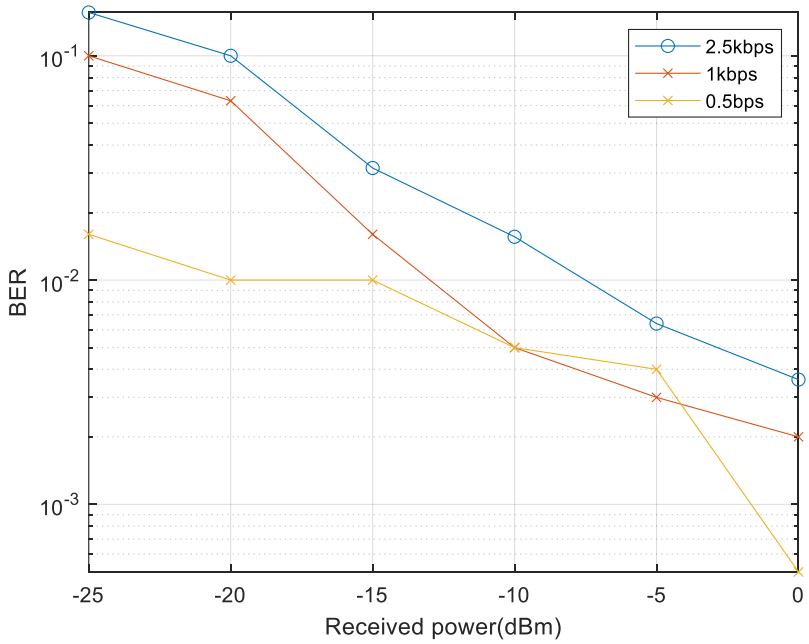

Figure 59. Measured BER vs received power.

Figure 59 shows the relationship between the BER and the received power for three different data rates: 2.5 kbps, 1 kbps, and 0.5 kbps. As expected, the BER decreases with increasing received power for all transmission rates, indicating improved signal quality and detection performance at higher power levels. At low received powers (around –25 dBm to –15 dBm), the BER is relatively high due to the weak backscattered signal and the dominance of noise. However, as the received power increases, the BER rapidly drops, reaching values below 10^{-3} for 0.5 kbps when the received power approaches 0 dBm.

Moreover, the results clearly show that lower data rates achieve better BER performance, since they require less bandwidth and provide higher energy per bit. In contrast, the 2.5 kbps transmission exhibits the highest BER across all power levels, reflecting the trade-off between data rate and reliability. These results confirm that the backscatter link performance strongly depends on both the received power and the modulation rate, emphasizing the importance of optimizing data rate according to available signal strength.

5. Time-Synchronized Multi-Sensor Backscatter Prototypes

This section presents the development and experimental synchronization of two time-synchronized, multi-sensor backscatter prototypes designed for wireless communication. The experiments were conducted inside an anechoic chamber to ensure a controlled and interference-free environment for wireless testing. As illustrated in Figure 60, the chamber effectively suppresses external RF interference and minimizes reflections from surrounding surfaces, thereby providing an ideal environment for accurate backscatter signal analysis.

The experimental setup consists of three main components. First, a pair of directional horn antennas is mounted on adjustable tripods and aligned face-to-face. The transmitting antenna, connected to a signal generator, emits a CW, while the receiving antenna is linked to a USRP B210 SDR platform that captures the backscattered signals. Second, the measurement and control equipment— including the signal generator, USRP receiver, and a computer running GNU Radio for signal processing— is arranged on a central table, along with additional instruments for monitoring signal quality. Third, a backscatter sensing tag, integrating multiple sensors, is placed between the two antennas. This tag modulates the incident CW signal according to real-time sensor data and reflects the modulated waveform toward the receiver.

This carefully designed experimental configuration enables accurate evaluation of backscatter modulation performance and supports reliable acquisition and analysis of multi-sensor data within a low-noise environment.

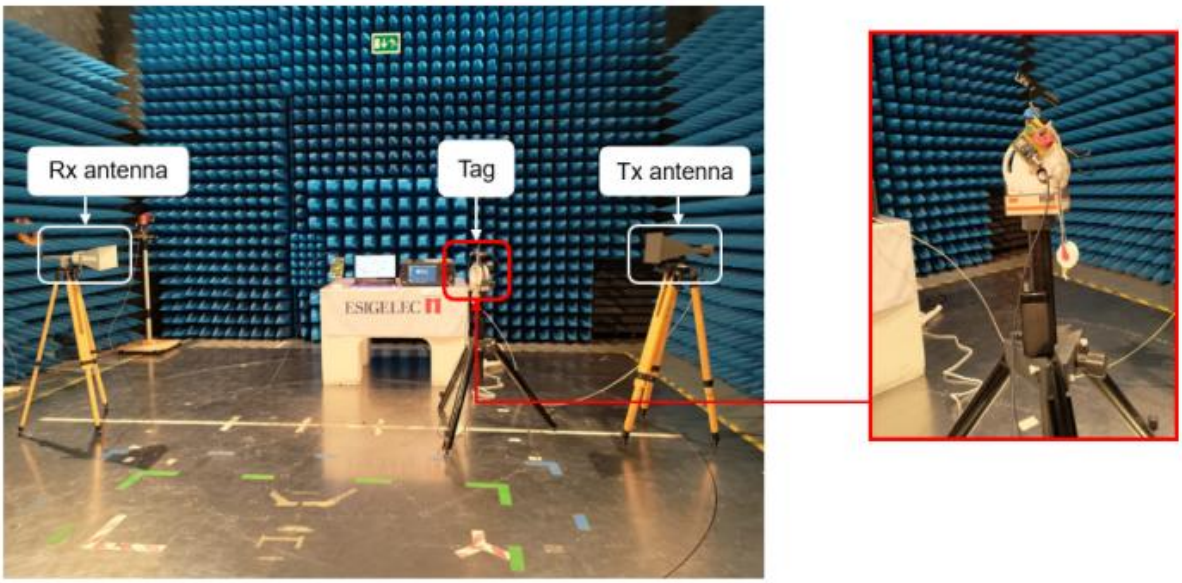

Figure 60. Experimental setup in the anechoic chamber, showing the Rx and Tx antennas and the backscatter tag.

5.1. Prototype 1: Single-Sensor Backscatter Tag

The operation of the first backscatter prototype was previously detailed in Chapter 3. In this section, we focus on the experimental validation of the tag's functionality by analyzing the data recovered at the receiver. The prototype integrates an LM335 analog temperature sensor, and the tag modulates the CW signal according to real-time temperature readings. Figure 61 presents the experimental results of the temperature data transmission and reception process. In Figure 61(a), the voltage waveforms obtained from both the oscilloscope (black trace) and the USRP B210 receiver (red trace) are shown, clearly revealing the transmitted binary sequence. A zoomed-in view is provided in Figure 61(b), where the demodulated signal is decoded into binary form, corresponding to the temperature value measured by the LM335 sensor.

At the time of measurement, the ambient temperature was approximately 18°C, which was accurately reflected in the received binary code: 0000010010. These results validate the proper functionality and demonstrate the reliability of the first backscatter-based sensing prototype for real-time temperature monitoring within a low-power ambient backscatter communication system.

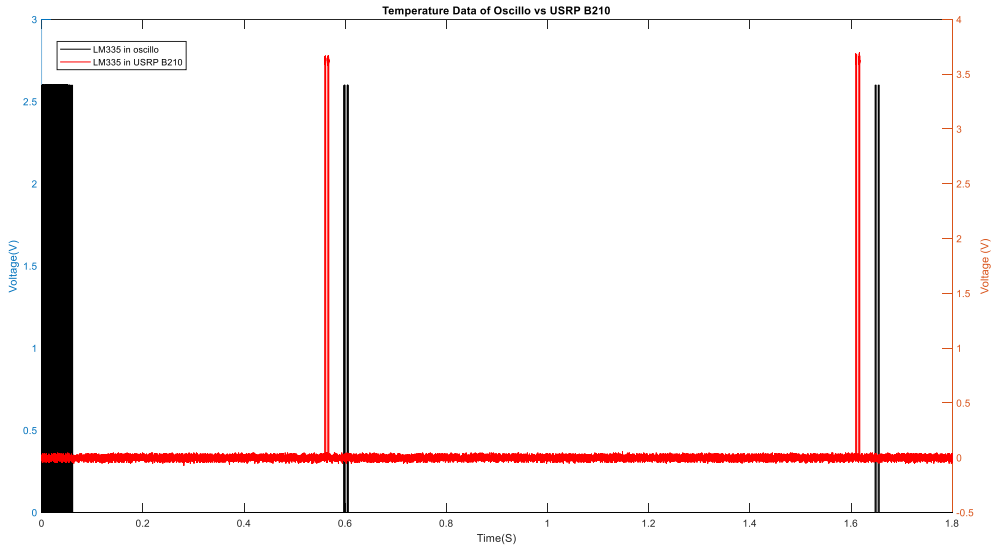

(a)

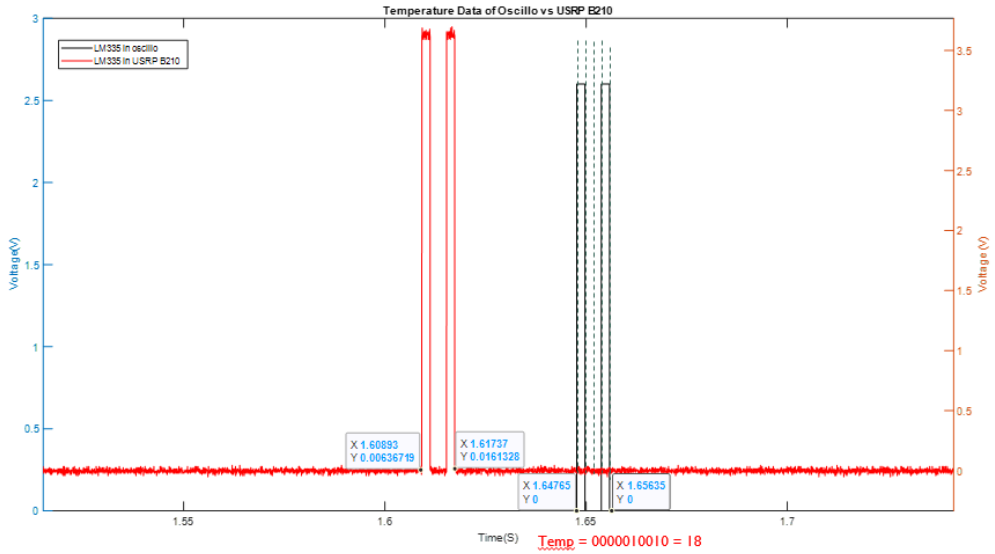

(b)

Figure 61. (a) Received waveform comparison between oscilloscope and USRP B210;

5.2. Prototype 2: Low-Cost Biomedical Backscatter System (PM4P)

This prototype (Figure 62) integrates multiple biomedical sensing modules with wireless connectivity for real-time health monitoring. It incorporates the MAX30100 optical sensor for measuring heart rate and oxygen saturation (SpO_2) [3], the DS18B20 digital sensor for body temperature [4], and the AD8232 analog front-end module for ECG signal acquisition [5]. These sensors are interfaced with an ESP8266 microcontroller, which provides Wi-Fi connectivity. A 5G external antenna is connected to enable enhanced long-range

communication, while a 2.4 GHz embedded antenna is integrated on the PCB for standard wireless transmission. The system is designed for compact, low-power, and wearable health monitoring applications. This prototype builds upon the architecture introduced in our previous work [6].

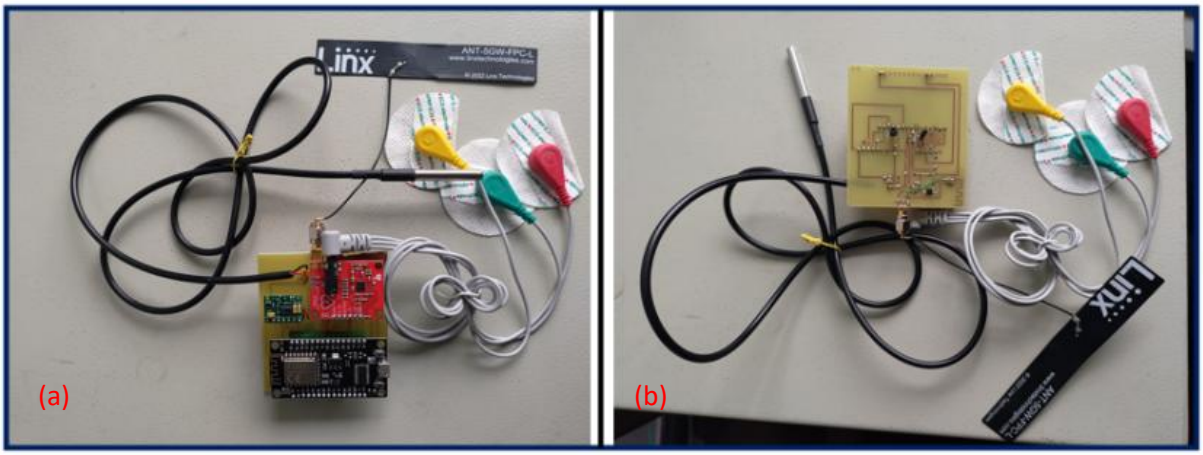

Figure 62. (a) Front view and (b) back view of the biomedical monitoring system prototype integrating the MAX30100, DS18B20, and AD8232 sensors with the ESP8266 microcontroller. The design features a 5G external antenna and a 2.4GHz PCB-embedded antenna for wirel

To address both energy-efficiency and cost constraints, the Patient Monitor for 4 Parameters (PM4P) system was developed using the Node MCU microcontroller. The three integrated sensors used, along with their respective measured parameters, are summarized in Table 9:

Sensor	**Measured Parameter**
MAX30100	SpO_2, BPM
AD8232	ECG
DS18B20	Temperature (T)

Table 9. Biomedical Sensors and Measured Parameters

To validate the prototype, a rigorous experimental testing process was conducted in parallel with industrial-grade patient monitoring systems to evaluate its performance and reliability. The results showed that although the PM4P exhibited slight measurement deviations, it remained sufficiently accurate for practical implementation. By integrating Internet of Things (IoT) technologies with ambient backscatter communication, the PM4P provides a promising, low-cost, and energy-efficient solution that meets the fundamental requirements for real-time health monitoring in resource-constrained environments. To further assess the system's wireless biomedical data transmission capability via backscatter, a series of controlled experiments were

conducted using the MAX30100, DS18B20, and AD8232 sensors. The collected sensor outputs were binary-encoded and used to control an RF switching circuit that modulated the antenna's impedance, thereby altering the reflection coefficient of the incident CW signal. The resulting backscattered waveform was captured and analyzed using a USRP B210 SDR receiver. In a first experiment, the MAX30100 sensor was used to demonstrate the system's capability to transmit SpO_2 data through backscatter modulation. The setup again involved a CW carrier generated within an anechoic chamber to minimize external interference and unwanted reflections. The backscatter tag modulated the incident RF signal according to the SpO_2 measurement obtained from the MAX30100 sensor. Specifically, an SpO_2 level of 94% was encoded into the binary sequence (01011110), which was used to control the RF switch, modulating the antenna's impedance accordingly.

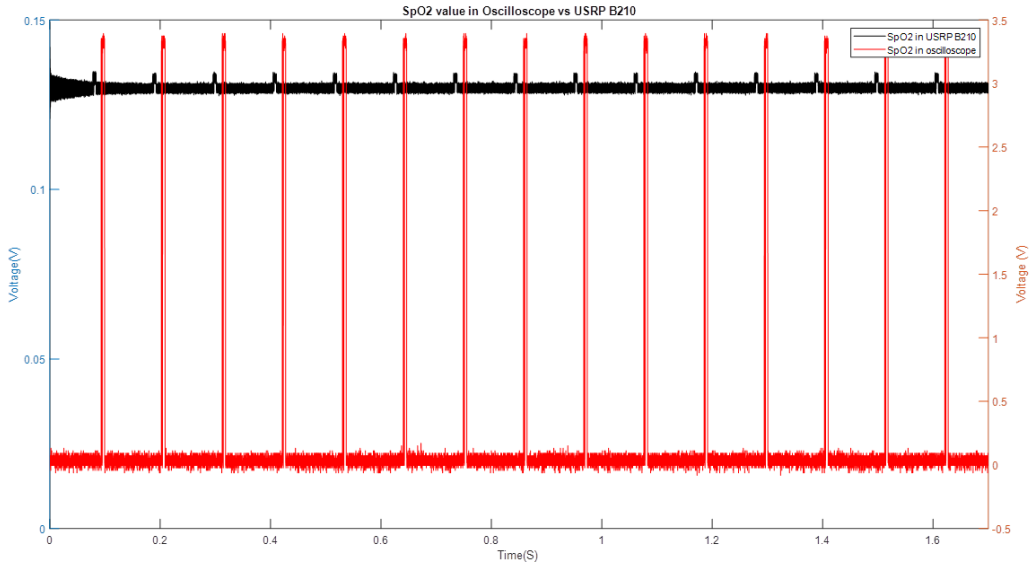

(a)

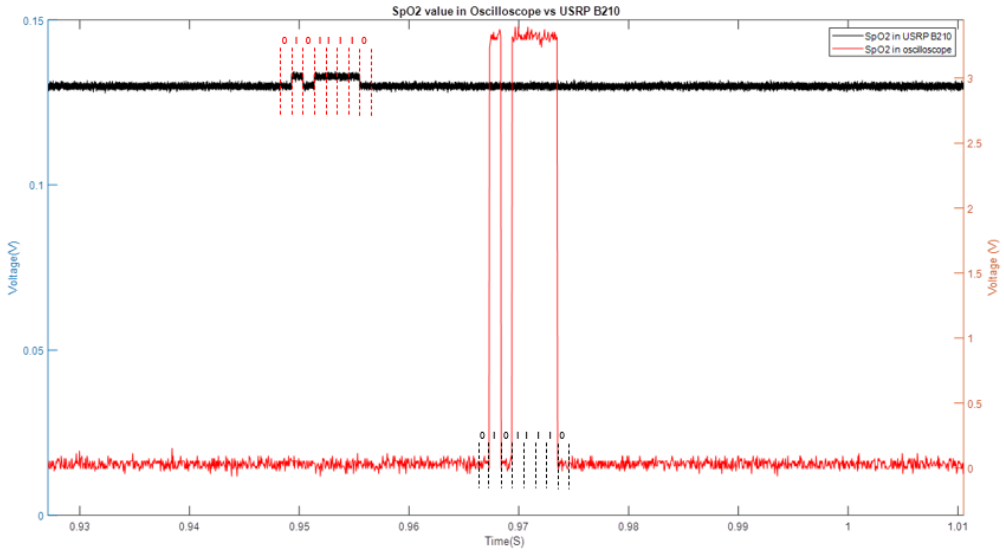

(b)

Figure 63. Time-Domain Response of Backscattered Signal Corresponding to SpO_2 Data Transmission Using MAX30100 Sensor: (a) Overall Transmission View, (b) Zoomed-In View Highlighting Binary-Encoding of SpO_2 Value.

The amplitude variations observed in the received backscattered signal (Figure 63) closely correspond to the binary-encoded SpO_2, thereby confirming the system's effectiveness in wirelessly transmitting vital-sign information through backscatter communication. These findings validate the prototype's suitability for low-power wireless health monitoring applications.

In addition to SpO_2, the MAX30100 optical sensor also measured the heart rate, which was recorded at 92 beats per minute (BPM). This value was encoded as the binary sequence (01011100), which was then used to modulate the antenna impedance through the RF switch, enabling backscatter-based transmission. As illustrated in Figure 64, subfigure (a) shows the complete temporal response, while subfigure (b) presents a zoomed-in view that clearly highlights the binary-encoded waveform. These results further confirm the system's capability to support multi-parameter physiological monitoring using ambient backscatter communication.

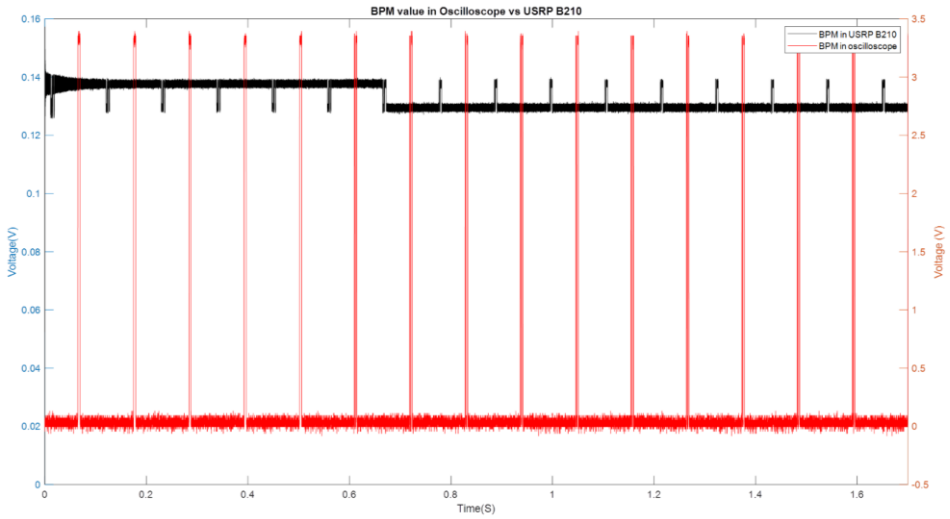

(a)

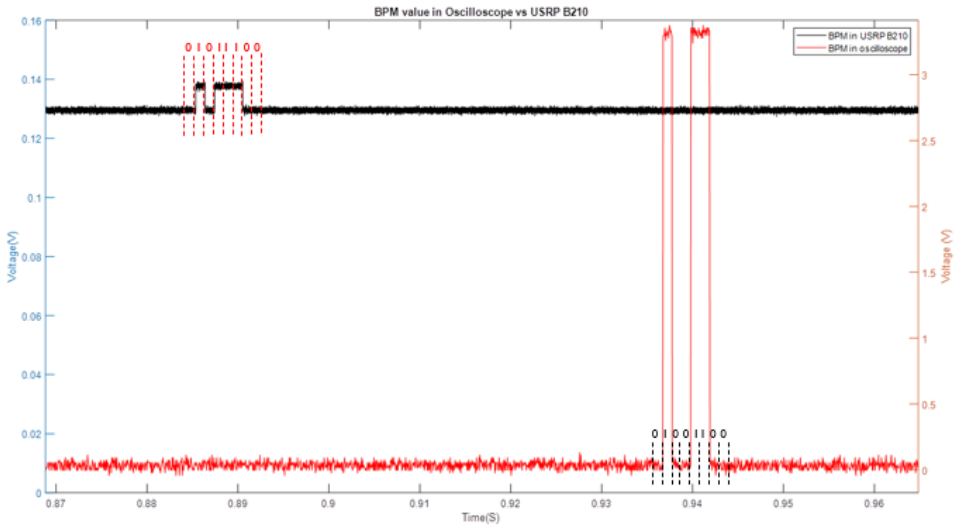

(b)

Figure 64. Time-Domain Response of Backscattered Signal Encoding BPM Data Captured by USRP B210 Receiver: (a) Overall Transmission View, (b) Zoomed-In View Showing Binary-Encoding of BPM Value.

Additionally, the AD8232 ECG sensing module was employed to assess the system's capability to wirelessly transmit bio-signals through backscatter modulation. As with the previous experiments, a continuous wave (CW) carrier was generated within an anechoic chamber to ensure a controlled and interference-free environment. The backscatter tag modulated the carrier signal based on the ECG data acquired from the AD8232 sensor. In this test, an ECG value of 640 (in digital units) was converted into the binary sequence

(10100000), which was then used to control the RF switch circuit, thereby modulating the antenna reflection coefficient accordingly.

As shown in Figure 65, subfigure (a) presents the complete time-domain waveform of the backscattered signal, while subfigure (b) provides a zoomed-in view that highlights the binary-encoded transmission pattern. The amplitude variations captured by the USRP B210 receiver clearly correspond to the binary bits of the ECG data, with the modulation clearly visible in the central portion of the plot. These results confirm the system's effectiveness in reliably transmitting complex physiological signals, such as ECG, thereby reinforcing its applicability for wireless health-monitoring systems.

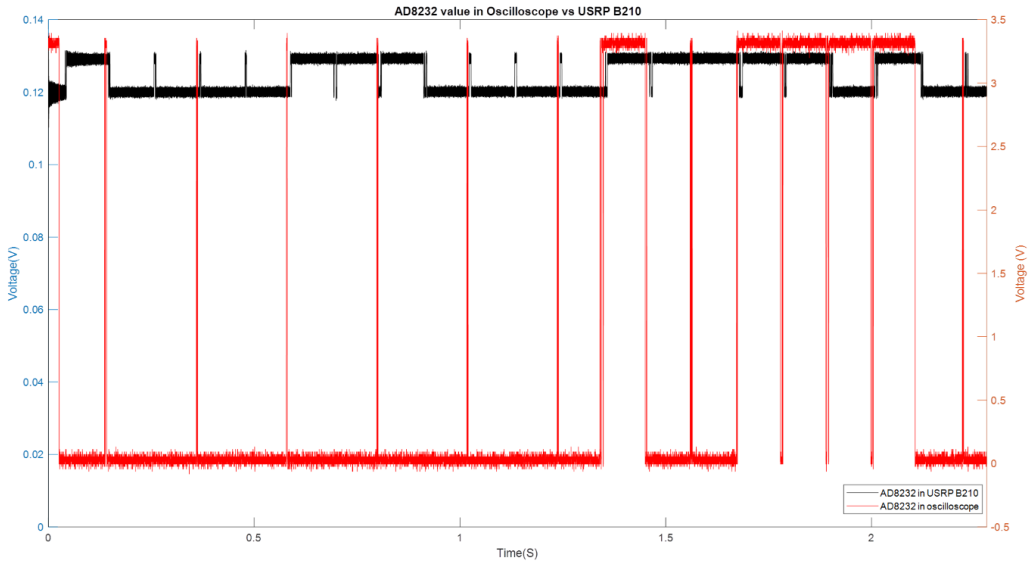

(a)

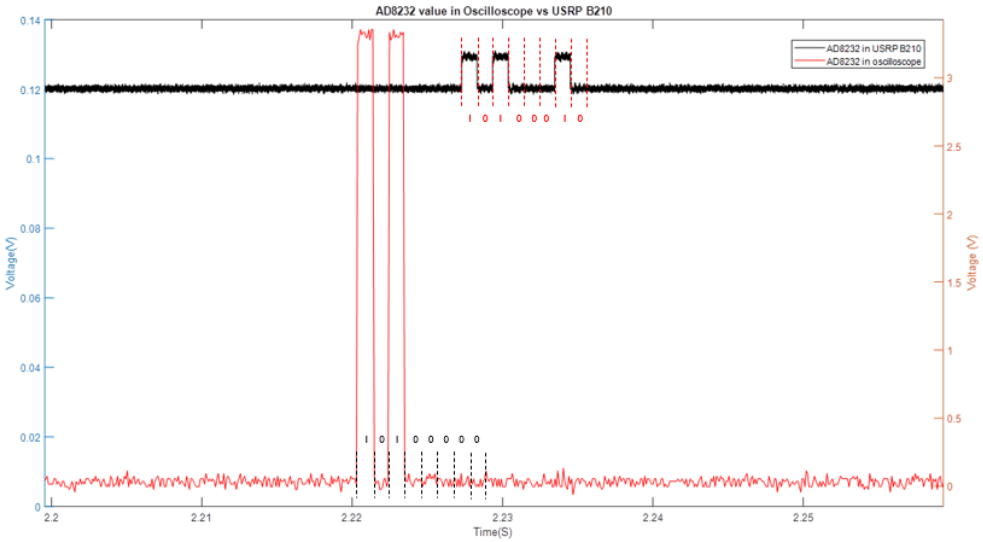

(b)

Figure 65. Time-Domain Response of Backscattered Signal Encoding ECG Data Captured by USRP B210 Receiver: (a) Full Transmission View, (b) Zoomed-In View Showing Binary-Encoding of ECG Value.

5.3. Effect of Sample Rate on Signal Reception at 3.5 GHz

To further assess the robustness of the proposed ambient backscatter communication system, a series of controlled experiments was conducted to compare the transmitted and received signals for all sensors operating simultaneously at a carrier frequency of 3.5 GHz. The main objective of this investigation was to evaluate how the sampling characteristics of the receiver influence the quality and fidelity of the received backscattered waveform. In these experiments, four physiological and environmental parameters were transmitted: heart rate (BPM), blood oxygen saturation (SpO_2), body temperature, and electrocardiogram (ECG) signal. A composite digital sequence was constructed by sequentially encoding the sensor readings into binary format and modulating them through the RF switching circuit. The resulting backscattered waveform was captured using two measurement instruments: an oscilloscope connected directly to the tag output, and the USRP B210 software-defined radio receiver, configured to sample at 1 MSps.

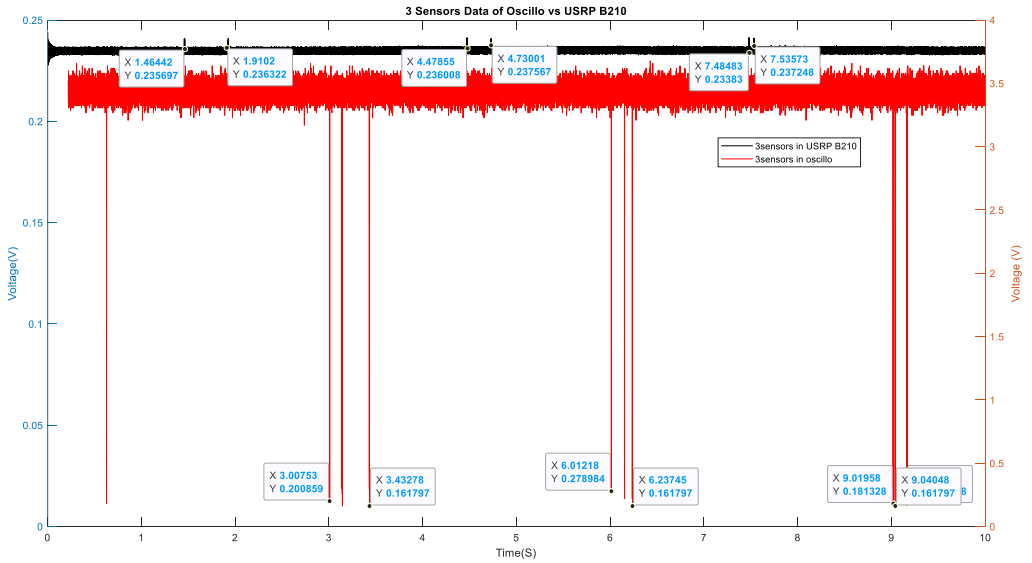

Figure 66. Time-domain response of backscattered signal encoding all biomedical sensor data captured by the USRP B210 receiver and compared with oscilloscope data.

As shown in Figure 66, the complete backscattered waveform includes four distinct groups of pulses, each corresponding to one of the sensing channels. The red trace represents the

signal recorded by the oscilloscope, which provides higher temporal resolution and wider bandwidth, while the black trace corresponds to the signal acquired and sampled by the USRP B210 SDR. Despite the limited sampling rate of the USRP, the waveform preserves the overall shape and temporal structure of the transmitted signal, thereby demonstrating successful reception.

To emphasize the differences in signal fidelity, Figure 67 presents a zoomed-in view of the same waveform. It can be observed that the oscilloscope trace exhibits sharper transitions and more precise voltage levels, particularly at the rising and falling edges of each pulse. In contrast, the USRP-recorded waveform appears slightly smoothed due to its lower sampling resolution. Nevertheless, the bit-level transitions remain clearly discernible, allowing accurate demodulation and decoding of the transmitted binary sequences.

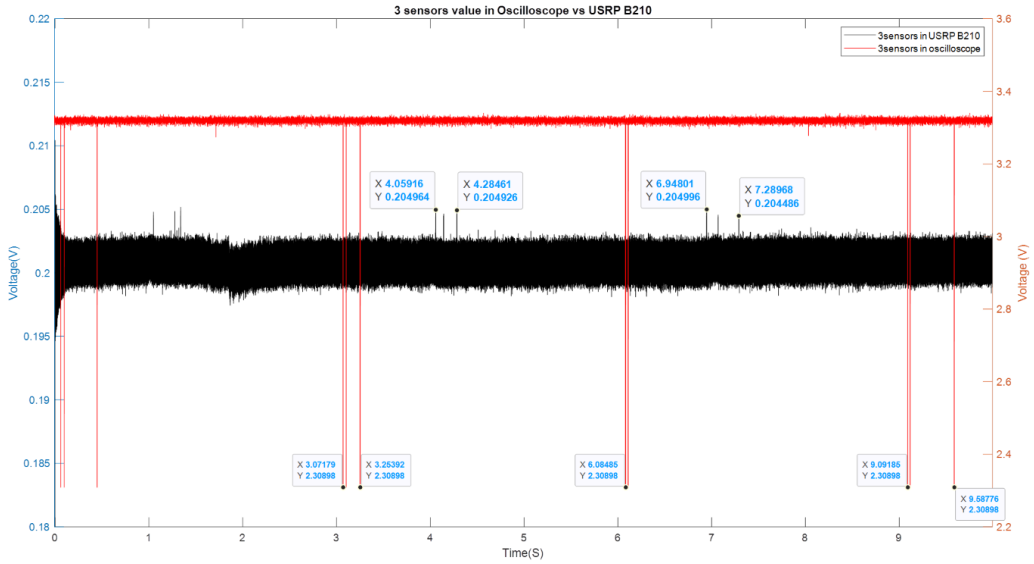

Figure 67. Zoomed time-domain comparison of backscattered signal encoding biomedical data captured by the USRP B210 and oscilloscope, showing signal details and timing alignment.

A more detailed comparison is presented in Figure 68, where subplot (a) shows the original transmitted waveform comprising the four sensor-generated signals, while subplot (b) juxtaposes the oscilloscope and USRP receptions. Despite minor variations in amplitude and temporal alignment, both signals clearly reveal the four encoded data blocks. The sampling characteristics and internal processing of the USRP result in a slight delay and pulse broadening, yet the data remains reliably detectable.

These results highlight the system's robustness to sampling limitations constraints and confirm the feasibility of reliable data reception even with low-cost SDR platforms. The inherent

resilience of the backscatter link, combined with the use of simple digital modulation, enables accurate transmission of multi-sensor data over ambient RF carriers, thereby paving the way for practical implementations in real-world wireless health monitoring applications.

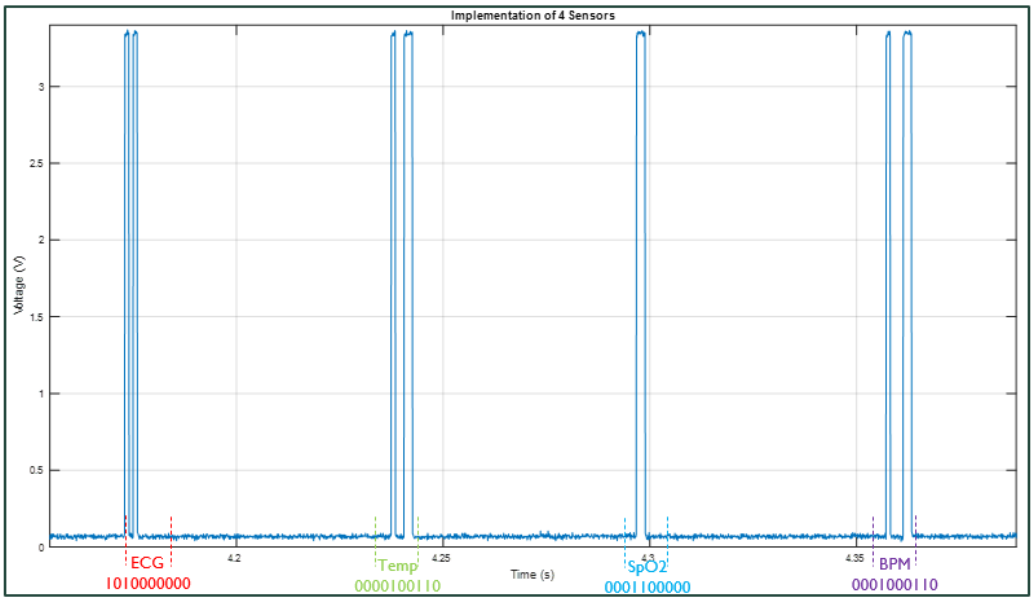

(a)

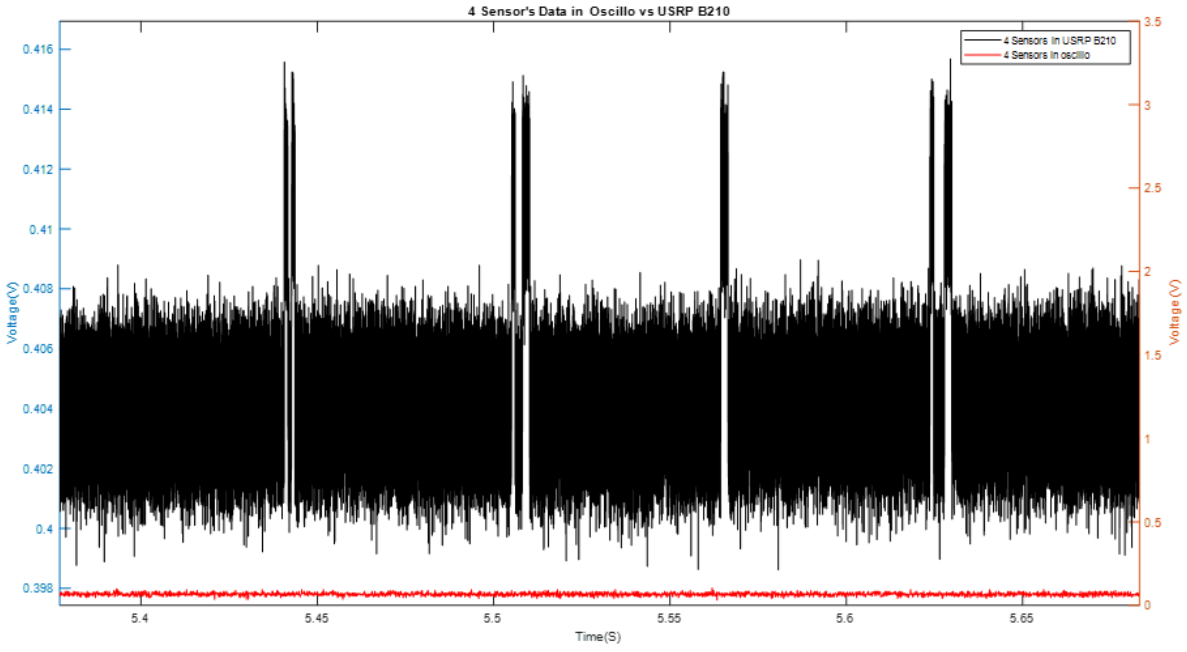

(b)

Figure 68. (a) Transmitted signal encoding four biomedical parameters (ECG, temperature, SpO_2, and BPM). (b) Received backscattered signal captured by the USRP B210 and oscilloscope, showing signal degradation and timing variation.

To optimize both data-acquisition efficiency and power consumption in the sensor system, a periodic activation-and-sleep strategy was implemented, as illustrated in Figure 69. The system operates on a 5-second duty cycle, during which three distinct data packets are transmitted. Packet 1 includes data from the AD8232 (ECG), DS18B20 (temperature), and MAX30100 (SpO2 and BPM) sensors, collected during an activation period of 0.190 seconds. Following this, the system enters a sleep mode lasting 2 seconds to conserve energy. Packet 2 is dedicated to temperature measurement using the LM335 sensor, after which the system undergoes another sleep period of 2.7 seconds. Finally, Packet 3 replicates the structure of Packet 1, collecting and transmitting ECG, temperature, SpO2, and BPM data. This cycle ensures timely physiological monitoring while maximizing battery lifetime through strategically scheduled sleep intervals.

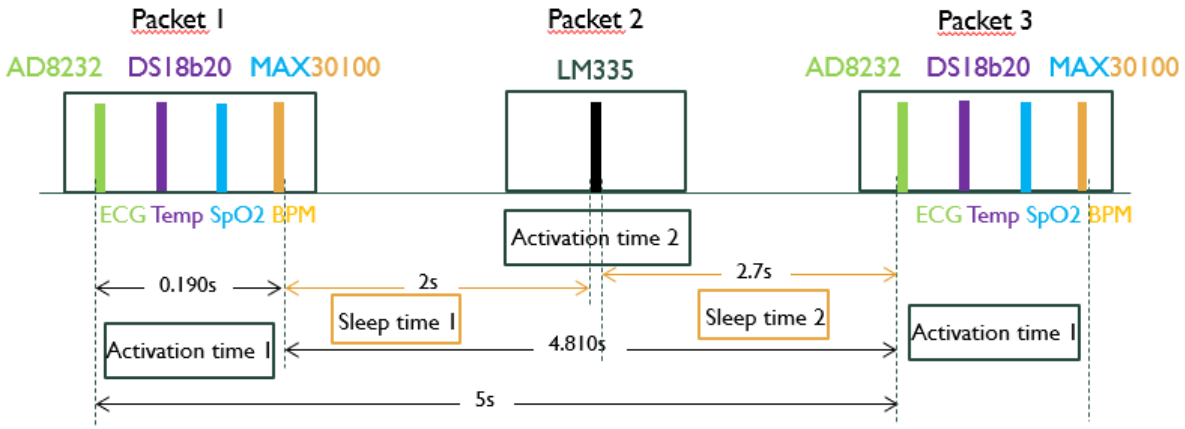

Figure 69. Method of implementation for 4 sensors.

The developed multi-sensor prototype integrates multiple biomedical sensors with a wireless communication module to enable real-time physiological monitoring. At the core of the system is the ESP8266 microcontroller, which provides integrated Wi-Fi connectivity for local data processing. In parallel, the system incorporates a backscatter communication module that leverages ambient 5G carrier waves as the excitation source, thereby extending its wireless communication capabilities.

In Figure 70 the overall design incorporates the AD8232 analog front-end module for electrocardiogram (ECG) signal acquisition, providing detailed information on cardiac activity. Additionally, the MAX30100 optical sensor is used to measure both blood oxygen saturation (SpO2) and heart rate (BPM), while temperature monitoring is achieved using two sensors the digital DS18B20 and the analog LM335ensuring measurement redundancy

and improved accuracy. As previously mentioned, the backscatter communication module operates in conjunction with a 5G Linx antenna, which enhances the communication range and reliability and reliability by supporting stable and efficient wireless data transmission of physiological parameters. This integration enables continuous monitoring and remote acquisition of vital signals, making the system particularly suitable for wearable health monitoring and telemedicine applications.

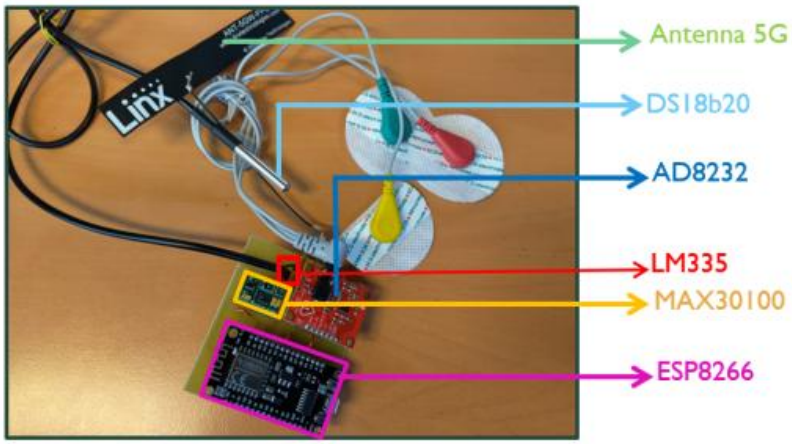

Figure 70. Final prototype for 4 sensors.

Figure 71 presents a comparative analysis of sensor signal transmission and reception using an oscilloscope and the USRP B210 SDR. The transmitted waveforms from four sensors SpO2, heart rate (BPM), ECG, and temperature are shown on the left, displaying sharp and clearly distinguishable voltage peaks. On the right, the corresponding received signals captured by the USRP are visualized, highlighting two zoomed-in sections: the upper subplot shows the successful reception of the four sensor signals, while the lower subplot focuses on the LM335 temperature sensor, which is also correctly detected. Despite the presence of a noticeable time delay between transmission and reception, and a higher noise floor in the USRP data, the main signal peaks are identifiable, demonstrating the system's ability to distinguish and decode multiple sensor outputs. However, the reduced signal clarity and increased noise in the USRP reception highlight the importance of careful parameter tuning particularly of sampling rate, gain, and synchronization to ensure reliable and accurate signal acquisition in wireless sensing applications.

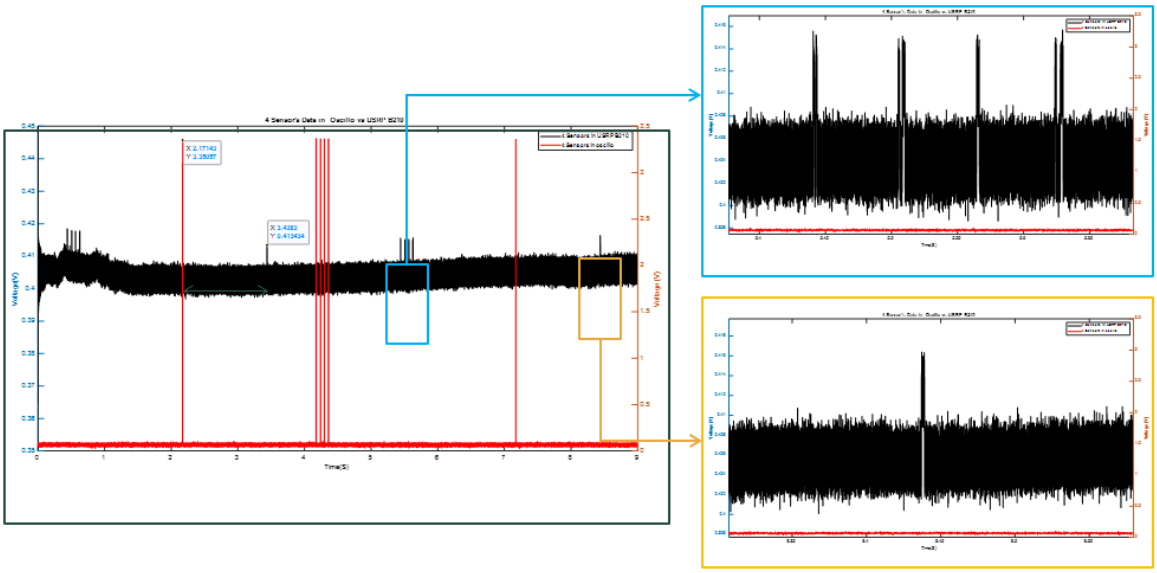

Figure 71. Received backscatter data of 4 sensors.

6. Recovering Backscatter Information from Ambient RF Sources

In this work, we focus on extracting backscattered data from ambient RF signals without relying on dedicated carrier emitters. By leveraging naturally occurring RF sources, such as Wi-Fi access points or FM radio transmitters, the system enables low-power communication from passive devices. The backscattered signal, which is modulated onto the ambient carrier, is often weak and buried within noise and interference. To recover the embedded information, we employ advanced signal-processing techniques to isolate and demodulate the subtle amplitude and phase variations introduced by the backscatter device. This method shows the potential for creating simple and battery-free wireless sensing systems that use common ambient signals like 5G and Wi-Fi.

6.1. Backscattered Signal Behavio in Wi-Fi Based Systems

The spectrum-analyzer measurement illustrates the presence of ambient Wi-Fi- signals within the 2.4 GHz ISM band. The frequency sweep ranges from 2.2 GHz to 2.6 GHz, with the received power expressed in dBm. A prominent spectral peak is observed at approximately 2.439 GHz, corresponding to a received power of -46.19 dBm (Figure 72). This strong component likely originates from a nearby Wi-Fi transmitter operating on Channel 6, which is centered at 2.437 GHz and is commonly used in typical Wi-Fi deployments. A secondary, less intense peak appears at 2.447 GHz, with a received power of -62.48 dBm, possibly indicating overlapping-channel activity or interference from another access point. The ambient noise floor remains relatively stable between -70 dBm and -75 dBm, suggesting minimal background interference apart from the identified Wi-Fi

sources. Overall, this measurement confirms the existence of significant ambient Wi-Fi activity in the surrounding environment, particularly concentrated around the central 2.4 GHz Wi-Fi channels.

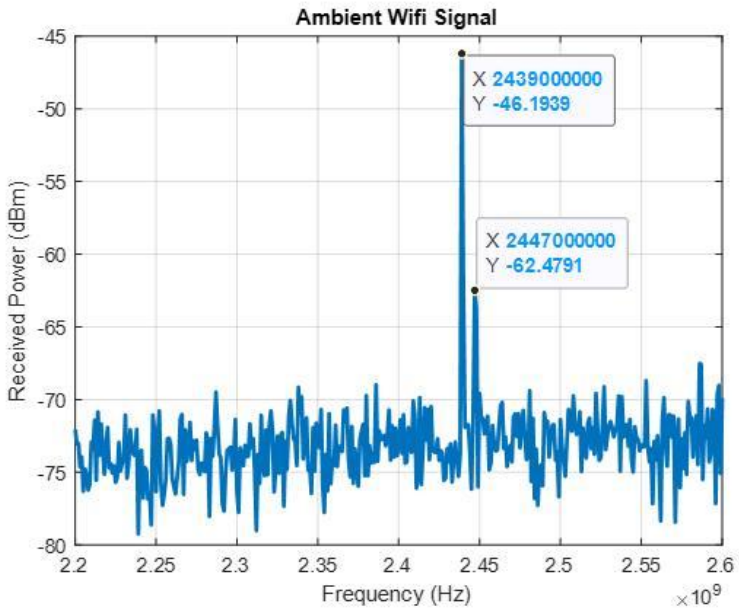

Figure 72. Power spectrum of ambient Wi-Fi signal in the 2.4 GHz ISM band.

Figure 73 illustrates the operating principle of an ambient backscatter communication system that leverages existing Wi-Fi signals. At the top center, a Wi-Fi antenna emits ambient RF signals, which are naturally present in the environment and not specifically directed toward any device. These ambient signals propagate through space and reach a low-power tag, shown on the left side of the figure. As discussed in Chapter 1, the tag does not generate its own RF signal; instead, it modulates the incoming ambient Wi-Fi waveform by selectively reflecting tit— a process known as backscatter modulation. The modulated, reflected wave, referred to as the backscattered signal, is then received by the receiver setup depicted on the right side. This receiver, typically a USRP B210 SDR, captures and demodulates the backscattered signal to recover the transmitted data.

The plot in the receiver section compares two signals: the red trace represents the data as transmitted by the tag, while the black trace corresponds to the received and demodulated signal. The alignment of the peaks between the two confirms the successful recovery of the transmitted information. This technique enables ultra-low-power or battery-free communication, making it ideal for applications in the Internet of Things (IoT), passive sensing, and RF identification (RFID) systems.

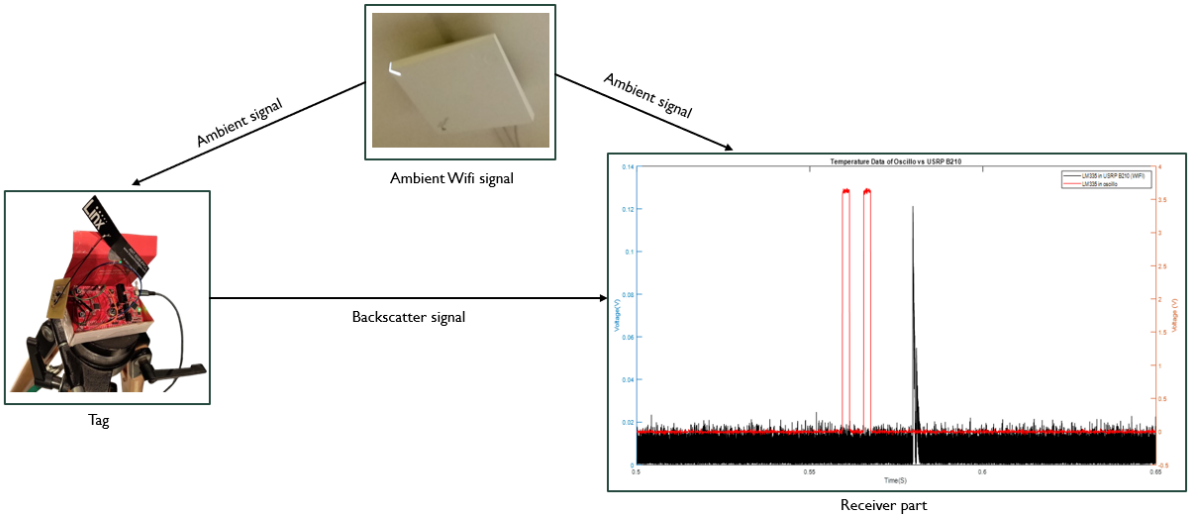

Figure 73. Backscatter communication using ambient Wi-Fi signal for temperature data transmission.

Figure 74 presents a visualization of backscattered signal captured from a tag transmitting temperature information using ambient Wi-Fi signals. The main plot on the left show's voltage versus time, where two sets of waveforms are overlaid: the red trace represents the original signal transmitted by the tag, while the black trace corresponds to the received and demodulated waveform obtained using a USRP B210 SDR receiver. The circled regions highlight distinct types of information: the black circles identify segments corresponding to temperature data, whereas the blue circles indicate other data sections potentially related to system control, synchronization, or identification.

The inset on the right provides a zoomed view of one of the temperature data segments a clearer view of the demodulated waveform. In this close-up, the binary sequence (00010011) is extracted, representing 8 bits of information that corresponds to the decimal value 19, likely associated with a temperature reading. This binary-to-decimal conversion demonstrates that the backscatter system is not only capable of modulating and transmitting information using ambient RF signals, but also of accurately encoding real-world sensor data such as temperature for remote sensing applications. The strong alignment between the transmitted (red) and received (black) traces confirms successful decoding, further validating the effectiveness of ambient backscatter communication for low-power data transmission.

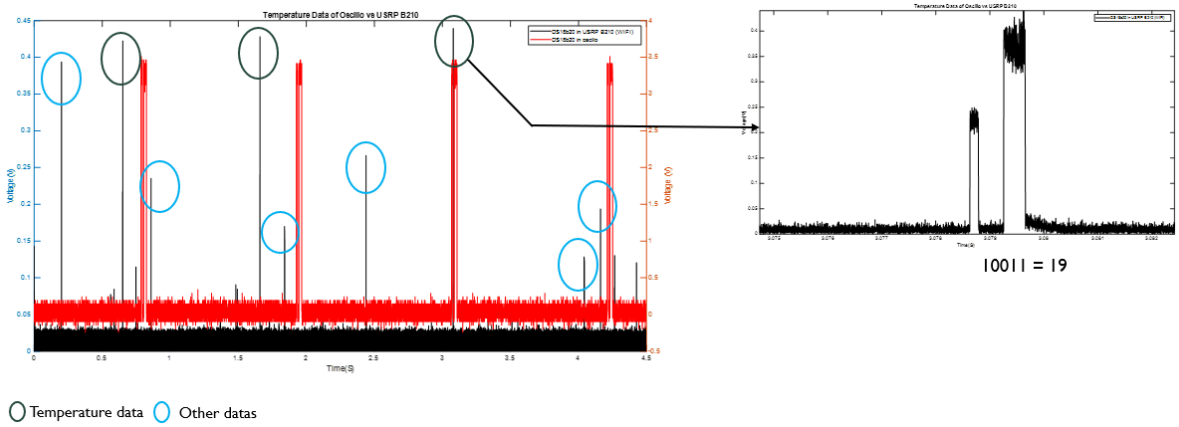

Figure 74. Decoding of temperature data from backscattered signal using ambient Wi-Fi transmission.

6.2. Backscattered Signal Behavior in 5G Base Station-Oriented Communication Systems

To assess the feasibility of utilizing ambient 5G signals for backscatter communication, we examined the received power spectral density (PSD) across various sub-6 GHz frequencies in a typical urban environment. Figure 75 presents four representative measurements of ambient 5G downlink signals captured within the 3.4–3.85 GHz range. Each plot reveals distinct carrier peaks, with received power levels ranging approximately from –53.5 dBm to –60.3 dBm, indicating the presence of strong and stable 5G downlink transmissions.

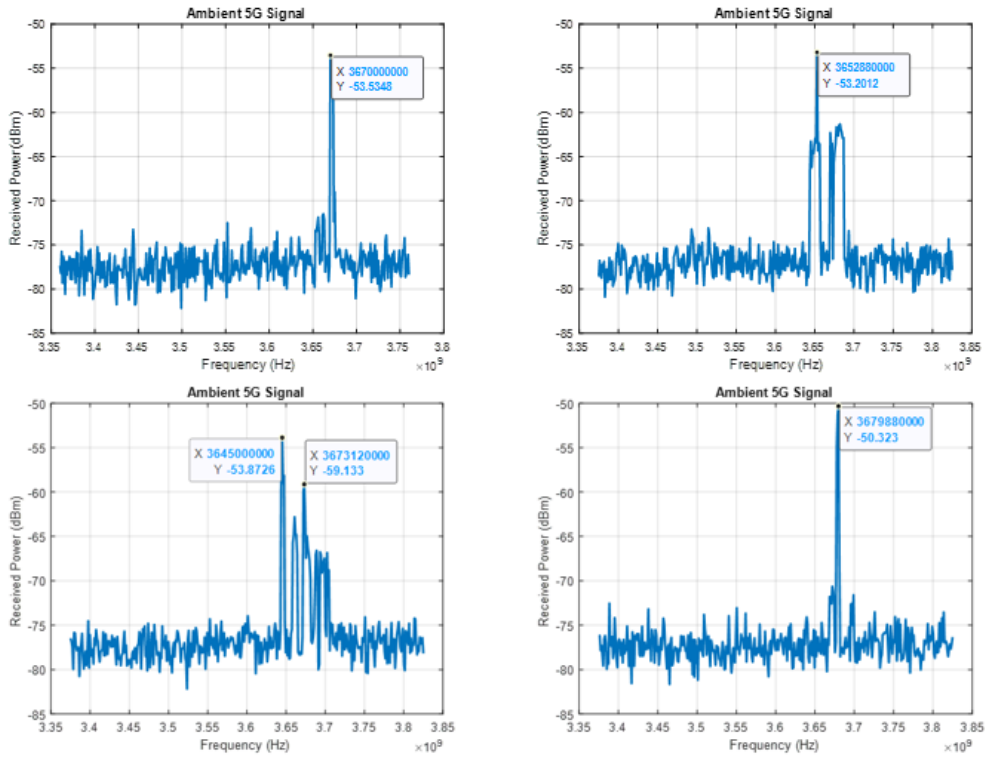

Figure 75. Power spectral density of ambient 5G signals captured at different frequency bands.

The variability observed across the plots both in frequency and power highlights the dynamic nature of the ambient spectrum, influenced by factors such as proximity to the base station, propagation conditions, and beamforming orientation. These ambient carriers, particularly those around 3.627 GHz with higher received power, offer promising opportunities for passive tag modulation in backscatter systems, providing sufficient signal strength for reliable reflection-based communication.

Figure 76 illustrates the experimental setup used to evaluate the feasibility of ambient 5G backscatter communication. The testbed was deployed in an urban outdoor environment, where a 5G base station, installed on the rooftop of a nearby residential building, served as the source of ambient RF signals. The central image highlights the overall field arrangement, showing the line of sight (LoS) between the base station and the receiver system positioned on a tripod. This receiver setup includes a directional antenna, a software defined radio (SDR), and a laptop for signal acquisition and processing. A passive backscatter tag, composed of a microcontroller and a reconfigurable load connected to an antenna, is mounted nearby on a fence post. The inset images provide close-up views of the base station, the receiving equipment, and the tag assembly. This configuration enables the reception of ambient 5G signals and their interaction with the backscatter tag, thereby allowing the characterization of the reflected signal under real-world propagation conditions.



Figure 76. Outdoor experimental setup for backscatter communication using ambient 5G signals.

Figure 77 presents the demodulated backscattered signal of the LM335 temperature sensor embedded in an ambient 5G environment. The main plot shows the spectral analysis of the received signal, where distinct peaks are observed above the noise floor. These spectral peaks correspond to data bits transmitted by the LM335 tag using backscatter modulation.

The points enclosed in green boxes represent successfully received data symbols from the LM335, with amplitude levels significantly higher than the surrounding noise, thereby confirming their detectability. The red boxes denote regions where the received power remains at the noise-floor level, indicating the absence of modulated information. The blue circles highlight additional spectral components that do not correspond to valid data bits, possibly arising from environmental reflections or system artifacts.

The inset plot provides a zoomed-in view of a decoded data sequence, where individual bits are distinguished by the presence or absence of spectral peaks, enabling the binary sequence "0001000" (decimal 16) to be accurately recovered. This result validates the system's capability to decode binary sensor data using ambient 5G signals as the excitation source, thereby demonstrating the practical feasibility of ultra-low-power backscatter sensing in real-world deployment scenarios.

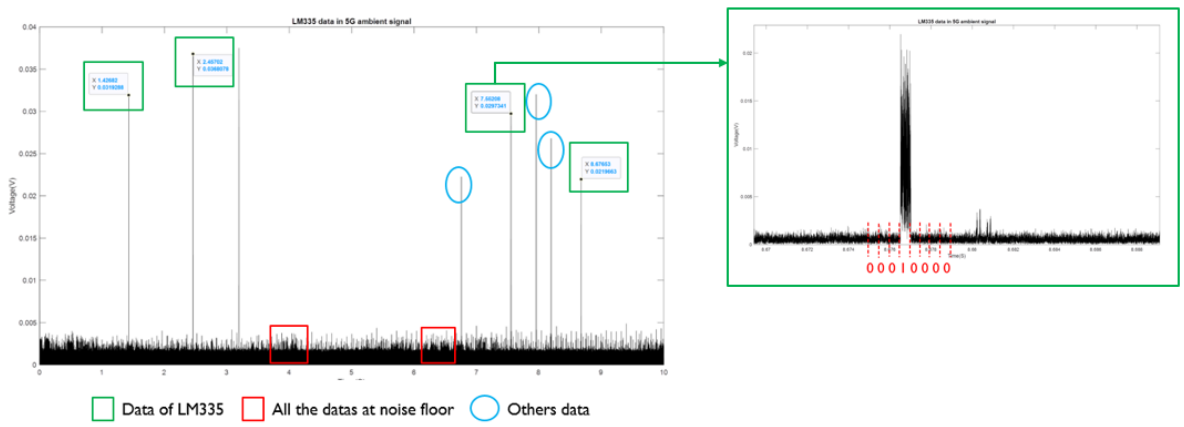

Figure 77. LM335 sensor data extraction using 5G ambient signal with backscatter modulation.

7. Conclusion

This chapter presented a comprehensive experimental validation framework for the ambient backscatter communication system proposed in this thesis. By integrating SDR tools, real-time signal processing, and custom-designed multi-sensor prototypes, we demonstrated the feasibility and reliability of backscatter-based wireless sensing in a variety of configurations. The results confirmed the accuracy of the bistatic propagation model and emphasized the influence of antenna orientation, sampling rate, and receiver sensitivity in the backscatter link performance. The measured BER trends were consistent with theoretical expectations, and the signal recovery process under different environmental and RF conditions was successfully illustrated and validated.

Through the deployment of two time-synchronized backscatter prototypes, including a biomedical sensor platform, we demonstrated that practical, low-cost, and energy-efficient IoT solutions can be realized using ambient RF energy and simple modulation strategies. In addition, we explored the system's adaptability to ambient RF sources, such as Wi-Fi and 5G, thereby revealing new opportunities for passive communication leveraging existing wireless infrastructure.

Overall, the experimental findings support the theoretical developments presented in previous chapters and validate the proposed approach for real-world ambient backscatter communications. These results lay a solid foundation for future research on multi-tag synchronization, adaptive thresholding, and large-scale deployments in heterogeneous wireless environments.

References

[1] USRP B210 SDR kit - Dual Channel Transceiver(70MHz - 60GHz), Datasheet, Ettus Research, [online]. Available : https://www.ettus.com/wp-content/uploads/2019/01/b200-b210_spec_sheet.pdf

[2] ESP8266EX Datasheet, Espressif Systems, [Online]. Available: https://www.espressif.com/sites/default/files/documentation/0a-esp8266ex_datasheet_en.pdf.

[3] MAX30100 Pulse Oximeter and Heart-Rate Sensor Datasheet, Maxim Integrated, [Online]. Available: https://datasheets.maximintegrated.com/en/ds/MAX30100.pdf.

[4] DS18B20 Programmable Resolution 1-Wire Digital Thermometer Datasheet, Maxim Integrated, [Online]. Available: https://datasheets.maximintegrated.com/en/ds/DS18B20.pdf.

[5] AD8232 Single-Lead, Low-Power Heart Rate Monitor Front End Datasheet, Analog Devices, [Online]. Available: https://www.analog.com/media/en/technical-documentation/data-sheets/AD8232.pdf.

[6] Saha, M. S., Lefki, M., Baccar, S., & Kadi, M. (2025). Development and Validation of a Low-Cost, Low-Power Patient Monitoring System Using AmBC Technique. In Proceedings of the International Multi-Conference on Systems, Signals and Devices (SSD 2025). IEEE. https://doi.org/10.1109/SSD64182.2025.10989912.

General Conclusion

This doctoral research has investigated the design, modeling, and experimental validation of bistatic AmBC system operating with 5G-NR signal. The motivation behind this work stems from the growing demand for low-power and low-cost connectivity solutions in IoT applications, where billions of sensors are expected to coexist in future networks. By exploiting 5G signals already present in the environment as carriers, 5G-NR AmBC provides an energy-efficient paradigm for large-scale deployments. Nevertheless, several challenges needed to be addressed, particularly regarding the feasibility of bistatic links, the severe attenuation of backscattered signals, and the design of practical tag and a dedicated receiver architecture.

The first contribution of this thesis, presented in Chapter 1, established a comprehensive state of the art. The fundamental principles of AmBC were described, including the modulation techniques and the classification of system architectures. The potential of 5G NR signals as ambient carriers was highlighted, together with the main challenges related to propagation, interference, and receiver design. This survey positioned the thesis within the broader research landscape and identified the scientific gaps addressed in the subsequent chapters.

The second contribution, detailed in Chapter 2, focused on the feasibility analysis of bistatic AmBC links based on standardized 3GPP propagation models. The study considered UMa, UMi, and RMa architectures in both LOS and NLOS conditions. A complete bistatic link budget framework was developed, including path loss modeling, received sensor power, receiver sensitivity, available path loss, and achievable range. Simulation results revealed that free-space assumptions largely overestimate feasibility, while 3GPP models provide more realistic insights. UMi and NLOS scenarios were shown to be the most constraining, while UMa-LOS and RMa-LOS offer the most favorable conditions. The analysis also emphasized the decisive role of sensor insertion losses and bandwidth in determining the achievable range. This study helps determine the optimal configuration of system components based on the predicted operating ranges under the considered scenarios.

The third contribution, presented in Chapter 3, addressed the design and experimental validation of a backscatter tag prototype operating at 3.5 GHz. The prototype integrated a microcontroller, an RF switch, a 5G antenna, and sensing elements such as temperature and biomedical sensors. A BPSK modulation scheme based on impedance switching was developed and employed for backscattered temperature data transmission. Moreover, a comprehensive theoretical propagation model based on the geometrical configuration (distances and angles) was proposed to predict the received power at the receiving node. Experimental campaigns were carried out

in controlled environments (anechoic and semi-anechoic chambers), showing good agreement between theoretical predictions and measurements, and confirming the feasibility of 5G-based bistatic AmBC links.

The fourth contribution, developed in Chapter 4**,** focused on the **receiver** architecture and experimental validation in real environments**.** An SDR-based receiver was implemented using a USRP B210 and GNU Radio, with a dedicated flowgraph including magnitude extraction, filtering, and threshold detection. Performance was assessed through BER measurements and multi-sensor synchronization experiments. Validation campaigns in corridors and outdoor environments demonstrated the practical operation of the system under realistic conditions, while highlighting the trade-offs between sensitivity, bandwidth, and system complexity.

Taken together, these contributions provide a complete exploration of bistatic AmBC using 5G signals, from theoretical feasibility analysis to hardware implementation and experimental validation. The thesis advances the field in several key aspects:

- It offers a rigorous analytical framework to evaluate the feasibility of bistatic AmBC in realistic scenarios. It demonstrates the practical feasibility of a developed 5G-based AmBC tag prototype operating at 3.5 GHz.
- It implements an SDR-based receiver system designed to recover backscattered signals carrying the sensor's measured temperature in the presence of dominant ambient carriers. It validates the concept experimentally in both controlled and real-world conditions (indoors and outdoors).

Despite these advances, several challenges remain open. The range of AmBC links is still limited, especially in dense urban and NLOS environments. The strong power asymmetry between the direct 5G signal and the backscattered component continues to constrain receiver design. Moreover, scalability to large numbers of sensors and integration with higher-layer protocols remain to be addressed.

Future work could explore advanced directions such as the integration of reconfigurable intelligent surfaces (RIS) to enhance link reliability, the use of machine learning techniques for robust detection under low SNR conditions, and the extension of AmBC to multi-band and 6G networks. Another promising avenue is the development of cooperative AmBC schemes, where multiple tags jointly exploit ambient signals to extend coverage and reliability.

In conclusion, this thesis demonstrates that bistatic AmBC with 5G NR carriers is a feasible and promising approach for enabling sustainable IoT connectivity. Through analytical modeling, hardware prototyping, and experimental validation, the work provides both

theoretical and practical insights that contribute to bridging the gap between concept idea and real-world implementation.

Appendix

1. Available Path Loss (APL) Comparison for RMa, UMa, and UMi (LOS/NLOS)

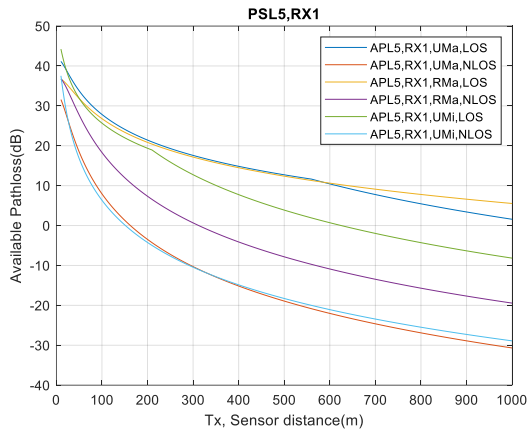

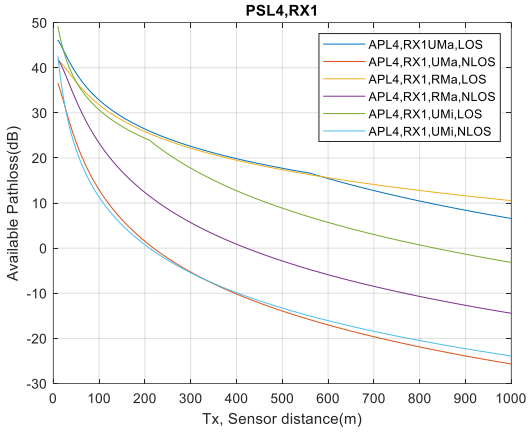

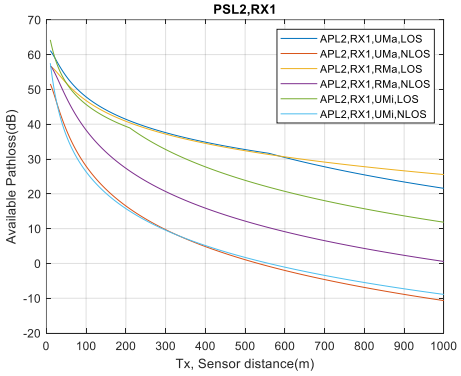

(a)

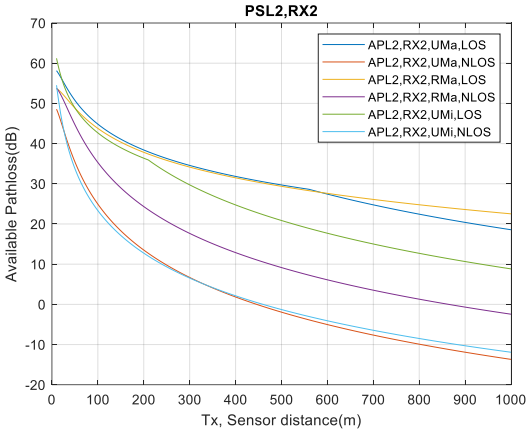

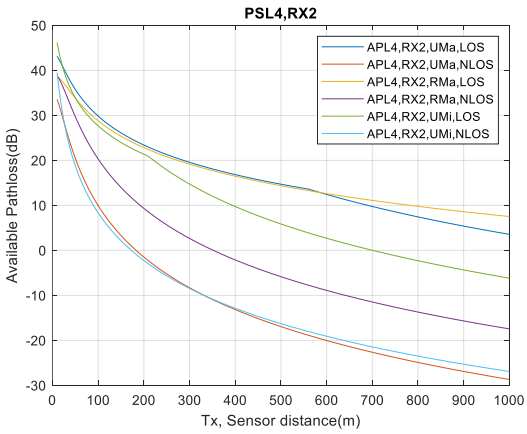

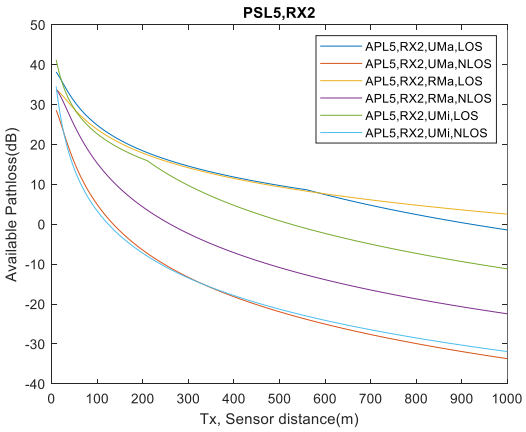

(b)

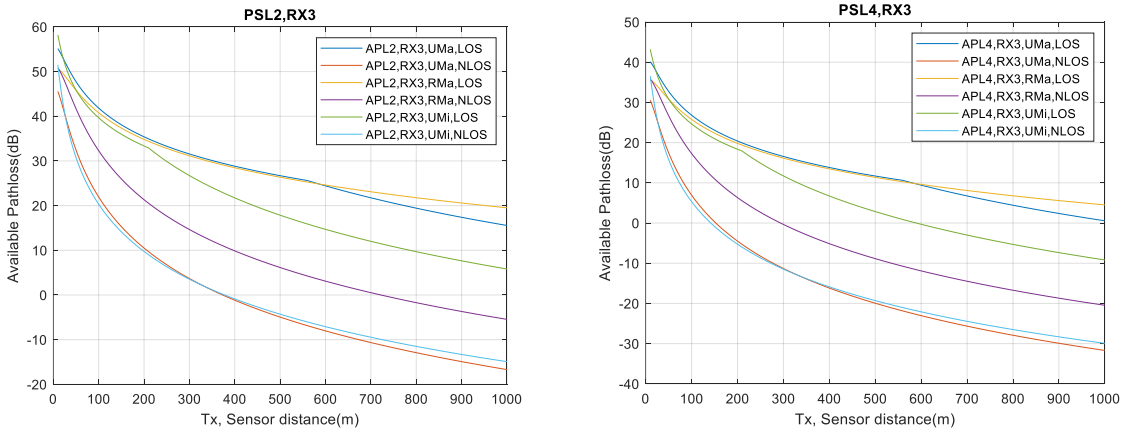

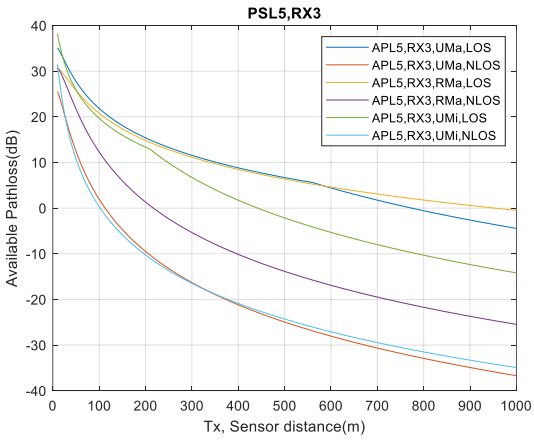

(c)

Figure 78. Comparison of Available Path Loss (APL) variations as a function of the TX–Sensor distance for the three receiver sensitivities (RX1, RX2, RX3) and different sensor loss levels (PSL = 5, 10, 15, 25, 30 dB).

2. BackCom Range Evaluation for the RMa Scenario

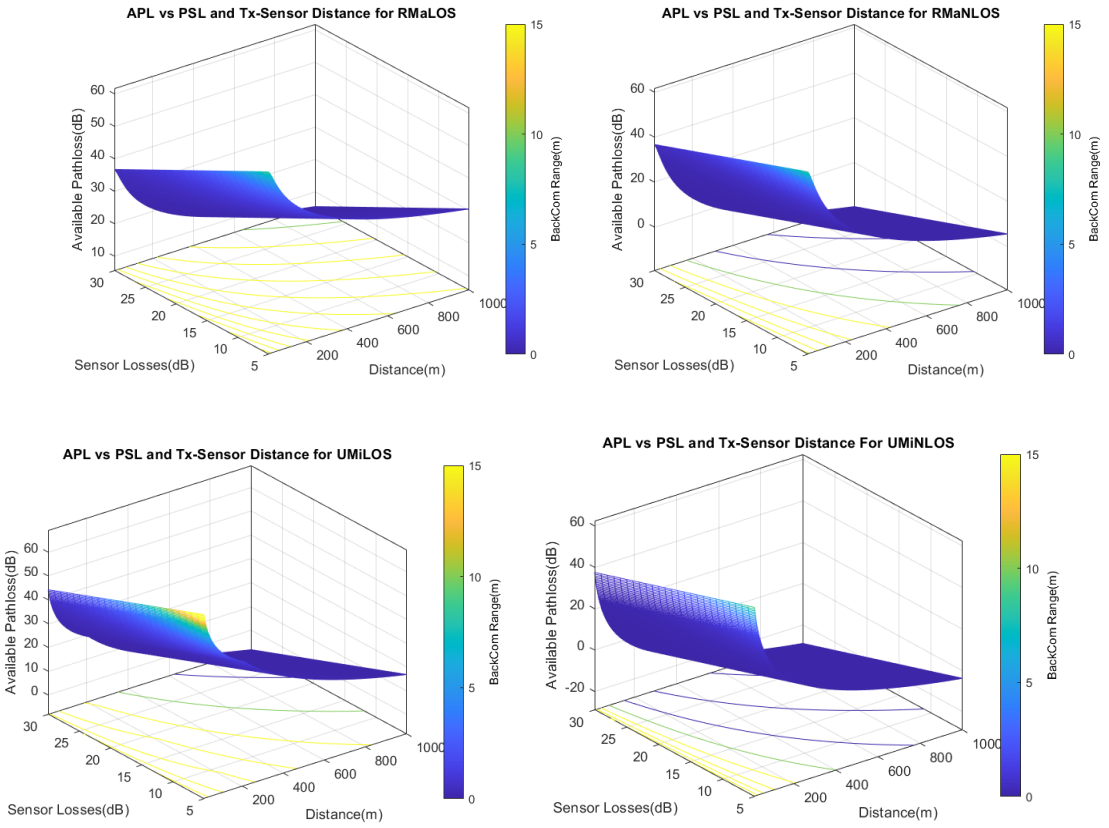

Figure 79. Estimated bistatic BackCom range as a function of sensor losses (PSL) and TX–Sensor distance under different 3GPP propagation environments Umi and Rma in LOS and NLOS conditions.

3. 3D representation of the Available Path Loss (APL) for the UMa Scenario

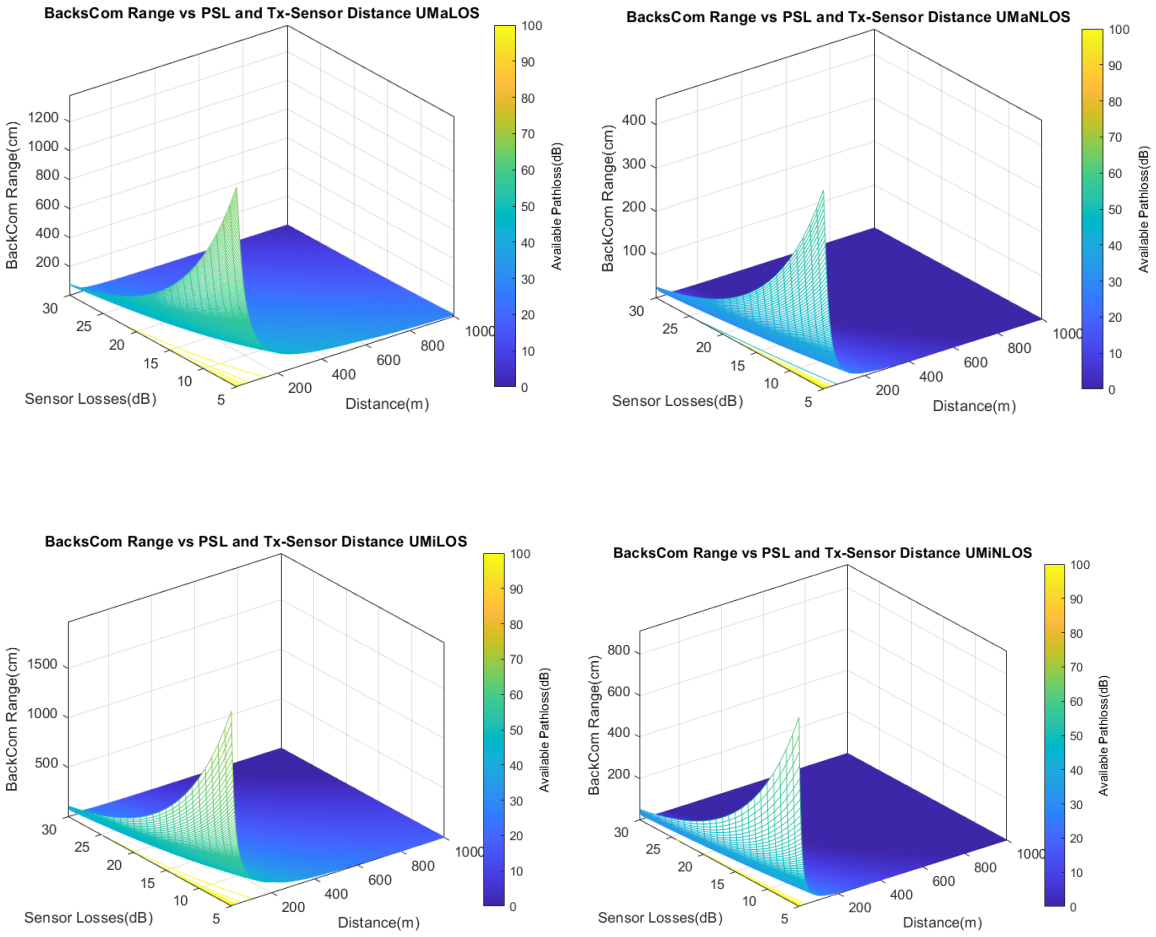

Figure 80. 3D representation of the Available Path Loss (APL) as a function of TX–Sensor distance and sensor losses (PSL) for different propagation models Rma and Umi under LOS and NLOS conditions.

4. Cartography of Available Path Loss for Different Bandwidths under the UMa Scenario

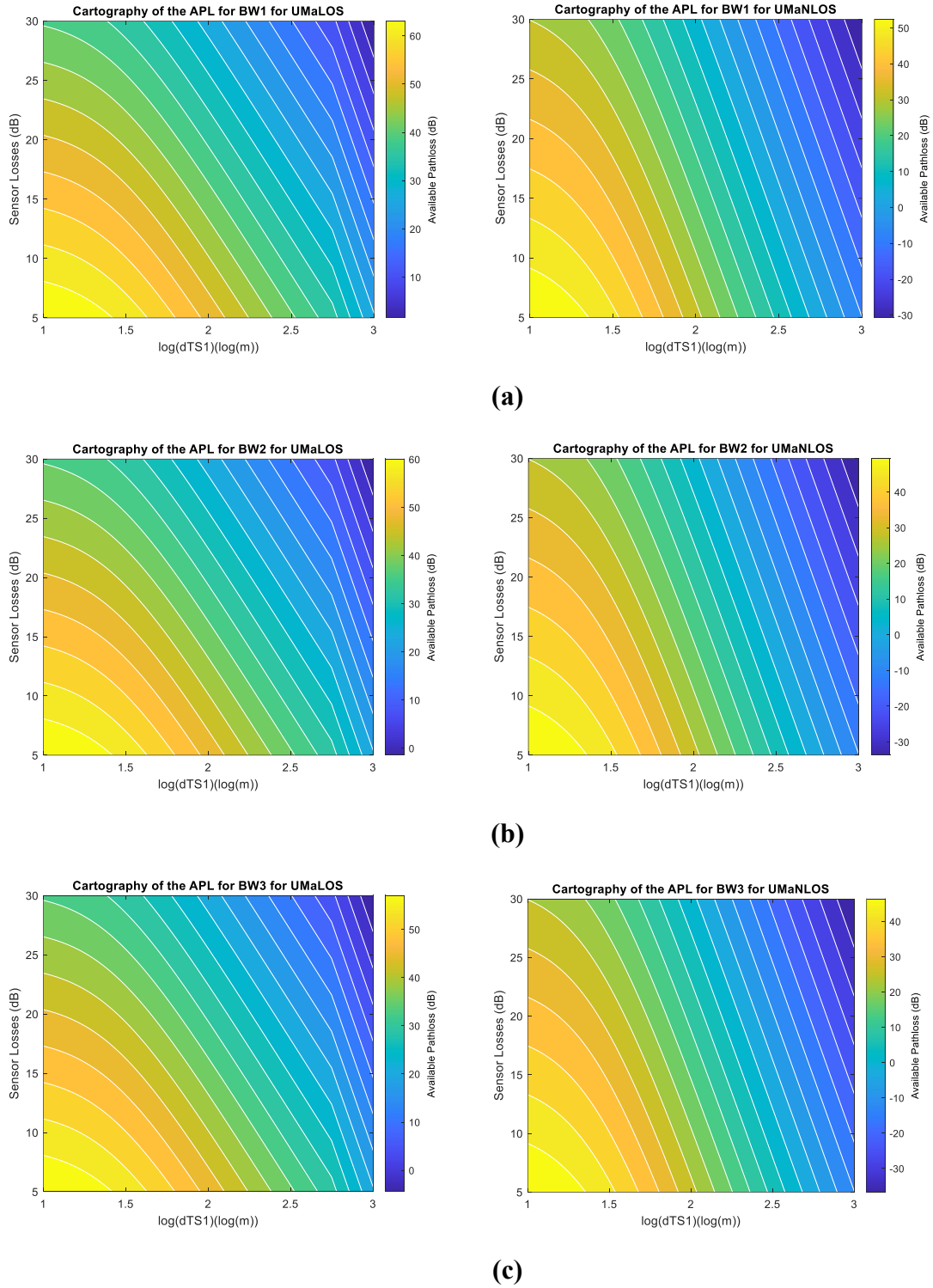

Figure 81. Available Path Loss (APL) versus TX–Sensor distance and sensor losses (PSL) for (a) BW_1 = 5 MHz, (b) BW_2 = 10 MHz, and (c) BW_3 = 20 MHz under UMa LOS/NLOS conditions.

5. Cartography of Available Path Loss for Different Bandwidths under the RMa Scenario

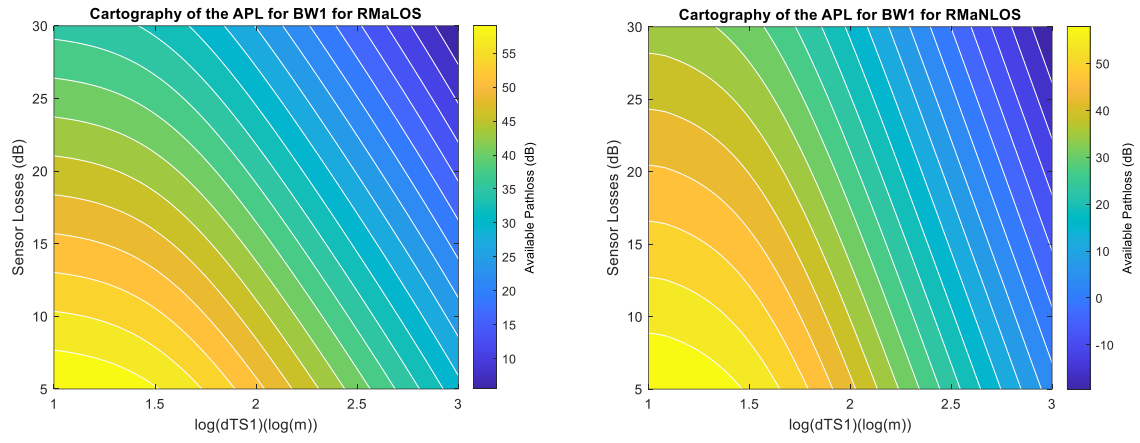

(a)

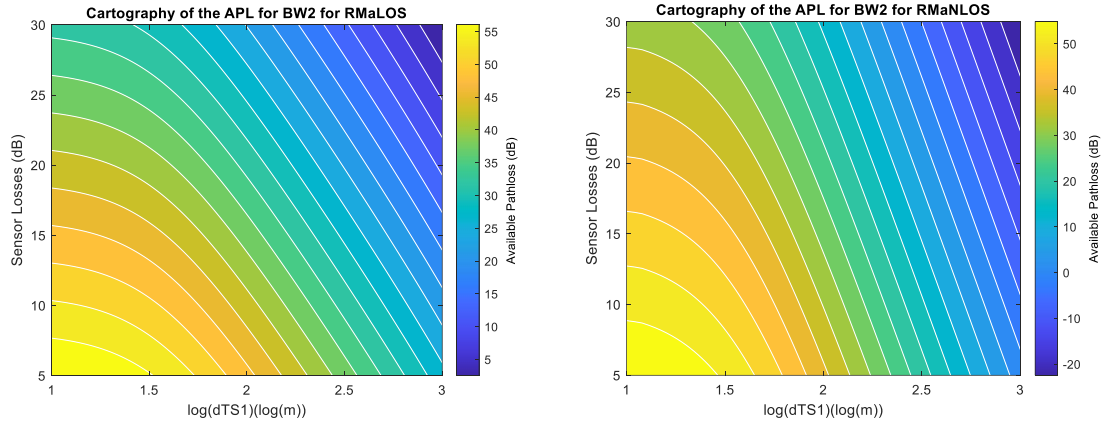

(b)

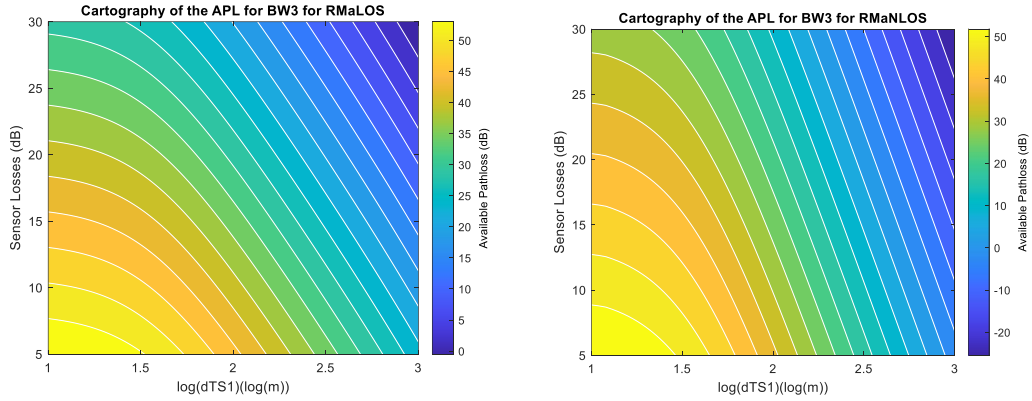

(c)

Figure 82. Available Path Loss (APL) versus TX–Sensor distance and sensor losses (PSL) for (a) BW_1 = 5 MHz, (b) BW_2 = 10 MHz, and (c) BW_3 = 20 MHz under RMa LOS/NLOS conditions.

6. Available BackCom Range under Different Propagation and Bandwidth Conditions for the UMi Scenario

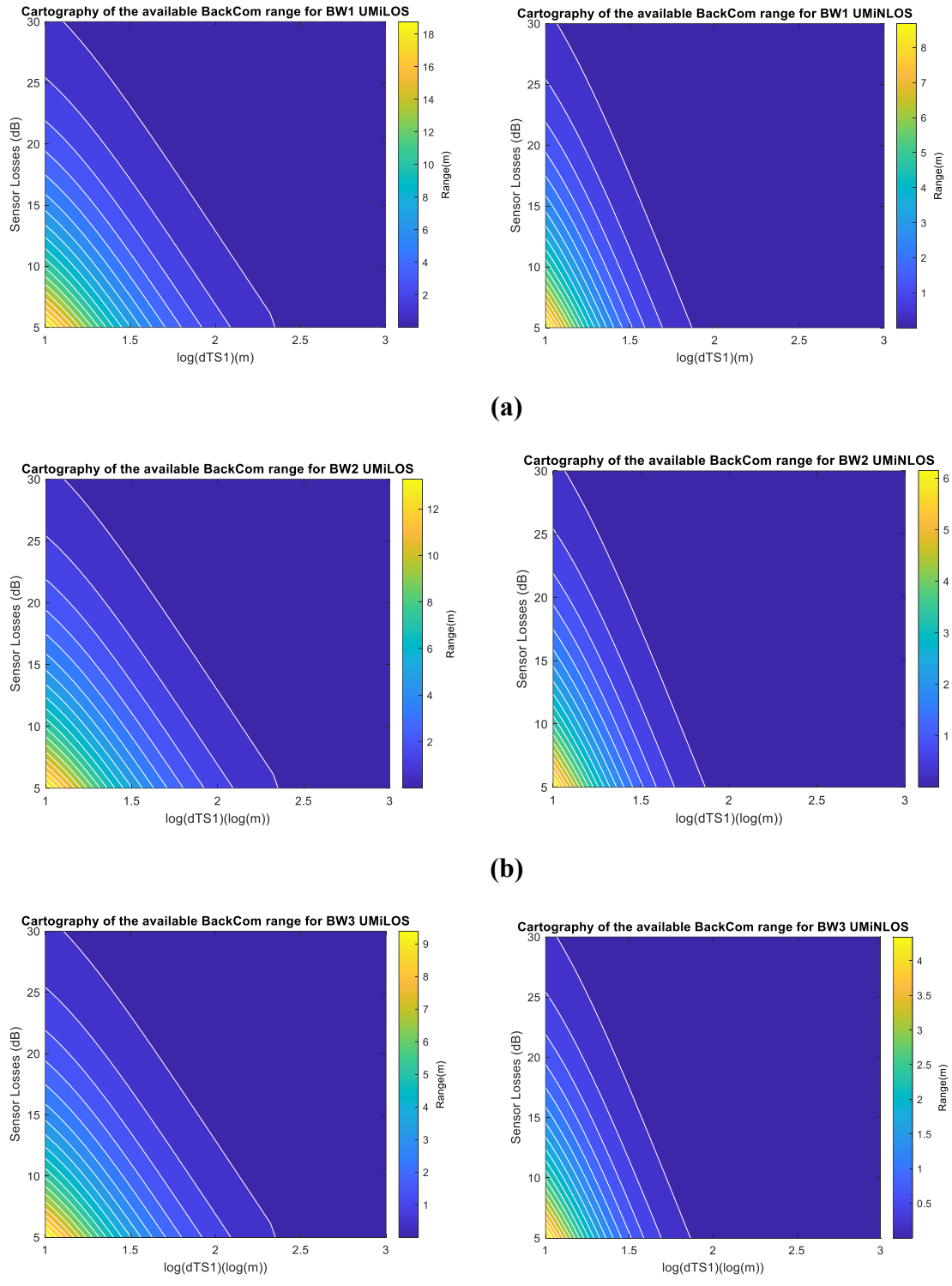

(a)

(b)

(c)

Figure 83. BackCom range maps (ρ) versus TX–Sensor distance and PSL for (a) BW_1 = 5 MHz, (b) BW_2 = 10 MHz, and (c) BW_3 = 20 MHz under UMi LOS/NLOS conditions.

7. Available BackCom Range under Different Propagation and Bandwidth Conditions for the UMi Scenario

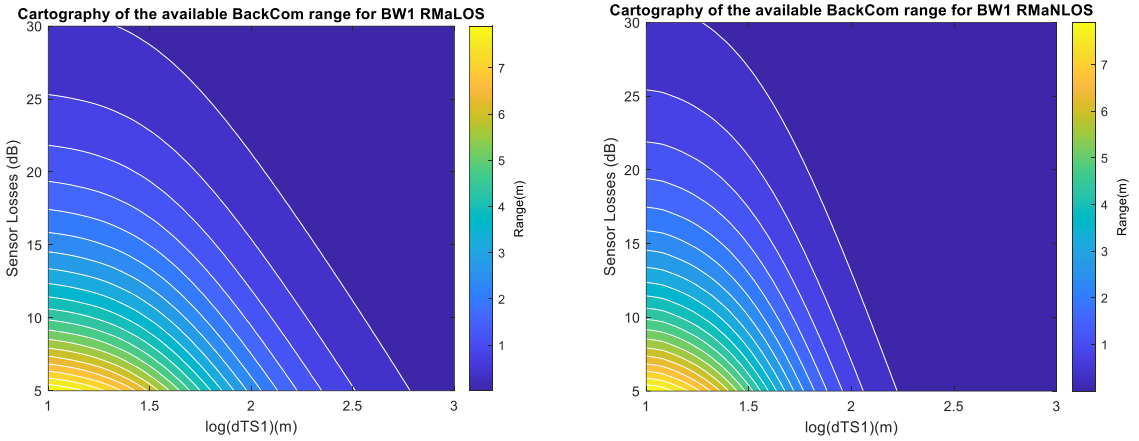

(a)

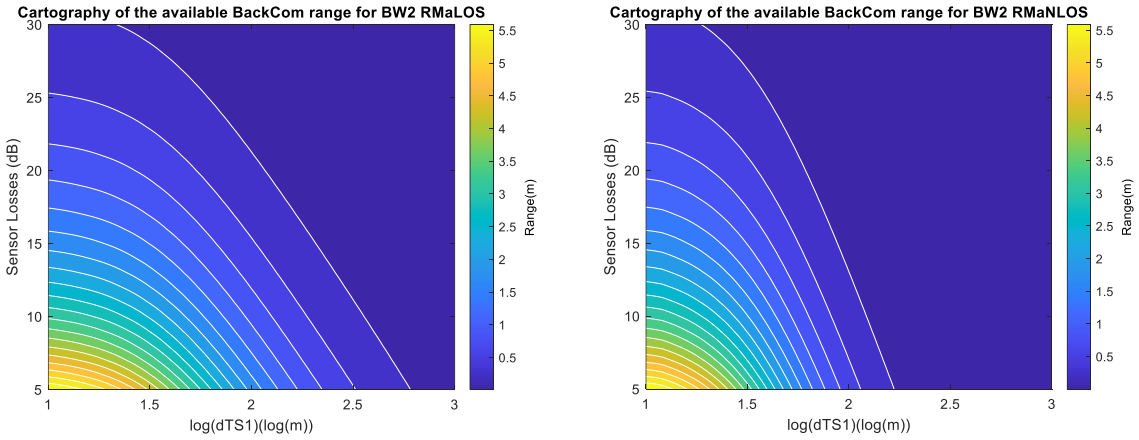

(b)

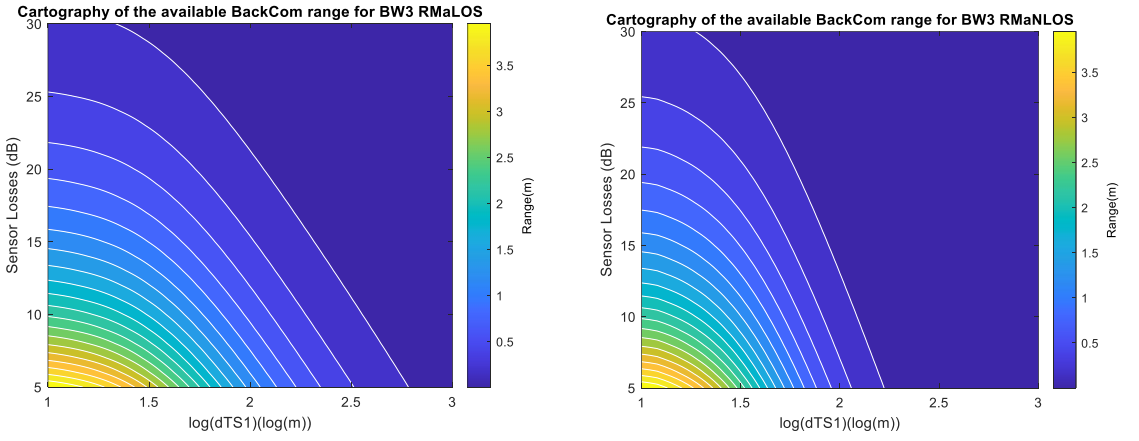

(c)

Figure 84. BackCom range maps (ρ) versus TX–Sensor distance and PSL for (a) BW_1 = 5 MHz, (b) BW_2 = 10 MHz, and (c) BW_3 = 20 MHz under RMa LOS/NLOS conditions.

List of publications

Journal papers

1. **M. Lefki**, M. S. Saha, S. Baccar, M. Kadi, H. Shall and M. Ghorbel, "Bistatic 5G-NR Ambient Backscatter Communication: Propagation Study and Experimental Validation in Anechoic Chambers," in *IEEE Journal of Radio Frequency Identification*, vol. 9, pp. 739-757, 2025, doi: 10.1109/JRFID.2025.3587632.
2. **M. Lefk**i, M. S. Saha, S. Baccar, M. Kadi, H. Shall and M. Ghorbel, "Innovative Receiver Strategies for Enhanced Performances in Ambient Backscatter Communication Systems" (to be submitted).
3. Moni Sankar Saha, Sahbi Baccar, **Mariem Lefki**, Moncef Kadi, H. Shall, M. Ghorbel, "Design of a Flexible Low Power Multi-Sensor Wearable Platform with Wi-Fi Backscatter for Health Monitoring", (to be submitted).

International Conferences with Proceedings

1. **M. Lefki**, S. Baccar, H. Shall, M. Ghorbel and M. Kadi, "5G Ambient Backscatter Communications: Achievable Range and Power Levels in an Urban Environment," *2022 IEEE 12th International Conference on RFID Technology and Applications (RFID-TA)*, Cagliari, Italy, 2022, pp. 74-77, doi: 10.1109/RFID-TA54958.2022.9924037.
2. **M. Lefki**, S. Baccar, M. Kadi, H. Shall and M. Ghorbel, "A First Prototype of an Ambient Backscatter Communication Tag Working in 5G-NR Frequency: Experimental Test and Power Levels Measurements," *2024 IEEE International Conference on RFID Technology and Applications (RFID-TA)*, Daytona Beach, FL, USA, 2024, pp. 58-61, doi: 10.1109/RFID-TA64374.2024.10965177.
3. M. S. Saha, **M. Lefki**, S. Baccar and M. Kadi, "Development and Validation of a Low-Cost, Low-Power Patient Monitoring System Using AmBC Technique," *2025 IEEE 22nd International Multi-Conference on Systems, Signals & Devices (SSD)*, Monastir, Tunisia, 2025, pp. 902-907, doi: 10.1109/SSD64182.2025.10989912.
4. M. S. Saha, S Baccar, M Kadi, **M Lefki**, M Grzeskowiak, "Investigation of Displacement Effects of Tag on Reader: A Study on Antenna Performance and Power Dynamics", International Conference on Electrical, Computer and Energy Technologies (ICECET), Paris, 7/2025.

5. S. Baccar, **M. Lefki**, M. S. Saha, M. Kadi, H. Shall and M. Ghorbel, "*Investigation of Power Levels and Phase Variations from Interference Between Ambient Backscattered and Direct Signals in 5G-NR Free Space and Indoor Scenarios",* IEEE RFID-TA 2025 (accepted).

National Conferences

1. **M. Lefki**, S. Baccar, H. Shall, M. Ghorbel, M. Kadi "Development of a 5G Backscatter Communication Tag's Architecture for RF signal propagation in an urban environment", 10ème Conférence Plènière GDR Ondes, December 2023, Marseille.